

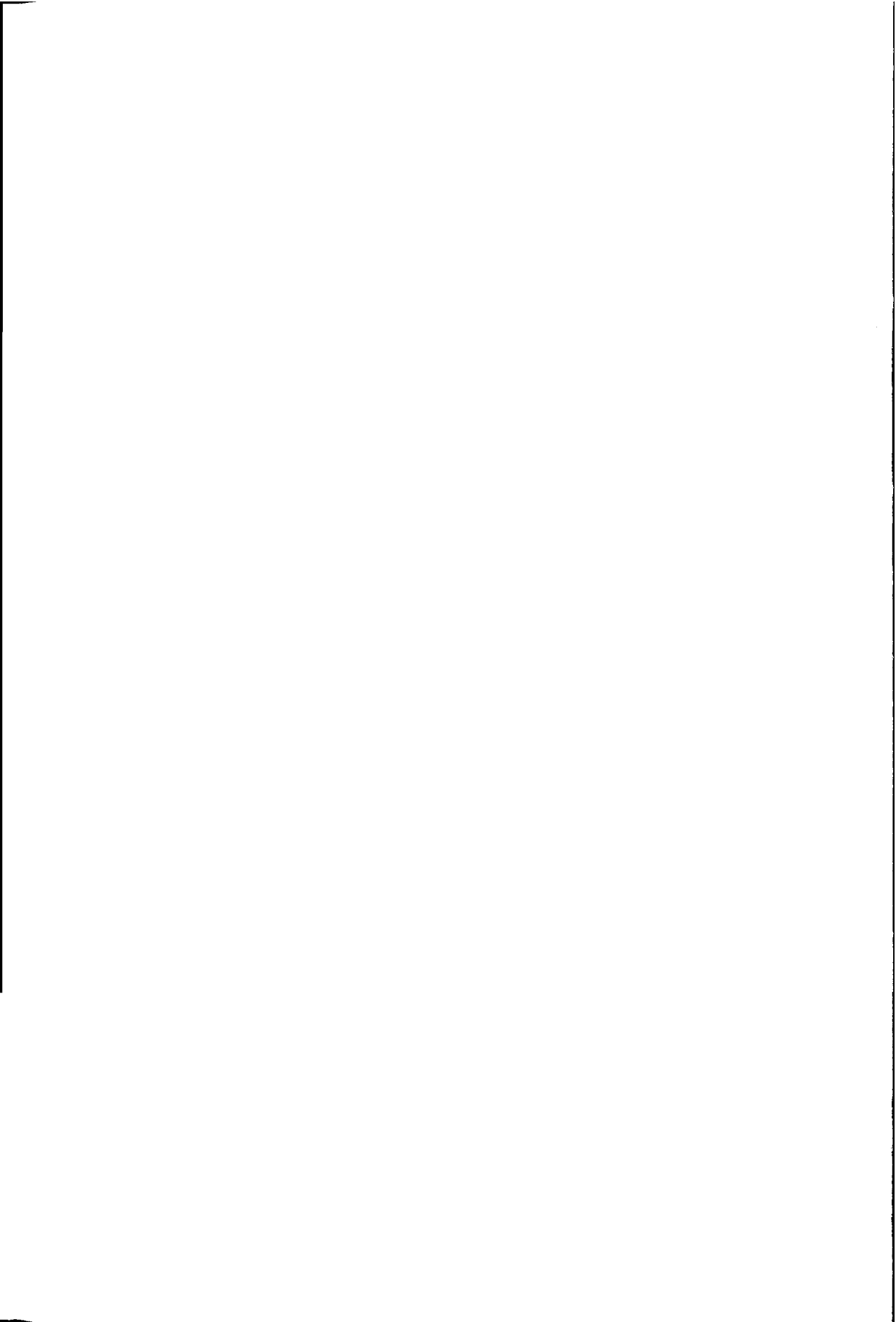
3585

7/29/16

20

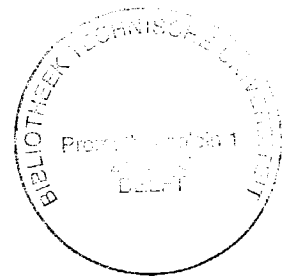
TR 3585

**Modelling Steel Fibre Reinforced Concrete
for Structural Design**



Modelling Steel Fibre Reinforced Concrete for Structural Design

Proefschrift



ter verkrijging van de graad van doctor
aan de Technische Universiteit Delft,
op gezag van de Rector Magnificus prof.ir. K.F. Wakker,
voorzitter van het College voor Promoties,
in het openbaar te verdedigen op maandag 30 oktober 2000 om 13.30 uur

door Alain Geoffré KOOIMAN

civil ingenieur
geboren te Capelle aan den IJssel.

Dit proefschrift is goedgekeurd door de promotor:

Prof.dr.ir. J.C. Walraven

Samenstelling promotiecommissie:

Rector Magnificus,
Prof.dr.ir. J.C. Walraven,
Dr.ir. C. van der Veen,
Dr.ir. D.A. Hordijk,
Prof.dr.ir. J.G.M van Mier,
Prof.dr.-ing. H.W. Reinhardt,
Prof.dr.ir. L. Vandewalle,
Prof.ir. A. Vrouwenvelder,

Technische Universiteit Delft, voorzitter.
Technische Universiteit Delft, promotor.
Technische Universiteit Delft, toegevoegd promotor.
TNO Bouw.
Technische Universiteit Delft.
Universiteit Stuttgart, Duitsland.
Katholieke Universiteit Leuven, België.
Technische Universiteit Delft.

ISBN 90-73235-60-X

Copyright © 2000 by A.G. Kooiman

Cover design by J.M. Brans and A.G. Kooiman

All rights reserved.

No part of the material protected by this copyright notice may be reproduced or utilised in any other form or by other means, electronic or mechanical, including photocopying, recording or by any information storage and retrieval system, without permission from the author.

Printed by Optima Grafische Communicatie, Rotterdam

Summary

As the number of practical applications of Steel Fibre Reinforced Concrete (SFRC) increases, the demand for standardised test methods and design guidelines arises. To satisfy these demands, test methods need to be evaluated so that a proper choice for the most suitable test method can be made. Furthermore, it is necessary to develop a procedure that will convert test results to a reliable material model for SFRC.

A reliable material model, however, does not necessarily lead to reliable SFRC structural applications. Insight into the structural behaviour of SFRC is required to increase the reliability of SFRC structures. A clear understanding of the material's post-cracking behaviour and the parameters that influence this behaviour is therefore of paramount importance.

To understand the behaviour of SFRC, Part I of this thesis deals with several material properties. Based on the pullout behaviour of individually embedded steel fibres, it shows that the matrix quality, the fibre characteristics and the fibre orientation are important parameters that influence the post-cracking behaviour of SFRC (Chapter 2).

After an assessment of available test methods, the three-point bending test has been chosen to test the post-cracking behaviour of SFRC (Chapter 3). Tests on practical standard test specimens showed that the post-cracking behaviour of SFRC is characterised by a relatively large scatter in energy absorption capacity, which is expressed by the coefficient of variation V_G . The coefficient of variation depends on the matrix quality, the fibre volume and the fibre distribution. It showed that the fibre distribution strongly depends on the way of pouring and the method of compaction of the test specimens. In test specimens with a beam depth and beam width 7.5 times larger than the fibre length, the observed coefficient of variation is considerably smaller than in case of 'standard' specimens, of which the cross-sectional dimensions were only 2.5 times the fibre length.

Part II deals with modelling methods to describe the post-cracking behaviour of SFRC. The available modelling methods are described and evaluated, after which a choice is made to describe the post-cracking behaviour by means of inverse analysis of SFRC cross-sections subjected to a bending moment (Chapter 4).

Several parameters influence the computations in an inverse analysis. With the help of a simple computational procedure, the influence of these parameters was systematically investigated. Based on this parameter survey and a comparison of computed results with measurements, it showed that a bilinear stress-crack width relation accurately describes the softening behaviour of SFRC (Chapter 5).

In part III, the material behaviour in the laboratory is translated to its behaviour in structural applications. The effectiveness of the fibre reinforcement in test specimens is theoretically determined as a function of the mean fibre orientation, which is related to the production process of the test specimens. After relating this theoretical effect to the bilinear post-cracking relation, it is shown that the mean projected embedded fibre length is directly related to the critical crack width in the stress-crack width relation. In addition, it shows in what way the direction of pouring, the flowing distance, the method of compaction and the geometrical boundaries affect the fibre orientation in structural applications. As a consequence, the fibre orientation efficiency can be predicted for several structural applications, such as steel fibre reinforced underwater concrete slabs and prefabricated SFRC tunnel segments. Hence, the flexural behaviour of a structural SFRC cross-section in practice can be predicted (Chapter 6).

When designing a structure, several uncertainties have to be accounted for. In practice, these uncertainties are processed into safety factors. In addition to the accuracy of the modelling method used, scatter in load and resistance are accounted for in the determination of material safety factors for the post-cracking behaviour of SFRC, based on standard reliability methods (Chapter 7).

Part IV shows that the resulting design model can be easily used to perform structural design calculations, although these calculations are limited to cross-sectional analyses. Design calculations are made for SFRC tunnel segments, making use of the design relation developed in the previous parts. The case under consideration is the first shield tunnelling project in the Netherlands, also known as the 2nd Heineoord tunnel (Chapter 8). It shows, however, that the resistance to the bending moments is not at all critical. The resistance to splitting stresses, however, is critical.

This thesis provides a procedure to develop a reliable, bilinear stress-crack width relation to describe the post-cracking behaviour of SFRC. With the help of inverse analysis, the material model can be used to make cross-sectional calculations with sufficient accuracy, taking several material parameters into account. The main question for the future, however, is how to model the post-cracking behaviour of SFRC so that the redistributing capacity of the material can be fully utilised in structural calculations. In addition, the resistance to splitting stresses needs to be examined in more detail.

Alain Kooiman

Acknowledgements

This thesis reports on a research project carried out at the Stevin Laboratory of the Delft University of Technology. Financial support of the Civil Engineering Department of the Directorate-General of Public Works and Water Management, the Dutch Centre for Underground Construction (COB) and the Dutch Foundation for Technical Sciences (STW) is gratefully acknowledged.

I would like to express my sincere recognition to my supervisor Joost Walraven for creating the opportunity and providing optimum conditions to carry out this PhD research project. Apart from that, I really appreciate his support and patience for letting me express and develop myself by other means than my research work. His critical comments along the way formed a valuable contribution to this thesis.

My deepest gratitude goes out to my daily supervisor Cor van der Veen. I would like to thank him for his inspiring positivism and his guidance during the research project. His encyclopaedic professional knowledge is very well respected. Furthermore, he was always there when I needed a pat on the back or a small talk.

The experimental work would not have been realised without the enthusiastic dedication of Albert Bosman and the expert help of Fred Schilperoort. I am very grateful for them carrying out the numerous tests and solving all technical problems. Of course, I want to thank Ger Nagtegaal for his IT-support and all my other colleagues of the Concrete Structures Group for their assistance during my research project. In addition, I would like to record my appreciation to Peter Roelfstra and Jan Stroband for their advice in the design of the experiments.

Words of thanks are addressed to Rene Braam, Steffen Grünwald, Bas Obladen and Petra Schumacher who read preliminary versions of this thesis and gave me feedback on content, language and style. For preparing all drawings in this thesis, I thank 'Mental Theo' Steijn, who's work is highly appreciated.

I owe special thanks to Roland de Waal, my roommate and friend, for sharing all the good and bad times in the lab. I would not have managed to achieve many things without him. I also thank Arjen van Rhijn and Allard Elgersma for the laughs in PSOR and my homeboys for letting me be myself.

Finally, I would like to thank my parents, brother and girlfriend for their love, support and patience.

Alain Kooiman

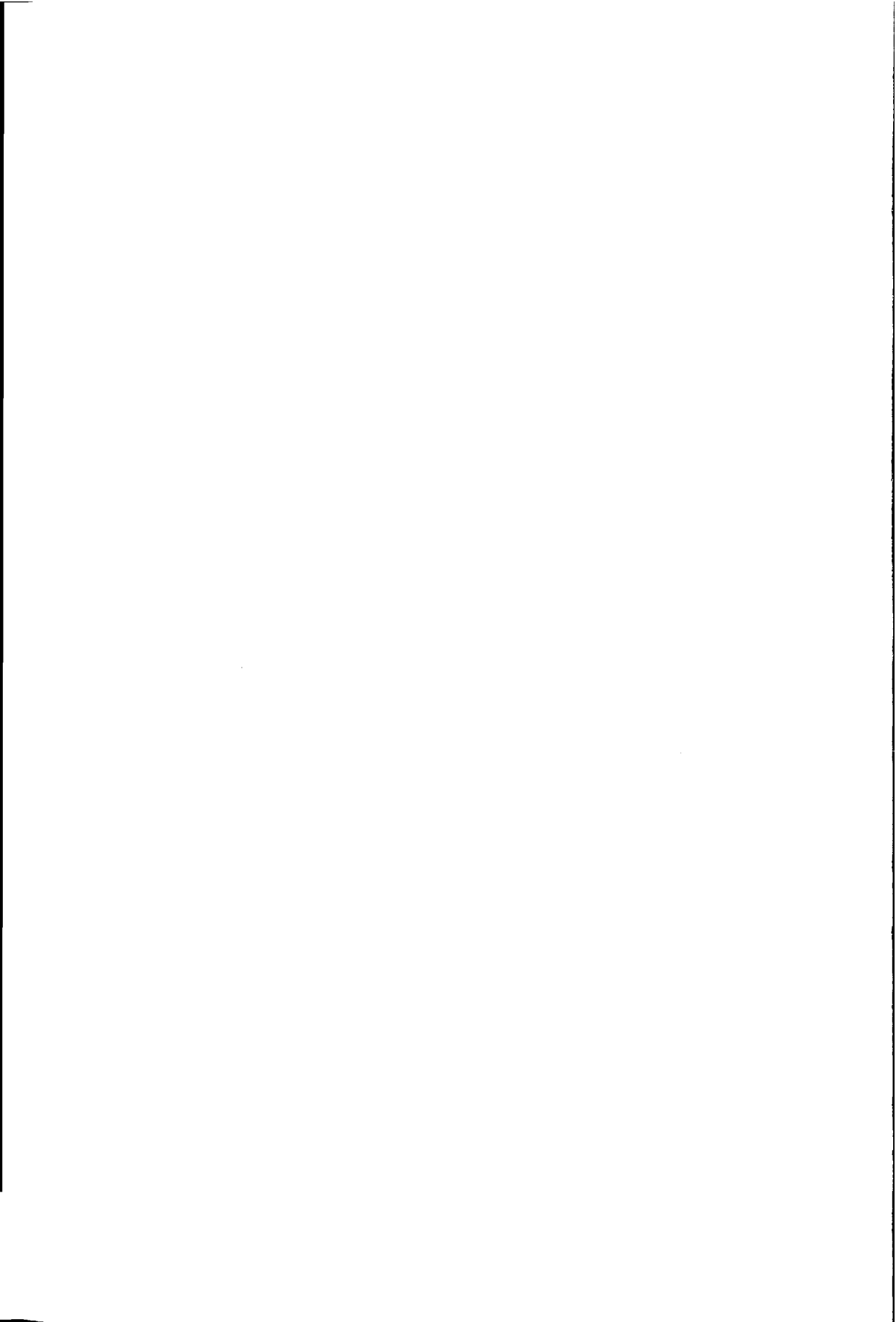


Table of Contents

Summary

Acknowledgements

1	Introduction	1
1.1	Scope	1
1.2	Research objective	2
1.3	Research strategy	2
1.4	Outline of thesis	3

PART I PROPERTIES OF SFRC

2	Material properties of SFRC	5
2.1	Introduction	5
2.2	Rheological properties of SFRC	6
2.2.1	Design of SFRC mix compositions	6
2.2.2	Workability of SFRC mixtures	9
2.3	Properties of hardened SFRC	11
2.3.1	Pull-out behaviour of steel fibres	11
2.3.2	Tensile behaviour of SFRC	14
2.3.3	Compressive behaviour of SFRC	16
2.3.4	Flexural behaviour of SFRC	18
2.3.5	Shear behaviour of SFRC	19
2.4	Durability of SFRC	19
2.4.1	Resistance to corrosion	19
2.4.2	Mechanical durability	20
2.5	Severe load conditions	21
2.6	Concluding remarks	22
3	Experimental research on SFRC	23
3.1	Introduction	23
3.2	Assessment of testing methods	23
3.2.1	Criteria for a suitable testing method	23
3.2.2	Bending tests	24

3.2.3	Splitting tests	25
3.2.4	Uni-axial tensile tests	27
3.2.5	Multiple Criteria Assessment of test methods	28
3.2.6	Experimental research by means of three-point bending tests	29
3.3	Experimental programme	30
3.3.1	Research parameters	30
3.3.2	Test set-up	30
3.3.3	Specimen sizes	32
3.3.4	Production and curing of specimens	33
3.4	Test results	34
3.4.1	Energy absorption capacity G_{fc} and coefficient of variation V_G	34
3.4.2	Effect of matrix quality on mean G_{fc} and V_G	35
3.4.3	Effect of fibre characteristics on mean G_{fcm} and V_G	36
3.4.4	Effect of fibre volume on mean G_{fc} and V_G	37
3.4.5	Testing size effects on the post-cracking behaviour	38
3.4.6	Effect of the production process on the fibre distribution	41
3.5	Concluding remarks	42

PART II MODELLING SFRC

4	Evaluation of existing modelling methods for SFRC	45
4.1	Introduction	45
4.2	Description of existing modelling methods	46
4.2.1	Stress-crack width methods	46
4.2.2	Crack band method	51
4.2.3	Stress-strain methods	52
4.3	Assessment of existing modelling methods	59
4.3.1	Discussion of existing modelling methods	59
4.3.2	Demands for a suitable and reliable modelling method	62
4.4	Concluding remarks	64
5	Development of improved constitutive relations for SFRC	67
5.1	Introduction	67
5.2	Attaining constitutive relations via inverse modelling	67
5.3	Analysis of SFRC cross sections with the multi-layer approach	74
5.3.1	Effect of the simulation procedure	74
5.3.2	Influence of the compressive behaviour	75
5.3.3	Influence of the tensile behaviour	76
5.3.4	The effect of the dimensions of the cross-section	83
5.4	Discussion of results	85
5.5	Concluding remarks	86

PART III DEVELOPMENT OF A SAFETY PHILOSOPHY FOR SFRC

6	From specimen to structure	87
6.1	Introduction	87
6.2	Fibre orientation, efficiency and effectiveness	88
6.3	Fibre orientation and effectiveness in test specimens	93
6.3.1	Effect of casting and compaction on fibre orientation and effectiveness	93
6.3.2	Effect of fibre effectiveness on the flexural behaviour of SFRC	96
6.4	Fibre orientation and average efficiency in promising practical applications	99
6.5	Concluding remarks	105
7	Reliability in design of SFRC structures	107
7.1	Introduction	107
7.2	Determination of characteristic values	108
7.2.1	Statistical parameters of physical variables	108
7.2.2	Effect of the coefficient of variation on the characteristic strength values	109
7.3	Probabilistic design in general	111
7.3.1	Standard reliability methods	111
7.3.2	Effect of coefficient of variation and reliability index on partial factors	116
7.3.3	Accuracy of the reliability method	118
7.4	Bilinear design relationship for the post-cracking behaviour of SFRC	119
7.5	Material testing and quality control	121
7.6	Concluding remarks	122

PART IV CASE STUDY

8	Design of SFRC tunnel segments	123
8.1	Introduction	123
8.2	Loads and limit states	124
8.2.1	Load conditions and structural design models	124
8.2.2	Limit states in the design of tunnel linings	128
8.3	Design of SFRC tunnel segments for the 2 nd Heinenoord tunnel	129
8.3.1	Introduction of the case	129
8.3.2	Material properties	131
8.3.3	Partial safety factors for structural design	132
8.3.4	Maximum cross sectional forces and working load of thrust jacks	134
8.3.5	Design calculations of SFRC tunnel segments	135
8.4	Concluding remarks	142

PART V FINAL REMARKS

9	Conclusions and future perspectives	143
9.1	Conclusions	143
9.2	Future perspectives	145
	Bibliography	147
	Appendices	
A	Scenarios for Multiple Criteria Analysis of testing methods	155
B	Compensation of specimen's weight in determination of G_{Ic}	157
C	Orientation efficiency close to a boundary	159
	Notations and symbols	163
	Samenvatting	167
	Stellingen	169
	Curriculum Vitae	

Chapter 1

Introduction

1.1 Scope

Fibre Reinforced Cementitious Composites (FRCC) is the generic term for a large group of composites with a variety of properties. Cementitious composites, such as concrete, are materials that are characterised by brittle failure behaviour in tension. The reason for adding fibres to cementitious composites is to improve this tensile behaviour. Generally speaking, fibres can increase the tensile strength and the ductility of brittle materials. To what extent the tensile behaviour can be improved depends on a number of parameters. Fibre characteristics, fibre quantity, fibre distribution in the matrix, fibre orientation with regard to the crack plane and the quality of the cementitious matrix surrounding the fibres all affect the tensile behaviour at the same time. In this dissertation the focus is on Steel Fibre Reinforced Concrete (SFRC).

In the past decades a lot of research has been carried out on SFRC. Various efforts have resulted in an increasing number of applications over the past years. Pavements, for example, have been constructed with SFRC in different countries all over the world. Quite recently, SFRC has also been implemented in pilot projects for other applications, such as for an underwater concrete floor at the Potsdamer Platz in Berlin [Falkner and Henke, 1995] and in prefabricated tunnel segments for a tube section in the 2nd Heineoord tunnel, near Rotterdam [Kooiman et al, 1998].

With the increasing number of applications in practice, the demand for standardised test methods and design rules grows. Test methods need to be practical, which means they have to be relatively cheap and simple to carry out and design models should be effective, easy to use and reliable. Quite recently, the RILEM Technical Committee 162 TDF published Draft Recommendations on how to test and model the behaviour of SFRC [RILEM TC 162 TDF, Jan-Feb 2000], [RILEM TC 162 TDF, March 2000]. These Recommendations are the first serious attempts to meet the demand for practical tests and reliable material relations. The stress-strain material relation for the uni-axial behaviour of SFRC, as proposed by the RILEM Committee, is based on the earlier published relation of the German Concrete Society [DBV-Merkblatt, 1992]. The latter has been used in the design of SFRC tunnel segments applied in the 2nd Heineoord tunnel [Kooiman, 1997].

During modelling of the material behaviour in the design of the tunnel segments, the author encountered several issues that needed further investigation. One issue was that the derivation of the tensile component of the stress-strain diagram follows a rather strange

procedure. Vertical deformations, i.e. the deflection measured at mid-span of a tested beam specimen, need to be translated to horizontal strains in the material relation. Another important issue was that the test results on 'standard' SFRC beams showed that the scatter in the post-cracking behaviour is relatively large compared to the scatter in compressive and tensile strength values of plain concrete. As a consequence, safety factors developed for plain concrete might not apply for the post-cracking behaviour of SFRC.

1.2 Research objective

The main objective of this research project is to develop a procedure that will lead to a reliable material model for SFRC, which is based on a proper safety philosophy and can be used in structural design calculations.

In practice, insight into the structural behaviour of SFRC will increase the reliability of SFRC structures. Therefore, a clear understanding of the material's behaviour and the parameters that influence this behaviour is of paramount importance. A procedure aimed at obtaining a design model for SFRC would be quite valuable in this respect. Not only could such a procedure contribute to the applicability of SFRC in practice, it could also enhance people's general understanding of the material's behaviour. As a consequence, the structural reliability in reality would be increased.

In the development of a procedure to generate a reliable design model one has to deal with several uncertainties. An important aspect of a design model is the reliability of the model itself in relation to the test results. In addition, a certain variation occurs in the material's behaviour, which has to be accounted for in this design model. In the end, however, it should be suitable for making reliable structural design calculations. The model should therefore be able to predict the material's behaviour in practical applications.

1.3 Research strategy

To achieve the objective of this research project the following strategy was developed: the project was divided into five levels, the first four levels of which form this dissertation. Since all levels are closely related to one another the project was carried out in a more or less iterative manner. This is schematically reproduced in Figure 1.1.

The research started out with a literature survey on SFRC and its applicability to the linings of tunnel structures [Kooiman, 1996]. Afterwards, experiments were carried out at the Delft University of Technology's Stevin Laboratory [Kooiman, 1997] to support the design of SFRC tunnel segments. After a design review was made, 128 tunnel segments were produced. The production process was evaluated and additional experiments followed to determine the material properties in practice [Kooiman, 1998]. Finally, the segments were installed in the 2nd Heineoord tunnel in 1998.

In a relatively short period of time, all five levels in Figure 1.1 had been run through. Subsequently much insight was gained into the basic problems of designing a SFRC structure in general and SFRC tunnel linings in particular. The research then focussed on the first three levels and the blanks that were encountered in the first loop. Level IV was thoroughly investigated by De Waal [De Waal, 1999].

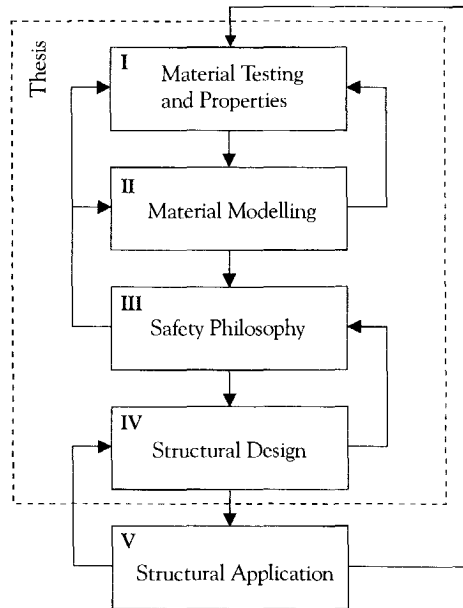


Figure 1.1 The research project as an iterative process

1.4 Outline of thesis

This thesis is subdivided into five parts. Part I coincides with level I of figure 1.1, part II with level II, part III with level III and part IV with level IV. Level V of Figure 1.1 is not discussed in this thesis, but has been discussed by Kooiman [Kooiman et al., 1999] in the past. Part V ends this thesis with some final conclusions and future perspectives.

Part I deals with testing the mechanical properties of SFRC and the parameters that influence these properties. It aims at providing a clear understanding of the material's behaviour and consists of two chapters.

In Chapter 2 an overview of the characteristic properties of SFRC is presented. The chapter discusses the general properties of fresh and hardened SFRC in contrast to plain concrete. The properties of hardened SFRC are explained by virtue of the pullout behaviour of individual fibres and the factors that influence this behaviour. Finally, durability aspects and some other properties are described, because they are also of great importance for structural applications.

Chapter 3 reports on the extensive experimental research that was carried out at the Delft University of Technology's Stevin Laboratory. It expands on the effect of certain parameters on the post-cracking behaviour of SFRC beams and shows their influence on the scatter in the post-cracking behaviour.

The second part of this thesis is concerned with the modelling of SFRC. After a discussion of several types of existing models and combining different elements from these models, a material relation is developed that is justified by test results.

Part two also consists of two chapters. In Chapter 4, existing modelling tools for FRCC are described, after which they are evaluated using several criteria. On the basis of the conclusions given in Chapter 4 a procedure is used to obtain a suitable material model for SFRC. This procedure is presented in Chapter 5 along with the information required to determine a bilinear stress-crack width relation.

Part III of the thesis explains the reliability methods used in the design model. The objective of this part is to relate the material's behaviour to structural application and to enhance the reliability of SFRC structures by taking the necessary precautions in the design phase.

Part three is divided into two chapters and starts with the basic problems attached to making a structural design with SFRC as outlined in Chapter 6. This chapter deals with the influence of the production process on fibre distribution and orientation and the efficiency of fibre reinforcement relative to the orthogonal direction(s) of the tensile stress in test specimens and promising structural applications of SFRC.

Subsequently, Chapter 7 translates various uncertainties into design factors. Essentially, the scatter in the post-cracking behaviour is accounted for by using simple statistical relations. After presenting several reliability methods, material safety factors are determined for different types of SFRC mixtures.

In part IV a case study is presented. Chapter 8 shows how to transform the material model into a design model and how to apply it to the design of tunnel segments. The material model of Chapter 5 and the design philosophy discussed in Chapter 7 are used to make an improved SFRC tunnel segment design for the 2nd Heineoord tunnel.

The last part and at the same time the last chapter of the dissertation presents final conclusions based on this research project and provides future perspectives concerning SFRC and FRCC in general.

Chapter 2

Material properties of SFRC

2.1 Introduction

This chapter discusses the influencing parameters of the behaviour of hardened SFRC. It is supposed to enhance the understanding of the material's behaviour and will provide a basis for experimental research into the aspect of scatter in the post-cracking behaviour. It starts with the rheological properties of SFRC, since the workability can strongly influence several stages of the production process [Kooiman, 1998]. The latter is supposed to strongly affect the post-cracking behaviour of the composite material.

To understand the mechanical behaviour of hardened concrete on a macro level it is wise to zoom in to the meso or even micro level. Therefore, the pullout behaviour of an individual fibre will be discussed. The various parameters that influence this behaviour are presented and the influence of these parameters will be shown. The pullout behaviour is used to explain the mechanical behaviour of SFRC, presented in the subsequent sections.

The tensile behaviour of SFRC changes substantially compared to plain concrete. Depending on the amount and type of fibres used both the peak load and the ductility can be increased. Explanations will be presented for the fact that the tensile strength can be increased by virtue of fibre addition whereas this is hardly possible with regard to the compressive strength. Although small fibre volumes do not really increase the tensile strength, they do increase the deformation capacity in uni-axial tension. In bending, however, the flexural load-bearing capacity can be increased at low fibre volumes as long as the matrix strength, the fibre characteristics and the fibre volume are well tuned.

Because the insight into the structural behaviour needs to be increased, the shear behaviour and the time dependent behaviour are discussed as well. Although some questions still remain on these parts, a lot of answers can be found in literature. The latter also applies for the behaviour of SFRC under severe loading conditions, such as fire.

In the end, the influencing parameters on the material behaviour of SFRC are summarised to provide a basis for Chapter 3.

2.2 Rheological properties of SFRC

2.2.1 Design of SFRC mix compositions

In the design of SFRC mix compositions, the same volume-based design procedure can be used as for plain concrete. The cement volume, calculated through the cement weight c divided by the cements' specific gravity ρ_c , the water volume V_w , the aggregate volume, calculated through the aggregate weight g divided by the aggregates' specific gravity ρ_g , and the pore volume V_p form the plain concrete matrix. The fibres can be considered as additional (coarse) aggregates in the mixture. Since the total volume of the combined materials and the air volume V_p in a cubic meter of SFRC must be constant, the volume and weight of the separate components can be calculated using the following equation:

$$\frac{c}{\rho_c} + V_w + \frac{g}{\rho_g} + V_p + V_f = 1 \quad (2.1)$$

The fibre volume V_f can be derived from the added fibre weight F and ρ_f :

$$V_f = \frac{F}{\rho_f} \quad (2.2)$$

Obviously, it is quite simple to calculate weights and volumes of the separate components in the mix. However, this will not automatically lead to a mixture that satisfies all demands. Each mix composition to be used in practice depends on the demanded workability and mechanical properties that are related to the structural application. In addition, each fibre type has its own effect on the workability and the mechanical behaviour. General effects will be discussed with respect to the following components that form SFRC:

- Cement
- Water
- Aggregates
- Air volume
- Steel fibres

Cement

The application of steel fibres in concrete does not influence the required type (Portland or blast furnace cement) or the performance of the cement in its chemical reaction with water. The type of cement is determined by the required strength or strength development, by durability aspects and the maximum heat dissipation that is allowed. The composition and the fineness of the cement [Souwerbren, 1995] determine the performance of the cement in reaction with water.

In case of composing SFRC mixtures it is recommended to increase the cement weight by approximately 10 % compared to plain concrete mix compositions. Due to the addition of fibres to the mix, a larger internal surface needs to be moistened by the cement paste. This means that as the volume of the cement paste in the mix increases, the fibre volume can be enlarged without influencing the workability.

Water

When the amount of water has to be determined it always results in a conflict between the need of a workable mixture and a natural intent to reduce the water binder factor (wbf). The latter is to serve the need for durable and strong concrete. Since in SFRC the cement paste volume has to be enlarged when compared to plain concrete mixtures, the amount of water is often increased. Of course, this should preferably not lead to a lower quality of the composite material. Therefore, the wbf must be kept constant and the amount of water needs to be increased proportionally to the amount of cement. Additives, such as superplasticizers, are often used when a low wbf is required to ensure a relatively high strength and durable concrete.

Aggregates

A number of adaptations need to be made to the aggregate content when fibres are added to the concrete mix. Firstly, from a workability point of view it is recommended to limit the grain size to half the fibre length [Johnston, 1996]. As the maximum grain size decreases, the fibres will be more randomly distributed and orientated in the mix, which is visualised in Figure 2.1. Furthermore, limiting the maximum grain size $d_{g,max}$ enhances the workability and decreases the probability of so-called fibre balling. Fibre balling also tends to occur in case of mixtures with discontinuous grading curves and/or a relatively small amount of fine aggregates. It is therefore recommended to increase the percentage of fine material ($d_{grain} < 2 \text{ mm}$) with regard to the total amount of aggregates.

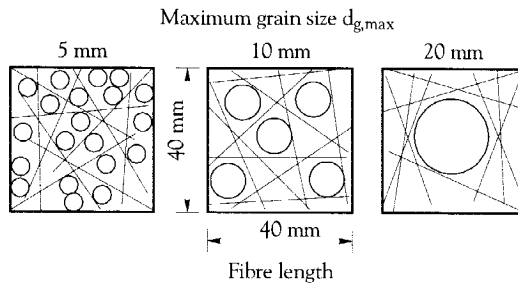


Figure 2.1 Effect of maximum grain size on randomness of fibre distribution and orientation [Johnston, 1996]

Secondly, the ratio of fines/total aggregate volume needs to be adjusted to attain an optimum packing density. Figure 2.2 demonstrates the decrease in packing density when fibres are added to the mix. It shows the need for a larger amount of fine aggregates to diminish the decrease in packing density. The packing density decreases when the fibre volume is increased, when the content of fine aggregates is decreased and/or when the fibre's aspect ratio (L_f/d_f) is increased [Bartos & Hoy, 1996], [Hoy & Bartos, 1999]. Depending on the fibre volume the optimum packing density is reached when the fine to total aggregate ratio is between 40 and 60% [ACI Committee 544, 1993]. The total aggregate grain volume should be decreased by the fibre volume since the fibres are considered as aggregates from a workability point of view.

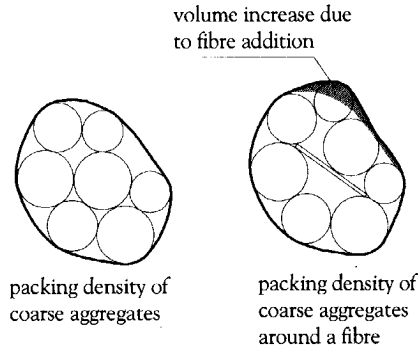


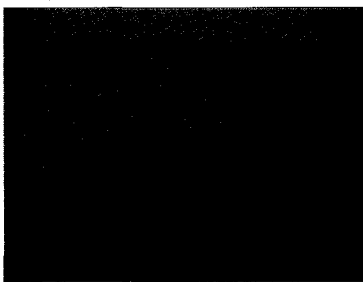
Figure 2.2. Effect of fibre addition on packing density [Bartos & Hoy, 1996]

Air volume

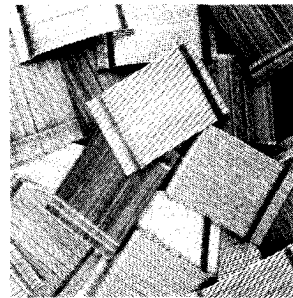
In the design of concrete mixtures the air volume is usually assumed to be 1.5 to 2.0% [Souwerbren, 1995]. In the case of SFRC, it is recommended to assume an air volume of 4-8% in the mix design [ACI Committee 544, 1993]. However, when the mix composition is well adjusted the air volume will approach the same value as occurs in plain concrete.

Steel fibres

As Figure 2.3a shows, steel fibres are available in several shapes and sizes. They can be manufactured from drawn steel wire, cut from thin plates or milled from steel cubes. The first family of steel fibres is characterised by its circular cross-section. The cross-section of the other two fibre types is either square or varies per fibre. Next to straight fibres numerous differently shaped fibres have been developed to increase the pullout resistance (for the pullout behaviour of steel fibres see section 2.3.1). Some steel fibre manufacturers altered the shape of the fibre shaft, while others focussed on the shape of the fibre-ends. One manufacturer even tried to combine both ideas.



(a) Eurosteel, DRAMIX and Twincone fibres



(b) glued DRAMIX fibres

Figure 2.3 Examples of different fibre types.

Just as varying as the fibre shape is the fibre size. The diameter or cross-sectional dimension varies in the range of 0.15 to 1.5 mm, whereas the length is in between 40 and 150 times the diameter. The aspect ratio, which is defined as the ratio between the fibre length L_f and the fibre diameter d_f , is often used as a characterising parameter.

The tensile strength of the steel fibres is usually between 400 and 1200 N/mm². However, in medium and high strength concrete the fibres might break as a result of the relatively high pullout resistance due to high bond strength. To prevent the fibres from breaking, an option is to increase the fibre's tensile strength. Fibres with a tensile strength of 2700 N/mm² have already been applied in structures [Kooiman et al., 1999]. Other options to prevent fibre breaking are to apply shorter fibres and/or to increase the fibre volume.

Depending on the maximum grain size $d_{g,max}$, the aspect ratio L_f/d_f and the fibre type, the fibre volume fraction that can be applied in practice varies considerably. Table 2.1 shows the influence of the maximum grain size and the aspect ratio on the maximum fibre volume fraction $V_{f,max}$ for hooked-end fibres in case of dry mixtures. These hooked-end fibres are sometimes glued together to increase $V_{f,max}$ (see Figure 2.3b) for practical applications.

Table 2.1 $V_{f,max}$ for different aspect ratios and maximum grain size for hooked-end fibres

d_{max}	$L_f/d_f = 60$	$L_f/d_f = 75$	$L_f/d_f = 100$
4 mm	2.0 %	1.6 %	1.2 %
8 mm	1.5 %	1.3 %	0.9 %
16 mm	1.0 %	0.9 %	0.7 %
32 mm	0.6 %	0.5 %	0.4 %

The addition of steel fibres to concrete mixtures puts additional demands to the design of the mix composition. The American Concrete Institute developed a guideline to simplify this mix design [ACI Committee 544, 1993]. The guideline gives ranges for all components described above to ensure a good quality mix composition (see Table 2.2). However, the effect and importance of additives like superplasticizers have not been mentioned.

Table 2.2 ACI guideline on SFRC mix design [ACI Committee 544, 1993]

Component	$d_{max} = 10 \text{ mm}$	$d_{max} = 20 \text{ mm}$	$d_{max} = 38 \text{ mm}$
wcr [-]	0.35-0.45	0.35-0.50	0.35-0.55
cement [kg/m ³]	360-600	300-540	280-420
aggregates:			
fine/total [%]	45-60	45-55	40-55
air volume [%]	4-8	4-6	4-5
V_f straight fibres [%]	0.8-2.0	0.6-1.6	0.4-1.4
V_f deformed fibres [%]	0.4-1.0	0.3-0.8	0.2-0.7

2.2.2 Workability of SFRC mixtures

Generally, the workability decreases as fibres are added to the mix. This can be explained by the fact that needle-shaped elements are introduced in a mixture of spherical elements and water. It results in a much stiffer mixture and sometimes in fibre balling. The probability of fibre balling increases when the maximum fibre volume is reached for a given maximum grain size and aspect ratio or when the volume of coarse aggregate is too high relative to the total aggregate volume. Of course, production aspects can also be the cause of fibre balling, e.g. when the total amount of fibres is added at once.

Other problems might occur during production. For example, the stiff SFRC mixtures that were used in the experimental research for the 2nd Heinenoord tunnel did not flow from the skip as the frictional stresses at the wall-mixture interface were too high. After inserting a poker vibrator the mix started to flow from the skip into the mould. On the other hand the

compactability of the mixture proved to be quite well. This behaviour of the stiff SFRC mixture showed that the addition of fibres strongly influences two different aspects of workability: the flow (or mobility) and the compactability of the fresh mix.

As the addition of fibres influences the above mentioned workability aspects, separate production stages will be affected. However, the production stages themselves also influence the fibre addition's efficiency in the hardened state. The next production stages have been evaluated:

- Mixing stage
- Placing stage
- Compacting stage
- Finishing stage

Mixing stage

There are two reasons for the fact that mixing times tend to be prolonged compared to plain concrete mixes. Firstly, the fibres need to be added gradually to the mix to prevent fibre balling. Secondly, the fibres need to be dispersed randomly in the mix, which requires some additional mixing time. In practice, the production process of the SFRC segments for the 2nd Heineoord tunnel showed that mixing time was doubled due to the fibre addition [Kooiman, 1998]. This was a result of the fact that the fibres were glued together. In that case, extra mixing time is necessary to dissolve the glue before the fibres can be dispersed.

Placing stage

The placing stage can be significantly influenced by the addition of steel fibres to a plain concrete mixture as it reduces the flowing capacity and mobility of the fresh mix [Bartos, 1996]. Obviously, this flowing capacity and mobility can be improved by adjusting the mix composition or adding a superplasticizer. By increasing the content of superplasticizer the internal friction can be decreased, so that the flow through a skip is not obstructed. However, the mobility of the mixture (i.e. the time it takes to flow through an inverted cone) is more or less determined by the viscosity of the mix. The most important factors that influence the viscosity of a SFRC are the maximum packing density and the volume of solids in the mix [De Larrard, 1999].

In case of the production of SFRC tunnel segments for the Second Heineoord tunnel a stiff mix was used. In first instance this stiff mixture blocked the openings between the skip and the conveyor belt, which was meant to transport the mix to the mould. After increasing these openings these problems were solved. Tests showed that the probability of blocking strongly decreases when dimensions of openings are larger than twice the fibre length [Nemegeer, 1999].

Theoretically, the fibre orientation is influenced in a zone near the geometrical boundaries of the structure [Soroshian & Lee, 1990]. In addition to the dimensions and shape of the structure, the workability of the mixture strongly influences the fibre orientation. As a result, the pouring direction as well as the flow direction tends to orient the steel fibres. It is, therefore, expected that the average orientation of the added fibres in slabs differs from the orientation in tunnel segments. The fibre efficiency in the hardened state, however, depends not only on the average fibre orientation, but also on the orthogonal direction(s) of the occurring tensile stress [Schönlin, 1988]. This is investigated in more detail for the application of SFRC in tunnel segments, see Chapter 6.

Compacting stage

In the past, compactability tests showed that the volume fraction of coarse aggregates, the fibre volume and the aspect ratio determine the compactability of the fresh fibrous concrete [Mangat & Swamy, 1974]. It is often recommended to vibrate the concrete externally to prevent 'weak spots'. However, external vibration can initiate a particular flow in the mould and tends to orient the fibres perpendicular to the direction of vibration. In addition, the fibres tend to segregate as the vibration energy and the total vibration time need to be increased.

Finishing stage

The finishing technique is strongly affected by the addition of fibres. Levelling with a screed board for instance causes a problem, as the fibres tend to hook behind the screed board. As a result, the surface will be ripped open. After scouring a relatively even surface can be produced. However, fibres tend to stick out at corners and edges. In the case of the 2nd Heinenoord tunnel, the latter was even a reason for the contractor to demand an extra epoxy layer on the surface to prevent the fibres to cause any (more) damage to the rubber, watertight seal at the shield machine's tail [Kooiman et al., 1999].

In case of plain concrete different methods have been developed to monitor the workability of the fresh concrete. These methods have been widely used in laboratories as well as on construction sites. They are relatively simple to carry out and provide reliable results. However, these conventional testing methods do not apply for SFRC mixtures. The slump test, for example, does not provide representative results for the workability of low to very low workability mixes and is therefore not quite suitable for stiff SFRC mixtures. Lab tests showed that in case of the SFRC mixture used in the Second Heinenoord tunnel, there was no settlement measured at all after removing the cone. Researchers had already encountered this problem [Bartos, 1996] and therefore used the compaction (or Walz) test in those cases. In some countries, workability testing methods for SFRC have been developed. For example, in the United States the inverted cone test has been widely applied and the so-called VeBe test was introduced to test the compactability of the fresh mix. In France, Lesage developed the LCL workabilitymeter.

2.3 Properties of hardened SFRC

2.3.1 Pullout behaviour of steel fibres

Pullout tests are widely accepted as one of the basic tests to provide information about the expected post-cracking behaviour of a fibre reinforced cementitious composite. The basic test performed is the test in which a single fibre is pulled out of a block of matrix material. In the past, this test has been used to provide input for fracture mechanical modelling of FRC [Stang et al., 1995]. In this section, it is used to gain insight into the parameters that determine the (post-cracking) behaviour of SFRC.

The pullout behaviour of an individual steel fibre is determined by its own characteristics, the quality of the cement matrix and the orientation of the fibre with regard to the pullout direction. As a matter of fact, the interfacial bond between the fibre and the

matrix is a very important aspect to consider. According to Stang et al [Stang et al., 1990], the fibre to matrix bond quality has a significant influence on the ability of the fibres to stabilise micro cracks that are formed in the early stages of a load history. If larger cracks are allowed to occur in later stages, the fibre pullout process strongly influences the total energy consumption of the cracking process, if the fibres don't yield nor break.

When considering the fibre to matrix bond characteristics the following two approaches have been used in the past: the stress and fracture approach. Stang et al. [Stang et al., 1990] show that in both cases one parameter characterises the friction and the another the (adhesive) bond. Figure 2.4 shows the theoretical pullout load versus slip relation for a single, straight steel fibre [Naaman, 1999]. Figure 2.4 is plotted on a small scale to demonstrate the effect of the debonding process, whereas Figure 2.5 presents the same relation up to the stage of complete pullout.

In Figure 2.4, the ascending portion (OA) of the relation is associated with elastic or adhesive bond. In the next portion of the curve (AB), debonding is initiated and progresses until full debonding occurs (BC). Afterwards, frictional decaying causes a decrease in pullout load with increasing slip, as a result of the decreasing embedded fibre length.

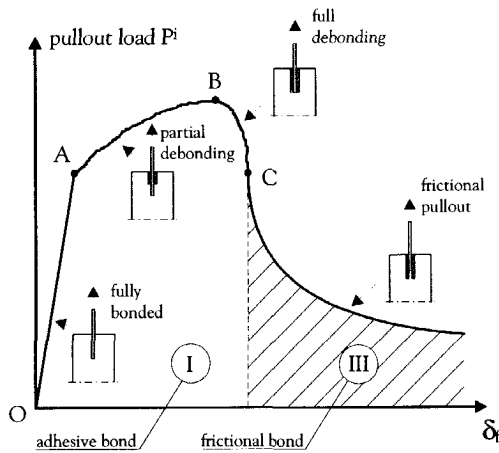


Figure 2.4 Typical pullout load versus end-slip relationship for a straight steel fibre (a close-up) [Naaman, 1999]

In some cases, when the matrix strength and thus the maximum bond stress is high, the stress in the fibre can exceed the fibre yield strength before the maximum pullout load is reached. To avoid fibre rupture, the fibre bridging stress σ_f^i must be smaller than the fibre yield stress f_{fu} , which is a function of the embedded fibre length L_{fe} , the maximum bond stress at the fibre to matrix interface τ_0 and the fibre diameter d_f :

$$\sigma_f^i = \frac{4 \cdot \tau_0 \cdot L_{fe}}{d_f} < f_{fu} \tag{2.3}$$

Another typical pullout load versus end-slip relation is shown in Figure 2.5. It shows that in case of a hooked-end steel fibre, mechanical anchorage or mechanical bond can increase the pullout load considerably when compared to straight steel fibres. Several researchers

succeeded in modelling the pullout behaviour of these hooked fibres [Van Gijsel, 1999], [Weiler et al., 1999], [Alwan, et al. 1999].

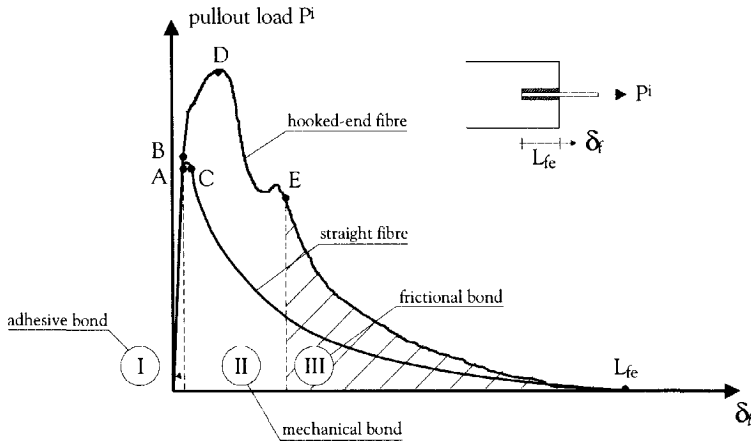


Figure 2.5 Typical pullout load vs. end-slip relationship for a straight and a hooked-end fibre [Alwan, et al. 1999]

When the pullout behaviour of an individual fibre is translated to the mechanical behaviour of SFRC cross-sections it is necessary to also incorporate the efficiency of an individual fibre and the efficiency of a group of fibres.

The efficiency of a single fibre depends on the angle between the fibre alignment and the direction of the pullout load, i.e. the so-called inclination angle [Bartos & Duris, 1994]. Figure 2.6 shows the effect of this inclination angle on the tensile load-bearing capacity of a single fibre, embedded in a cementitious matrix. It appears that not only the inclination angle, but also the type of fibre strongly influences the maximum pullout load. The Fibraflex fibres are flexible fibres, whereas the Harex HCSF are steel wire fibres with hooked-ends and the Harex SF 32 are chopped fibres. The Harex fibres have a much higher bending stiffness when compared to the Fibraflex fibres. As the inclination angle increases, the steel fibres are subjected to larger shear and bending stresses. Van Gijsel [Van Gijsel, 2000] shows that this might lead to plastic deformation of the fibre or damage at the surface of the matrix. Due to the fact that the fibre characteristics differ from each other, their pullout behaviour is not identical. In addition, the pullout response is also dependent on the matrix properties in the vicinity of the fibre and its ability to withstand cracking or spalling due to the additional local flexure as a result of fibre bending at increasing inclination angles. In case of relatively low strength matrices, damage that might occur at the surface of the matrix will result in a decrease of the effective embedded fibre length and thus a decrease in fibre efficiency.

Obviously, the efficiency of a group of fibres depends on the average fibre orientation. In addition, the fibre spacing is also of importance. As the distance between fibres becomes smaller, the probability of a mutual influence of stress fields can cause the pullout resistance per fibre to decrease [Naaman & Shah, 1976].

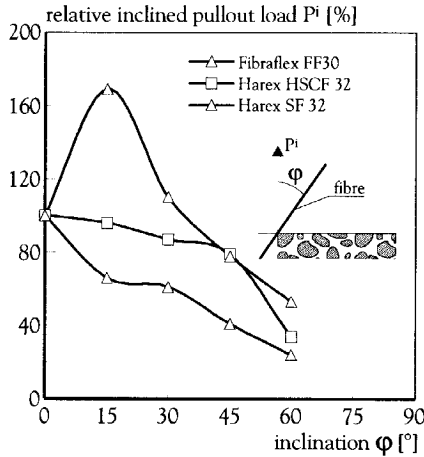


Figure 2.6 Effect of inclination angle on tensile load-bearing capacity [Bartos & Duris, 1994]

2.3.2 Tensile behaviour of SFRC

Plain concrete is characterised by its brittle failure behaviour in tension. The objective of fibre additions in concrete is often to obtain a ductile failure behaviour. The effect of fibre addition on the tensile behaviour is clearly shown in Figure 2.7 in which typical uni-axial tensile stress-crack opening displacement (COD) relations for SFRC are compared to the relation typical for plain concrete.

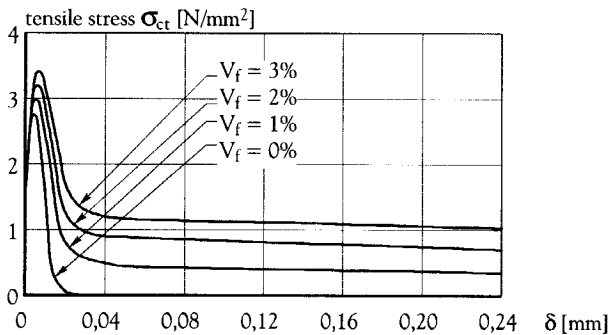


Figure 2.7 Typical stress-crack opening displacement relations for SFRC and plain concrete [Maidl, 1995]

The difference between the tensile behaviour of SFRC and plain concrete is obvious. Due to fibre addition, the tensile strength can be increased. After the peak stress is reached, a sudden decrease in load-bearing capacity is followed by a low-level, post-cracking plateau that results from continuous frictional pullout of the fibres. The shape of the stress-COD relations from Figure 2.7 corresponds with the pullout load versus slip relation of straight fibres shown in Figure 2.5. To analyse this tensile behaviour more in depth the stress-crack width relation can be subdivided into three parts:

- Linear elastic stage
- Micro cracking stage
- Macro cracking and fibre slipping stage

Linear elastic stage

The addition of fibres has a minor influence on the linear elastic stage since Young's modulus of the composite E_{fc} is hardly affected by the addition of fibres. The influence of the matrix' Young's modulus E_c overrules the contribution of the fibres' Young's modulus. Since the fibre volume V_f is often relatively small, the contribution of the fibres in the determination of E_{fc} [Keer, 1984] is negligible, as follows from equation (2.4).

$$E_{fc} = \eta_{\theta} \cdot \eta_l \cdot E_f \cdot V_f + E_c \cdot V_c \quad (2.4)$$

with the orientation efficiency factor η_{θ} and the length efficiency factor η_l , which are explained in Chapter 4.

Micro cracking stage

The randomly orientated and distributed fibres can resist micro cracking in a very early stage. Suppose that one micro crack is bridged by a fibre. According to the pullout behaviour of an individual fibre, debonding starts on the shortest embedded length until full debonding occurs. The micro crack will then start to grow, which will eventually lead to a macro crack that co-operates with other micro cracks formed. The interfacial bond characteristics between fibre and matrix are very important with respect to the resistance to micro cracking. In addition, a large number of fibres (large volume of micro fibres) will also contribute to this resistance. The development of so-called High Performance Fibre Reinforced Cementitious Composites (HPFRCC) is based on these principles [Shah et al., 1999].

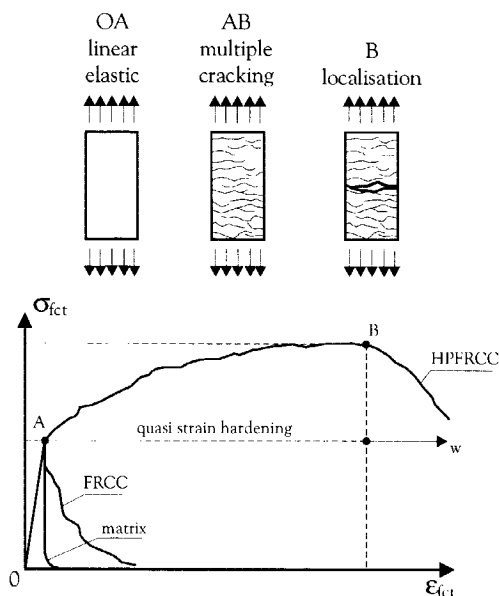


Figure 2.8 Definition of high performance fibre reinforced cementitious composites [Li & Wu, 1992]

A HPFRCC is characterised by a dense matrix and a high volume of short fibres ($L_f < 13$ mm). These kinds of composites show quasi strain hardening after reaching the matrix strength [Li & Wu, 1992]. Quasi strain hardening behaviour occurs if the uni-axial tensile stress of the composite is higher than the cracking strength (see Figure 2.8). This quasi-strain hardening behaviour is generally accompanied by multiple cracking and related to a high energy absorption capacity. Typically, conventional fibre reinforced concrete exhibits localisation of damage, immediately after the first crack occurs in the concrete matrix. Therefore, it does not qualify as 'high performance'.

Macro cracking stage

After a macro crack has formed in conventional SFRC and the peak load has been reached, a steep drop in the load-bearing capacity is often found in uni-axial tensile tests. The post-cracking plateau is influenced by the frictional stresses at the fibre to matrix interface, the fibre volume (see Figure 2.8), the fibre characteristics (compare the pullout behaviour of a straight and a hooked-end fibre in Figure 2.5) and the average fibre orientation efficiency. However, in practice the fibre distribution also seems to be quite important and may not be neglected. Uni-axial tensile tests on cores, drilled from cubes, proved that the measured fracture energy strongly correlates with the coincidental number of fibres in the cross section [Stroband, 1998]. Furthermore, tests on cores drilled from slabs cast in practice demonstrated that the amount of fibres can vary significantly [Taerwe et al, 1999].

2.3.3 Compressive behaviour of SFRC

In design models for compressive behaviour of plain concrete it is common practice to assume that for stresses below the peak stress, the longitudinal strains, i.e. the relative deformations parallel to the loading direction, are uniformly distributed over the measuring length.

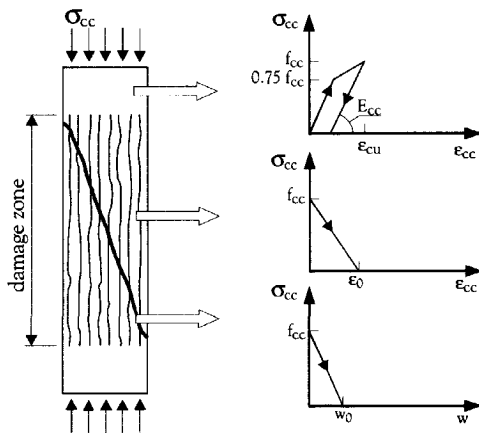


Figure 2.9 The Compressive Damage Zone (CDZ) model for plain concrete [Markeset, 1993]

In her Compressive Damage Zone (CDZ) model, Markeset [Markeset, 1993] distinguishes two failure modes. Firstly, after the linear elastic response, longitudinal cracking occurs in a limited part of the specimen, which is called the damage zone. This longitudinal cracking is initiated

at a stress between $0.75 \cdot f_{ct}$ and the peak stress f_{ct} . Secondly, when the peak stress is reached, lateral deformations occur within the longitudinal tensile cracks until the specimen fails, i.e. when the longitudinal cracks in the damage zone coalesce to form a shear band and the adjoining parts start sliding relative to each other.

Figure 2.9 illustrates the failure behaviour of a plain concrete prism in uni-axial compression and provides a schematisation for a calculation procedure, according to the CDZ model. It is shown that, beyond the peak, the CDZ model makes a distinction between the material behaviour within and outside the damage zone. Outside the damage zone unloading is assumed, while inside the damage zone the softening branch of the stress-strain relation describes the fracture process. The final sliding failure is described by a stress-displacement relationship.

In the past, several researchers proved that the addition of steel fibres will not strongly affect the compressive strength of the composite [Maidl, 1995], [König & Kützing, 1999]. Figure 2.10 shows that the compressive strength is more or less equal to the strength of the plain matrix, but ductility increases significantly after cracking. If it is supposed that the failure behaviour of SFRC in compression is similar to that of plain concrete, the latter can be explained by the fact that the effect of fibres in the presence of cracks is mainly based on preventing lateral deformations (i.e. lateral crack opening displacements) and not strengthening in the direction of the compressive stress. As the shear capacity is increased due to the addition of fibres (see section 2.3.5), it is expected that a shear band as in Figure 2.9 will not occur. In the scope of this research, it is assumed that the CDZ model of plain concrete also applies for SFRC, except for the development of the shear band. Thus, it is assumed that after the development of longitudinal cracks in a damage zone and after reaching the peak load, lateral displacements only take place within the longitudinal cracks.

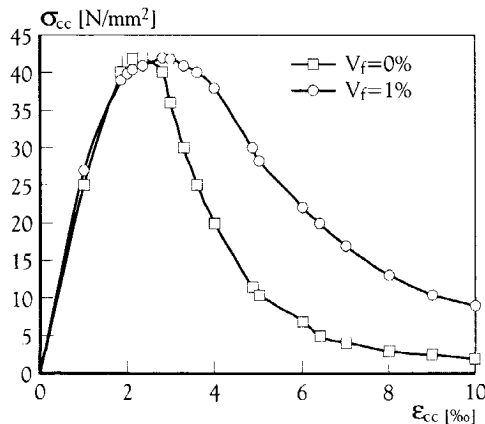


Figure 2.10 Typical behaviour of SFRC in compression ($f_{icm} = 42 \text{ N/mm}^2$) [König & Kützing]

For the purpose of design, Taerwe and van Gijsel [Taerwe & van Gijsel, 1995] proposed the following relation for the softening stress-strain curve of high strength concrete ($f_{cc} > 50 \text{ N/mm}^2$) reinforced with hooked-end steel fibres:

$$\frac{f_{fc}(p)}{f_{fcc}} = \frac{1}{1 + [(p-1)/(q-1)]^2} \quad (2.5)$$

with

$$p = \frac{\epsilon_{fc}}{\epsilon_{fcc}} > 1 \quad (2.6)$$

$$q = [1.1035 - 0.4212 \cdot (\frac{f_{fcc}}{50})] \cdot RI - 0.8037 \cdot (\frac{f_{fcc}}{50}) + 2.8797 \quad (2.7)$$

$$RI = V_f \cdot \frac{L_f}{d_f} \quad (2.8)$$

2.3.4 Flexural behaviour of SFRC

In the past, flexural tests have been used to determine toughness values for SFRC. In this way, different composites could be easily tested and compared to one another. The toughness value is the area under the load-deflection or load-displacement curve up to a defined deflection or displacement. The latter differs per code or recommendation. Compared to plain concrete, the toughness increases considerably as the fibre volume, the aspect ratio and/or the interfacial bond strength increases. However, caution is needed at high bond strengths since the fibres' tensile strength may be reached. When the fibres break, the potential toughness can not be reached. Figure 2.11 presents typical load-displacement curves for three-point bending tests.

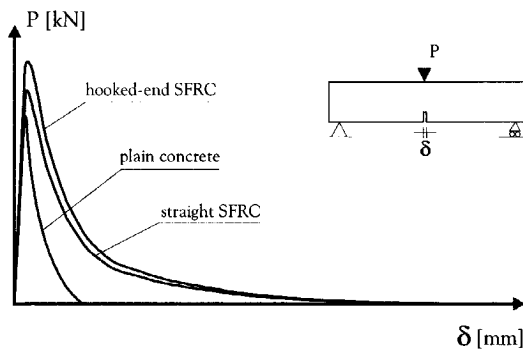


Figure 2.11 Typical behaviour of SFRC in bending

Hillerborg et al. [Hillerborg et al., 1976] showed that the flexural tensile strength of concrete depends on the brittleness ratio that is defined by the material properties and the specimen geometry. It was demonstrated that the uni-axial tensile softening relation, or stress-crack width relation, is quite important in that respect. It is because of this softening curve that the flexural strength exceeds the uni-axial tensile strength.

As it has already been shown, the softening curve of SFRC is strongly influenced by the addition of steel fibres. In the case of SFRC cross-sections subjected to bending moments,

the post-cracking or softening relation leads to a redistribution of stresses after cracking, as Figure 2.12 illustrates. As a result, the neutral axis (n.a.) shifts upward in the direction of the compression zone (c.z.) and a new state of equilibrium can be reached. Based on this mechanism, SFRC is capable of resisting increasing loads even with a cracked tensile zone. Although the same applies for plain concrete, SFRC is much more ductile. As a result, the maximum moment capacity of the composite exceeds the moment capacity of the plain matrix. The relative increase of the moment capacity of SFRC depends on the same factors that influence the pullout behaviour of an individual fibre. In the next chapter it will be shown that the fibre distribution also influences this behaviour.

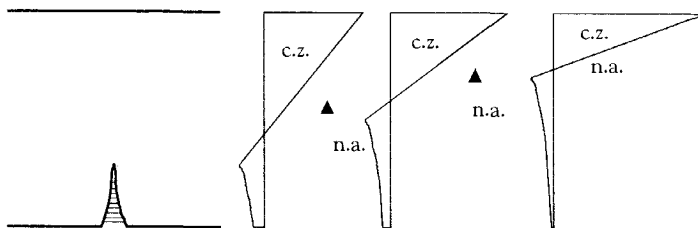


Figure 2.12 Redistribution of stresses in SFRC cross-section subjected to bending

2.3.5 Shear behaviour of SFRC

Fibres can also be used as shear reinforcement in beams or similar structural applications. Tests have shown that a significant increase of the shear strength can be accomplished by adding fibres to the mix. Depending on the maximum shear force stirrups can be replaced by steel fibres. Most tests, however, have been carried out with longitudinal steel reinforcement to sustain high flexural moments [Narayanan & Darwish, 1987], [Imam, 1995], [Campioni & Mindess, 1999]. In addition to the previously described parameters that influence the post-cracking behaviour, such as the fibre characteristics and the matrix quality, the increase of the shear strength also depends on the amount of longitudinal steel reinforcement.

Another type of shear failure can occur due to a so-called punching shear load in slab-column connections. In [Theodorakopoulos & Swamy, 1999], a simple engineering model has been presented to design slab-column connections. It has been shown that the model predicts test results quite satisfactorily. Again, the punching shear resistance depends on the fibre volume, the fibre orientation, etc.

2.4 Durability aspects of SFRC

2.4.1 Resistance to corrosion

When assessing the chemical durability or corrosion resistance of SFRC a distinction has to be made between cracked and uncracked sections. In the case of uncracked SFRC, the steel fibres near the concrete surface corrode very quickly in the carbonation zone. In this zone carbon dioxide from the air penetrates into the concrete and attacks the protective alkaline environment of the steel fibres. The depth of this carbonation zone depends on the density of

the matrix. For concrete used in practice, the depth of this zone is 15-20 mm [Souwerbren, 1995]. Adding fillers, such as fly ash or silica fume, can reduce this depth.

Beyond the carbonation zone corrosion cannot propagate since the fibres are all individually embedded in the matrix and do not form an electrical conductor. In addition, corrosion of the fibres in the carbonation zone cannot cause any concrete spalling since the increase in fibre diameter will not introduce such high peak stresses that any damage is caused. A possible chain reaction and further deterioration of the cross-section is therefore not to be expected.

Durability tests of Kosa and Naaman [Kosa & Naaman, 1990] showed that initially the increased fibre diameter and the corrosion products on the fibre's shaft improve the interfacial fibre/matrix bond. However, after a longer period of time the effective fibre diameter decreases and the fibres will tend to break instead of slip through the matrix.

Obviously the durability of SFRC structures will be affected when cracks appear. Mangat and Gurusamy [Mangat & Gurusamy, 1987] showed that the flexural behaviour of pre-cracked specimens exposed to a marine environment is not affected for crack widths up to 0.2 mm. As a matter of fact, the energy absorption capacity of the cracked specimens improved when compared to uncracked and sealed specimens. This was explained by the effect of self-healing.

2.4.2 Mechanical durability

Just like plain concrete, the mechanical behaviour of SFRC does not only refer to direct and short term loading. It is also a matter of resisting stresses initiated by a restrained deformation due to shrinkage and/or by sustained loads. In both cases the deformations of the structure are time dependent.

Behaviour in the case of shrinkage

Three types of shrinkage are known. Firstly, chemical shrinkage can occur as the water reacts with the cement and forms the cement matrix. Often this problem is recognised in high strength concrete where the water content is quite low. Secondly, plastic shrinkage results from water evaporating from the fresh mixture. Finishing the concrete surface in a proper manner, for example by applying curing methods, avoids any 'spider-web' surface cracking. The third kind of shrinkage is drying shrinkage. Problems due to this type of shrinkage might occur as water evaporates from capillary voids. The higher the water content, the more water can evaporate and the larger the drying shrinkage is.

The three types of shrinkage can only lead to cracking when deformations are restrained and the stresses from these restrained deformations exceed the tensile strength of the composite. Given a certain mix composition, the shrinkage of SFRC depends on the curing process, the concrete's age, the fibre characteristics, the aspect ratio and the fibre volume [Balagaruh & Shah, 1992]. Although fibre additions cannot prevent shrinkage to occur, in the case of cracking due to shrinkage fibres might have an impact. According to Ong and Paramisivam [Ong & Paramisivam, 1989] fibres can slow down the cracking process and reduce crack widths. They showed that at increasing fibre volumes, the average crack width could be reduced considerably as a result of multiple cracking.

Behaviour under sustained loads

Not much research has been carried out on the time dependent behaviour of SFRC under sustained loading conditions. Based on test results from [Edgington et al., 1974], it is assumed that the time dependent behaviour under compressive loading (creep) is not influenced by any fibre addition.

Recently, tests have been carried out on cracked SFRC sections under sustained bending loads. Both Stroband [Stroband, 1998] and Chanvillard and Roque [Chanvillard & Roque, 1999] used notched beam specimens, but the specimen sizes differed. In both cases the specimens were pre-cracked to obtain a crack opening typical for the one accepted in practice when considering chemical durability (up to 0.3 mm). The test results matched in a way that both researchers report an increase in crack opening in time at sustained loading and a less rapid increase as time proceeds. The time span, however, differed. Stroband tested the specimens for 365 days while the maximum time span of Chanvillard was 110 days. Stroband tested the beams at a load level of 60% of the maximum load in the pre-cracking stage, while Chanvillard tested at an 80% level. In their concluding remarks, both researchers stated that further research is necessary.

2.5 Severe loading conditions

In the case of severe loading conditions the following properties of SFRC have been evaluated:

- Fatigue resistance
- Impact and explosion resistance
- Fire resistance

Fatigue resistance

The fatigue resistance of concrete strongly increases when fibres are added to the mix. The fibres will keep the matrix together, even after cracking. Given a certain composition of the concrete mix, the fatigue resistance depends on the fibre volume, the aspect ratio and the fibre type used. As the fibre volume increases, the maximum flexural stress resisted at a given number of load cycles also increases. Tests on SFRC beams carried out by Johnston and Zemp [Johnston & Zemp, 1995], however, showed that the failure mechanism depends on a certain critical fibre volume. Below this critical value the fibres tend to break, whereas the fibres slip from the matrix at higher volumes. As a result, the energy absorption capacity is much higher at volumes above the critical volume. Johnston and Zemp [Johnston & Zemp, 1995] report a critical fibre volume V_f between 0.5 and 0.75 %.

Impact and explosion resistance

Just like the resistance to fatigue the resistance to other types of dynamic loading, such as impact and blast loads, increases when fibres are added to the concrete. As fibres are also present near the surface of the structural element, they prevent the concrete from spalling or shattering and reduce damage considerably, as was demonstrated in various tests [Kaushik & Menon, 1989], [Sun et al., 1999].

Fire resistance

It is not exactly known in what way and to what extent the fire resistance is affected by the addition of fibres. Not much research has been carried out on the fire resistance of SFRC and some test results contradict. In theory, the fire resistance could increase when compared to plain or conventionally reinforced concrete. A rapid temperature increase within the concrete will not result in peak stresses that cause spalling of concrete, as the expansion of the fibres' dimensions is limited. In the case of conventionally reinforced concrete, the increase in diameter of the reinforcement bars often leads to damage. The addition of plastic fibres could increase the fire resistance as they melt very quickly and create additional pores. The increase in pore volume could serve as an expansion system for the water that evaporates from the initial pore structure.

2.6 Concluding remarks

The discussion in this chapter on the pullout behaviour of individual steel fibres shows that the (post-cracking) behaviour of steel fibre reinforced concrete is influenced by the following parameters:

- The interfacial bond between matrix and fibre
- The fibre characteristics (shape, aspect ratio, tensile strength)
- The fibre orientation

Pullout tests on multiple fibres and uni-axial tensile tests on SFRC cylinders showed that the following parameters may be added:

- The fibre density, i.e. the accidental fibre distribution
- The fibre volume

Obviously the post-cracking behaviour of SFRC is improved as for instance the interfacial bond strength or the added fibre volume is increased. The fact is, however, that SFRC exhibits a relatively large scatter in the post-cracking behaviour. The next chapter deals with this scatter and shows how the main influencing parameters affect this scatter.

Chapter 3

Experimental research on SFRC

3.1 Introduction

As demonstrated in Chapter 2, several parameters influence the post-cracking behaviour of SFRC. Fibre characteristics, fibre quantity, fibre distribution in the matrix, fibre orientation relative to the crack plane and the quality of the concrete matrix surrounding the fibres all affect this behaviour at the same time. Consequently, variations in these parameters cause a certain scatter in the post-cracking behaviour. Since the coefficient of variation can considerably affect the characteristic values of the post-cracking stresses in a material model (see section 7.2), such as the stress-crack width relationship, it is important to understand the causes of this scatter.

In this chapter the occurrence of scatter in the post-cracking behaviour of SFRC is analysed. The effects of the earlier mentioned parameters on the mean values and the scatter in test results will be shown.

The testing method used in this experimental research was not chosen arbitrarily. In an overview, the available testing methods will be discussed, based on specific criteria. A 'Multiple Criteria Assessment' (MCA) was used to evaluate these testing methods.

3.2 Assessment of testing methods

3.2.1 Criteria for a suitable testing method

According to Van Mier [Van Mier, 1997], there can be several reasons for organisations, practitioners and researchers to decide on a standard test. The first reason is to determine certain parameters that are needed in an accepted model that is used in building practice. Secondly, the test method can be used to compare results obtained in different laboratories or as a benchmark problem for numerical models. Finally, it could be used as a means of quality control in practice.

In deciding which method is most suitable for testing the post-cracking behaviour of SFRC, the M624 research committee of the Dutch Centre for Underground Construction focussed on different aspects concerning the testing procedure and the applicability of the measurements in generating a uni-axial material relation. The following criteria were defined to assess the testing procedure itself:

- the complexity of the test set-up
- the complexity of preparing the specimens
- the complexity of execution
- the reproducibility of the tests
- the costs (of labour) and the applicability in practice
- acceptance of test method by researchers

The applicability of the measurements has been evaluated based on:

- the complexity of processing the test results into a uni-axial material relation
- the reliability of the test results

3.2.2 Bending tests

The two best known and widely used types of tests are the so-called four-point and three-point bending tests. The difference between the two bending tests, as shown in Figure 3.1, is obvious. The beam in the three-point bending test is loaded at mid span, while the span of the specimen in the four-point bending test is divided into three parts of equal size.

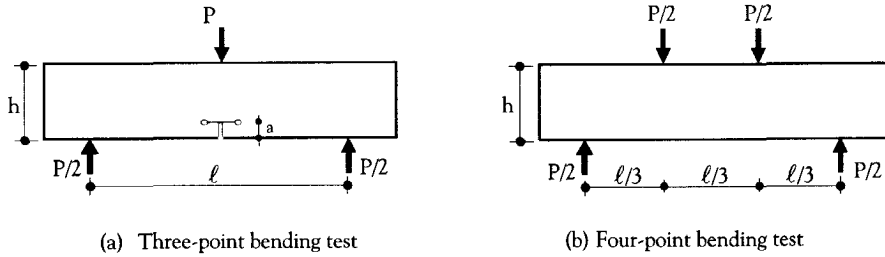


Figure 3.1 Bending tests

In both cases the test specimens can be shaped with or without a notch, although notched specimens are usually not applied in case of a four-point bending test. The latter was originally developed to incorporate the effect of variation in the material's strength. Therefore, the beam is loaded such that a constant bending moment occurs in the section between the two upper point loads. The first crack will appear at the weakest cross-section. Depending on the mix composition, the added fibre volume, the distance between the two point loads on top and the span to beam depth ratio, multiple cracking can occur in SFRC beams [Kooiman, 1997]. However, since the location of the discrete crack(s) cannot be predicted, it is complicated to measure crack opening displacements. Often, the mid-span deflection is measured in addition to the load. The area under the load-deflection curve is a measure for the energy absorption capacity.

In a three-point bending test the first crack will always appear in the vicinity of mid-span. However, the exact location of the first crack might vary. To localise the crack, a notch is often applied so that the Crack Opening Displacement (COD) can be measured. The advantage is that a direct relation is found between the bending moment and the crack width. On the other hand, the cross-section at mid-span is not necessarily the weakest cross-section.

When considering the criteria for the testing procedure itself, it is obvious that the test set-up, for both bending tests illustrated in Figure 3.1, is the same. In both cases a closed-loop system is used to execute the tests on a deformation-controlled basis, which is necessary to measure the post-peak softening behaviour. Boundary conditions, such as the support system used, can have a large effect on the experimental results [Guinea et al., 1992].

Furthermore, the tests are relatively simple to perform and are reproducible in case of constant testing conditions. The preparation of the specimens is also quite similar for both tests. In case of the four-point bending test some additional pieces of material are necessary to correctly measure the mid-span deflection. On the other hand, in the three-point bending test the notch demands some attention.

As a result of the fact that the preparation of the specimens and the execution of the tests is quite similar, the costs are almost the same. In addition, both bending tests have been found to be quite applicable and well accepted in practice.

When considering the criteria for the applicability of the test results, it is found that in both cases it is difficult to process the test results into an uni-axial material relation. An inverse analysis is the only way to do this. However, in case of load-deflection diagrams it is almost impossible to process the test results, since the measured deformation is then perpendicular to the occurring stresses. The latter is in contrast to the uni-axial material relation that is to be generated.

The second and last criterion with respect to the applicability of the test results concerns the reliability of the test results. This reliability is usually related to the scatter in test results, which depends on many influencing parameters. An important parameter is the specimen size. In case of plain concrete, the minimum size of the test specimen is usually linked to the maximum size of the largest material component in the concrete, which normally is the maximum grain size. Many assume that a fivefold increase of the specimen size (width and/or height) over the largest aggregate size is sufficient to consider the specimen homogeneous [Van Mier, 1997].

In SFRC the largest material feature is often the steel fibre itself. Standardising a ratio of five would result in large beam specimens if long steel fibres (30-60 mm) were added to the mix. This is not quite practical because the specimens will become extremely heavy. The effect of the specimen size on the scatter in the post-cracking behaviour will be shown in section 3.4.5.

3.2.3 Splitting tests

The 'Brazilian' splitting test

Splitting tests have been carried out for many years to determine the tensile strength of plain concrete. One of the best known tests is the load-controlled Brazilian splitting test on a cylinder [Neville, 1978], as illustrated in Figure 3.2.

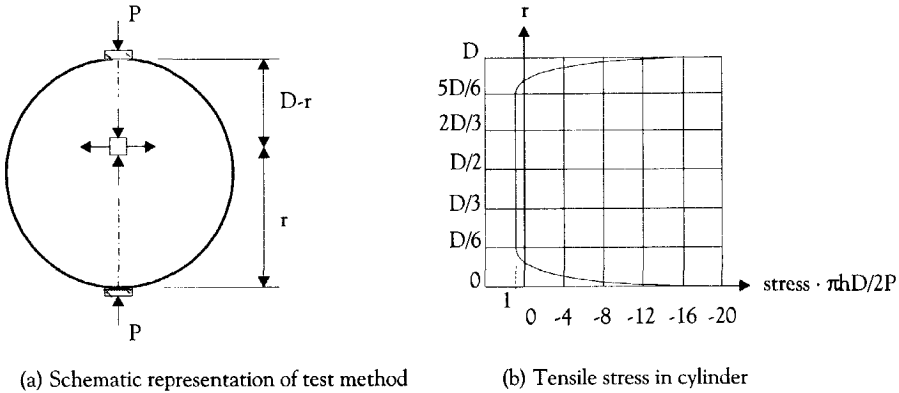


Figure 3.2 The 'Brazilian' splitting test [Neville, 1978]

Although the Brazilian splitting test can be carried out in a simple press, a closed-loop system is necessary to enable deformation-controlled testing of the post-cracking behaviour of SFRC. The specimens can be produced in the laboratory or can be cores drilled from cubes or from structures in practice. The cylinders are tested by applying loads on opposite sides of the specimen's circumference, which cause a tensile splitting stress perpendicular to the loading direction. The specimens are placed between the platens of the press, although narrow strips of packing material are often interposed between the platens and the specimen to introduce the loads uniformly and to prevent spalling/crushing. Linear Variable Displacement Transducers (LVDT's) can be used to measure the horizontal displacements at the two circular head sides of the specimens. Since the test set-up, the preparation of the specimens and the execution of the experiments are quite simple the costs per test are low.

The test method can be used as a quality control test. Laboratory tests could easily be compared to tests on cores drilled from practice.

For an uncracked specimen, Figure 3.2b shows that in horizontal direction compressive stresses occur in the vicinity of the loads, but a nearly constant tensile stress occurs in the centre part of the specimen. When the tensile strength of the plain matrix is reached, a crack will develop over the vertical diameter. After cracking due to splitting a second failure mechanism is initiated. Due to the fact that the cylinder is split into two parts, each half is eccentrically loaded and thus subjected to bending. Researchers have observed radial cracks as a result of this second mechanism and found a hump in their measurements [Lilliu & Van Mier, 1999]. This secondary mechanism seems to be influenced by the boundary conditions. Processing the test results into a uni-axial relationship seems therefore to be quite difficult.

The wedge-splitting test

Another splitting test is the so-called wedge-splitting test developed by Tschegg and Linsbauer [Tschegg & Linsbauer, 1986]. In Figure 3.3 the specimen and loading procedure are shown. In this test a cube or cylinder is split from one side by a wedge. The test must be carried out in a deformation controlled way, and the crack opening displacement (COD) is measured on top of the specimen as indicated in Figure 3.3c or on both sides of the specimen as described by Stroband [Stroband, 1998].

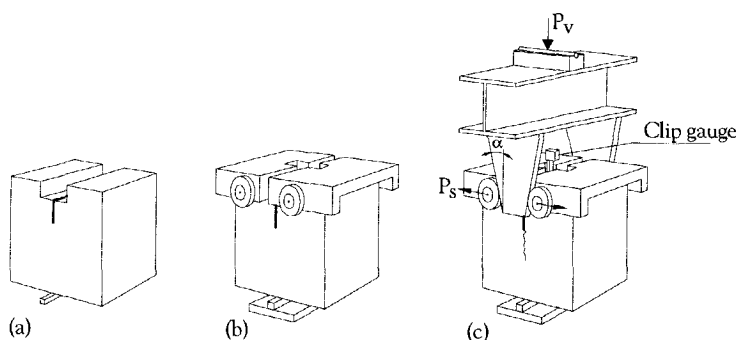


Figure 3.3 Specimen and loading procedure of the wedge-splitting test method [Van Mier, 1997]

Just like the Brazilian splitting test, the wedge-splitting test can be carried out in a standard laboratory press. The specimens need to be fabricated in specially designed moulds so that a cavity is produced, which enables the auxiliary devices to be placed on the specimens. These devices guide the wedge.

According to Stroband [Stroband, 1998] the wedge-splitting test is easier to carry out than both bending tests described in section 3.2.2. Despite the fact that the reproducibility of the test is good and the costs are quite low the test method is not widely applied and is internationally still not really accepted for determining the post-cracking behaviour of SFRC.

Considering the criteria for the applicability of the test results, the complexity of processing the results into a uni-axial material relation is similar to that for the bending tests. Again from the measured load-crack opening displacement curve, the tensile strain-softening diagram must be determined through an inverse analysis. With respect to the reliability of the test results Stroband reported that the pouring direction considerably affects the test results [Stroband, 1998]. Splitting the specimens perpendicular to the pouring direction resulted in a fracture energy values that was twice as high as in case of splitting in line with the pouring direction. However, this is a fundamental problem and is an issue in other testing methods too.

3.2.4 Uni-axial tensile tests

In theory, the uni-axial tensile test, as shown in Figure 3.4a, is the best testing method to determine the uni-axial post-cracking behaviour of SFRC, because the test results can be directly processed into a uni-axial material relation. On the other hand, there are some disadvantages bound to this testing method.

The necessary test set-up, for instance, is quite complex. This is the result of the specimen's behaviour at crack initiation. When the tensile strength is reached, a crack appears on one particular side of the specimen. As a consequence, bending moments can be introduced if the deformation is restrained (see Figure 3.4b). To avoid any restrained deformations, rotating plates can be installed, which results in an even more complex test set-up. In addition, the prismatic or cylinder-shaped specimens can be notched to localise the crack in advance. Special care and attention is required to ensure that the weak interfaces between the concrete, the glue and the steel platens do not fail.

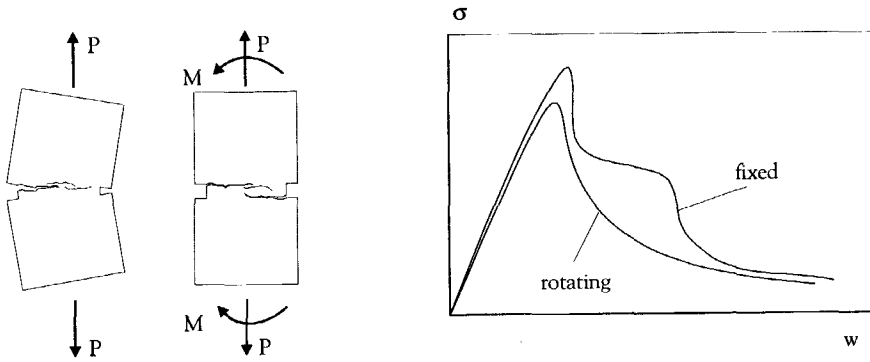


Figure 3.4 Effect of fixed and rotating loading plates in uni-axial tensile tests [Van Mier, 1997]

Due to the complex test set-up a uni-axial tensile test is not easy to carry out and demands highly trained and experienced personnel. Furthermore, the preparation time of the tests is much longer than in the case of bending and splitting tests. As a consequence, the costs per experiment are relatively high and the applicability of the test method is low.

When considering the reliability of the test results, Stroband [Stroband, 1998] showed that in case of testing SFRC for practical applications ($V_f < 1\%$) the scatter in test results is relatively high. It was found that the fracture energy was strongly correlated to the number of fibres in the cross-section.

3.2.5 Multiple Criteria Assessment of test methods

To determine the most suitable method for testing the post-cracking behaviour of SFRC a Multiple Criteria Assessment (MCA) was carried out. In Table 3.1 the five previously discussed test methods were evaluated using the criteria mentioned in section 3.2.1 and the weight factors defined by the M624 research committee of the Dutch Centre for Underground Construction, as presented by Stroband [Stroband, 1998]. Each test method scores points per criterion. This score can vary between 1 (worst case) and 5 (best case) and is multiplied by a weight factor to obtain weighted values (Π). The total score (Σ) is shown for each test in the last row of Table 3.1.

Table 3.1 Multiple Criteria Analysis of test methods for testing the post-cracking behaviour of SFRC

Criteria	weight factor	Four-point bending test		Three-point bending test		Brazilian splitting test		Wedge-splitting test		Uni-axial tensile test	
		score	Π	score	Π	score	Π	score	Π	score	Π
1. Complexity of test set-up	1	3	3	3	3	5	5	4	4	1	1
2. Complexity of preparation	2	4	8	3	6	5	10	3	6	1	2
3. Complexity of execution	3	3	9	3	9	3	9	3	9	1	3
4. Reproducibility of the tests	10	3	30	3	30	2	20	3	30	3	30
5. Costs per experiment	1	3	3	2	2	5	5	4	4	1	1
6. Acceptance of test method	6	2	12	5	30	3	18	3	18	3	18
7. Processing complexity	2	2	4	3	6	4	8	3	6	5	10
8. Reliability of test results	10	3	30	3	30	1	10	3	30	3	30
Total score Σ			99		116		85		107		95

Table 3.1 demonstrates that the three-point bending test is the most suitable test method according to the criteria and weight factors used. The criteria and weight factors in Table 3.1 were chosen subjectively. However, they were chosen according to the point of view that the reason of testing is to develop a suitable and reliable model that can be used in building practice.

Table 3.1 provides quite a static picture. Another MCA outcome is most likely to happen when one or more heavy weight factors, such as the three important criteria 4, 6 and 8, change. For instance, when the weight scale is altered from 1-10 to 1-5, the total scores change significantly. Scenario A in Appendix A shows that although the three-point bending test still is the preferred test method, the difference in total score between this test and the wedge-splitting test is marginal. In case the criterion of acceptance by the scientific community is not considered (see scenario B in Appendix A), the wedge-splitting test seems more suitable. Again, the difference in total score between wedge-splitting test and the other test methods is very small. Obviously, conclusions concerning the best test method cannot be made from the Multiple Criteria Assessment carried out in this section.

3.2.6 Experimental research by means of three-point bending tests

In the experimental programme carried out in the scope of this research, the three-point bending test was chosen to investigate the variation in the post-cracking behaviour of SFRC. This choice is based on several arguments.

Firstly, a simple, cheap and reliable test method is necessary to meet the demand from practice for standard test and suitable design methods. Amongst others the three-point bending test is a reasonably simple, cheap and reliable test.

Secondly, structural applications of SFRC (bedding supported slabs, underwater concrete, shield tunnel linings) are mainly subjected to bending moments. Because of the possibility of redistributing stresses in these statically indeterminate structures, the application of SFRC can increase the load-bearing capacity enormously when compared to the load-bearing capacity of one single cross-section [Schnütgen, 2000]. Before studying the load-bearing capacity of such a structure, the occurrence of multiple cracks needs to be examined. However, when testing SFRC mix compositions that are used for slabs and underwater concrete by means of a bending test, only one crack occurs. The location of this single crack cannot be predicted in case of a four-point bending test. A three-point bending test is much more convenient, because the crack opening displacement needs to be measured for modelling purposes (see Chapter 5).

Thirdly, Kooiman [Kooiman, 1997] showed that in case of SFRC with a relatively high compressive strength and a maximum practical fibre volume, multiple cracking can be observed in a four-point bending test. It was found, however, that the occurrence of more than one crack depended on geometrical boundary conditions, such as the distance between the two point loads on top of the beam. However, before studying crack patterns and crack distances, it is necessary to be able to analyse a single cross-section in bending. The three-point bending test enables the analyses of a single cross-section.

Finally, the three-point bending test has been recommended by the RILEM Technical Committee 162-TDF to test and model the softening behaviour of SFRC [RILEM TC 162-TDF].

3.3 Experimental programme

3.3.1 Research parameters

Until now, it has never been investigated in what way and to what extent the scatter in the post-cracking behaviour is affected by fibre addition. To investigate the occurrence of scatter it is important to determine the main research parameters. In the concluding remarks of Chapter 2, the influencing parameters on the post-cracking behaviour of SFRC were summarised. Although it is hard to influence fibre orientation and fibre distribution, it is obvious that varying the matrix quality, the fibre characteristics and/or the fibre volume will cause a change in the post-peak softening relation. Table 3.2 shows the parameters varied within the scope of this research.

Table 3.2 Main research parameters to investigate the occurrence of scatter

Research variables	Qualitative change	Quantitative change
Matrix quality	Compressive strength	59.3 - 81.1 N/mm ²
Fibre volume	Fibre dosage	40 - 60 kg/m ³ ($V_f = 0.51-0.77\%$)
Fibre characteristics	Aspect ratio L_f/d_f	60 - 80
	Tensile strength fibres	1100 - 2700 N/mm ²

Based on the SFRC mix composition that was applied in the tunnel segments for the second Heinenoord tunnel, mix 1 and 2 in Table 3.3 were used in this experimental research. In both mixes river gravel with a maximum grain size of 16 mm was used.

Table 3.3 Concrete mix compositions used in experiments

Mix components	mix 1	mix 2
Portland cement	87.5 kg/m ³ CEM I 52.5	87.5 kg/m ³ CEM I 52.5
Blast furnace cement	262.5 kg/m ³ CEM III/B 52.5	262.5 kg/m ³ CEM III/B 42.5
Sand 0-4 mm	43 %	48 %
Gravel 4-16 mm	57 %	52 %
Superplasticiser	1.4 % (relative to cement)	1.0 % (relative to cement)
Water/binder ratio	0.42	0.45

Table 3.4 shows the mean cube compressive strength f_{ccm} and the mean tensile splitting strength $f_{ctm, spl}$ of mix 1 and 2, reinforced with 60 kg/m³ hooked-end steel wire fibres, having an aspect ratio L_f/d_f of 60/0.75 and a tensile strength of 1200 N/mm².

Table 3.4 Mean compressive and tensile splitting strengths

	f_{ccm} (N/mm ²)	$f_{ctm, spl}$ (N/mm ²)
mix 1	81.1	4.6
mix 2	59.3	3.5

3.3.2 Test set-up

Testing frame

The tests were carried out in a stiff, steel test frame. In this frame, the test specimens were supported by steel roller supports that were placed on roller support systems (see Figure 3.5). The central support was connected to a load cell that was fixed to the test frame.

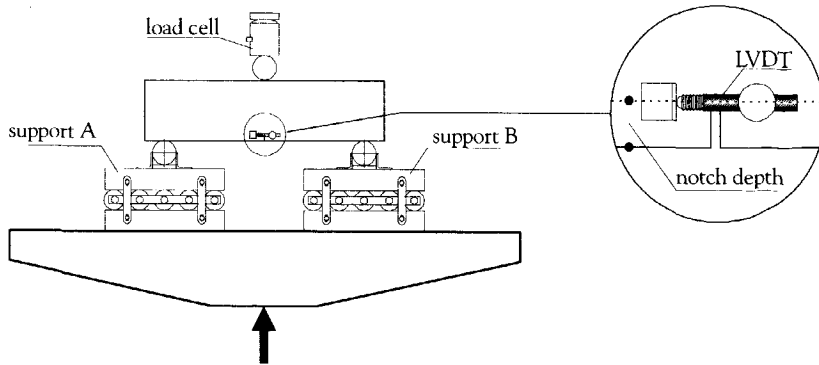


Figure 3.5 Set-up three-point bending test

Support systems

For three-point bending tests, Guinea et al. [Guinea et al., 1992] analysed the influence of the experimental equipment on the fracture energy of plain concrete. It was found that energy dissipation at fixed supports resulted in a considerable contribution to the apparent fracture energy, when compared to results with roller bearings. To avoid as much frictional resistance as possible, roller support systems were used to support the beams in the research described below. Two steel rolls with a diameter of 60 mm were fixed on top of the roller support systems. Although in this case both support systems were able to move freely in horizontal direction they slightly differed from one each other, as Figure 3.6 shows. Rubber strips made it possible for one roll to rotate freely so that a restrained deformation as a result of torsion could not occur. Torsion was expected as a result of non-symmetrical size differences and a non-homogeneous fibre distribution in the cross-section.

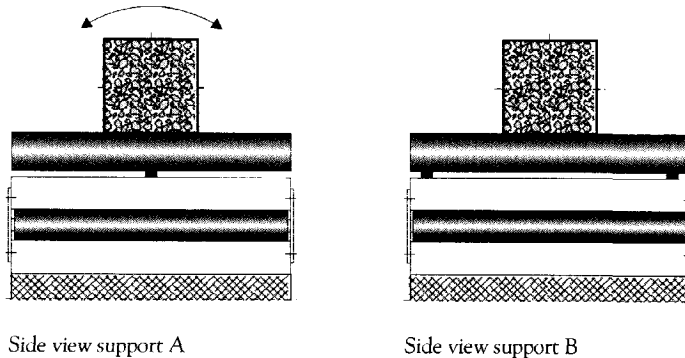


Figure 3.6 Roll support systems

Deformation controlled testing

To investigate the post-cracking behaviour of (steel fibre reinforced) concrete it was necessary that the tests were performed on a deformation controlled basis. This was provided by a closed-loop system, controlled by the deformation measured at the notch tip. Due to the fact that fibres tend to segregate when test specimens are compacted, there is difference in deformation between both sides. Therefore, it was decided to control the test by averaging the

measured deformations on both sides of the specimen. In the initial test series, the rate of testing was 1 $\mu\text{m/s}$. Later, in the second test series the beams have been loaded up to the very large deformations ($> 20 \text{ mm}$). The rate of testing in that case was also 1 $\mu\text{m/s}$. However, after a crack opening displacement of 5 mm, the rate of testing was increased up to 50 $\mu\text{m/s}$.

Measurements

To measure the applied loads a load cell was connected to the steel roll on top of the beam that introduced the point load at mid-span. The capacity of this load cell was 400 kN with a measurement accuracy of 0.05 kN. On top of the load cell a hinge was applied to prevent possible effects of restrained deformations due to torsion. Linear variable displacement transducers (LVDT's) were used to measure the crack opening displacement (COD), i.e. the horizontal displacement of the LVDT at the notch tip (see Figure 3.5), on both sides of the beam. In the initial test series the maximum displacement of these LVDT's was 5 mm with an accuracy of 1.2 μm and the measuring length was 40 mm. Later, in the second test series the beams were loaded up to the larger deformations ($> 20 \text{ mm}$). The maximum displacement of the LVDT's was 100 mm with an accuracy of 21 μm . The measuring length in that case was 100 mm.

3.3.3 Specimen sizes

According to Bažant [Bažant, 1984], the span to beam depth ratio ℓ/h has to be higher than $2\frac{1}{2}$ to prevent energy dissipation at the supports. Furthermore, the notch depth to beam depth ratio a/h should be in the range of 0.15 – 0.5 and the notch width should be smaller than half the maximum grain size. In the experimental research carried out within the scope of this dissertation the dimensions met the demands of Bažant.

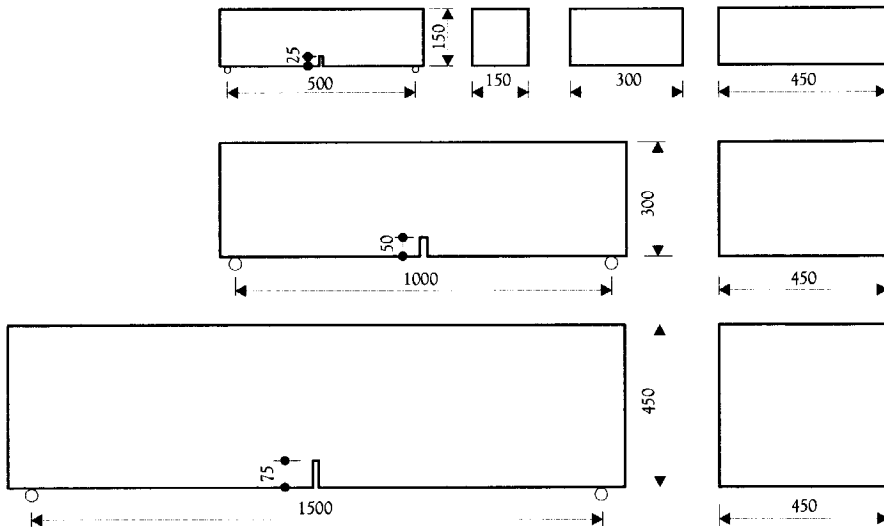


Figure 3.7 Specimen sizes tested within the scope of this research

Following the recommendations of the RILEM Technical Committee 162 TDF [RILEM TC 162-TDF, 2000], standard specimen sizes (150x150x600) were initially used to investigate the effect of the influencing parameters from Table 3.2 on the scatter in the post-cracking behaviour of SFRC. In a later stage larger specimens were also tested to investigate the influence of the specimen size on (scatter in) the post-cracking behaviour (see Figure 3.7). Since Bažant [Bažant, 1984] showed that the flexural tensile strength depends on the span to beam depth ratio and the notch depth to beam depth ratio, ℓ/h and a/h have been kept constant in any case.

3.3.4 Production and curing of specimens

Each test series consisted of six test beams and six cubes. Three cubes were used to determine the compressive strength and three to check the tensile splitting strength. The rib length of these cubes was 150 mm. These standard tests were carried out by force-control in a hydraulic press. In case of the tensile splitting stress 3 mm thick and 15 mm wide strips of triplex were interposed between the loading platens and the specimen.

The small test beams were initially poured in steel moulds (size accuracy ± 1.5 mm). Later, in the second test series, they were cast in a mould with a size accuracy of ± 5 mm, just like the larger beams. The procedure for casting the specimens and filling the moulds is shown in Figure 3.8a, which is according to the Draft Recommendation of the RILEM TC 162 TDF [RILEM TC 162-TDF, 2000]. After the specimens were compacted, plastic cover sheets were used to prevent early drying of the specimens. In the first test series, the 'standard' beam specimens were compacted by placing the steel moulds on a vibration table. In contrast, the larger beams were compacted by means of vibration motors underneath the mould in which they were poured.

All specimens were stored in the laboratory for 1 or 2 days (at a temperature varying from 18 to 24 degrees) until they could be demoulded and placed into a climate-conditioned room at a constant temperature of 20 degrees and a relative humidity of approximately 95%. All test specimens were tested at an age of 28 days ± 1 day. The loading direction was perpendicular to the pouring direction (see Figure 3.8b). Before testing, the specimens were notched with the help of a diamond saw.

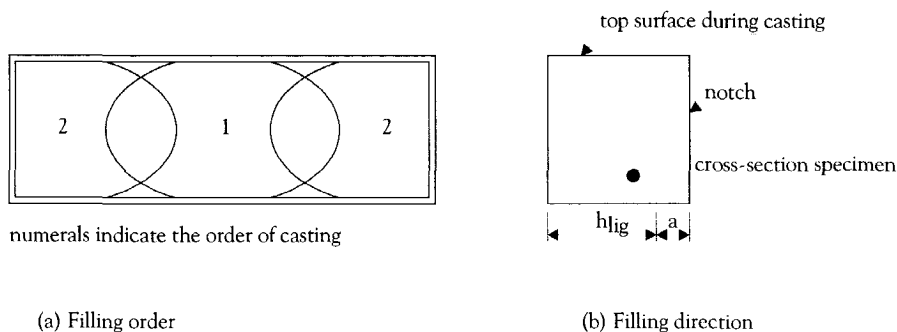


Figure 3.8 Filling procedure for casting the specimens, according to RILEM [RILEM TC 162-TDF, 2000]

3.4 Test results

3.4.1 Energy absorption capacity G_{fc} and coefficient of variation V_G

To analyse the post-cracking behaviour of SFRC, it is common practice to determine toughness values. The toughness of steel fibre reinforced concrete D_{fc} is determined by calculating the area under the load-displacement curve [ACI Committee 544, 1988]. In case of SFRC, the ductility increases considerably compared to plain concrete. Therefore the tail of the load-displacement diagram is often cut at displacements that are 10 to 20 times larger than the maximum displacement for plain concrete, [RILEM TC 162-TDF, 2000]. Usually the surface below the linear elastic part of the load-displacement diagram is subtracted from the total toughness value of SFRC to determine the effect of the fibre addition. In case of low fibre volumes, this is necessary to determine the real contribution of the fibre addition. In case of the fibre volumes applied in the scope of this research, however, the surface beneath the linear elastic branch of the load-displacement diagrams is negligible compared to the considered toughness values of SFRC. Therefore, the contribution of the concrete matrix has been taken into account in the toughness values presented hereafter.

To enable a comparison of test results from different beam sizes the toughness value D_{fc} was divided by the beam's cross-section above the notch. For that same reason, the effect of the beam's weight had to be taken into account. The effect of the beam's dead load on the actual energy absorption capacity, however, is in case of SFRC relatively small compared to plain concrete (see Appendix B).

According to RILEM TC-89 FMT [RILEM TC-89 FMT, 1990], the following equation can be used to calculate the energy absorption capacity G_{fc} of the cross-section up to a certain crack opening displacement δ :

$$G_{fc}(\delta) = \frac{D_{fc}(\delta)}{b \cdot (h - a)} \quad (3.1)$$

With G_{fc}^i as the energy absorption capacity of the i^{th} test specimen at crack opening displacement δ and G_{fcm} as the mean value of the energy absorption capacity of the test series (consisting of n tests), the standard deviation $s_G(\delta)$ was calculated as follows:

$$s_G(\delta) = \sqrt{\frac{\sum_i^n (G_{fc}^i(\delta) - G_{fcm}(\delta))^2}{n - 1}} \quad (3.2)$$

The scatter in the post-cracking behaviour of SFRC can be quite large. At the same time the mean value of the energy absorption capacity can vary significantly. To visualise the combined effect, the coefficient of variation V_G can be determined by the following equation:

$$V_G(\delta) = \frac{s_G(\delta)}{G_{fcm}(\delta)} \quad (3.3)$$

3.4.2 Effect of matrix quality on mean G_{fc} and V_G

Characteristic load-crack opening displacement ($P-\delta$) curves as a result of bending tests on 'standard' SFRC specimens ($150 \times 150 \times 600 \text{ mm}^3$) are shown in Figure 3.9 and 3.10 for mix 1 and 2 from Table 3.3. In both mixtures, 0.77 % (or 60 kg/m^3) hooked-end, steel wire fibres with an aspect ratio of 80 ($L_f/d_f = 60/0.75$) were added. All other $P-\delta$ curves have been published in a laboratory report by Kooiman [Kooiman, 1998]. As Figure 3.9 and 3.10 show, a considerable scatter occurred in the post-cracking stage of the test results. It is obvious that the scatter in the higher strength SFRC of matrix 1 exceeds the scatter in the test results of matrix 2.

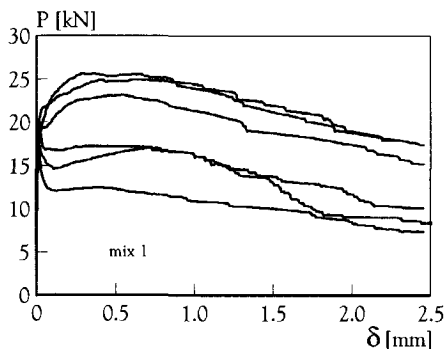


Figure 3.9 $P-\delta$ curves matrix 1

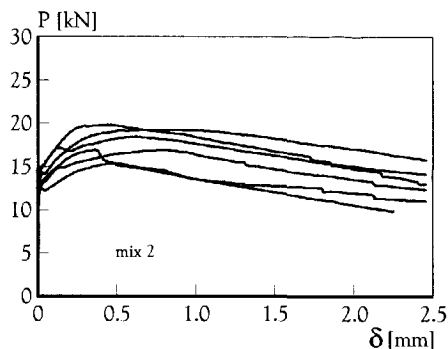


Figure 3.10 $P-\delta$ curves matrix 2

Figure 3.11 shows the effect of the matrix quality on the post-cracking behaviour. Since the bond strength decreases as the concrete strength decreases, it is not surprising to see that the mean G_{fc} values for crack openings up to 2.5 mm are lower for the lower strength matrix. It can be seen that within the tested range of deformation, the energy absorption capacity G_{fcm} of the cross-section increases almost linearly.

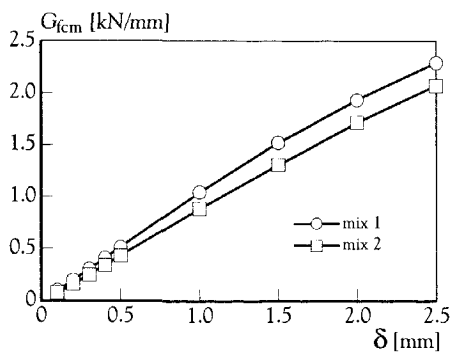


Figure 3.11 Effect of matrix quality on G_{fcm}

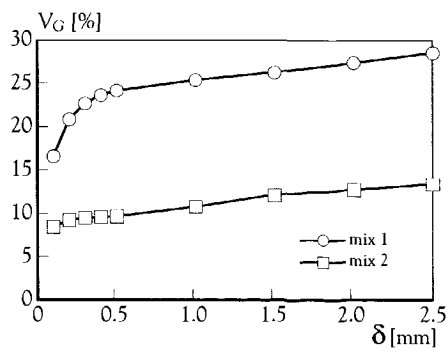
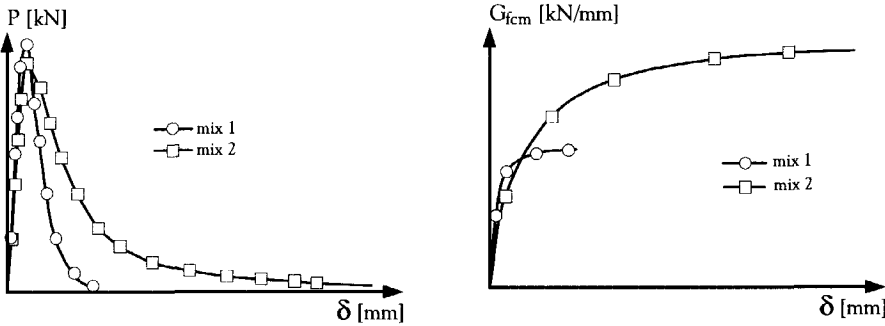


Figure 3.12 Effect of matrix quality on V_G

Figure 3.12 shows that the coefficient of variation V_G is considerably smaller for the lower strength concrete matrix of mix 2 as a result of the much smaller scatter in test results. During testing it was observed that the fibres in the high strength matrix of mix 1 tended to break, in

contrast to the pullout behaviour of the fibres in mix 2. Relating the observations to Figure 3.12, it seems that the increase of V_G is caused by fibre rupture. In the next section, however, it will be shown that this increase in scatter is not due to the breaking of fibres.

In case of the high strength concrete matrix of mix 1 the fibres tended to break after reaching the maximum load, which was clearly heard during testing. Consequently, the deformation capacity and maybe even the energy absorption capacity of the specimens made of mix 1 may be smaller than in specimens made of mix 2 (see Figure 3.13). Due to the fact that measurements were only performed up to a deformation of 2.5 mm, a possible difference in deformation capacity could not be proven. In the subsequent test series the specimens were tested up to their maximum deformation.



(a) Possible effect on load-displacement curve

(b) Possible effect on energy absorption capacity

Figure 3.13 Possible effect of fibre breaking on the mean deformation capacity and G_{fcm} of mix 1 and 2

3.4.3 Effect of fibre characteristics on mean G_{fc} and V_G

To investigate the effect of certain fibre characteristics on the scatter in the post-cracking behaviour of SFRC mix 1 of Table 3.3 was also tested with two other fibre additions. Figure 3.14 shows that the mean G_{fc} values were not very sensitive to the small changes in aspect ratio (from 80 to 65) and to an increase in fibre strength (low carbon = 1100 N/mm² vs. high carbon = 2700 N/mm²) in this particular range of deformations.

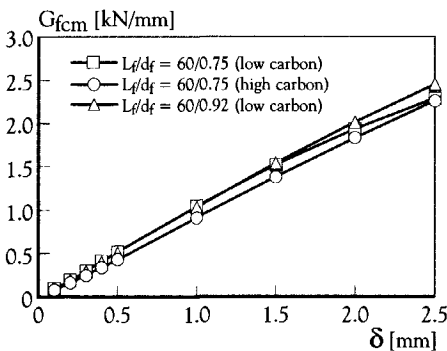


Figure 3.14 Effect of fibre characteristics on G_{fcm}

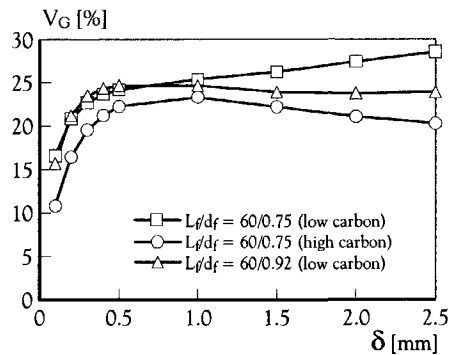


Figure 3.15 Effect of fibre characteristics on V_G

The results shown in Figure 3.15 indicate that in this particular range of deformations, the aspect ratio and the fibre strength have a minor impact on the coefficient of variation V_G . However, an increasing coefficient of variation can be observed for a crack tip opening displacement of over 1.0 mm for the lower strength fibres. In that range the maximum V_G seems to be reached for the higher strength fibres. After noticing that the maximum load in the load displacement curves of mix 2 in Figure 3.10 occurs at a crack opening of 0.5-1.0 mm, it is evident that fibre rupture only occurs after reaching the maximum load level. This is confirmed by the observations during execution of the bending tests.

In a second experimental programme various bending tests were carried out up to the maximum deformation δ_0 . In this case mix 2 was used instead of mix 1. Not only a 60 kg/m³ fibre addition was tested with an aspect ratio of 60/0.75 = 80, but also a mixture with 60 kg/m³ fibres and an aspect ratio of 30/0.5. The mean values of the energy absorption capacity are plotted in Figure 3.16. It is obvious that the aspect ratio significantly influences the mean energy absorption capacity at large deformations. Figure 3.17 confirms that the effect of the aspect ratio on the coefficient of variation V_G is small. In the lower strength matrix of mix 2, V_G initially decreased after which the scatter increased. This is attributed to fibre pullout after the peak load was reached.

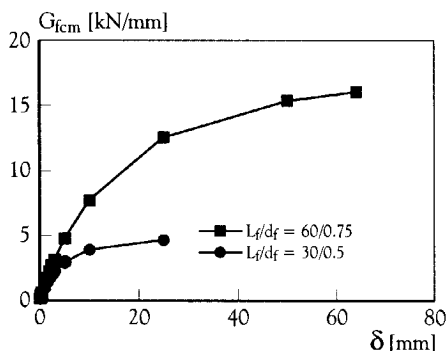


Figure 3.16 Effect of aspect ratio on G_{fcm}

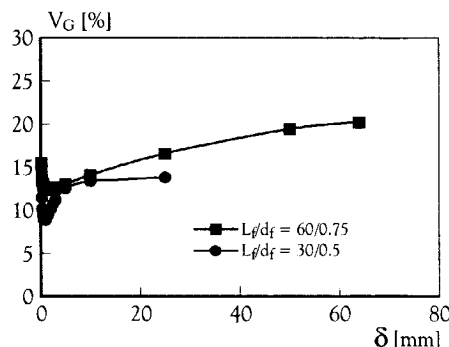


Figure 3.17 Effect of aspect ratio on V_G

3.4.4 Effect of fibre volume on mean G_{fc} and V_G

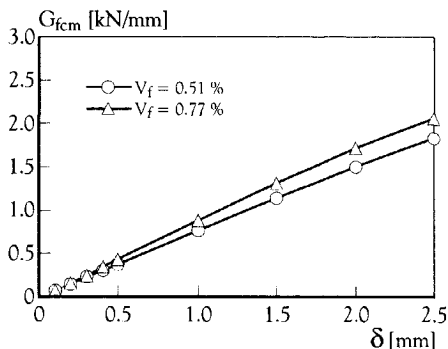


Figure 3.18 Effect of fibre characteristics on G_{fcm}

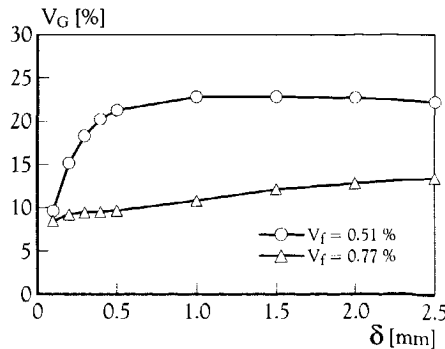


Figure 3.19 Effect of fibre characteristics on V_G

To investigate the effect of fibre volume on the occurrence of scatter in the post-cracking behaviour two different fibre volumes were added to mix 2. Figure 3.18, as expected, shows that the mean G_{fc} values decreased as the added fibre volume decreased. Figure 3.19 shows that the coefficient of variation is much higher for the mix with the lower fibre volume. It is obvious that the scatter in the post-cracking behaviour increases considerably as the fibre volume is lowered. Again the steep increase occurs just after cracking, within the first 0.5 mm of deformation.

3.4.5 Testing size effects on the post-cracking behaviour

The size effect is an important, if not the utmost important, aspect of every theory in physics. In the past, research has shown that the latter also applies for concrete. Various types of experiments have been conducted to model the size effect in concrete so that the reliability in design of concrete structures could be enhanced. Two of the best known models for predicting size effects in plain concrete are Bažant's Size Effect Law [Bažant, 1984] and the so-called Fractal Scaling Law by Carpinteri and Chaia [Carpinteri & Chaia, 1995]. Both types of models have to be fitted to experimental data. According to Van Vliet [Van Vliet, 2000], this is not the right approach to study size effects since the models do not incorporate physical mechanisms. In his opinion, physical mechanisms should be incorporated to obtain the correct behaviour of a material volume. Furthermore, Van Vliet shows that it is important to separate material size effects from structural size effects when testing size effects in concrete by means of experiments, especially in uni-axial tensile tests where a bending mechanism is likely to occur at crack initiation (see Figure 3.4).

In the scope of this research the three-point bending test was used to investigate the effect of an increase in material volume on the energy absorption capacity G_{fc} and the scatter in the post-cracking behaviour of SFRC. The dimensions of the cross-section were varied according to Figure 3.7. To avoid any structural size effects in case of increasing the beam depth, the ratio span length was increased in such a way that the span length to effective beam depth ratio ℓ/h_{lig} was kept constant.

Effect of the beam depth on the mean G_{fc} values and scatter

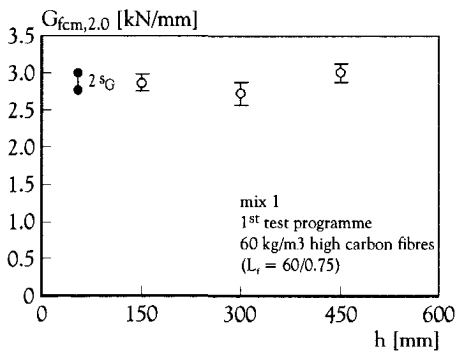


Figure 3.20 Effect of beam depth on $G_{fc,m,2.0}$

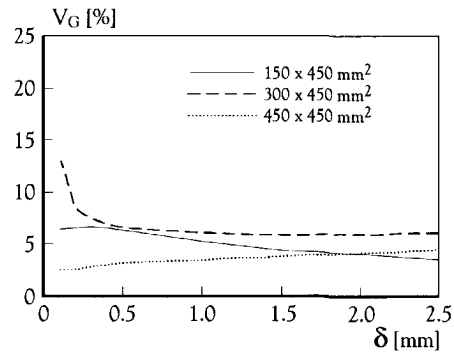


Figure 3.21 Effect of beam depth on V_G

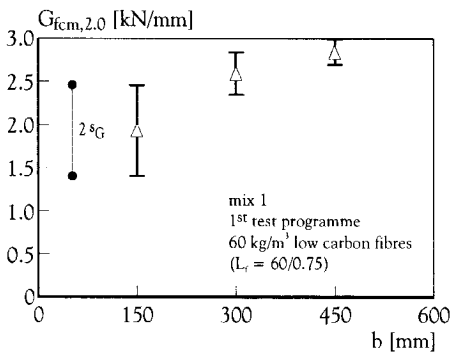
Figure 3.20 shows the effect of the beam depth h on the mean energy absorption capacity G_{fc} and the standard deviation s_G at a crack opening of 2.0 mm. The presented figure results from test series on 450 mm wide beams made of mix 1 of Table 3.3. It seems as if there is no material size-effect, since the mean values do not deviate much from each other ($<10\%$).

Furthermore, it seems as if the beam depth does not influence the scatter. Figure 3.20 shows that the standard deviation is almost constant and Figure 3.21 proves that the coefficient of variation is not only almost constant, but also quite small (5%). As will be shown later, the latter has something to do with the large beam width.

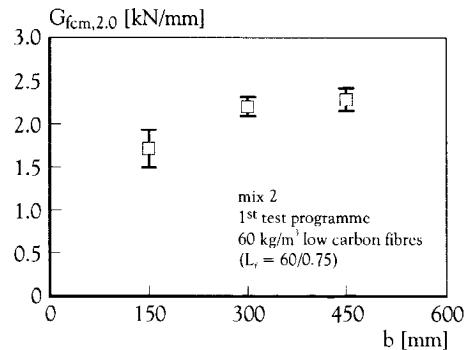
Effect of the beam width on the mean G_{fc} values and scatter

Figure 3.22a shows the effect of an increasing beam width on the mean value of the energy absorption capacity G_{fc} and the standard deviation s_G at a crack tip opening displacement of 2 mm for mix 1 of Table 3.3. In Figure 3.22b G_{fc} is presented for mix 2. Quite surprisingly the effect of an increasing beam width seems quite significant with respect to the mean values of the energy absorption capacity G_{fc} . In both mix compositions of Table 3.3 the G_{fc} values increased with increasing beam width.

Next to the observed increase in energy absorption capacity per unit cross-sectional area the scatter reduces as the beam width b increases. The trend in Figure 3.22a and 3.22b was also observed in the SFRC mixture with the higher tensile strength steel wire fibres. The corresponding values for $G_{fc,2.0}$ and s_G and the values for the higher strength fibres in mix 1 are presented in Table 3.5.



(a) Effect of beam width for mix 1



(b) Effect of beam width for mix 2

Figure 3.22 Effect of beam width on energy absorption capacity $G_{fc,2.0}$ and standard deviation s_G

As Figure 3.22a and 3.22b show, and as can be seen in Table 3.5, considerable variations occur in mean G_{fc} values between the 150 mm wide test specimens and the others (compare G_{fc} values within the separate columns). Two aspects could have caused the variations in G_{fc} values. Firstly, variations could have occurred as a result of differences in the mean matrix quality between different beam widths, since each test series was poured from one separate batch. Cube tests, however, showed no large deviations in compressive strength ($<10\%$) between the separate batches. Secondly, the different pouring and vibration processes could have caused variations between the 'standard' test specimens and the wider beams.

Table 3.5 Mean values of the energy absorption capacity per cross-sectional area at $\delta = 2.0$ mm

	mix 1 DRAMIX RC 80/60 BN		mix 2 DRAMIX RC 80/60 BN		mix 1 DRAMIX RC 80/60 BP	
	$G_{fcm,2.0}$ [kN/mm]	s_G [kN/mm]	$G_{fcm,2.0}$ [kN/mm]	s_G [kN/mm]	$G_{fcm,2.0}$ [kN/mm]	s_G [kN/mm]
b = 150 mm	1.93	0.53	1.71	0.22	1.83	0.39
b = 300 mm	2.60	0.24	2.20	0.11	2.79	0.25
b = 450 mm	2.84	0.15	2.29	0.13	2.87	0.12

To eliminate possible variations due to the production process additional experiments were carried out. Since practical boundary conditions made it impossible to cast all eighteen specimens of the three different series (6x3) at once, two ‘standard’ 150x150x600 mm³ test specimens, two 300x150x600 mm³ beams and two 450x150x600 mm³ specimens were cast from the same batch. This was repeated two times to complete the number of specimens in a test series (each series consisted of 6 repetitions). To minimise variations in fibre distribution and orientation between differently sized test specimens, all specimens were cast in the same mould, using the pouring procedure shown in Figure 3.8a, and compacted with the same vibration motors and compacting energy.

Figure 3.23 shows the results of the additional testing programme on mix 2 of Table 3.3. In contrast to the earlier test series the energy absorption capacity $G_{fcm,2.0}$ is now more or less constant for increasing beam width. As expected, the scatter is now larger than the scatter in the earlier test series. This increase can be explained by the fact that in this additional testing programme six test specimens of the same size were poured from three batches instead of a singular batch that was used before to cast a test series. Although the standard deviations are more or less equal at $\delta = 2.0$ mm, Figure 3.24 shows that at larger displacements the scatter decreases as the beam width increases.

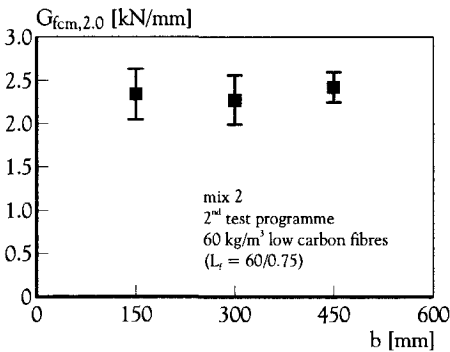


Figure 3.23 Effect of increasing beam width on $G_{fcm,2.0}$

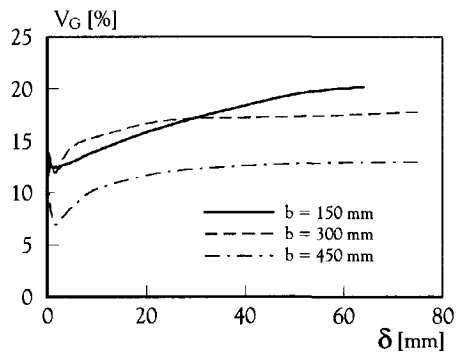


Figure 3.24 Effect of increasing beam width on V_G

After comparing Figure 3.23 with Figure 3.22b it is clear that the $G_{fcm,2.0}$ values for beam widths over 150 mm do not deviate much from one another (maximum deviation = 6%). In contrast, the $G_{fcm,2.0}$ values for the standardised, 150 mm wide beams deviate more than 25% from one another. This large deviation can only be caused by differences in the filling and compacting process of the small beams ($b = 150$ mm) between the initial tests and the additional test programme, since all other conditions (mix composition, fibre addition, dimensions) were kept constant. In the next section this is further analysed.

3.4.6 Effect of the production process on the fibre distribution

Effect of the number of fibres in the cross-section on G_{fc} values

To analyse the effect of the production process a little bit deeper the specimens were broken after testing in order to count the number of fibres in the failed cross-section. A steel frame with elastic bands was used to divide the effective depth of the cross-section into six layers while the width was divided into 75 mm wide parts (see Figure 3.25).

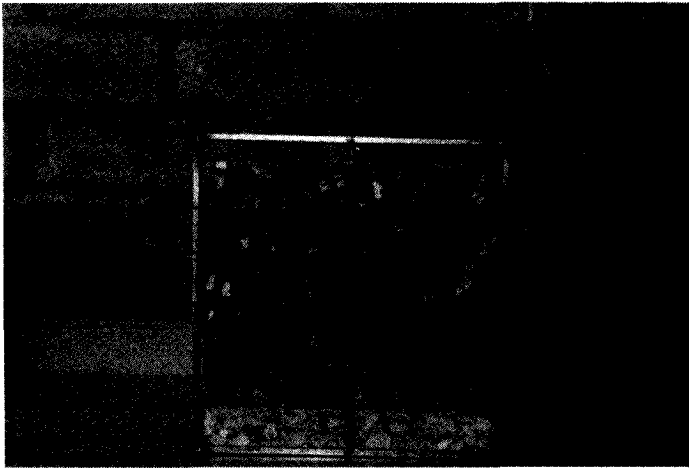


Figure 3.25 Determination of the number of fibres in a cross-section

In Figure 3.26 and 3.27 the number of fibres per cross-sectional area is plotted for mix 2 at increasing beam width. Figure 3.26 presents the mean number of fibres per cm^2 in the beams of the earlier test series of which the $G_{fc,2.0}$ values were shown in Figure 3.22b. Figure 3.27 represents the mean number of fibres in the beams of the second test series of which the $G_{fc,2.0}$ values are shown in Figure 3.23.

Figure 3.26 shows that the number of fibres per cm^2 in the 150 mm wide beams is much lower than in the wider beams. This is rather strange since the added fibre quantity was not altered. On the other hand, Figure 3.27 shows that the number of fibres per cross-sectional area was more or less constant in case of the additional test series, in which all beams were poured and compacted in the same way.

The filling of the moulds and the compacting process of the small beams in the first test series caused a smaller number of fibres at mid-span. This can be concluded after confirming that the number of fibres in the 150 mm wide beams of other mix compositions tested showed the same trend.

When comparing Figure 3.26 to Figure 3.22b and Figure 3.27 to Figure 3.23 it seems as if the energy absorption capacity is directly related to the amount of fibres in the crack plane. This confirms the findings of Stroband [Stroband, 1998] who found a strong correlation between the number of fibres in the cross-section and the fracture energy derived from uniaxial tensile tests.

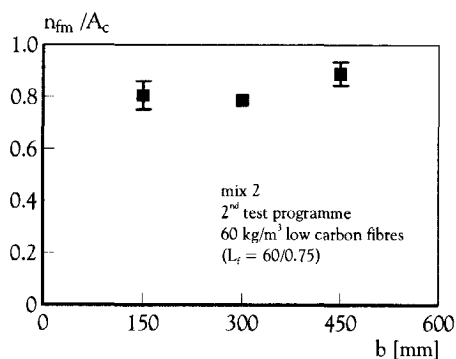
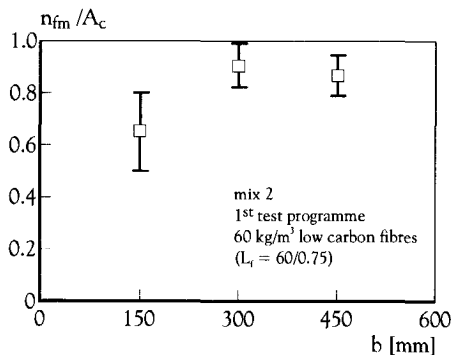


Figure 3.26 Number of fibres per cm² in 1st test series Figure 3.27 Number of fibres per cm² in 2nd test series

Effect of the fibre distribution in the cross-section on the scatter in the post-cracking behaviour

As the mean G_{fc} values seem to depend on the number of fibres in the cross-section, it is expected that the scatter in the post-cracking behaviour can also be explained by the variation in fibre distribution. Figure 3.9 and 3.10 demonstrate that in three of the six load-displacement diagrams of Figure 3.9 the load drops immediately after cracking. The question is why these curves drop and in the other three test cases ascend after cracking.

After comparing the amount of fibres in the two layers just above the notch of specimens, it was evident that in two of the three ‘dropping’ beams the number of fibres was much lower than in case of the beams that demonstrated ascending curves. It is expected that the fibres just above the notch, in the specimens with dropping curves, were immediately pulled out of the matrix. In the other ‘dropping’ beam the number of fibres was also lower, but in addition the fibres were not all randomly distributed. A clustering of fibres had occurred in the lowest layer, which leads to a smaller efficiency (and pullout capacity) per fibre, as was mentioned in section 2.3.1.

3.5 Concluding remarks

The experimental research showed that the quantified scatter, i.e. the coefficient of variation V_G , largely depends on the matrix quality and the number of fibres in the cross-section. Obviously, the number of fibres in the cross-section is related to the applied fibre volume. In practice, however, the number of fibres in a cross-section can vary significantly due to variations in the placement and vibration process. The scatter in the post-cracking behaviour in practice can therefore also differ from the scatter in the laboratory.

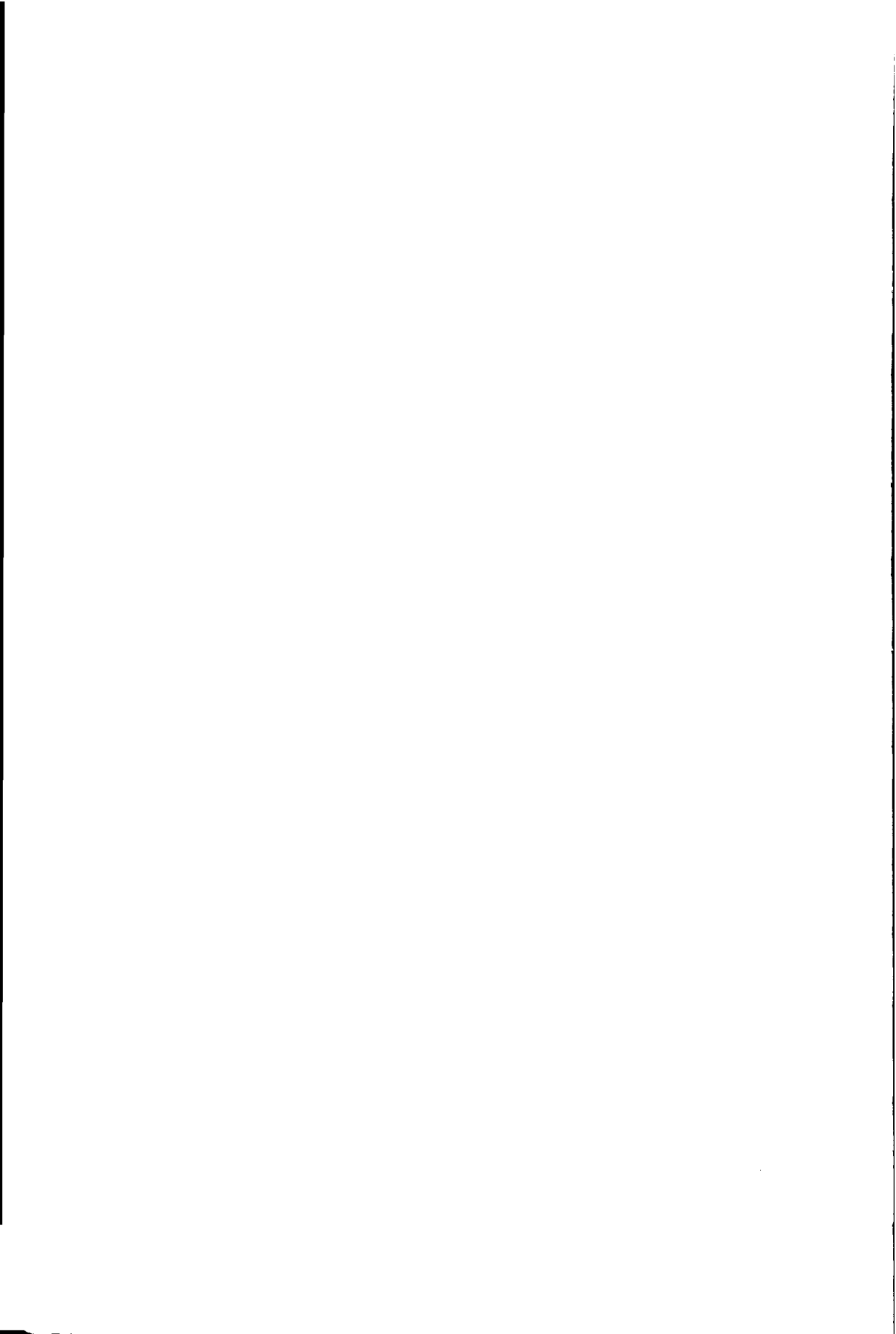
The test results showed that for a hooked-end steel wire fibre addition, the coefficient of variation V_G will not exceed a value of 20% in medium strength SFRC ($f_{cc} < 60 \text{ N/mm}^2$) at fibre volumes larger than 0.75%. However, they also proved that V_G increases up to a value of approximately 30% after decreasing the fibre volume (to 0.5 %) or increasing the concrete compressive strength (to 80 N/mm²).

For small deformations (up to 2.5 mm), the fibre characteristics themselves do not really seem to influence the scatter in the post-cracking behaviour in medium or high strength concrete. However, in the case of high strength concrete the high interfacial bond stress

between the fibres and the matrix may cause fibre yielding/breaking. This may lead to a decrease in deformation capacity, a smaller energy absorption capacity and a larger scatter at deformations larger than 2.5 mm.

Alteration of the beam width did not significantly influence the mean number of fibres per cross-sectional area, as long as the casting procedure and compacting process was the same for all test specimen. However, as soon as the pouring and vibration conditions change the mean number of fibres in the cross-section is seriously affected and, as a consequence, the energy absorption capacity too.

The beam size does seem to influence the scatter. Test results proved that the coefficient of variation V_G decreased as the beam width increased, depending on the corresponding displacement.



Chapter 4

Evaluation of existing material models for SFRC

4.1 Introduction

As the number of structural applications of SFRC has increased in the past decades, the demand for a suitable and reliable design model has arisen. To answer this demand several researchers and research committees developed methods to generate a material model. In these modelling activities emphasis was put on the tensile behaviour and especially the post-cracking behaviour of the composite material.

Three methods can be distinguished to model the softening behaviour of (quasi-brittle) materials. The first modelling method, the so-called stress-crack width method, is based on the fictitious crack model of Hillerborg et al. [Hillerborg et al., 1976] and has been dealt with in two different ways in the past. The first approach described in this chapter is the micro-mechanical approach developed by Li et al. [Li et al., 1993]. Based on micro-mechanical parameters a semi-analytical model has been developed to describe the post-cracking behaviour of SFRC. The micro-mechanical parameters in this model can be determined experimentally. The second approach is based on inverse analysis and iterations. Software packages, such as Softfit [Roelfstra & Wittmann, 1986], have especially been developed to determine the softening relationship.

The second modelling method is based on the crack band theory developed by Bažant and Oh [Bažant & Oh, 1983]. In this theory, they define a zone where distributed micro cracks spread out. The width of this so-called fracture process zone is taken into account in the model, which results in a stress strain-relationship for this particular crack band width instead of a stress-crack opening relation for a line crack.

The third and last modelling method described in this chapter is the so-called stress-strain method. Starting point of this method is that the fibre reinforced cementitious composite resembles a homogeneous continuum, which deforms when stressed and fails when the ultimate stress or strain limit is exceeded [DBV-Merkblatt, 1992], [RILEM TC 162-TDF, 2000].

In this chapter the three existing modelling methods are described comprehensively. After the descriptions, the models will be discussed. In the end, some final conclusions will be the basis for the development of an improved design relationship in the following chapters based on the demands for a suitable and reliable modelling method.

4.2 Description of existing modelling methods

4.2.1 Stress-crack width methods

The most direct way to derive a post-cracking material relation is still by means of deformation-controlled uni-axial tensile tests. Measurements at uni-axial tensile testing result in a uni-axial tensile stress σ_{ct} as a function of the measured crack opening displacement δ :

$$\sigma_{ct}(\delta) = \frac{P(\delta)}{A} \tag{4.1}$$

According to the Fictitious Crack Model (FCM) of Hillerborg et al. [Hillerborg et al., 1976], the σ - δ relationship can be split into a stress-strain relation for the linear-elastic behaviour of the concrete outside the crack and a stress-crack width relation for the softening behaviour in the cracked section. The FCM is illustrated in Figure 4.1.

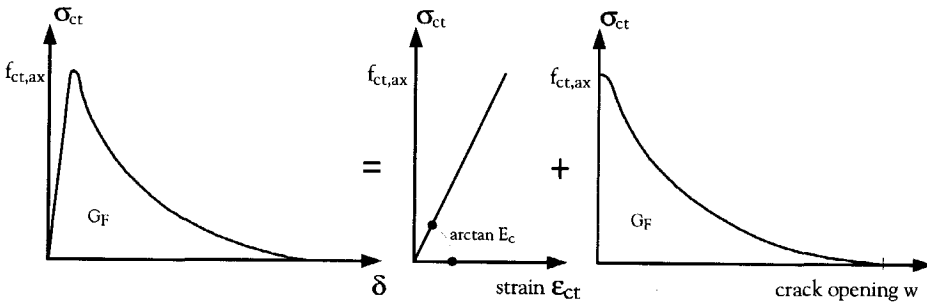


Figure 4.1 Fictitious Crack Model: separation of σ - δ relation in a σ - ϵ and a σ - w relation [4.1]

In the Fictitious Crack Model, it is assumed that over a certain length from the fictitious crack tip stresses can be transferred in a so-called cohesive zone till the critical crack width w_0 is reached. This is presented in Figure 4.2. This zone can be extended when fibres are added to the plain concrete mix. The length of the cohesive zone then depends on the length of the crack that is bridged by fibres.

Depending on whether the material in uni-axial tension is experiencing multiple cracking or localisation of cracks, the overall constitutive behaviour for use in structural calculations should be chosen accordingly. In the research described here, the focus is on normal SFRC that shows no quasi strain hardening and therefore no multiple cracking in uni-axial tension. In that case, the stress-crack width relation is a part of the constitutive relation.

Hillerborg and Rots [Hillerborg & Rots, 1989] showed that stress-crack width relations can be easily applied in structural calculations. Structural calculations can be formulated either as non-linear finite element calculations through the discrete crack approach or through a semi-analytical approach.

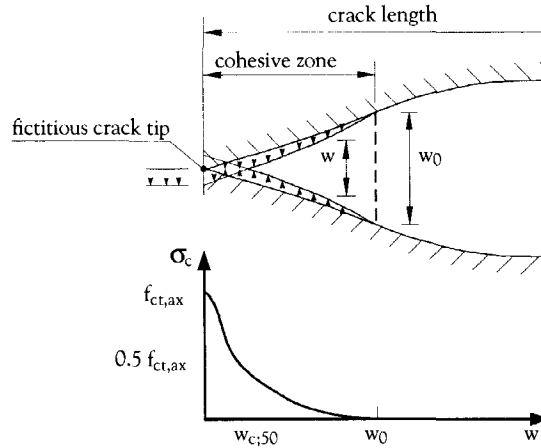


Figure 4.2 Fictitious Crack Model [Hillerborg et al., 1976]

Micro-mechanical modelling

Based on the fictitious crack model of Hillerborg et al. [Hillerborg et al., 1976] and on micro-mechanical concepts, Li et al. [Li et al., 1993] developed a semi-analytical modelling procedure to obtain a post-cracking material relation for Fibre Reinforced Cementitious Composites (FRCC). By analysing the fracture processes in FRCC under uni-axial tension, they accomplished to derive equations that can be used to determine a stress-crack width relation. For the case of a single fibre system and no fibre rupture the model of Li et al. [Li et al., 1993] describes the stress σ_{fcr} carried across a crack in fibre reinforced concrete as a function of the crack width w :

$$\sigma_{fcr}(w) = \sigma_{ct}(w) + \sum_{i=1}^{n_f} \sigma_f^i(w) + \sigma_{ps}(w) \quad (4.2)$$

The first term in equation (4.2) is defined by the following empirical softening relation for plain concrete:

$$\sigma_{ct}(w) = \frac{f_{ct,ax}}{1 + \left(\frac{w}{w_{c;50}} \right)^p} \quad (4.3)$$

In equation (4.3) p is the shape factor of the softening curve and $w_{c;50}$ is the characteristic crack width, i.e. the crack width corresponding to a reduction of the stress-carrying capacity to 50% of the tensile strength $f_{ct,ax}$ (see Figure 4.2). Both the shape factor and the characteristic crack width must be determined experimentally. Several researchers have proposed different softening relations in the past, such as Wolinski et al. [Wolinski et al., 1987].

In the second term of equation (4.2) n_f is the number of different fibre pullout systems in the cross-section considered and σ_f^i is the fibre bridging contribution of the i^{th} fibre system. The term expresses the so-called fibre bridging stress and is based on the pullout behaviour of a single fibre, as described in section 2.3.1. This pullout behaviour can be modelled by a simple cohesive interface characterisation in which any deformation of the matrix is disregarded. This allows for a unique relation between the fibre bridging stress and the displacement of the fibre relative to the crack surface. The fibre bridging stress is in that case proportional to the frictional resistance τ between the fibre and the matrix [Wang et al., 1988].

The frictional resistance τ is a function on its own. In the following regular relation slip-softening as well as slip-hardening can be taken into account:

$$\tau = \tau_0 \quad \text{for } \delta \leq \delta^* \quad (4.4a)$$

$$\tau = \tau_0 + a_1\delta + a_2\delta^2 \quad \text{for } \delta > \delta^* \quad (4.4b)$$

In equation (4.4) δ^* is the crack opening corresponding to complete debonding:

$$\delta^* = \frac{\tau L_f^2 (1 - V_f) E_c}{((1 - V_f) E_c + V_f E_f) E_f d_f} \quad (4.5)$$

The crack opening δ in equation (4.4) is the crack width without the so-called Cook-Gordon effect. This Cook-Gordon effect induces an additional matrix separation when a crack tip reaches the fibre. This is illustrated schematically in Figure 4.3.

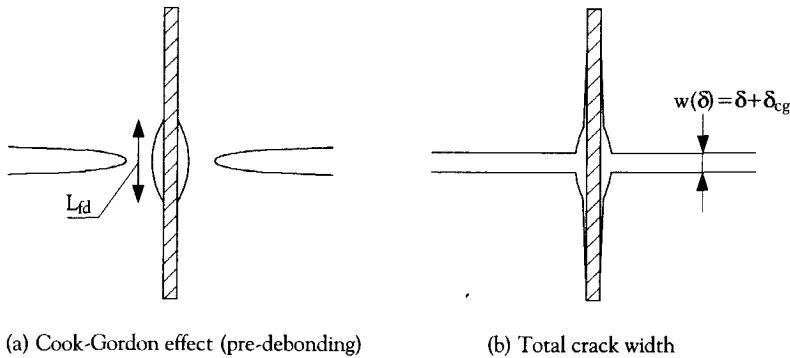


Figure 4.3 The Cook-Gordon effect according to [Li et al., 1993]

As the crack tip approaches the fibre, pre-debonding occurs at the fibre matrix interface. When the crack tip finally reaches the fibre, elastic stretching of the fibre segment and further frictional debonding at the interface lead to an additional crack opening. The additional crack opening displacement can be estimated as follows:

$$\delta_{cg} = \frac{4L_{fd}P}{\pi d_f^2 E_f} \sigma_f^i \quad (4.6)$$

So that the total crack width becomes:

$$w(\delta) = \delta + \delta_{cg} \quad (4.7)$$

The fibre bridging stress σ'_f of an individual fibre system can now be calculated indirectly as a function of the total crack width w . The determination of the total fibre bridging contribution, i.e. the second term of equation (4.2), is obtained by integration of the individual contribution of the fibres for all possible fibre positions and various fibre orientations relative to the crack. The orientation and distribution function can be changed to accommodate any fibre orientation and distribution.

Prior to any crack opening the fibre is already stressed. The third term in equation (4.2) expresses this phenomenon. This so-called pre-stressing term takes into account that the fibres carry load through elastic straining when the first crack is formed:

$$\sigma_{ps}(w) = f_{ps}^o \frac{w^* - w}{w^*} \quad \text{for } w \leq w^* \quad (4.8a)$$

$$\sigma_{ps}(w) = 0 \quad \text{for } w > w^* \quad (4.8b)$$

In equation (4.8) the crack width w^* is the crack width where the pre-stress is eliminated and the fibre is completely debonded:

$$w^* = \delta^* + \delta_{cg} \quad (4.9)$$

and

$$f_{ps}^o = \eta_\theta \eta_l \epsilon_{ct} E_f V_f \quad (4.10)$$

The orientation efficiency factor η_θ depends on several parameters, as will be shown in section 6.2. The length efficiency factor η_l can be determined using the following equation:

$$\eta_l = 1 - \frac{\epsilon_{ct} E_f d_f}{4L_f \tau_0} \quad (4.11)$$

Even though the model described above provides a basic understanding of the influence of the micro-mechanical parameters on the shape of the stress-crack width curve, a simplified approach is sometimes needed for interpretation and fitting of experimental data. The inverse modelling approach is such a simplified approach.

Inverse modelling

The second approach available to obtain a stress-crack width relation for SFRC is the so-called inverse modelling approach. An inverse modelling procedure is quite straightforward and easy to carry out with the help of computers. Van Mier [Van Mier, 1997] describes the procedure as follows:

'In an inverse modelling procedure, a softening diagram is assumed, and in a numerical analysis of the fracture geometry under consideration, the deviation between the computational and experimental results is calculated. Depending on this deviation and the permissible error, the analysis is repeated using a modified softening diagram. The procedure is repeated until the error has become small enough to fall within predetermined boundaries'.

In an inverse modelling procedure, the softening diagram or stress-crack width relationship for fibre reinforced concrete can be schematised in different ways. The idealised relationship can be described with a different number of degrees of freedom. The simplest stress-crack width relationship is shown in Figure 4.4a. It can be described with only one degree of freedom. Figure 4.4b shows relationships with two degrees of freedom. Figure 4.4c shows relationships with three degrees of freedom. Figure 4.4d shows relationships with four degrees of freedom.

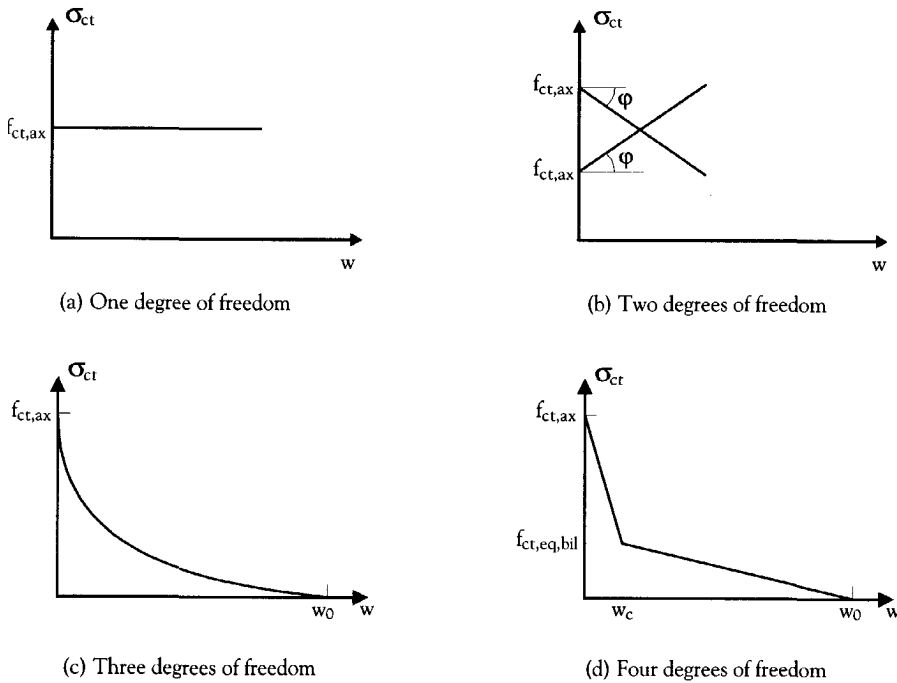


Figure 4.4 Idealised σ - w relationships

Relationships that approach the post-cracking behaviour adequately in practice often have three or more describing parameters (degrees of freedom). Stang and Aarre [Stang & Aarre, 1992] proposed a relationship similar to equation (4.3) with three degrees of freedom, while Wolinski et al. [Wolinski et al., 1987] proposed equation (4.12) for plain concrete. The latter is a relationship with three degrees of freedom and can be used to model concrete using the uni-axial tensile strength $f_{ct,ax}$ and empirical variations of the critical crack width w_0 and the shape parameter p (see also Figure 4.4c):

$$\sigma_{ct}(w) = f_{ct,ax} \cdot \left[1 - \left(\frac{w}{w_0} \right)^p \right] \tag{4.12}$$

Others, like Roelfstra and Wittmann [Roelfstra & Wittmann, 1986], used a bilinear approximation of the softening relationship, as illustrated in Figure 4.4d. This bilinear relationship is characterised by four describing parameters and can be expressed by:

$$\sigma_{ct}(w) = f_{ct,ax} - \frac{w}{w_c} (f_{ct,ax} - f_{ct,eq,bil}) \quad \text{for } w \leq w_c \quad (4.13a)$$

$$\sigma_{ct}(w) = f_{ct,eq,bil} \cdot \frac{w_0 - w}{w_0 - w_c} \quad \text{for } w_c < w \leq w_0 \quad (4.13b)$$

4.2.2 Crack band method

Related to the stress-crack width models is the crack band model for fracture of plain concrete, presented by Bažant and Oh [Bazant & Oh, 1983]. In this theory they define a zone where distributed micro cracks spread out, as Figure 4.5 illustrates. The width of this so-called fracture process zone is taken into account in their model, which results in a stress-strain relationship for this particular crack band width instead of a stress-crack width relation for an infinitely small band width. The model is based on the assumption that fracture in a heterogeneous material can be modelled as a band of parallel, densely distributed micro cracks as opposed to stress-crack width models where a cohesive zone is assumed between the fictitious crack tip and the macro crack.

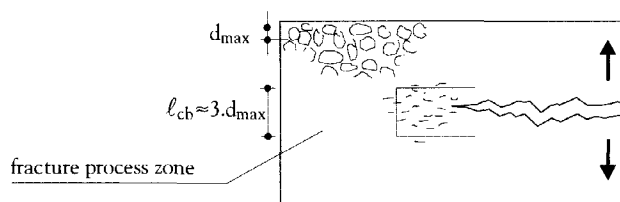


Figure 4.5 'Definition' of the crack band theory according to Bažant and Oh [Bazant & Oh, 1983]

Bazant and Oh [Bazant & Oh, 1983] claimed that if the relation of the normal stress σ_{ct} and the relative displacement δ across a line crack is identical to the relation of σ_{ct} and the displacement $\delta = \epsilon_c \cdot l_{cb}$ obtained by accumulating the strains due to micro cracking over the crack band width l_{cb} , the line crack model and the crack band model are equivalent.

In finite element analyses of fracture processes, the crack band method is often used as one of the two existing approaches to perform this kind of analyses. In contrast to the line crack models used in the so-called discrete crack approach, the stress-strain relation based on the crack band theory is associated with the so-called smeared crack approach.

The stress-strain relation used in the smeared crack approach is characterised by three parameters. In addition to the width of the crack band (the fracture process zone), the material fracture properties in the model are characterised by the uni-axial stress limit and the fracture energy. According to Bažant and Oh [4.4], the fracture energy G_F is the energy consumed in the formation and opening of all micro-cracks per unit area of plane and is defined by:

$$G_F = l_{cb} \int_{\epsilon(\sigma_{cr})}^{\epsilon(0)} \sigma_c(\epsilon) \cdot d\epsilon_c \tag{4.14}$$

The crack band width might be determined computationally, but is not an objective parameter. It depends on the selected mesh and its parameters: size, shape and angle of the mesh line along which the crack band advances with the crack direction.

4.2.3 Stress-strain methods

The favourable post-cracking behaviour of SFRC is addressed best in statically indeterminate structures subjected to bending loads. In these kind of structures the material behaviour can result in a redistribution of stresses in the cracked cross-section as well as in the structure itself. When dimensioning such a structure or structural member the ideal way of modelling is to model both the compressive and tensile behaviour in one stress-strain relationship. In literature, several recommendations have been published concerning test and design methods based on this stress-strain approach: the German stress-strain model [4.5] and the modelling procedure of the RILEM Technical Committee 162 [4.6] will be described hereafter.

The German stress-strain model

The first design guideline for SFRC that made use of a stress-strain relation is the German Concrete Society's 'Bemessungsgrundlagen für Stahlfaserbeton im Tunnelbau'. This guideline shows how to generate an idealised stress-strain diagram for the use in design calculations of tunnel structures. The stress-strain relation is based on experimental results derived from four-point bending tests taking into account the scatter in the post-cracking behaviour, the effect of geometrical variations between test specimen and structure, the effect of sustained load conditions and the difference between lab tests and quality control tests in practice.

Figure 4.6 shows the stress-strain diagram of SFRC. In compression, the stress-strain diagram is the equivalent of the one for plain concrete prescribed by the German design code (DIN 1045). The value of the compressive strength in this diagram is the design value according to that same design code.

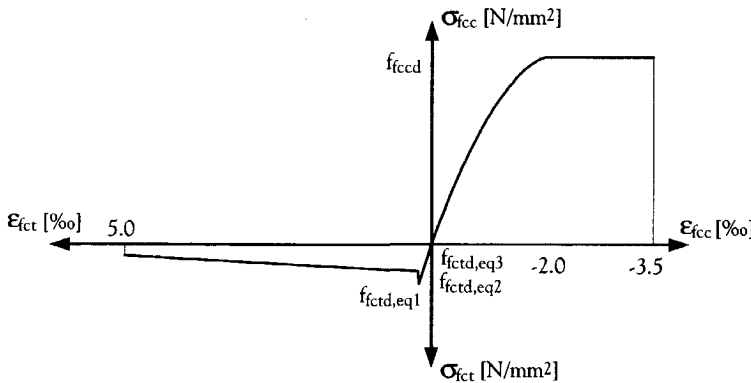


Figure 4.6 Stress-strain diagram according to [DBV-Merkblatt, 1992]

In the tensile zone, the stress drops after reaching the peak stress. The strain limit at which this drop takes place is determined by Young's modulus and the peak stress. In the German guideline this peak stress is the design value of the flexural strength determined from results of four-point bending tests. This design value is calculated by:

$$f_{ctd,fl} \leq (0.8 - r) \cdot k \cdot f_{ctk,fl} \quad (4.15)$$

with

$r = 0$ when a normal compressive force is present in the cross-section,

$r = 0.25$ in case of pure bending or when a normal tensile force is present in the cross-section,

$k = 0.9$ to account for the difference between suitability tests and quality control tests.

In equation (4.15), $f_{ctk,fl}$ is the lower limit value of the 80% confidence interval of the mean value of the flexural strength of SFRC and can be determined as follows:

$$f_{ctk,fl} = f_{ctms,fl} - \frac{s_f \cdot t_{10,n-1}}{\sqrt{n}} \quad (4.16)$$

with n as the number of tests and $t_{10,n-1}$ according to the statistical tables for t-tests. The mean flexural strength $f_{ctms,fl}$ can be determined as follows:

$$f_{ctms,fl} = \frac{\sum_{i=1}^n f_{ct,fl}^i}{n} \quad (4.17)$$

with

$$f_{ct,fl}^i = \frac{P_{max} \cdot l}{b \cdot h^2} \quad (4.18)$$

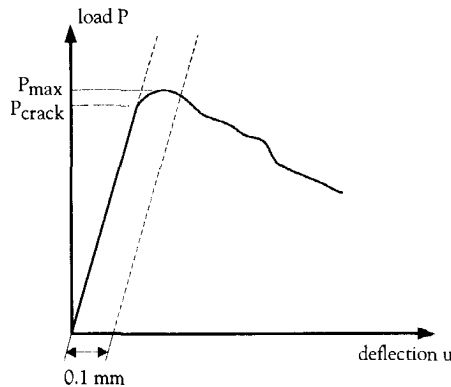


Figure 4.7 Procedure to determine the load at first cracking according to [DBV-Merkblatt, 1992]

The flexural strength $f_{fct,fl}^i$ can be determined from the measured load-deflection diagram of a single four-point bending test, which was schematically presented in Figure 3.1b. In equation (4.1) the load P_{max} is the highest measured load within the first 0.1 mm deflection interval as illustrated in Figure 4.7.

When the flexural strength is calculated, the tensile peak stress in the stress-strain diagram is known. Now, one is able to determine the linear elastic strain limit from the Young's modulus. At this strain limit the stress drops to a post-cracking stress of $f_{fctd,eq,2}$ (see Figure 4.6). Furthermore, it is assumed that a tensile stress capacity remains in the post-cracking region up to a tensile strain limit of 5‰. At this particular strain limit the stress capacity is reduced to $f_{fctd,eq,3}$. The design values for the post-cracking behaviour can be calculated as follows:

$$f_{fctd,eq,2} = 0.37 \cdot \xi \cdot k \cdot f_{fctm,eq,2} \tag{4.19a}$$

$$f_{fctd,eq,3} = 0.37 \cdot \xi \cdot k \cdot f_{fctm,eq,3} \tag{4.19b}$$

In equation (4.19a) and (4.19b), three post-cracking factors are used. The first factor is equal to 0.37 and expresses the difference between the tensile stress in the uncracked section and the equivalent tensile stress in the cracked section. Based on the assumption that the depth of the compressive zone in the cracked stage is 1/10 of the beam depth or structural thickness (see Figure 4.8a), the equivalent flexural tensile stress in the post-cracking stage can be determined by multiplying the linear-elastic stress with 0.37.

Secondly, the transformation factor ξ is used to take long-term loading into account (factor 0.85) and to account for differences in geometry between the test specimen and the structure for structural thickness larger than 150 mm (see Figure 4.8b).

Finally, the third post-cracking factor k expresses the difference between suitability tests in the lab and quality control tests in practice and equals 0.9.

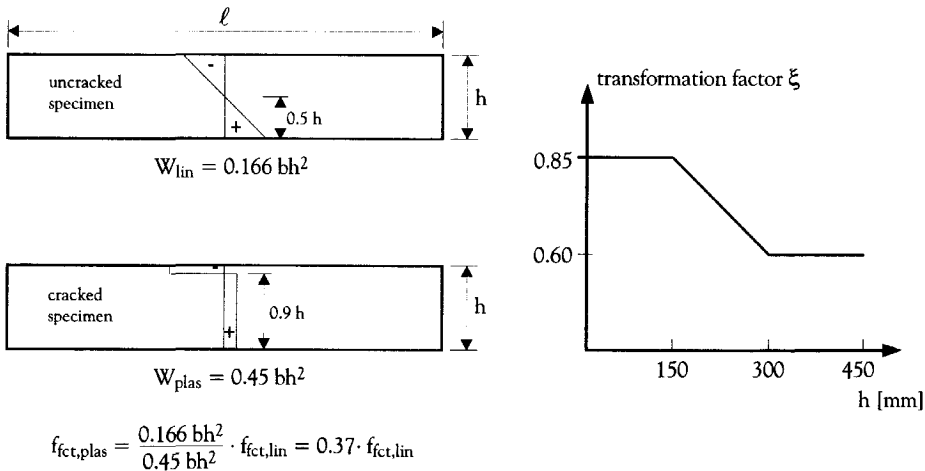


Figure 4.8 Post-cracking factors

The mean value of the equivalent tensile stress in the post-cracking behaviour used in equations (4.19a) and (4.19b) is not the average value derived from the test results but the lower limit value of the 80% confidence interval of the mean value of the total population. This value can be determined as follows:

$$f_{fctm,eq,2} = f_{fctms,eq,2} - \frac{s_f \cdot t_{10}}{\sqrt{n}} \quad (4.20a)$$

$$f_{fctm,eq,3} = f_{fctms,eq,3} - \frac{s_f \cdot t_{10}}{\sqrt{n}} \quad (4.20b)$$

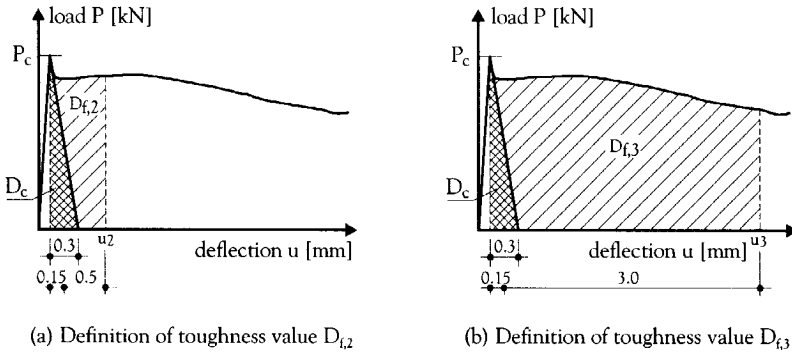


Figure 4.9 Definition of the toughness values according to [DBV-Merkblatt, 1992]

The average of the equivalent tensile stress $f_{fctms,eq}$ can be determined from the bending test series using the following equation:

$$f_{fctms,eq} = \frac{\sum_{i=1}^n f_{fct,eq}^i}{n} \quad (4.21)$$

By calculating the toughness values $D_{f,2}$ and $D_{f,3}$ underneath the load-deflection diagram up to defined deflections u_2 and u_3 , it is possible to determine the equivalent tensile stresses $f_{fct,eq,2}^i$ and $f_{fct,eq,3}^i$ of one single test result. The shaded areas in Figure 4.9 show the fibres' contribution $D_{f,2}$ and $D_{f,3}$ to the total toughness D_{fc} . The contribution of the plain concrete D_c is not taken into account in the determination of the equivalent tensile stresses:

$$f_{fct,eq,2}^i = \frac{D_{f,2} \cdot l}{0.5 \cdot b \cdot h^2} \quad (4.22a)$$

$$f_{fct,eq,3}^i = \frac{D_{f,3} \cdot l}{3.0 \cdot b \cdot h^2} \quad (4.22b)$$

RILEM-model

The second design guideline for SFRC that makes use of a stress-strain relation is the RILEM Draft Recommendation on test and design methods for SFRC [RILEM TC 162-TDF, 2000]. Just like the German guideline, this guideline shows how to generate an idealised stress-strain diagram for the use in design calculations (see Figure 4.10).

Compared to the German guideline, RILEM’s design guideline is intended for all kinds of structural applications and loading conditions. Furthermore, the stress-strain relation is based on three-point bending tests instead of four-point bending tests.

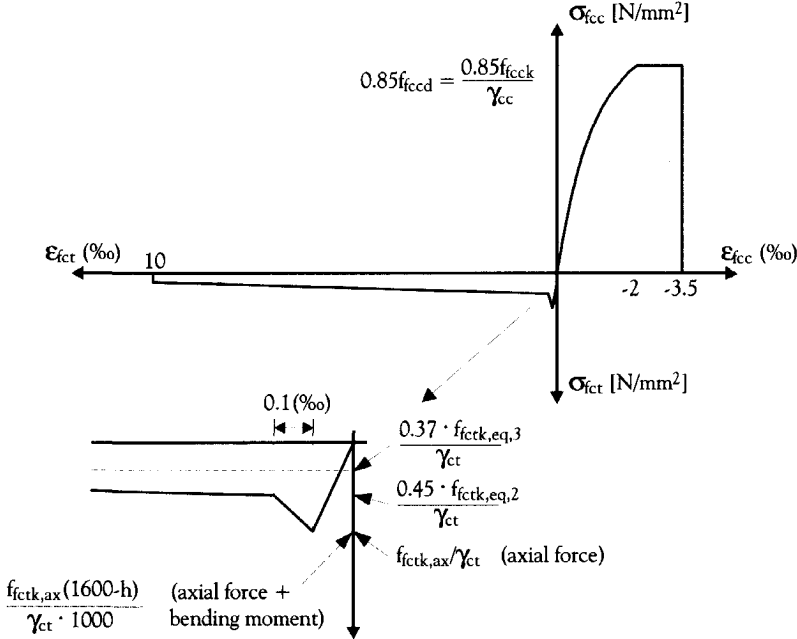


Figure 4.10 Stress-strain diagram according to [RILEM TC 162-TDF, 2000]

The stress-strain diagram in Figure 4.10 shows that in compression the same relation is used as in the German recommendation. The characteristic value of the cylinder compressive strength is multiplied by 0.85 to include the time dependent behaviour. It is then divided by a partial (material) safety factor γ_{cc} to create a design value. According to Eurocode 2, $\gamma_{cc} = \gamma_{ct} = 1.5$.

In contrast to the German guideline, the diagram of Figure 4.10 does not drop immediately after reaching the peak stress in the tensile zone, but decreases more gradually over a range of 0.1‰. Again, Young’s modulus and the uni-axial tensile strength determine the strain limit of the linear elastic range. Figure 4.10 shows that the peak stress depends on the presence of a bending moment in the cross-section. In case of uni-axial loading conditions the design value of the peak stress is:

$$f_{fctd,ax} = \frac{f_{fctk,ax}}{\gamma_{ct}} \tag{4.23}$$

In case of flexural loading conditions the peak stress can be calculated as follows:

$$f_{fctd,fl} = \frac{f_{fctk,ax} \cdot (1600 - h)}{\gamma_{ct} \cdot 1000} \quad (4.24)$$

The characteristic value of the uni-axial tensile stress $f_{fctk,ax}$ is expressed by:

$$f_{fctk,ax} = 0.7 \cdot f_{fctm,ax} \quad (4.25)$$

with

$$f_{fctm,ax} = 0.3 \cdot (f_{fck})^{\frac{2}{3}} \quad (4.26)$$

According to [4.6], the design value of the flexural strength $f_{fctd,fl}$ can also be determined by:

$$f_{fctd,fl} = \frac{f_{fctk,fl}}{\gamma_{ct}} \quad (4.27)$$

with

$$f_{fctk,fl} = f_{fctms,fl} - \frac{s_f \cdot t_{10}}{\sqrt{n}} - 1.645 \cdot s_f \cdot \left(1 + \frac{s_f \cdot t_{10}}{f_{fctms,fl} \cdot \sqrt{n}}\right) \quad (4.28)$$

and

$$f_{fctms,fl} = \frac{\sum_{i=1}^n f_{fct,fl}^i}{n} \quad (4.29)$$

The flexural strength $f_{fct,fl}^i$ from a single three-point bending test is determined as follows:

$$f_{fct,fl}^i = \frac{3 \cdot P_{crack} \cdot l}{2 \cdot b \cdot h_{lig}^2} \quad (4.30)$$

Similar to the determination of the load at first crack in the German method (Figure 4.7), the load at first crack P_{crack} is the highest measured load within a particular deformation interval of the measured load-deflection diagram. According to [RILEM TC 162-TDF, 2000], however, the interval is now 0.05 mm wide.

Now that the peak stress is known, it is possible to determine the linear-elastic strain limit from the Young's modulus. At this particular strain limit the stress capacity reduces to $f_{fctd,eq,2}$ at a strain limit equal to the linear elastic strain limit plus 0.1‰. The post-cracking stress capacity gradually decreases to a post-cracking stress level of $f_{fctd,eq,3}$ at an ultimate strain limit of 10‰. The design values for the post-cracking behaviour can be calculated as follows:

$$f_{fctd,eq,2} = \frac{0.45 \cdot f_{fctk,eq,2}}{\gamma_{ct}} \quad (4.31a)$$

$$f_{fctd,eq,3} = \frac{0.37 \cdot f_{fctk,eq,3}}{\gamma_{ct}} \quad (4.31b)$$

In equation (4.31a) and (4.31b), the first factor takes into account the change in section modulus after cracking. In contrast to the German recommendation, the post-cracking factors now differ for $f_{fctd,eq,2}$ and $f_{fctd,eq,3}$. This seems more logical since the crack length is not constant: just after crack initiation the crack length will be small, but as the deformation increases the crack will grow. The transformation factor ξ in equation (4.19a) and (4.19b) has been left out in equation (4.31a) and (4.31b). Long-term loading and size effects are not taken into account when modelling the post-cracking behaviour. If applicable, however, these effects should be regarded in design calculations.

The characteristic values of the equivalent tensile stresses in the post-cracking behaviour used in equations (4.31a) and (4.31b) are determined by the following equations:

$$f_{fctk,eq,2} = f_{fctms,eq,2} - \frac{s_f \cdot t_{10}}{\sqrt{n}} - 1.645 \cdot s_f \cdot \left(1 + \frac{s_f \cdot t_{10}}{f_{fctms,eq,2} \cdot \sqrt{n}}\right) \quad (4.32a)$$

$$f_{fctk,eq,3} = f_{fctms,eq,3} - \frac{s_f \cdot t_{10}}{\sqrt{n}} - 1.645 \cdot s_f \cdot \left(1 + \frac{s_f \cdot t_{10}}{f_{fctms,eq,3} \cdot \sqrt{n}}\right) \quad (4.32b)$$

The average values of the equivalent tensile stress $f_{fctms,eq,2}$ and $f_{fctms,eq,3}$ can be determined from the bending test series:

$$f_{fctms,eq} = \frac{\sum_{i=1}^n f_{fct,eq}^i}{n} \quad (4.33)$$

By calculating the toughness values $D_{f,2}$ and $D_{f,3}$ underneath the load-deflection diagram up to defined deflections u_2 and u_3 , it is possible to determine the equivalent tensile stresses $f_{fct,eq,2}$ and $f_{fct,eq,3}$ of one single test result. The shaded areas in Figure 4.11a and 4.11b represent the toughness contributed by the fibres. The contribution of the plain concrete D_c is again not taken into account in the determination of the equivalent tensile stresses from a single three-point bending test:

$$f_{fct,eq,2}^i = \frac{3}{2} \cdot \left(\frac{D_{f,2,I}}{0.65} + \frac{D_{f,2,II}}{0.50} \right) \cdot \frac{L}{b \cdot h_{lig}^2} \quad (4.34a)$$

$$f_{fct,eq,3}^i = \frac{3}{2} \cdot \left(\frac{D_{f,3,I}}{2.65} + \frac{D_{f,3,II}}{2.50} \right) \cdot \frac{L}{b \cdot h_{lig}^2} \quad (4.34b)$$

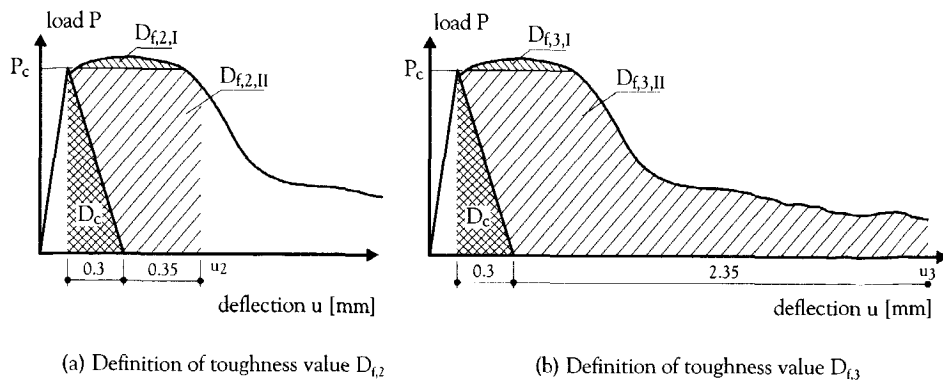


Figure 4.11 Definition of the toughness values according to [RILEM TC 162-TDF, 2000]

4.3 Assessment of existing modelling methods

4.3.1 Discussion on existing modelling methods

Micro-mechanical approach

The micro-mechanical approach described in section 4.2.1 is quite valuable to enhance the understanding of the behaviour of SFRC. It can be used to determine the influence of micro-mechanical parameters and fibre characteristics on the post-cracking behaviour of FRC in general and to optimise SFRC mix compositions.

Despite the important work of Li et al. [Li et al., 1993], the author questions the predictive capacity of the modelling procedure because of three reasons. The first reason is that too many parameters need to be verified experimentally before a model can be generated that fits the uni-axial test results with sufficient accuracy. It is therefore of little practical value. Secondly, in the integration process to solve the second term of equation (4.2), it is assumed that the fibres are randomly oriented and distributed in a three-dimensional space. As sections 6.3 and 6.4 will show, this assumption is not valid and an analytical solution for this second term is therefore not feasible. Thirdly, the model was only validated up to a deformation of 0.3 mm. According to Li et al. [Li et al., 1993], this is no problem since a large part of the reinforcement in practice is only placed to reduce and control the crack widths in the Serviceability Limit State (SLS). As section 2.4.1 has already shown, for durability reasons crack widths should be kept smaller than 0.2 mm. So they seem to have an argument. However, section 3.4.2 has shown that the failure capacity of statically determinate beams in three-point bending tests may be reached at crack widths over 0.3 mm. Therefore, it is questionable whether or not Ultimate Limit State (ULS) calculations can be made with the micro mechanical model.

Inverse analysis approach

Instead of the micro mechanical approach a simplified approach is sometimes needed for interpretation and fitting of experimental data. The inverse analysis approach seems more practical than the micro-mechanical approach, because less parameters have to be verified experimentally. Furthermore, the initially assumed and finally determined stress-crack width

relation can describe the complete post-cracking behaviour from crack initiation up to the critical crack width. This means that both SLS and ULS calculations can be made for structures in practice.

On the other hand, the determination of a stress-crack width relation via inverse analysis does not create a full understanding of the material's (post-cracking) behaviour. Insight can only be gained by trial and error. Furthermore, the approach does not result in an unambiguous stress-crack width relation. If the initially assumed relation only holds one degree of freedom, the accuracy of best fit is rather poor. When more describing parameters are used the computed curve fits the mean test results more accurate, but the solution is not unique.

Stress-crack width relations that describe the post-cracking behaviour of conventional SFRC suggest localisation of deformation directly after crack initiation. In structural applications this is not necessarily the case. Applied in statically indeterminate structures, the composite material has often proven that multiple cracking is feasible. In those cases, redistribution of stresses does not only take place in the initially cracked cross-section, but also in other parts of the structure. It is hard to model multiple cracking in a structural analysis with Finite Element Methods. Assumptions have to be made concerning crack patterns and crack spacing when a stress-crack width relation is used in such an analysis.

Crack band method

The crack band model is based on the assumption that fracture in a heterogeneous material can be modelled as a band of parallel, densely distributed micro cracks as opposed to stress-crack width models where a singular line crack is assumed. Combined with the stress-strain relation for concrete in compression, the crack band model can be used to make cross-sectional calculations for concrete structures subjected to bending. The applicability of the model, however, is limited to cross-sectional analyses.

Since the crack band method is quite similar to the stress-crack width method the same advantages and disadvantages also apply for the crack band model. However, considering the most promising structural applications of SFRC, i.e. statically indeterminate structures such as slabs or tunnel linings, the author questions the applicability of the crack band model in design calculations. Instead of the crack band width, information on crack distances forms the basis of a non-linear constitutive relation (next to a criterion for crack formation of course). In case the crack band width is used in finite element calculations, the generated (macro) crack spacing is too small, which will most probably lead to an overestimation of the load-bearing capacity at structural failure.

The German stress-strain method

The advantage of the stress-strain method in general is that the complete uni-axial behaviour of SFRC is modelled in one diagram. As a result, it is easy to use in analyses of cross-sections subjected to bending, which is perfect when considering that in most (promising) structural applications for SFRC bending is the governing action.

The German guideline has been the first attempt to generate a reliable design model for SFRC. The stress-strain relation is based on four-point bending tests taking into account the scatter in the post-cracking behaviour, the effect of geometrical variations between test

specimen and structure, the effect of sustained load conditions and the difference between suitability testing in the lab and quality control in practice.

Although the design guideline is more complete compared to the existing stress-crack width modelling methods and the crack band model, the author argues the following points:

- In the stress-strain relation, the flexural strength is used as the peak stress instead of the uni-axial tensile strength. It is the author's opinion that the uni-axial tensile stress should be used as peak stress as the softening behaviour is also accounted for in the model. As Hillerborg et al [Hillerborg et al., 1976] showed, it is the softening behaviour that contributes to the fact that the flexural strength exceeds the uni-axial tensile strength.
- In the determination of the uni-axial tensile strength, it is not clear why a reduction factor $r = 0.25$ is used to reduce the peak stress when the cross-section is subjected to bending moments.
- The ultimate strain limit is set at 5‰. This limit seems to be arbitrarily chosen, as the measured vertical displacements do not suit the horizontal strains.
- When calculating the equivalent tensile stresses to describe the post-cracking behaviour, only the contribution of the fibres is accounted for in the determination of the toughness values. It is the author's opinion that after cracking the toughness value of the plain concrete matrix should be taken into account as it contributes to the softening behaviour of the composite material.
- The three post-cracking factors used in equation (4.19) are disputable. The first factor that expresses the difference between the tensile stress in the uncracked section and the equivalent tensile stress in the cracked section does not change at increasing strain limits. This is strange since the crack depth increases when the strain, i.e. the relative horizontal deformation, increases. The second factor ξ is used to account for the effect of long-term loading (factor 0.85) and differences in geometry between the test specimen and the structure for a structural thickness over 150 mm. According to section 2.4.2, a long-term loading factor of 0.85 has not yet been proven. The third post-cracking factor k expresses the difference between suitability tests in the lab and quality control tests in practice. It is the author's opinion that the difference between the post-cracking behaviour in the lab and the behaviour in practice should not be separated from the structural application.
- The characteristic values have been calculated as the lower limit value of the 80% confidence interval of the mean value of the flexural strength from test results. Common practice is to calculate the lower bound strength value of a one-sided 95% confidence interval of the population.

In addition to the above mentioned point the author believes that:

- the applicability of the design guideline in SLS calculations is questionable since the guideline does not deal with crack width control.
- the applicability of the design guideline in ULS calculations is questionable since the guideline is only suitable for cross-sectional analysis. The mean crack spacing is unknown. As a result, the predictive capacity of the material model, i.e. the stress-strain relation based on mean stress values, is quite poor. After many cross-sectional analyses, Konter [Konter, 1999] found that test results could be best fitted using a fictitious length of 200 mm, which is equal to the length of the zone with a constant bending moment, according to the prescribed bending test.

RILEM's stress-strain method

At first sight, the RILEM's stress-strain diagram looks quite similar to the one in the German Concrete Society's guideline. However, after a closer look the following differences are recognised:

- The determination of the peak stress in tension is more clear than in case of the German guideline. However, in case of analysing cross-section subjected to bending moments, again the flexural strength is used, while the uni-axial tensile stress is used only in absence of a bending moment.
- There is no steep drop after reaching the peak stress.
- Only one post-cracking factor is used in RILEM's Draft Recommendation. The factor that expresses the difference between the tensile stress in the uncracked section and the equivalent tensile stress in the cracked section does now change at increasing strain limits. This is closer to reality. However, no long-term loading factor is available for the post-cracking behaviour if necessary.
- The ultimate strain limit of 10‰ is larger than in the German stress-strain diagram.
- The mean values of the population are calculated by determining the lower limit value of the two-sided 80% confidence interval of the mean value from test series. The characteristic strength values are the lower bound strength values of a one-sided 95% confidence interval of a Gaussian population.
- The safety philosophy is according to European standards [ENV 1992-1-1, 1991]. Partial safety factors are used to determine design values of the compressive strength and the tensile stresses.

Although RILEM's design guideline is more transparent than the German one and is more complete than the existing material models, the author does not agree with the determination of the tensile peak stress and the neglecting of the plain concrete's fracture energy in the determination of the equivalent (post-cracking) stresses. It is the author's opinion that the peak stress should be equal to the uni-axial tensile strength of the composite and that the softening behaviour and toughness of the plain concrete matrix should be taken into account in the determination of the post-cracking stresses.

Furthermore, the strain limits are still very disputable. As a result of the fact that nothing has been mentioned about crack spacing, the predictive capacity of this material model is very poor: it is hard to fit any test result when the strains cannot be transformed into discrete displacements.

In addition, Chapter 7 will show that the partial safety factor for the post-cracking behaviour is not equal to the one for the tensile stress in the linear-elastic zone, as suggested by RILEM TC 162-TDF.

4.3.2 Demands for a suitable and reliable modelling method

In theory, the ideal design model for SFRC should perfectly describe the material's uni-axial behaviour, but in practice this behaviour is not uniform.

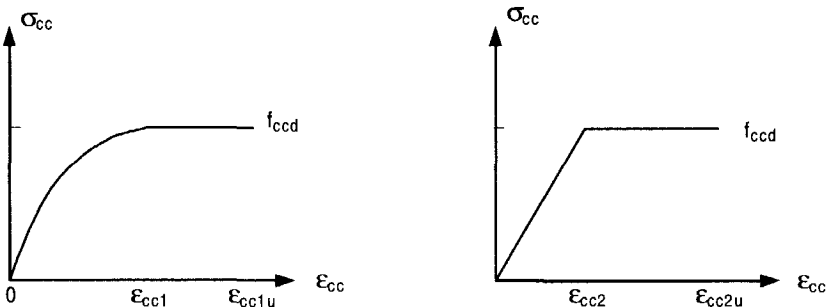
Several phenomena cause this non-uniform behaviour. Firstly, the post-cracking behaviour of a given fibre reinforced mix varies as a result of non-homogeneity of the composite material. As shown in Chapter 3, the coefficient of variation strongly depends on

the strength of the matrix and the number of fibres in the cross-section, which depends on the fibre volume and the fibre distribution.

Secondly, the tested behaviour of the material in the laboratory often differs from the structural behaviour in practice. This is due to the fact experiments in the laboratory are often carried out in a simplified manner. In the case of three-point bending tests, statically determinate beam specimens are subjected to a static point load for a relatively short time. In practice, these loading conditions differ from the conditions in the laboratory.

Thirdly, even when the structural boundary conditions are similar to those in the lab, differences in the production process might already lead to large variations. Section 3.4.6 showed that the placing process and vibration strongly influence the number and distribution of fibres in a cross-section. In addition to the pouring and flow directions, vibration also seems to influence the fibre orientation.

Common practice for modelling the uni-axial compressive behaviour of plain concrete is the stress-strain model presented in Figure 4.12. It shows two types of stress-strain diagrams according to Eurocode 2 [4.13]. Both idealised material models show that Eurocode 2 does not reckon with any post-peak softening behaviour of the concrete matrix under compressive loading, let alone any tensile softening behaviour. In contrast to plain concrete, however, the failure behaviour of SFRC is characterised by ductility, as was shown in Chapter 2 and 3. A suitable material model for SFRC should therefore include the material's softening behaviour. In the end, the model should represent the mean material's uni-axial behaviour, in compression as well as in tension, with sufficient accuracy.



(a) Parabolic design model for plain concrete

(b) Bi-linear design model for plain concrete

Figure 4.12 Design model for plain concrete in compression according to [ENV 1992-1-1, 1991]

In modelling, predictive capability is not only needed on a material level, but also on a structural level. Obviously, knowledge of the size-effect is of great importance for a reliable structural design. The latter has been well recognised in the past, which has resulted in advanced theoretical models explaining and predicting the size-effect in brittle and quasi-brittle materials in the past fifteen years.

Another important issue in predicting the structural behaviour of SFRC is the discrepancy between the short-term loading conditions in the lab and the often long-term loading conditions in practice. The stress capacity of plain concrete under sustained loads is lower than its capacity in short-term loading conditions. In the design codes for structural

concrete it is therefore common practice to apply a reduction factor, the long-term loading factor. For SFRC the same approach seems applicable, as was mentioned in section 2.4.2.

In addition to the size-effect and the effect of sustained loading, a third phenomenon typical for the use of fibre reinforcement in structural applications has to be dealt with. As mentioned in section 2.3.1, the efficiency of the fibre reinforcement depends on the angle between the fibre alignment and the direction of the pullout load. Since the production process and the geometrical boundary conditions related to the structural application strongly influence the fibres' distribution and orientation, the fibre efficiency in practice varies significantly. In the modelling procedure of SFRC, it is quite important to account for this phenomenon and to incorporate fibre efficiency into the model, as section 6.4 will show.

When the material model for SFRC approaches the mean material's uni-axial behaviour with sufficient accuracy, the natural scatter needs to be processed into the characteristic values and the transformation from specimen to structure has to be made. After that, these representative values need to be transformed into design values using so-called material factors. Together with the load factors, these probabilistically derived material safety factors depend on the scatter in material behaviour as well as the scatter in loading conditions. Chapter 7 will go into this matter in further detail.

Summarising the discussion above, a suitable and reliable design model for SFRC should satisfy the following demands:

1. The material model should predict or fit the mean softening behaviour from test results with sufficient accuracy.
2. Size-effects should be included in the model if necessary.
3. Reduction factors for sustained loading conditions should be available for use if necessary.
4. Reduction factors for varying fibre efficiency related to the structural application and its production process should be available for use if necessary.
5. Occurring scatter should be processed in the model: characteristic values should be determined from mean values and the quantified scatter.
6. Probabilistically determined safety factors should be used to transform the representative values into design values.

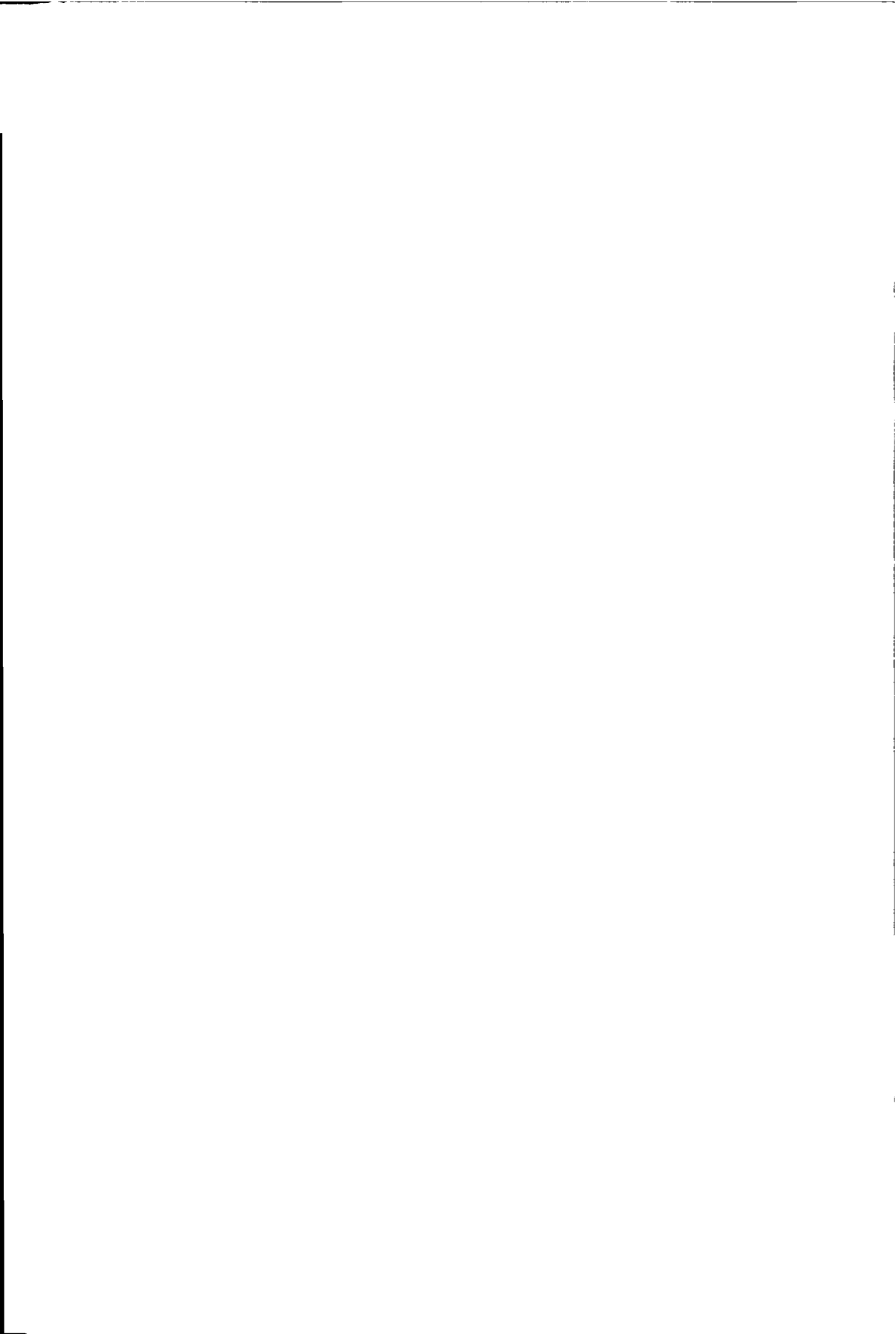
4.4 Concluding remarks

In this chapter the available modelling methods have been described and discussed. The micro-mechanical modelling approach is recognised as the most sophisticated modelling method and is found very suitable to gain insight into the fracture processes in SFRC. For scientists and other researchers, it provides the possibility to develop new or optimise old FRCC, but for engineers in practice it is not yet very suitable. Too many parameters need to be estimated or determined experimentally. In addition, the model has not been verified beyond crack openings of 0.3 mm. Since in bending the ultimate load-bearing capacity occurs at crack openings over 0.3 mm, the suitability of the approach is not clear.

The stress-strain models [DBV-Merkblatt, 1992], [RILEM TC 162-TDF, 2000] are also not very suitable to model the material behaviour of SFRC for use in structural design. Although these models can be used to fit results from bending tests when using the correct length parameter, they are a little bit misleading. When these models are used in finite

element calculations of SFRC structures in bending, they might suggest multiple cracking at an average crack spacing that is dependent on the mesh size. Up to this moment, it is not quite clear what the average crack spacing is and how this can be determined. As the effect of the assumed crack spacing on the ultimate load-bearing capacity of statically indeterminate structures in bending is assumed to be quite large, the stress-strain models described here might lead to an overestimation of the structural load-bearing capacity.

Therefore, a stress-crack width relation based on the Fictitious Crack Model of Hillerborg et al [Hillerborg et al., 1976] is more suitable for use in structural design. Such a relation initially suggests localisation of cracking. In structural finite element calculations, this might lead to a conservative design, but when assumptions concerning the crack spacing or crack pattern are introduced, the structural behaviour can be analysed from a safe starting point on. In the next chapter, it will be shown that such a relation can be determined with the help of inverse analysis of SFRC beam specimens.



Chapter 5

Development of improved constitutive relations for SFRC

5.1 Introduction

As Chapter 3 showed, the three-point bending test was chosen to test the post-cracking behaviour of SFRC. The tests, however, do not result in a stress-crack opening relation that is suitable for the use in design calculations. An inverse analysis is needed to model this uni-axial post-cracking behaviour of SFRC.

In this chapter a short but comprehensive description of the inverse modelling technique is given, which is followed by a thorough analysis of the simulation procedure.

To simulate the behaviour of SFRC subjected to a bending moment, load-crack opening displacement (P - δ) curves were computed with the help of the 'multi-layer' procedure developed by Hordijk [Hordijk, 1991]. After explaining the multi-layer procedure, insight is gained by determining the influence of the input parameters within the procedure. This analysis starts with the influence of the material's compressive behaviour on the simulated bending behaviour. Other influencing parameters are the input parameters that characterise the softening relation in tension, Young's modulus and the influence length. The latter is the length of a fictitious zone that is used to relate the discrete deformations in the cracked tensile zone to the relative deformations (strains) in the linear elastic region of the tensile zone and the deformations in the compressive zone.

The described inverse modelling technique was used to simulate bending tests on SFRC beams of different mix compositions and various dimensions. In the end, stress-crack opening relations can be easily developed for the mix compositions tested in the scope of this research.

5.2 Attaining constitutive relations via inverse modelling

As stated before, the inverse modelling procedure is quite straightforward and easy to carry out by the use of computers. Figure 5.1 shows a schematic representation of the inverse modelling procedure according to Roelfstra and Wittmann [Roelfstra & Wittman, 1986]. It can be subdivided into three levels.

The first level is the input level. On this level geometrical boundary conditions are set and assumptions are made concerning the uni-axial behaviour of the composite material.

The second level is the numerical level where the fracture geometry under consideration is analysed, which in this case is the cross-section of a notched SFRC beam.

The third level is the level where the accuracy of the load-crack opening displacement is checked. On this level, the deviation between the computational and experimental results is calculated. Depending on this deviation and the permissible error, the analysis is repeated using a modified softening diagram until the error is smaller than the predefined accuracy.

The fourth level is the output level. The final parameters of the tensile softening diagram satisfy the required accuracy.

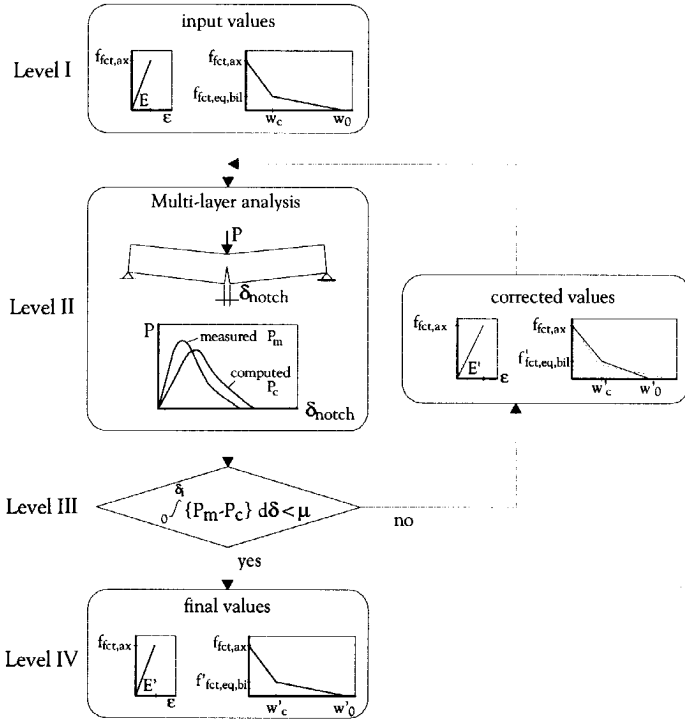


Figure 5.1 Inverse modelling procedure [Roelfstra & Wittman, 1986]

Starting points of the inverse modelling procedure

In the scope of this research, the inverse modelling procedure was used to find a suitable tensile softening diagram for SFRC that describes the load-crack opening displacement (P - δ) diagrams from three-point bending tests within a reasonable level of accuracy. An accurate description of this behaviour is necessary to be able to describe the flexural behaviour of SFRC structures in practice. The part of the P - δ diagrams that is of real practical interest is up to the peak load, as this peak load defines the ultimate load-bearing capacity of the cross-section. In case of statically indeterminate structures a small part of the P - δ curve after the peak load is also of practical interest, because of the possibility of redistribution of stresses in the structure resulting in an increase in load-bearing capacity. One of the aims of this research, however, was to gain insight in the post-cracking behaviour of SFRC. Therefore, the tail of the P - δ curve was also investigated.

Level I: the input level

In the input level of the inverse modelling approach, geometrical boundary conditions and the uni-axial material behaviour are set. In this modelling procedure, the effective beam depth h_{lig} (beam depth minus notch depth), the beam width b and the span length ℓ are input parameters concerning the geometry of the specimen. In addition, the mean compressive and tensile splitting strengths (see Table 3.4) of mix composition 1 and 2 of Table 3.3 are used to describe the material behaviour. The uni-axial material behaviour of SFRC is defined by setting three material relations:

1. A stress-strain diagram for SFRC in compression. In the analyses of SFRC cross-sections, the compressive behaviour is described by the mean compressive strength from standard cubic compressive tests and an assumption concerning the linear elastic and ultimate strain limits. The linear elastic strain limit in compression is set at 1.75‰, which corresponds to the design codes for structural concrete.
2. A stress-strain diagram for SFRC in linear elastic tension. The linear elastic behaviour in tension is determined by the uni-axial tensile strength of the SFRC under consideration and the linear elastic strain limit. The uni-axial tensile strength is related to the tensile splitting strength of the mix composition under consideration. Körmeling [Körmeling, 1986] showed that in the case of SFRC test specimens, the axial strength to splitting strength ratio was in the range of 0.7-0.8. The linear elastic strain limit is chosen in such a way that the linear elastic branch of the computed $P-\delta$ curve fits the elastic part of the measured curve.
3. A stress-crack width relation for the post-cracking behaviour of SFRC. As the next section will show, a bilinear softening relation for SFRC can satisfy both demands, depending on the parameters in this relation (see Figure 5.2) and the other input parameters in the inverse modelling procedure. For physical reasons, the input value of w_0 cannot exceed the maximum embedded fibre length of $\frac{1}{2} L_f$. In Chapter 6, the crack width w_0 will be related to the average projected embedded fibre length, after analysing the fibre orientation in the test specimens and estimating the fibre efficiency. In this chapter, only the effect of different w_0 -values on the load-crack opening displacements will be investigated. The other parameters to be varied in the inverse modelling procedure are the equivalent post-cracking strength $f_{fctm,eq,bi}$ and the characteristic crack width w_c .

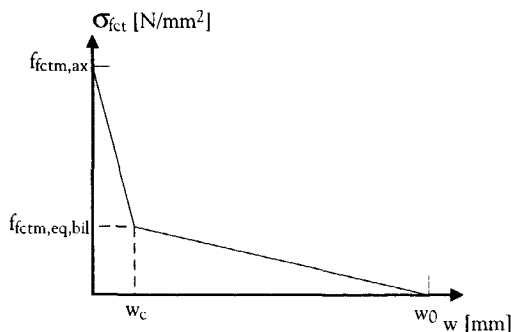


Figure 5.2 Bilinear tensile softening relation for SFRC

Level II: the simulation level

The simulation procedure used in level II of the inverse modelling procedure is based on the so-called multi-layer procedure developed by Hordijk [Hordijk, 1991]. This simulation procedure was used by Hordijk to study the bending behaviour of plain concrete. The reason for analysing SFRC cross-sections by means of the multi-layer procedure is because of the simplicity of the model. It can be easily programmed in a spreadsheet, in which parameters can be easily varied to investigate the effect of each parameter.

In contrast to Hordijk, who simulated load-deflection curves of plain concrete, the multi-layer procedure was used in the scope of this research to simulate and analyse load-crack opening displacement diagrams, such as those resulting from three-point bending tests as described in Chapter 3.

The multi-layer procedure is based on three principles. Figure 5.3 demonstrates the first principle of the multi-layer procedure. It shows that the beam is divided into two halves, which are connected by springs above the notch. Each spring represents the behaviour of a small layer. Furthermore, it is assumed that a linear displacement distribution describes the deformation over the effective beam depth.

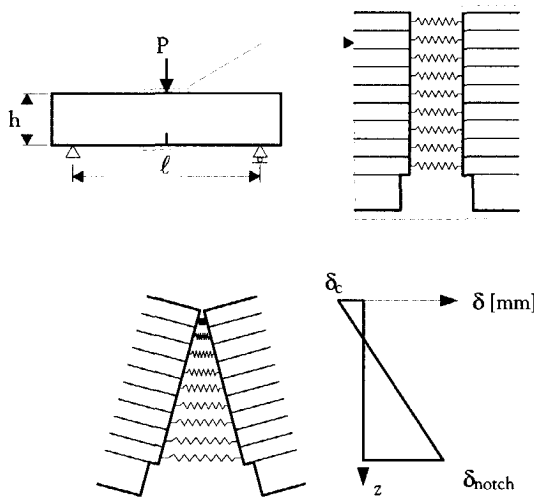


Figure 5.3 First basic principle of the multi-layer simulation procedure [Hordijk, 1991]

The second principle of the procedure is demonstrated in Figure 5.4. For each spring the deformation is determined by calculating the average deformation in the corresponding layer. For each layer, the stress can be determined from the stress-displacement relation of the springs. From the linear deformation distribution the corresponding contributions to the normal force N and the bending moment M are calculated for each layer. After adding the contributions of all layers, the internal force N and bending moment M are known. Equilibrium is found when N is equal to zero. The corresponding internal bending moment is equal to the external bending moment caused by the applied load on the beam. As a result, the external load can be easily determined from the internal bending moment.

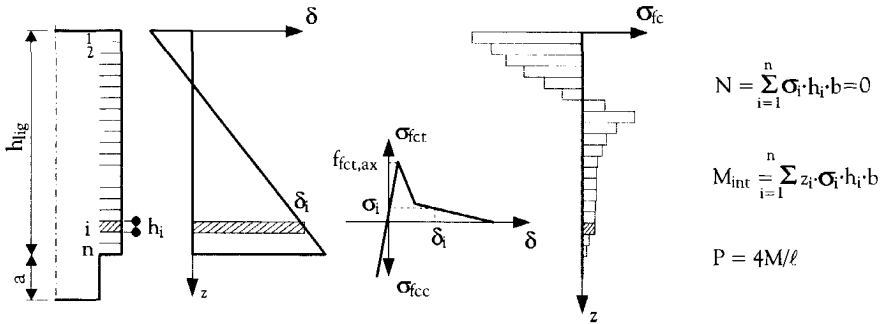


Figure 5.4 Second basic principle of the multi-layer simulation procedure [Hordijk, 1991]

The third principle of the model is the incremental procedure. In small steps the displacement at the notch tip is increased with a marginal displacement $\Delta\delta_{notch}$. After each step, iteration is necessary to accomplish the equilibrium of forces in the cross-section: the displacement at the top of the beam δ_c is adjusted until N is equal to zero. At this state of equilibrium, the crack opening displacement at the notch tip δ_{notch} and the bending load P that corresponds to the bending moment M , are plotted. By repeating the incremental steps, the load-crack opening displacement diagram is simulated, as Figure 5.5 demonstrates.

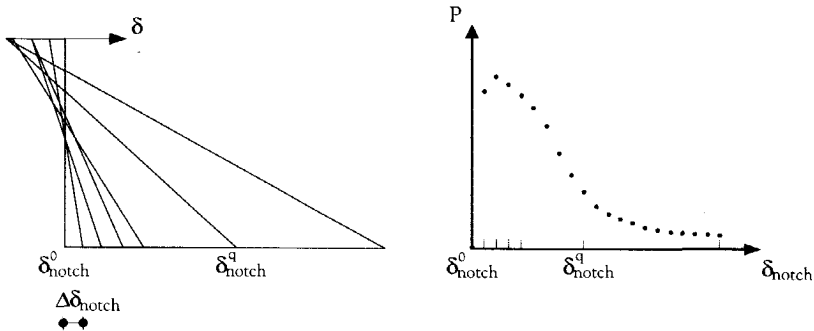


Figure 5.5 Third basic principle of the multi-layer simulation procedure

The multi-layer simulation seems quite straightforward to carry out. However, the stress-displacement characteristic of the springs is a combination of the uni-axial material relations set in the input level: the stress-strain relation for SFRC in compression, the linear elastic deformation in tension and the stress-crack width relation in tension. Because of the fact that the deformations in these relations are not compatible, Hordijk introduced a fictitious length parameter. According to Hordijk, the arbitrarily chosen length ℓ_i is the length of the ‘fracture zone’, which is the part of the beam that is replaced by springs. This length parameter is definitely not the same as the crack band width ℓ_{cb} , discussed in Chapter 4. To avoid any further misinterpretations, the fictitious length parameter ℓ_i will be called the influence length ℓ_i in the remaining of this thesis. By multiplying this parameter with relative deformations in compression and in linear elastic tension, strains are converted to discrete displacements so that load-crack opening displacement diagrams can be computed and compared to the mean results of three-point bending tests.

In his multi-layer simulations, Hordijk [Hordijk, 1991] showed that the influence length ℓ_i strongly affects the maximum load-bearing capacity of plain concrete cross-sections in bending and hardly influences the tail of the load-deflection curves. To check whether or not the same effects apply on the load-crack opening displacement diagrams, the exercise done by Hordijk was repeated. Figure 5.6 shows the input relations that describe the uni-axial behaviour of the concrete under consideration.

For concrete in compression, Figure 5.6a illustrates the bilinear stress-strain relation according to Eurocode 2. The simulations are carried out for mix 2 of Table 3.3, without the addition of fibres. As the concrete compressive strength is not influenced by the addition of fibres, the mean cube compressive strength is assumed to be equal to 59.1 MPa.

The linear elastic behaviour in tension is often defined by the uni-axial tensile strength $f_{ct,ax}$ and the corresponding strain limit $\epsilon_{ct,ax}$ (see Figure 5.6b). According to tensile tests carried out by Körmeling [Körmeling, 1986] on plain concrete with a mean cube compressive strength f_{ccm} of 55-60 N/mm², the displacement at the peak load was equal to 0.02 mm. The measuring length applied by Körmeling was 100 mm. Hence, the strain limit was equal to 0.2 ‰. The mean uni-axial tensile strength $f_{ctm,ax}$ in case of the tests of Körmeling was equal to 2.8 N/mm² for a testing rate of 0.125 μ m per second.

Figure 5.6c illustrates the assumed bilinear tensile softening relation for plain concrete, as proposed by Wittmann et al. [Wittmann et al., 1988]. In this case, the crack width w_0 was set at 0.5 mm.

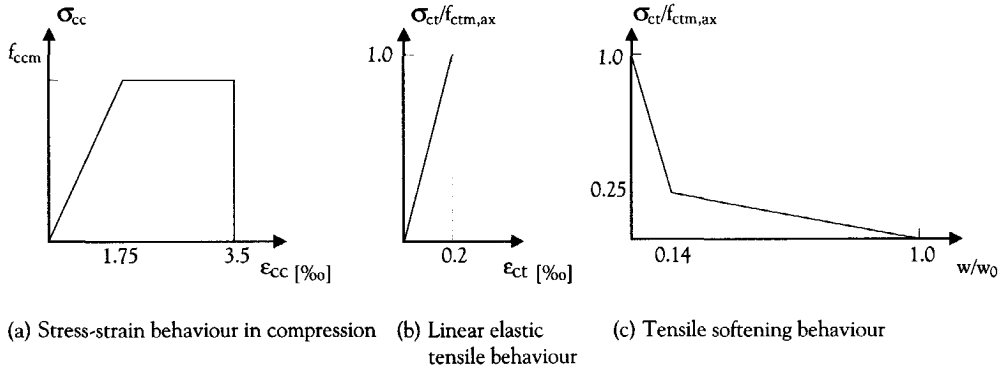


Figure 5.6 Input relations for plain concrete

Using the input material relations of Figure 5.6 in the multi-layer procedure, Figure 5.7 shows the effect of the influence length ℓ_i in case of 'standard' beam specimens (see section 3.3.3). Obviously, the influence length has the same impact on the load-crack opening displacement diagrams as Hordijk's fictitious length on the load-deflection diagrams. Figure 5.7 shows that the peak load increases when the influence length increases and that the tail of the bending behaviour is not affected. It can also be observed that the effect of the influence length on the pre-peak behaviour is relatively large. This is no surprise as the concrete stiffness in the procedure is directly related to the influence length ($\delta_c = \epsilon_c \cdot \ell_i$). In section 5.3, the effect of the influence length on the flexural behaviour of SFRC will be further analysed.

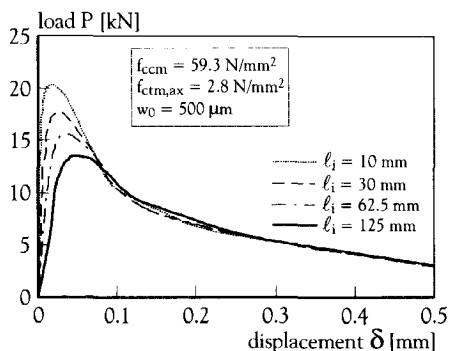
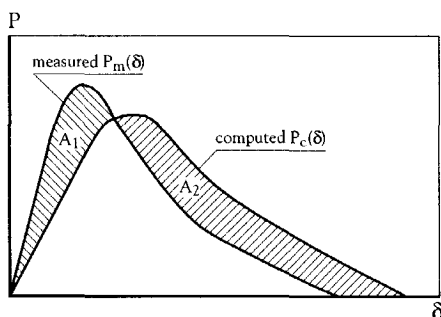


Figure 5.7 Effect of the influence length ℓ_i on simulated P- δ curves of plain concrete

Level III: the accuracy check

In the inverse modelling procedure carried out in this chapter, two checks are programmed to determine the accuracy of the simulations. Firstly, the area under the simulated P- δ curve is compared to the area under the measured P- δ curve. The simulated results are rejected when the maximum deviation in toughness ΔD_{\max} of 10% is exceeded (see Figure 5.8). In reality, the displacements do not reach a final value. For that reason, the tail is cut at a displacement where the tail of the P- δ curve is almost horizontal. In case of 30 mm long fibres, the tail was cut at a displacement of 20 mm, whereas for 60 mm long fibres this displacement was 70 mm.



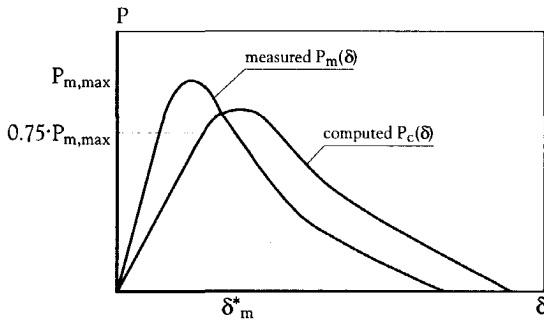
$$\text{if } A_1 < A_2 \text{ then } \Delta D = 1 - A_1/A_2$$

$$\text{if } A_1 > A_2 \text{ then } \Delta D = 1 - A_2/A_1$$

$$\Delta D_{\max} = 0.1$$

Figure 5.8 First accuracy check: comparison of toughness between computed and measured P- δ curves

The first criterion is not sufficient. Although the maximum deviation in toughness might be restricted to 10%, deviations in load might still exceed this 10%. Therefore, in a second criterion, the deviations between the measured load $P_m(\delta)$ and the computed load $P_c(\delta)$ are restricted to a maximum of 10% in the first part of the measured P- δ curve. As mentioned earlier, the first part of the P- δ curve is of most practical interest. In the scope of this research the deviations in load are checked up to a displacement δ_m^* , which corresponds to a 75% level of the peak load (see Figure 5.9).



for $\delta \leq \delta^*_m$:
 if $P_m(\delta) > P_c(\delta)$ then $1 - P_c(\delta)/P_m(\delta) < 0.1$
 if $P_m(\delta) < P_c(\delta)$ then $1 - P_m(\delta)/P_c(\delta) < 0.1$

Figure 5.9 Second accuracy check: comparison of load level between computed and measured P- δ curves

5.3 Analysis of SFRC cross-sections subjected to bending moments

5.3.1 Effect of the simulation procedure

This section shows that with the help of the multi-layer simulation procedure developed by Hordijk [Hordijk, 1991], the effect of each material input parameter that needs to be set on level I of the inverse modelling procedure (see Figure 5.1) can be analysed. As already mentioned in section 5.2, the multi-layer simulation procedure is used because of the simplicity of the procedure. Often, the introduction of simplicity is at the expense of the accuracy. In the multi-layer procedure, two parameters are of paramount importance with respect to this accuracy.

The first parameter that strongly influences this accuracy is the number of layers in the effective beam depth. Figure 5.10 shows the effect of the applied number of layers n . Obviously, the number of layers influences the peak load. Just like in Finite Element calculations, a balance needs to be found between the accuracy of simulations and the computational time that is necessary to carry out the analysis. In the scope of this research, this balance was found at $n = 500$. An increase in the number of layers hardly affects the P- δ curve, but strongly increases the computational time.

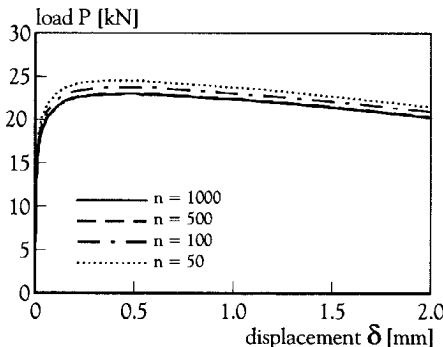


Figure 5.10 Effect of the number of layers in the multi-layer simulations

The second important parameter that influences the accuracy of the simulations is the influence length ℓ_i . An important issue in simulating the bending behaviour of plain concrete was that the initially assumed influence length ℓ_i considerably affected the peak value of the simulated load-displacement diagrams. Figure 5.11 shows that this effect is very limited in case of SFRC. However, Figure 5.11a shows that the assumed influence length ℓ_i can affect the ultimate deformation capacity in the simulated bending test. It shows that when the assumed influence length is equal to 10 or 30 mm, the cross-section fails. This is explained by the fact that a decrease of the influence length will decrease the deformation capacity in compression ($\delta_c = \epsilon_c \cdot \ell_i$). In the three-point bending tests, however, a sudden collapse of the cross-section was not observed. In the simulations, the assumed deformation capacity of the compressive zone is clearly not in correspondence with the deformation capacity in tension, which is related to the fibre length (in this case 60 mm). When the deformation capacity in uni-axial tension of the SFRC under consideration is smaller, as is the case in Figure 5.11b for the fibres with an aspect ratio L_f/d_f of 30/0.5, the deformation capacity of the compressive zone will play a less dominant role.

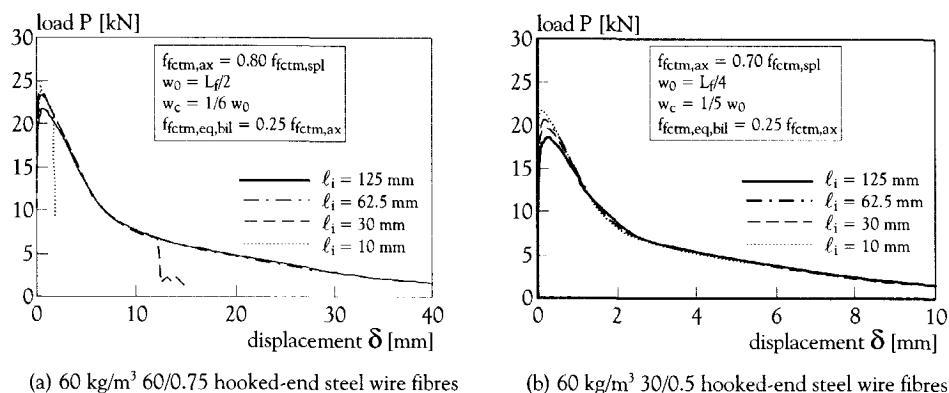


Figure 5.11 Effect of the influence length ℓ_i on simulated P - δ curves of SFRC

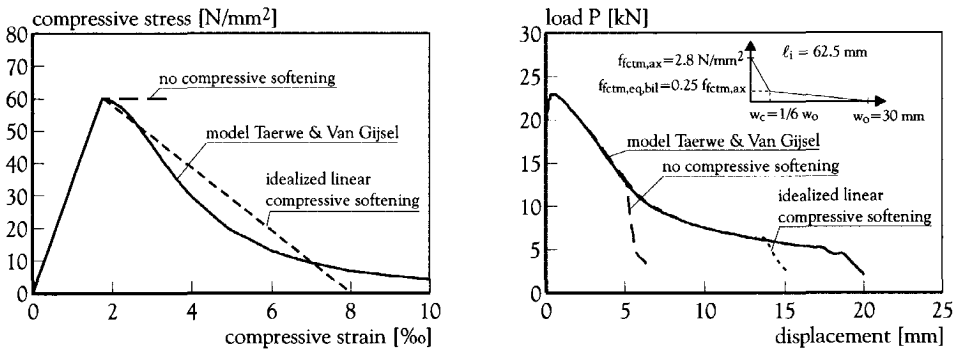
Although the maximum load-bearing capacity of SFRC is not very sensitive to the exact value of the influence length ℓ_i , the effect of ℓ_i on the rotational capacity of the cross-section is relatively large. The exact definition of the influence length is, therefore, quite a relevant issue. Pederson [Pederson, 1996], compared similar calculations with finite element calculations and found that $\ell_i = 0.5 \cdot h_{lig}$ is suitable. This is in agreement with Figure 5.11. In the remaining of this thesis, the influence length is set at $0.5 \cdot h_{lig}$.

5.3.2 Influence of the compressive behaviour

To analyse the influence of the deformation capacity and the post-peak behaviour in compression on the bending behaviour of SFRC, the three stress-strain models illustrated in Figure 5.12a were used in the multi-layer procedure described in section 5.2. In each of the three cases, the peak stress is 59.3 N/mm², which is equal to the mean compressive strength f_{ccm} of mix 2 of Table 3.3. It is assumed that the compressive strength is reached at a linear elastic strain limit of 1.75‰.

The first relation in Figure 5.12a is based on the stress-strain relation for plain concrete. It assumes a plastic material behaviour after reaching the linear elastic strain limit until the ultimate strain limit is reached at 3.5‰. The second relation is the model of Taerwe and Van Gijsel [Taerwe and Van Gijsel, 1995] to describe the post-peak behaviour of high strength concrete ($f_{ccm} > 50 \text{ N/mm}^2$) reinforced with steel fibres, which is already discussed in section 2.3.3. The third relation shows an idealised linear softening branch after reaching the peak stress up to a strain of 8‰.

Figure 5.12b shows the effect of the assumed post-peak behaviour in compression on the simulated load-displacement behaviour of a SFRC specimen in three-point bending for the assumed tensile behaviour and influence length ($\ell_i = \frac{1}{2} h_{fig}$). The P- δ curves show that the point of failure in bending depends on the deformation capacity in compression. For small ultimate strain limits, compressive failure occurs. The shape of the assumed post-peak behaviour in compression does not seem to influence the shape of the P- δ curves.



(a) Assumed stress-strain relationships in compression (b) Simulated flexural behaviour

Figure 5.12 Effect of the assumed post-peak behaviour in compression on the simulated P- δ curves

5.3.3 Influence of the tensile behaviour

The mix composition under consideration is mix 2 of Table 3.3, reinforced with 60 kg/m^3 of low carbon, hooked-end steel wire fibres. The mean cubic compressive strength of mix 2 (59.3 N/mm^2) is reached at a linear elastic strain limit of 1.75‰. A strain limit of 10‰ has been used in the assumption of an idealised (linear) compressive softening behaviour. The uni-axial tensile strength $f_{ctm,ax}$ is somewhere in between 0.7-0.8 of the tensile splitting strength $f_{ctm,sp}$.

Influence of the linear elastic strain limit

According to the Fictitious Crack Model (FCM) of Hillerborg et al. [Hillerborg et al., 1976], the tensile behaviour can be divided into a stress-strain relation for the linear elastic deformation and a stress-crack width relation for the post-cracking behaviour (see also Figure 4.1). The linear elastic component is determined by the uni-axial tensile strength of the SFRC under consideration and the linear elastic strain limit. Figure 5.13 shows the effect of different linear elastic strain limits on the simulated P- δ curve. Obviously, the influence on the load-bearing capacity can be neglected. In addition, the strain limit does not affect the tail any way. In the remaining of this chapter, a linear elastic strain limit of 0.8 ‰ has been applied.

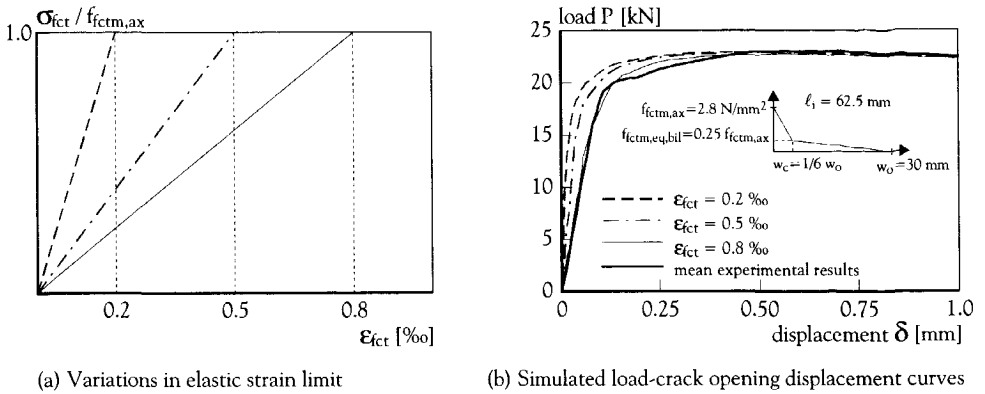


Figure 5.13 Effect of the linear elastic strain limit in tension on the simulated P-δ curves

As a consequence of the simulation procedure, the stiffness does not correspond to the real Young's modulus of the SFRC under consideration. However, the aim of this simulation procedure was to model the post-cracking behaviour of SFRC. For linear elastic calculations, the same approach can be used as in case of plain concrete.

Influence of the shape of the softening relationship

The post-cracking relation is determined by at least two parameters: the uni-axial tensile strength $f_{fct,ax}$ and the critical crack width w_0 . Depending on the chosen idealisation of the post-cracking behaviour, additional degrees of freedom determine the post-cracking relation. As was stated in section 4.2.1, relations that have proven to describe the post-cracking behaviour adequately often contain three or more parameters. Therefore, the two idealised stress-crack width relations shown in Figure 5.14a, were used to model the post-cracking behaviour of SFRC. In case of fibres with an aspect ratio L_f/d_f of 60/0.75, the maximum embedded fibre length of $L_f/2 = 30$ mm is used for the critical crack width w_0 .

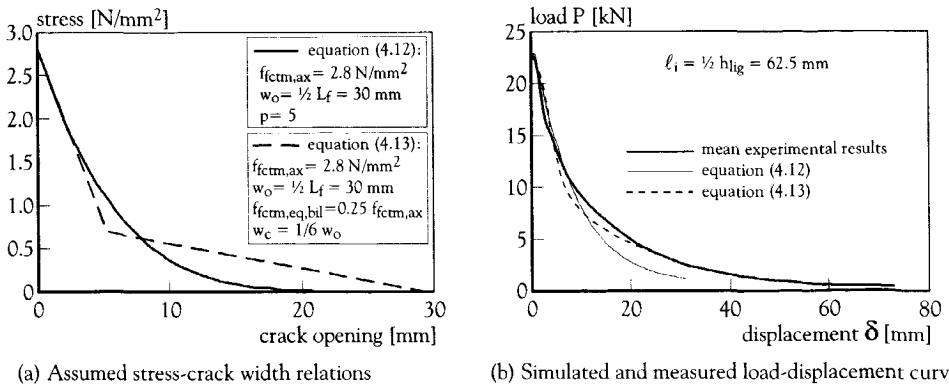


Figure 5.14 Effect of the assumed post-peak behaviour in tension on simulated load-displacement curves

Figure 5.14b shows the difference in computational results and compares the simulations with test results from 'standard' beams. The exponential relation describes the load-displacement curves quite well up to a crack opening displacement of 10 mm. Figure 5.14b, however, shows that a bilinear softening relation results in a much better fit of the test results than the exponential relation does. The exponential softening relation can not meet the demanded accuracy of 10% in toughness.

Influence of the mean tensile strength $f_{fctm,ax}$

The mean value of the uni-axial tensile strength $f_{fctm,ax}$ was derived from the mean tensile splitting strength, resulting from splitting tests on cubes (see Chapter 3). In the past, Körmeling [Körmeling, 1986] performed uni-axial tensile tests on cylinders and the same tensile splitting tests on cubes. Körmeling showed that in the case of plain concrete, with a mean compressive strength similar to the tested mix 2 of Table 3.3 ($f_{ccm} = 59.3 \text{ N/mm}^2$) in Chapter 3, the uni-axial tensile strength was 90-95 % of the tensile splitting strength. Körmeling's tests on SFRC proved that both strength values increased by virtue of the addition of fibres, although the tensile splitting strength showed a steeper increase than the uni-axial tensile strength. In the case of SFRC test specimens, the axial strength to splitting strength ratio was in the range of 0.7-0.8.

Figure 5.15 shows the effect of the mean uni-axial tensile strength on the computed P- δ curve, assuming a bilinear softening relation for the post-cracking behaviour. The mix composition under consideration is again mix 2 of Table 3.3, reinforced with 60 kg/m^3 hooked-end steel wire fibres, having an aspect ratio L_f/d_f of 60/0.75 and a tensile strength of 1200 N/mm^2 . The critical crack width $w_0 = L_f/2 = 30 \text{ mm}$, the characteristic crack width $w_c = 1/6 \cdot w_0 = 5 \text{ mm}$ and the equivalent post-cracking strength $f_{fctm,eq,bil} = 0.7 \text{ N/mm}^2$. The tensile strength values were calculated from the mean tensile splitting strength of mix 2 in Table 3.4 and the earlier mentioned range of axial strength to splitting strength ratios from Körmeling's experimental research. The tensile splitting strength of the composite was 3.5 N/mm^2 , as Table 3.4 already showed.

Figure 5.15a shows that the mean tensile strength influences the ultimate bending capacity: the higher the uni-axial strength value the higher the maximum bending load. The influence on the tail of the P- δ curve is marginal, as is demonstrated in Figure 5.15b, and can be neglected.

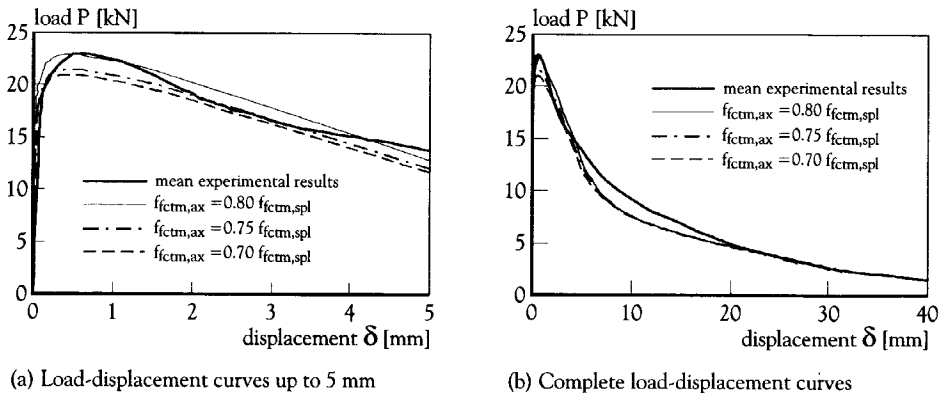


Figure 5.15 Effect of $f_{fctm,ax}$ on P- δ curves of mix 2, reinforced with 60/0.75 hooked-end steel wire fibres

Figure 5.16 shows the case in which the 60/0.75, hooked-end steel wire fibres in mix 2 are replaced by 60 kg/m³ of fibres with an aspect ratio L_f/d_f of 30/0.5. The mean compressive strength f_{fcm} of this SFRC was equal to 60 N/mm² and the mean tensile splitting strength $f_{fcm,spl}$ was 3.75 N/mm². In the simulations, the critical crack width w_0 was again assumed to be equal to $L_f/2 = 15$ mm and $w_c = 1/6 \cdot w_0 = 2.5$ mm.

After comparing Figure 5.16a with Figure 5.15a it shows that a lower bound tensile strength to splitting strength ratio seems more suitable for the shorter fibres, while the higher ratio of 0.8 seems more suitable for the fibres with an aspect ratio L_f/d_f of 60/0.75.

Figure 5.16b shows that the tail of the simulated load-displacement diagram of the 30/0.5 fibre reinforced concrete exceeds the actual capacity at large deformations. The critical crack width w_0 seems to be too high.

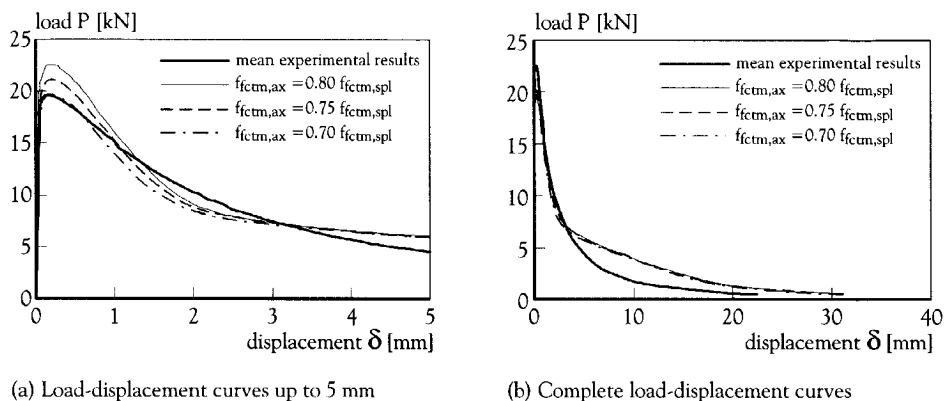


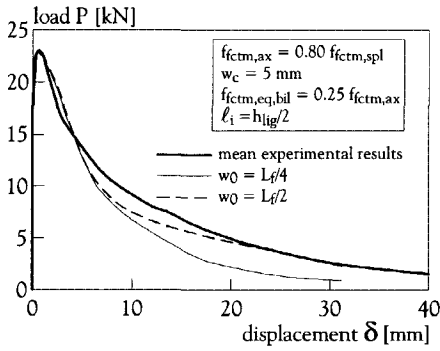
Figure 5.16 Effect of $f_{fcm,ax}$ on P - δ curves of mix 2, reinforced with 30/0.5 hooked-end steel wire fibres

Influence of the critical crack width w_0

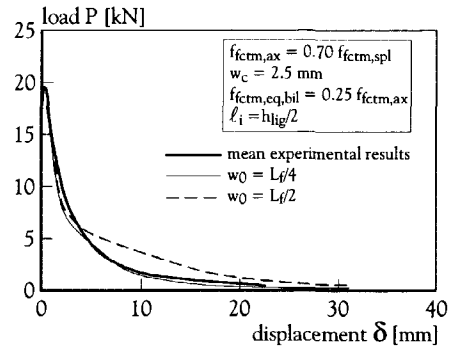
In their post-peak model of pullout behaviour for straight, round steel fibres, Soroushian and Lee [Soroushian & Lee, 1989] assumed that the critical crack width w_0 is equal to an average projected embedded fibre length of $L_f/4$. This length can be statistically derived, assuming a spatial-random fibre orientation and distribution, as will be shown in Chapter 6. In the case of mix 2 reinforced with 60/0.75 fibres the value for the critical crack width w_0 would then be equal to 15 mm.

However, Figure 5.17a shows that when the critical crack width is set at $L_f/4$, the tail of the simulated load-displacement curve does not describe the mean curve of the experiments. It shows that in case w_0 is equal to $L_f/2$, the tail of the measured load-displacement curve is described quite well. Obviously, altering the critical crack width w_0 does not have any effect on the first part ($\delta < 5$ mm) of the load-displacement curve.

Figure 5.17b shows that in case of fibres with an aspect ratio L_f/d_f of 30/0.5, the critical crack width of $L_f/4$ is quite suitable to describe the tail of the measured P - δ curve. It shows that in case w_0 is equal to $L_f/2$ the tail of the measured curve is overestimated.



(a) 60 kg/m³ 60/0.75 hooked-end steel wire fibres

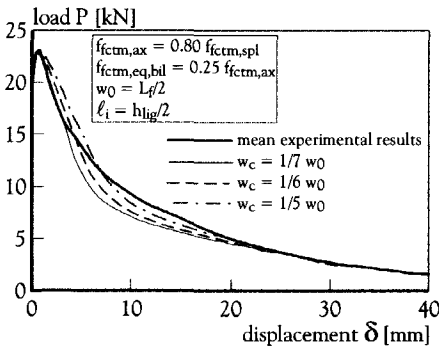


(b) 60 kg/m³ 30/0.5 hooked-end steel wire fibres

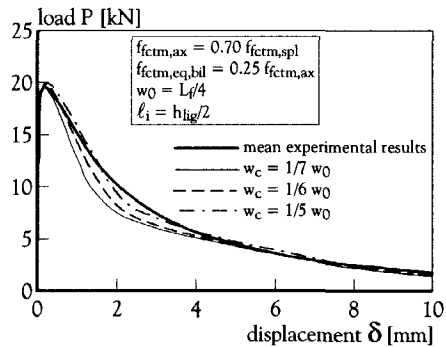
Figure 5.17 Effect of the critical crack width on the tail of the computed load-displacement curve

Influence of the characteristic crack width w_c

Assuming that the earlier analyses have resulted in optimum values for the tensile strength $f_{ctm,ax}$ and the critical crack width w_0 , the influence of the characteristic crack width w_c must be determined for both fibre additions. Figure 5.18 shows the effect of w_c on the computed load-displacement diagrams.



(a) 60 kg/m³ 60/0.75 hooked-end steel wire fibres



(b) 60 kg/m³ 30/0.5 hooked-end steel wire fibres

Figure 5.18 Effect of the characteristic crack width w_c on the computed load-displacement curve

Figure 5.18a shows the effect of w_c on the P - δ curves for the 60 kg/m³ of hooked-end steel fibres ($L_f/d_f = 60/0.75$) in mix 2 of Table 3.3, with w_c ranging from $1/7 \cdot w_0$ to $1/5 \cdot w_0$. The suitable characteristic crack width w_c is determined by the accuracy criteria in level III of the inverse modelling procedure. In case the deviation between the toughness values (area under the complete computed curve and mean experimental curve) would have been minimised, the most appropriate value for w_c would have been equal to $1/5 \cdot w_0$. However, in that case the maximum deviation in load in the first part of the P - δ curves, up to a displacement δ_m^* (at 75% of P_{max}), would have exceeded the allowed deviation of 10%. On the other hand, when the deviation in load between the computed curve and the mean experimental curve would

have been minimised, than $1/7 \cdot w_0$ would have been the most appropriate value for w_c . The deviation in toughness, however, would then have exceeded the 10% limit. Due to the two criterions set in level III of the inverse modelling procedure, the only suitable value for w_c is $1/6 \cdot w_0$. The simulations of the bending behaviour of the 'standard' SFRC test specimens with 30/0.5 mm steel fibres are shown in Figure 5.18b. In this case the accuracy check leads to $w_c = 1/5 \cdot w_0$.

Influence of the equivalent post-cracking strength $f_{fct,eq,bil}$

The influence of the equivalent post-cracking strength $f_{fct,eq,bil}$ is somewhat similar to the effect of the characteristic crack width. As Figure 5.19 shows, both parameters change the angle between the vertical stress axis and the first post-cracking branch of the bilinear stress-crack width relation. However, their influence on the stress-crack width relation differs, which is reflected in the effect on the load-crack opening displacement curves.

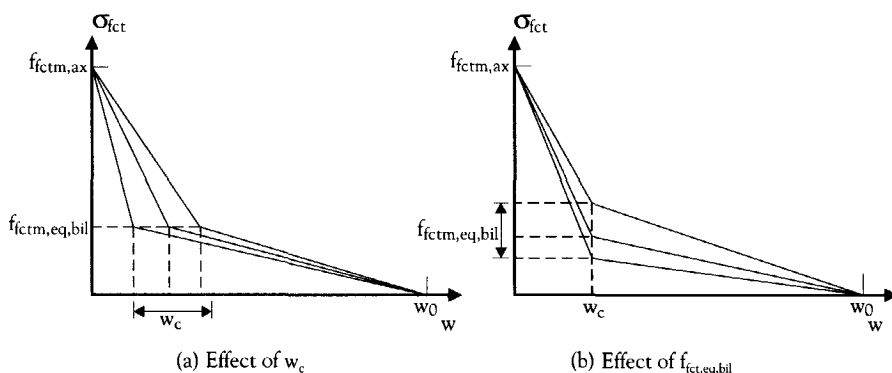


Figure 5.19 Effect of $f_{fct,eq,bil}$ and w_c on the stress-crack width relation

From Figure 5.20 it might be concluded that the optimal post-cracking strength $f_{fct,eq,bil}$ is somewhere between $0.2 \cdot f_{fct,ax}$ and $0.3 \cdot f_{fct,ax}$. In case of the 60/0.75 fibres, $f_{fct,eq,bil}$ is equal to $0.2 \cdot f_{fct,ax}$, whereas for the 30/0.5 fibres $f_{fct,eq,bil}$ is equal to $0.3 \cdot f_{fct,ax}$.

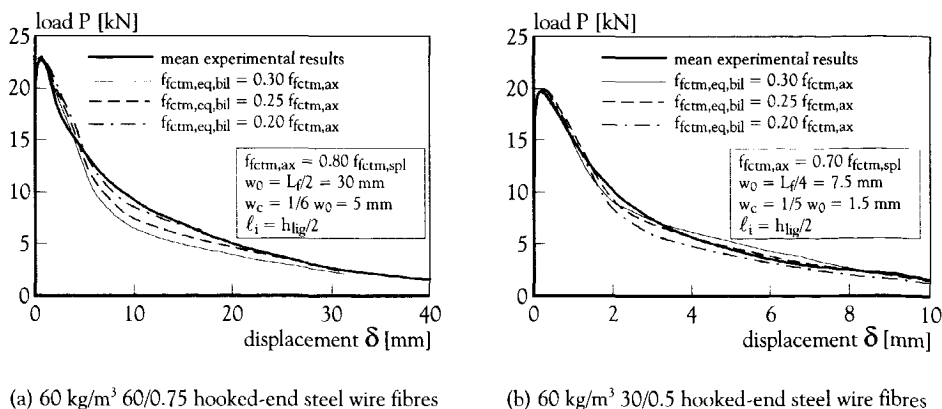


Figure 5.20 Effect of the equivalent post-cracking strength $f_{fct,eq,bil}$ on the computed load-displacement curves

In reality, the equivalent post-cracking strength $f_{fctm,eq,bil}$ depends on the fibre volume V_f , the aspect ratio L_f/d_f and the frictional bond between fibre and matrix. According to Glavind [Glavind, 1992], the frictional bond can be described by the bond factor α_f that depends on the packing density PD of the dry material, the water/binder ratio wbr and the fibre factor β_f that incorporates the difference in interfacial shear stress between different types of fibres:

$$\alpha_f = PD \cdot (wbr)^{-1} \cdot \beta_f \tag{5.1}$$

Hoy [Hoy, 1998] showed that the packing density PD depends on various parameters such as the fibre volume, the aspect ratio, grading curve, etc. For example, it has been shown that the packing density of a rounded coarse (14-20 mm) aggregate-fibre mixture decreases from 0.65 to 0.56 as the volume of hooked-end fibres ($L_f/d_f = 60/0.8$) increases from 0 to 1%. On the other hand, the decrease in packing density was marginal for a fine (0.15-5 mm) aggregate-fibre mixture, starting from a value of 0.64. Hoy's experiments showed that the optimum packing density of the aggregate-fibre mixture is reached at a ratio of fines to total aggregate volume of 50%. In case of mix 2, 48 % of fines and 52% of round coarse aggregates (4-16 mm) were used. According to predictions made by Hoy, the packing density of the aggregate-fibre mixture of mix 2 of Table 3.3 approaches the optimum value of 0.70.

After using the water/binder ratio of 0.45 from Table 3.3, the bond factor α_f can be calculated if the fibre factor β_f is known. For normal strength concrete (the mean compressive strength was approximately 50 N/mm²) and hooked-end steel wire fibres, Glavind [Glavind, 1992] found that β_f was equal to the mean frictional shear stress of 2.1 N/mm² derived from pullout tests. The fibre type used by Glavind was the same as the one used in the scope of this research. In addition, the matrix quality corresponded quite well to that of mix 2 (see Table 3.4). Hence, the fibre factor β_f is assumed to be equal to 2.1 N/mm², which leads to a bond factor α_f of 3.27 N/mm².

Glavind [Glavind, 1992] defined a fibre reinforcement factor λ_f :

$$\lambda_f = V_f \cdot \frac{L_f}{d_f} \cdot \alpha_f \tag{5.2}$$

For the SFRC of mix 2, reinforced with 60 kg/m³ ($\approx 0.77\%$) of 30/0.5 steel fibres, the fibre reinforcement factor $\lambda_f = 1.51$ N/mm². In case of 60 mm long fibres with a diameter of 0.75 mm, the fibre reinforcement factor λ_f equals 2.01 N/mm². After comparing these values with the values of the earlier determined equivalent post-cracking strength $f_{fctm,eq,bil}$, the fibre reinforcement ratio λ_f can be related to the equivalent post-cracking strength $f_{fctm,eq,bil}$:

$$f_{fctm,eq,bil} = \lambda_f \cdot c_f \tag{5.3}$$

where $c_f \approx 0.4$.

It is hard to check the validity of equation (5.3). However, in this context equation (5.3) is only meant to show the micro-mechanical parameters that influence the post-cracking behaviour.

5.3.4 The effect of the dimensions of the cross-section

Simulating various beam widths

Now that is clear in what way the material characteristics and influence length affect the simulated flexural behaviour, it is checked whether or not the load-displacement curves of test specimens with different dimensions can be simulated with sufficient accuracy. The earlier found values for the input parameters of the bilinear post-cracking relation resulted from inverse analyses of 'standard' beam specimen. Figure 5.21 shows the simulated and measured load-displacement diagrams of beams with varying beam widths. The beam depth was held constant. The exact dimensions of these beams are given in Figure 3.7.

Figure 5.21a shows the case of mix 2, reinforced with 60 kg/m^3 low carbon hooked-end steel wire fibres ($L_f/d_f = 60/0.75$). The mean results of the test series with various beam widths are well described up to a crack opening of 5 mm (the simulations are within 5% of the measurements). However, the measured load-displacement curves of the 300 and 450 mm wide beams are underestimated at displacements over 5 mm.

Figure 5.21b shows that in case of mix 2 reinforced with 60 kg/m^3 low carbon hooked-end steel wire fibres with an aspect ratio L_f/d_f of 30/0.5, the simulated load-displacement curves substantially underestimate the experimental results of the 300 and 450 mm wide beams.

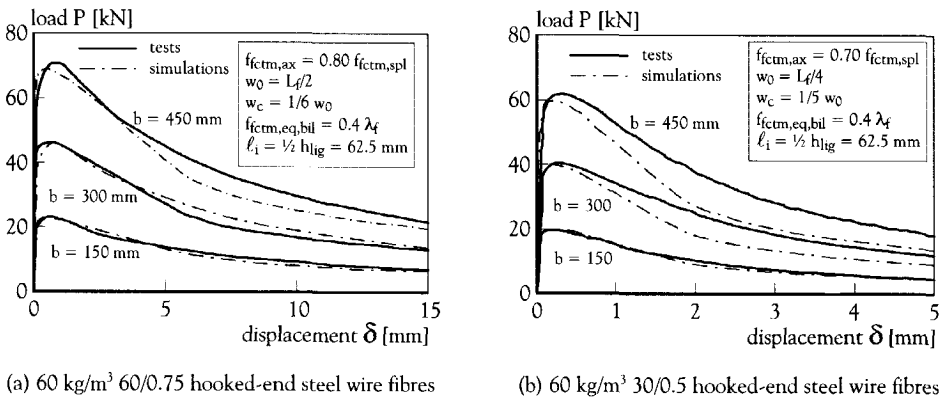


Figure 5.21 Simulated P- δ curves of differently sized SFRC beams

In case of the 60/0.75 fibres, Figure 5.22a shows that after inverse analysis the simulated load-displacement curves fit the mean experimental results much better. Compared to Figure 5.21a, the characteristic crack width w_c ($w_0/5$ instead of $w_0/6$) and the critical crack with w_0 ($0.425 \cdot L_f$ instead of $0.5 \cdot L_f$) are adjusted.

Figure 5.22b shows that after adjusting the critical crack width w_0 ($L_f/3$ instead of $L_f/4$) in case of the 30/0.5 fibres, the simulated load-displacement curves of both the 300 and 450 mm wide beams fit the mean experimental results much better. However, the simulated P- δ curve overestimates the mean results from bending tests on 150 mm wide specimens.

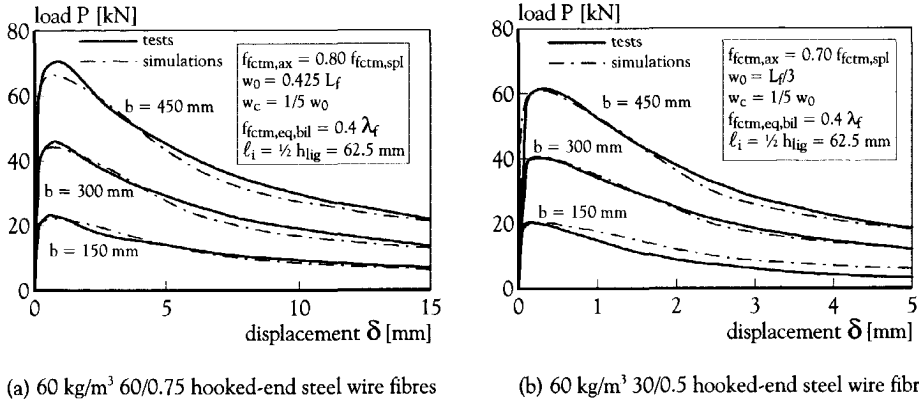


Figure 5.22 Simulated P-δ curves of differently sized SFRC beams after adjustment of post-cracking behaviour

Simulating various beam depths

In the scope of this research, specimens with various effective depths were tested. The tested beams were produced with mix 1 of Table 3.3. The added fibres (60 kg/m^3) are characterised by an aspect ratio L_f/d_f of 60/0.75 and by the fact that they were drawn from high carbon steel wire, which resulted in a relatively high tensile strength of 2700 N/mm^2 .

The experiments were carried out on 450 mm wide beams with an effective depth of 125, 250 and 375 mm. The test series were produced separately, but were poured in the same mould. The placement and compaction method used was the same for each test series that consisted of six test specimens. These specimens were cast from one batch, except for the deepest beams that were produced from two batches. The mean cube compressive strength was 71.5, 75.5 and 78.2 N/mm^2 respectively for the beams with an effective depth of 125, 250 and 375 mm. The beam depth to span length ratio was held constant at any time (see also Figure 3.7). The mean tensile splitting strengths were 4.18, 4.53 and 4.81 N/mm^2 . These values were converted uni-axial tensile strengths for the purpose of analysis by multiplying these values with the tensile strength to splitting strength ratio of 0.8 that was found earlier for 60 mm long fibres.

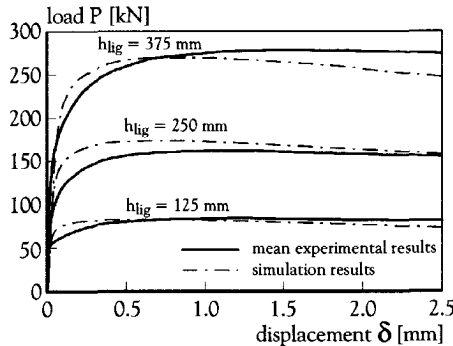


Figure 5.23 Simulated P-δ curves of SFRC beams with various effective beam depths

Figure 5.23 shows the simulated and the mean experimental P- δ curves for the high strength SFRC under consideration. The simulated load-crack opening displacement diagrams describe the mean experimental test results with sufficient accuracy (deviation < 10%). However, because of the fact that the beams were only tested up to a deformation of 2.5 mm, it is not clear how accurate the tail of the load-displacement diagram is simulated. The maximum load-level, however, is described rather well.

5.4 Discussion of results

In the previous section, it has been shown that mean P- δ curves from three-point bending tests can be described by means of a bilinear post-cracking relation. It has also been shown that this is based on certain assumptions within the multi-layer simulation procedure. The number of layers applied ($n = 500$) and the influence length used in the analyses ($l_i = \frac{1}{2} h_{ig}$) were found suitable after thorough investigations.

The analyses of SFRC cross-sections by means of the multi-layer procedure showed that the post-peak behaviour in compression does not influence the load-bearing capacity in bending. However, the assumption for the post-peak behaviour in compression can affect the deformation capacity of a SFRC cross-section. The effect of the ultimate compressive strain limit is considerable. It has been found that an idealised linear compressive softening branch up to 10‰ is a reasonable assumption.

The effect of the linear elastic strain limit in tension on the P- δ curve is negligible. Only the pre-peak behaviour of SFRC is influenced by this assumption. The analyses showed that in this case a strain limit of 0.8‰ resulted in the best fit.

Figure 5.24 shows the stress-crack width relation SFRC that can be used to fit mean P- δ diagrams from three-point bending tests. The describing parameters of this relation are the mean uni-axial tensile strength $f_{fctm,ax}$, the equivalent post-cracking strength $f_{fctm,eq,bil}$, the characteristic crack width w_c and the critical crack width w_0 .

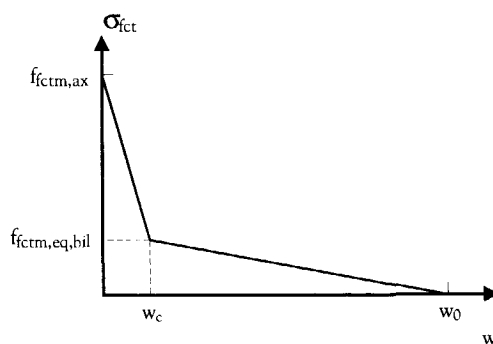


Figure 5.24 Bilinear post-cracking material relation for SFRC

After analysing medium strength SFRC cross-sections with 60 kg/m^3 of hooked-end, steel wire fibres, the describing parameters of the stress-crack width relation can be determined as follows:

- The value of the mean uni-axial tensile strength of the composite material is determined from the mean value of the tensile splitting strength $f_{\text{ctm, spl}}$ derived from splitting tests on cubes. The ratio $f_{\text{ctm, ax}}/f_{\text{ctm, spl}}$ is 0.7 for 30 mm long fibres and 0.8 for 60 mm long fibres.
- The equivalent post-cracking strength to tensile strength ratio $f_{\text{ct, eq, bil}}/f_{\text{ctm, ax}}$ is in between 0.20 and 0.30. The ratio $f_{\text{ct, eq, bil}}/f_{\text{ctm, ax}}$ is 0.3 for 30 mm long fibres and 0.2 for 60 mm long fibres.
- The ratio w_c/w_0 is in the range of 0.20.
- The critical crack width to fibre length ratio w_0/L_f is in the range of 0.33-0.425. In the next chapter, this will be further analysed. It will be shown that the critical crack width w_0 depends on the average fibre orientation, as a result of geometrical boundary conditions and the production process.

5.5 Concluding remarks

This chapter showed that in case of standard three-point bending tests the toughness values up to the predefined displacement limits could be described within the predefined accuracy of 10%. In addition, the load level of the mean experimental P- δ curve could also be described with an accuracy of 10%, up to a deformation δ_m^* beyond the peak load that corresponds to a load-level of 75% of the measured peak load.

It was shown that the equivalent post-cracking strength $f_{\text{ctm, eq, bil}}$ in bilinear stress-crack width relationship could also be determined by multiplying the reduction factor c_f (≈ 0.4) with the fibre reinforcement factor λ_f . Micro-mechanically oriented research is necessary for validation, as too many parameters have been estimated and the reduction factor c_f is a fitting parameter. However, this equation is not meant to provide an exact solution, but is used to indicate the parameters that influence the equivalent post-cracking strength.

When the bilinear post-cracking relation was applied in the analyses of the cross-sections of beams with a larger effective depth, it was found that the relation describes the peak load-level rather well.

Chapter 6

From specimen to structure

6.1 Introduction

The preceding chapter showed how to generate mean post-cracking relations of SFRC from bending tests. Based on these relations, it seems quite easy to recommend permissible design stresses, taking the scatter in test data into account. However, the post-cracking behaviour derived from test specimens does not necessarily provide the correct post-cracking relation for the use in structural design. One of the main reasons for possible errors is a deviation in preferred orientation between the fibre reinforcement in test specimens and the fibre reinforcement in structures. Consequently, the effectiveness of fibre reinforcement in structures strongly depends on the actual fibre orientation relative to the orthogonal direction(s) of the occurring tensile stress(es).

To ensure the use of correct post-cracking relations, the material behaviour obtained from test results should be translated into the material behaviour expected in a structure. This chapter will provide the necessary insight to translate the post-cracking behaviour obtained from three-point bending tests to the expected behaviour in typical structural applications of SFRC. It starts with explaining the general effect of fibre orientation on the effectiveness of fibre reinforcement. In addition, the effect of geometrical boundaries on the fibre orientation is discussed, after which the effect of compaction by external vibration is discussed. The latter is used to estimate the effectiveness of fibre reinforcement in test specimens.

Before making a translation to fibre efficiency in structures it is necessary to study structural applications of SFRC. In the scope of this research two promising structural applications of SFRC were assessed: underwater concrete slabs and segmental tunnel linings. Results from experimental research on drilled core specimens from pilot projects will clearly show that fibre reinforcement in practice tends to have a preferred orientation, depending on the production process and vicinity of geometrical boundaries. After a comparison of the effectiveness of the fibre reinforcement in these pilot projects and the estimated effectiveness in the test specimens, efficiency factors were developed to translate the fibre efficiency in SFRC test specimens to the practical applications under consideration.

6.2 Fibre orientation, efficiency and effectiveness

As Figure 2.6 in section 2.3.1 already showed, the efficiency of an individual steel fibre strongly depends on the inclination angle ϕ relative to the direction of the pullout load. Based on this figure, it was assumed that the maximum efficiency is reached when the fibre is in full alignment with the direction of this load and least efficient if it is perpendicular to it.

In the scope of this research, fibre efficiency and fibre effectiveness of fibre reinforcement are defined in accordance to the definitions given by Kameswara Rao [Kameswara Rao, 1979]. In principle, the term fibre efficiency is used to indicate the performance of an individual fibre with a certain orientation relative to the direction of the (tensile) stress or the direction of the crack opening displacement. The term effectiveness is used for the average value of the efficiency, obtained by considering all possible orientations the fibre can have.

Fibre effectiveness without restrictions on fibre orientation

In case of a one-dimensional system, the fibre efficiency is always optimal, since the fibre orientation is inevitably in line with the direction of the applied load. Theoretically, the fibre effectiveness equals 1.

The situation changes, however, when a two-dimensional system is considered. In that case, it is assumed that all fibres are randomly orientated in a plane. Figure 6.1 shows the 2D case in which the orientation angle θ between the embedded fibre length and the line crack (x-axis) can vary between 0 and $\frac{1}{2}\pi$. To determine the average efficiency or effectiveness of multiple fibres, the mean fibre orientation needs to be projected on the axis that represents the direction of the tensile stress, in this case the vertical axis. It is supposed that all fibres in the plane are subjected to parallel translation until their centre points coincide at the intersection of the x and y-axis. The effectiveness can be calculated as follows:

$$\eta_{\theta 2D} = \int_0^{\frac{\pi}{2}} \frac{\sin \theta \cdot d\theta}{\pi} = \frac{2}{\pi} \tag{6.1}$$

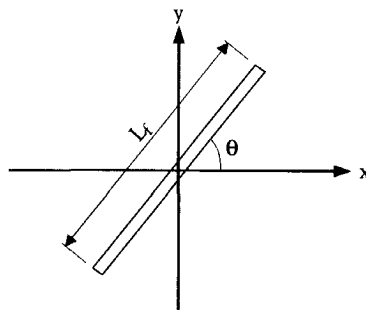
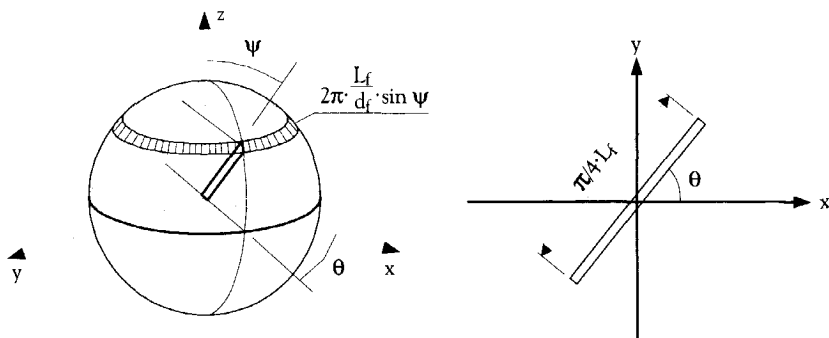


Figure 6.1 Two-dimensional fibre orientation system



(a) Randomly orientated fibres in three dimensions (b) Average projected length in x-y plane

Figure 6.2 Three-dimensional fibre orientation system

In the case that fibres can have any orientation in three dimensions, their end points cover the circumference of a sphere with diameter L_f , as Figure 6.2a shows. Romualdi and Mandel [Romualdi & Mandel, 1964] calculated the 3D effectiveness, assuming a uniform probability of the randomly orientated fibres, with the following equation:

$$\eta_{\theta 3D} = \frac{\int_0^{\pi} \int_0^{\pi} \sin \psi \cdot \sin \theta \cdot d\psi \cdot d\theta}{\pi^2} = \frac{4}{\pi^2} \quad (6.2)$$

In equation (6.2) it is assumed that all fibre orientations have the same probability of occurrence. However, this is not correct. The latter was proved by Stroeven [Stroeven, 1978], who calculated the spatial-random effectiveness based on geometric probability theory. Firstly, the average projected length $L_{f,xy}$ on the x-y plane was determined by multiplying the individual fibre projections with their contributions to these projections as a function of the orientation relative to the z-axis. These contributions have a circular shape of which the radius depends on the orientation angle ψ . It is clear that as the orientation angle increases, the contribution to the projected length increases; at increasing ψ the radius of the circle increases (see Figure 6.2a), which means that a larger number of fibre end-points form this circle. According to Stroeven's theory, the projected fibre length on the x-y plane can be determined as follows:

$$L_{f,xy} = \frac{\int_0^{\pi/2} L_f \cdot \sin \psi \cdot 2\pi \cdot \frac{L_f}{2} \cdot \sin \psi \cdot d\psi}{2\pi \cdot \frac{L_f}{2}} = \frac{\pi}{4} \cdot L_f \quad (6.3)$$

Secondly, after calculating the average projected length on the x-y plane, Stroeven [Stroeven, 1978] followed the same approach as Kameswara Rao [Kameswara Rao, 1979] did in the two-dimensional case:

$$\eta_{\theta_{3D}} = \int_0^\pi \frac{\frac{\pi}{4} \cdot \sin \theta \cdot d\theta}{\pi} = \frac{1}{2} \tag{6.4}$$

Obviously, the mean effectiveness of fibres in unidirectional, planar random and spatial-random reinforcement systems can be expressed by orientation efficiency factors $\eta_{\theta_{1D}}$, $\eta_{\theta_{2D}}$ and $\eta_{\theta_{3D}}$, equal to 1, $2/\pi$ and $1/2$, respectively. As a consequence, the projections of the mean fibre embedment lengths are $1/2 \cdot L_f$, $1/\pi \cdot L_f$ and $1/4 \cdot L_f$.

In determining $\eta_{\theta_{2D}}$ and $\eta_{\theta_{3D}}$, it was assumed that the fibre could orient itself freely in 2D or 3D space. However, this is only valid for fibre locations away from geometrical boundary surfaces of the specimen or structure. For locations closely situated near the side of the mould or formwork, the orientation will be restricted, which results in a change in effectiveness.

Effect of geometrical boundaries on fibre orientation and effectiveness

Several researchers have published theoretical models to describe the effectiveness of steel fibre reinforcement at geometrical boundaries. Kameswara Rao [Kameswara Rao, 1979], for instance, determined the effectiveness for a two-dimensional situation in which a fibre is located close to a boundary.

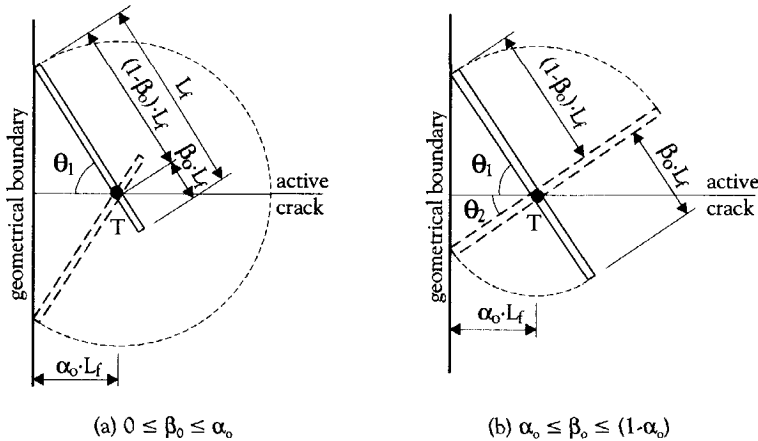


Figure 6.3 Fibre orientation at a point T near a boundary [Kameswara Rao, 1979]

As Figure 6.3 shows, Kameswara Rao [Kameswara Rao, 1979] examined all possible planar fibre orientations at a point T, which is at a distance $\alpha_0 \cdot L_f$ from the boundary and intercepts the fibre at a distance $\beta_0 \cdot L_f$. The possible orientations depend on the value of β_0 relative to α_0 ; if $0 \leq \beta_0 \leq \alpha_0$ the fibre tips can lie on the dotted line (see Figure 6.3a). The orientations are given by the angle θ between the straight line, joining point T to both fibre tips, and the active crack. Assuming that the tip of the fibre can lie anywhere on the dotted sector with equal chance, the effectiveness can be calculated as follows:

$$\eta_{\theta 2D}(\alpha_o, \beta_o) = \int_0^{\pi-\theta_1} \frac{\sin \theta \cdot d\theta}{\pi - \theta_1} = \frac{(1 + \cos \theta_1)}{\pi - \theta_1} \quad (6.5)$$

$$\text{where } \cos \theta_1 = \frac{\alpha_o}{(1 - \beta_o)}$$

In case $\alpha_o \leq \beta_o \leq (1 - \alpha_o)$, the mean efficiency will be different, because the possible fibre orientation is further restricted. Now, the effectiveness can be calculated with the help of the following equation:

$$\eta_{\theta 2D}(\alpha_o, \beta_o) = \int_{\theta_2}^{\pi-\theta_1} \frac{\sin \theta \cdot d\theta}{\pi - (\theta_2 + \theta_1)} = \frac{(\cos \theta_1 + \cos \theta_2)}{\pi - (\theta_2 + \theta_1)} \quad (6.6)$$

$$\text{where } \cos \theta_1 = \frac{\alpha_o}{(1 - \beta_o)} \text{ and } \cos \theta_2 = \frac{\alpha_o}{\beta_o}$$

In case $(1 - \alpha_o) \leq \beta_o \leq 1$, the situation is similar to the one represented by Figure 6.3b. The effectiveness can be determined as follows:

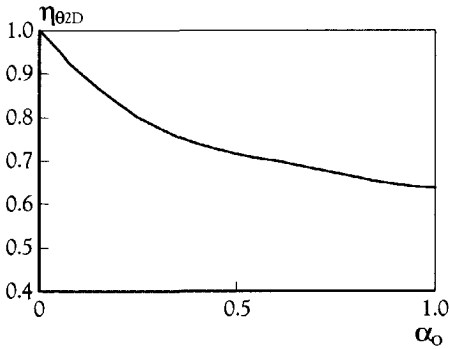
$$\eta_{\theta 2D}(\alpha_o, \beta_o) = \int_0^{\pi-\theta_2} \frac{\sin \theta \cdot d\theta}{\pi - \theta_2} = \frac{(1 + \cos \theta_2)}{\pi - \theta_2} \quad (6.7)$$

Equations (6.5), (6.6) and (6.7) are applicable as long as $0 \leq \alpha_o \leq 0.5$. If $0.5 \leq \alpha_o \leq 1$, equation (6.5) is to be applied for $0 \leq \beta_o \leq (1 - \alpha_o)$, equation (6.1) for $(1 - \alpha_o) \leq \beta_o \leq \alpha_o$ and equation (6.7) for $\alpha_o \leq \beta_o \leq 1$. In the case that $\alpha_o > 1$, there are no more restrictions in fibre orientation, which means that equation (6.1) applies, assuming a planar random situation. Appendix C shows how the orientation efficiency $\eta_{\theta 2D}$ varies with α_o and β_o .

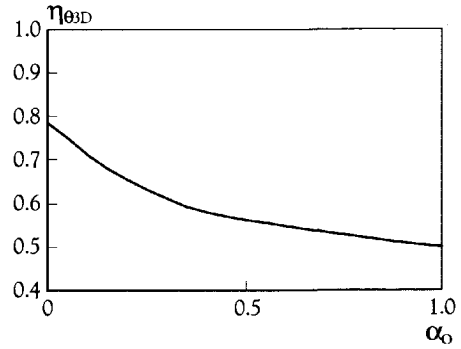
Assuming equal probability for all possible values of β_o , the fibre efficiency $\eta_{\theta 2D}(\alpha_o)$, which is a function of the distance to the boundary, is given by:

$$\eta_{\theta 2D}(\alpha_o) = \int_0^1 \eta_{\theta 2D}(\alpha_o, \beta_o) \cdot d\beta_o \quad (6.8)$$

The numerical values of $\eta_{\theta 2D}$ for various values of ξ are plotted in Figure 6.4a. It clearly shows that the effectiveness cannot be expressed by a unique efficiency factor, since $\eta_{\theta 2D}$ depends on the distance $\alpha_o \cdot L_f$ to the boundary. At the boundary itself the effectiveness is at its maximum, which is obvious, since in that case the fibre is perpendicular to the active crack. If α_o is equal to 1, the effectiveness is equal to $2/\pi$, which is in agreement with the planar-random situation described by equation (6.1).



(a) 2D-efficiency factor near boundaries



(b) Estimated 3D-efficiency factor near boundaries

Figure 6.4 Variation of orientation efficiency $\eta_{\theta 2D}$ and $\eta_{\theta 3D}$ with distance to boundary $\xi-L_f$

Obviously, the analysis of fibre effectiveness near boundaries is more complicated in a 3D-spatial than in a two-dimensional case. Following to the early work of Romualdi and Mandel [Romualdi & Mandel, 1964], Kameswara Rao [Kameswara Rao, 1979] supposed that it is of practical adequacy to multiply the 2D-effectiveness near boundaries with $2/\pi$ to obtain the 3D-effectiveness near boundaries. In the scope of this research, however, the statistical approach of Stroeven [Stroeven, 1978] was followed because the probability of occurrence in the determination of the fibre effectiveness is included. It is therefore supposed that the 3D-effectiveness near boundaries can be obtained by multiplying the 2D-effectiveness with $\pi/4$ (see Figure 6.4 b)

As a matter of fact, Stroeven [Stroeven, 1999] also developed a model for estimating the 3D-effectiveness as a function of the fibre orientation and the location relative to an active crack perpendicular to a boundary. This model is based on a random generation process of coordinates and orientations in which it is assumed that a fibre violating the boundary conditions is rejected. According to Stroeven this is in accordance with experimental data, but in the scope of this research the fibre density close to boundaries was found to be higher than in the bulk material. These latter findings are supported by findings of Hoy [Hoy, 1998], who observed that steel fibres aligned parallel to the surfaces of the containers used in packing density tests. According to Hoy [Hoy, 1998], the fibre density is likely to peak at a small distance from the boundary, after which the value decreases below the bulk fibre density and finally increases again towards the bulk value at a distance of half the fibre length. Figure 6.5 illustrates this assumption and shows the fibre and particle density close to a boundary as a function of the fibre length and particle size.

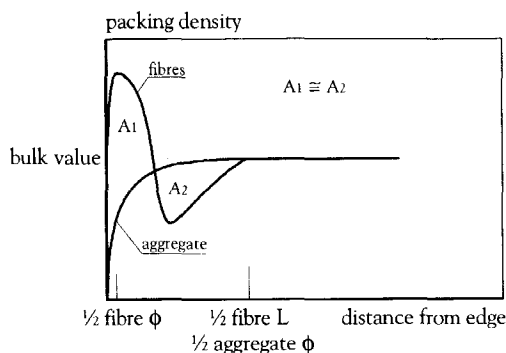


Figure 6.5 Fibre and particle density close to a boundary according to Hoy [Hoy, 1998]

6.3 Fibre orientation and effectiveness in test specimens

6.3.1 Effect of casting and compaction on fibre orientation and effectiveness

Visual observations during mixing and casting of test specimens can give an idea of the actual fibre orientation in the test specimen. In the past, photographic techniques have been used to provide additional information concerning the actual orientation.

One of the available methods to get a grasp on the fibre orientation is the x-ray technique, as was shown by Stroeven [Stroeven, 1978]. However, the problem with this technique is that it can only provide a two-dimensional representation of reality. Useful x-rays can only be made from thin slices, which causes it to be relatively expensive to carry out, and even then it is quite hard to quantify the effectiveness in efficiency factors.

Another way to try and get a grip on the fibre orientation is to perform photographic analyses of cut sections, as was done by Schönlin in the past [Schönlin, 1988]. He developed a method to determine the fibre orientation from photographs by calculating the orientation angles of individual fibres from the size of their cross-sections in the cut section.

Thanks to researchers like Stroeven and Schönlin, it is well accepted that casting and compaction by vibration of SFRC will generally result in an anisotropic matrix. Their work and that of others has shown that when casting test specimens, mould sides cause the fibres to initially orient themselves parallel to the wall or surface. Furthermore, as a result of external vibration, a preferred planar fibre orientation can dominate the fibre effectiveness, as has been shown by Edgington and Hannant [Edgington & Hannant, 1972]. Figure 6.6 shows a typical two-dimensional fibre orientation that was found after compaction by external vibration.

In addition to the planar-random orientation presented in Figure 6.6, the fibres also tend to sink down as a result of external vibration. In the scope of this research, this segregation was clearly observed after breaking the specimens and counting the fibres sticking out of the tested cross-sections. Soroushian and Lee [Soroushian & Lee, 1990] observed the same phenomenon in the past.

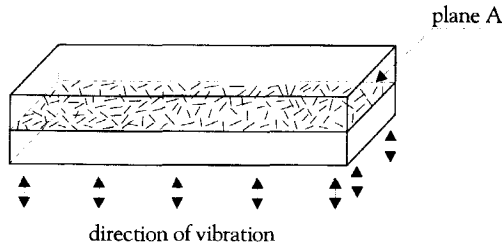


Figure 6.6 Planar-random fibre orientation after compaction by vibration [Edgington & Hannant, 1972]

Based on the early work of Edgington and Hannant [Edgington & Hannant, 1972], it is quite likely that a planar-random orientation also occurred in the beam specimens tested in the scope of this research. The specimens were rotated 90 degrees before testing so that a tendency to a 2D orientation, as illustrated in Figure 6.7, is expected.

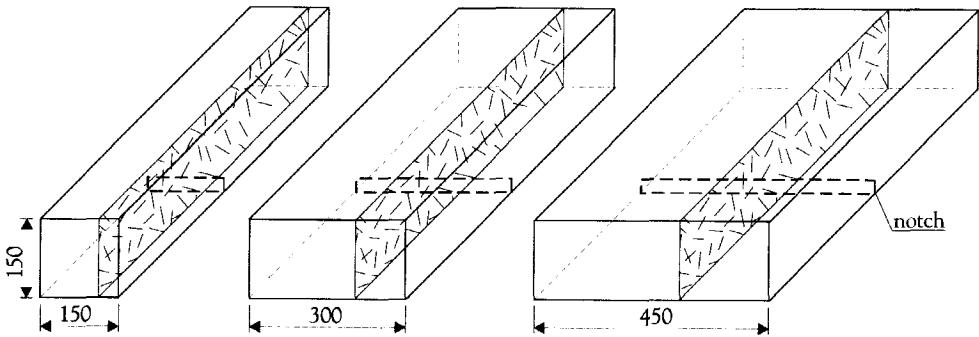


Figure 6.7 Assumed planar-random fibre orientation after compaction by vibration and rotation of test specimens

In case of a planar-random fibre orientation as illustrated in Figure 6.7, the mean fibre effectiveness would directly follow from equation (6.1) and be equal to $2/\pi$. However, as the previous section already showed, the boundary layers can affect the fibre orientation efficiency and the fibre density. Figure 6.8 shows to what extent the orientation efficiency in the cross-section above the notch is influenced by the boundary conditions, assuming that the fibre density is constant and is not affected by the geometrical boundaries in the external vibration process. As a result of the two-dimensional orientation, the orientation efficiency factor decreases from a value of 1 at the boundary to a planar-random value of $2/\pi$ at a distance L_c from the boundary

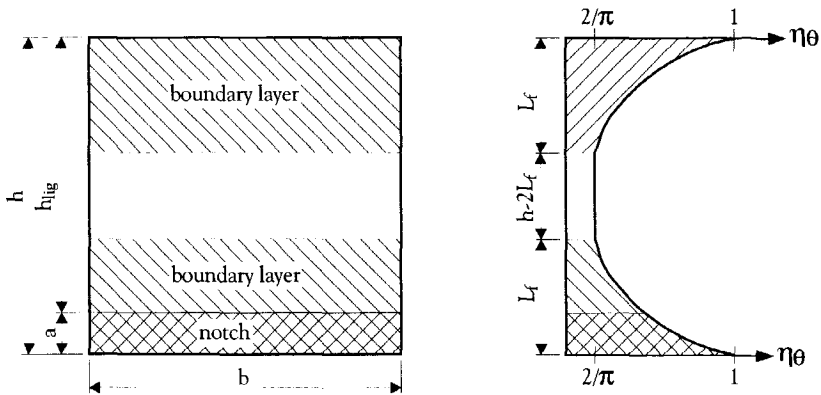


Figure 6.8 Influence of boundaries on fibre effectiveness after compaction by vibration and rotation of specimens

To determine the average effectiveness in the cross-section, it is advised to calculate the average orientation efficiency factor in the boundary layers. Based on equation (6.8), the average orientation efficiency factor in the upper boundary layer can be calculated as follows:

$$\eta_{\theta 2D,ave,ub} = \int_0^1 \int_0^1 \eta_{\theta 2D}(\alpha_o, \beta_o) \cdot d\alpha_o \cdot d\beta_o \quad (6.9)$$

Equation (6.9) results in an average effectiveness of the fibre reinforcement in the upper boundary layer of 75%. Obviously, the boundary layer is deeper, the longer the fibres. In case of the specimens tested in the scope of this research, the average orientation efficiency factor in the lower boundary layer depends on the notch depth to fibre length ratio a/L_f . As long as $0 < a/L_f < 1$, the average orientation efficiency factor in the lower boundary layer can be calculated as follows:

$$\eta_{\theta 2D,ave,lb} = \int_{\frac{a}{L_f}}^1 \int_0^1 \eta_{\theta 2D}(\alpha_o, \beta_o) \cdot d\alpha_o \cdot d\beta_o \quad (6.10)$$

Consequently, the average value of the fibre effectiveness in the cross-section of the specimens tested in the scope of this research can be expressed as follows:

$$\eta_{\theta,ave} = \frac{L_f \cdot \eta_{\theta 2D,ave,ub} + (h - 2L_f) \cdot \eta_{\theta 2D} + L_f \cdot \left(1 - \frac{a}{L_f}\right) \cdot \eta_{\theta 2D,ave,lb}}{h - a} \quad (6.11)$$

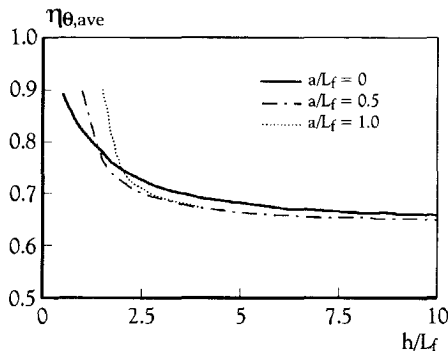


Figure 6.9 Average fibre orientation efficiency factor as a function of the beam depth to fibre length ratio assuming a boundary effect according to Figure 6.8

Equation (6.11) shows that the average value of the effectiveness is independent of the width of the specimens tested in this research. On the other hand, the beam depth and the fibre length are very important parameters. Figure 6.9 shows the average orientation efficiency factor as a function of the beam depth to fibre length ratio. It shows that the average orientation efficiency factor approaches the planar-random value of $2/\pi$ for a beam depth to fibre length ratio h/L_f over 7.5. Obviously, the orientation efficiency increases when h/L_f decreases, as the boundary layers become more dominant. Notice that at h/L_f values smaller than 2.5 the average orientation efficiency factor strongly increases.

With the help of Figure 6.9, the average orientation efficiency factor can be determined in case of the 30/0.5 and the 60/0.75 hooked-end steel wire fibres. In case of the 30/0.5 hooked-end steel wire fibres, h/L_f is equal to 5 so that the average orientation efficiency factor equals 0.66. The average orientation efficiency factor equals 0.70 in case of the 60/0.75 fibres, as h/L_f is 2.5.

6.3.2 Effect of fibre effectiveness on the flexural behaviour of SFRC

Comparison of experimental data with simulations based on theory

The previous section shows that when the effect of the production process of the specimens and the effect of the boundary conditions is predicted, the average orientation efficiency factor can be easily determined. But what is the effect of a preferred fibre orientation on the flexural behaviour?

As already mentioned in Chapter 5, the critical crack width w_0 in the bilinear post-cracking relation of the composite is supposed to be equal to the average projected embedment length of the fibres. The average projected fibre embedment length L'_{fe} can be determined as follows:

$$L'_{fe} = \eta_{\theta,ave} \cdot \frac{L_f}{2} \tag{6.12}$$

Table 6.1 shows the theoretically derived, average projected fibre embedment lengths, based on equation (6.12) and Figure 6.9, for the 30/0.5 and the 60/0.75 hooked-end steel wire fibres that were added to mix 2 of Table 3.3. For the reason of comparison, the empirically

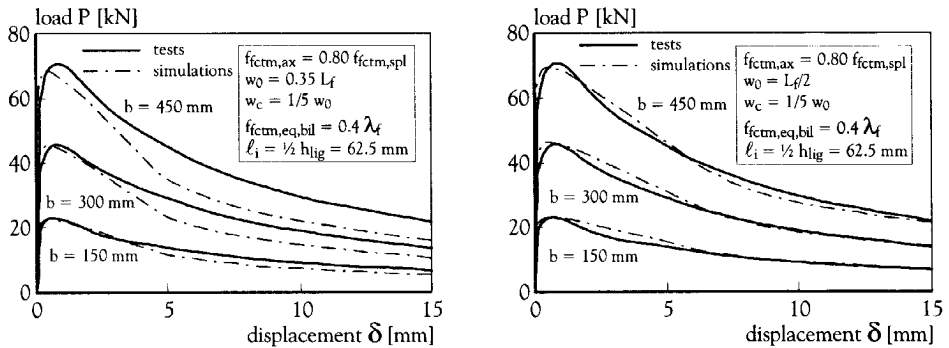
determined values of w_0 are also shown. These w_0 -values were determined in section 5.3.4 after inverse analyses of the mean test results.

In case of the 30/0.5 fibres, the theoretically derived L'_{fe} is equal to the w_0 -value that was found after inverse analyses of the experimental data in Chapter 5. Hence, the average projected embedment length seems to be a very good approximation of the critical crack width w_0 . However, in case of the SFRC with 60 kg/m^3 of 60/0.75 fibres, L'_{fe} does not fit the w_0 -value.

Table 6.1 Comparison between theoretically determined values of L'_{fe} and empirically determined values of w_0

Parameters	60 kg/m ³ hooked-end fibres with $L_f/d_f = 30/0.5$	60 kg/m ³ hooked-end fibres with $L_f/d_f = 60/0.75$
Theoretical L'_{fe}	$0.33 L_f$	$0.35 L_f$
Empirical w_0	$0.33 L_f$	$0.50 L_f$

In Figure 6.10 mean experimental results are compared to simulated results in case of the 60/0.75 fibre additions. The computations in Figure 6.10a are based on the theoretically derived L'_{fe} -value of $0.35 \cdot L_f$ for the critical crack width, while in Figure 6.10b the w_0 -value determined in section 5.3.4 was used as an input parameter.



(a) Theoretically determined w_0 from orientation efficiency (b) Empirically determined w_0 from inverse analysis

Figure 6.10 Comparison of simulated and experimental P - δ curves of 60 kg/m^3 60/0.75 hooked-end SFRC beams with various widths, using the theoretically determined orientation efficiency factor to determine L_f and the derived w_0 -value from inverse analyses from Chapter 5

Figure 6.10a shows that at large crack openings the simulated curves, which are based on the theoretically derived projection of the fibre embedment length, considerably underestimate the mean experimental results. Comparing these computed curves with the ones presented in Chapter 5 and again shown in Figure 6.10b, it shows that a w_0 -value higher than the theoretically determined value results in a better fit to the experimental curves, at least at large deformations. Based on this fact, it is hard to state that the average orientation efficiency factor and hence the projected fibre embedment length results in a good approximation of the critical crack width. On the other hand, it is obvious that the examined case is in a critical zone, as the beam depth to fibre length ratio h/L_f reaches the critical value of 2.5.

Figure 6.9 already showed that for beam depth to fibre length ratios smaller than 2.5 the fibre efficiency increases rapidly as a result of the boundary effect. However, this boundary effect was examined without taking any dynamic effects as a result of the external vibrations into account. Therefore, the boundary layers are restricted to a layer depth equal to the fibre length (see Figure 6.8). On the other hand, in case the effect of external vibration is accounted for, the depth of the boundary layer in which the fibre orientation is affected will most probably increase. If the latter is true, then the average orientation efficiency factor will be increased at a beam depth to fibre length ratio of 2.5.

Supposing that the actual orientation efficiency factor equals 0.85, Figure 6.11a once again compares simulated load-displacement diagrams with the experimental data. Although the measured load-displacement diagrams are slightly underestimated at larger crack widths, Figure 6.11b shows that the simulated curves approach the test results very well at smaller crack openings.

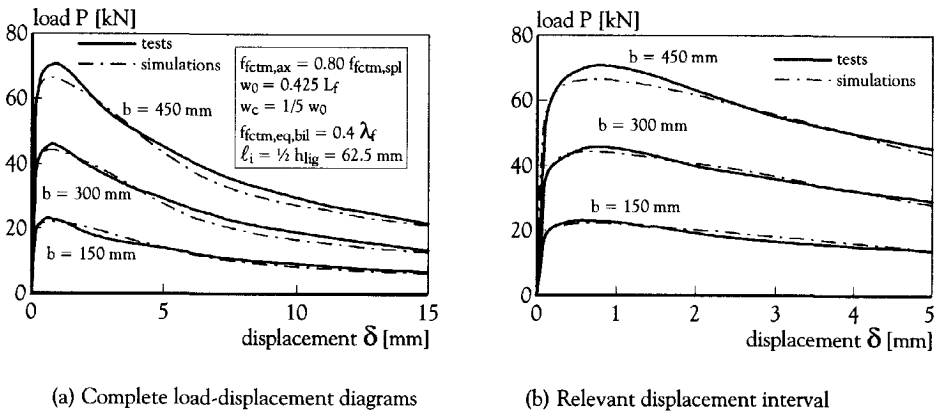


Figure 6.11 Comparison of simulated and experimental P- δ curves of 60 kg/m^3 60/0.75 hooked-end SFRC beams with various widths, using the estimated orientation efficiency factor η_θ to determine L'_{fe}

Discussion of theoretical approach

When calculating the average orientation factor, required to derive the average projected fibre embedment length, it was automatically assumed that all fibres in the cross-section equally contribute to the tensile component of the normal forces in the cross-section. This assumption, however, is only correct in case of a perfect uni-axial tensile test in which a parallel displacement of crack planes would occur. In contrast, three-point bending tests do not result in parallel displacements and, therefore, the fibres will not be equally stressed.

To check the effect of non-uniform fibre stressing, the two-dimensional orientation efficiency distribution shown in Figure 6.8 was programmed in the multi-layer simulation procedure. After simulating the bending behaviour once more, accounting for the complete 2D-orientation efficiency distribution, it became clear that the averaged orientation efficiency factor led to very accurate results, as the deviations between the computations with an average efficiency and the computations with a 2D efficiency distribution were negligible.

The second assumption that was made in calculating the averaged fibre efficiency factor concerned the fibre spacing. The fibre density was assumed to be constant in the cross-section, although Figure 6.5 showed that the geometrical boundaries definitely affect the fibre

density in the boundary layers. After testing the beams and counting the number of fibres, it was observed that the fibre density is higher in the vicinity of the boundaries, except near the casting surface as a result of segregation due to compaction by external vibration.

As the beams were rotated 90 degrees before testing, the effect of the difference in fibre density due to segregation seems negligible. In addition, the deformation-controlled tests performed, were based on the average of the measured displacements at the notch tip on both sides of the specimen. As for the effect of fibre spacing at the other two boundaries: the upper boundary is in the compressive zone and the lower boundary was notched (by sawing). As a result, their influence on the overall efficiency is very small.

6.4 Fibre orientation and efficiency in promising practical applications

Obviously, the average orientation efficiency is an important parameter in the development of suitable and reliable material relation for structural design. The previous section showed in a quantitative way that the production process of test specimens and the dimensions of the cross-sections in relation to the fibre length strongly influence this orientation efficiency factor. In addition, it showed how the average orientation efficiency factor influences the bilinear post-cracking relation and as a result the flexural behaviour of test specimens. It seems therefore of great importance to translate the average orientation efficiency in 'standard' test specimens to the fibre effectiveness in structural applications.

As the fibre orientation in practice depends on the way of casting and compaction, it is necessary the gain insight into the production processes of specific structural applications. From these production processes the preferred fibre orientation can be determined, after which the average orientation efficiency can be derived. In the scope of this research two types of promising structural applications were assessed: underwater concrete slabs and prefabricated tunnel segments.

Fibre orientation and orientation efficiency in underwater concrete slabs

As stated before, it is important to assess the production process to see and understand how the fibres tend to orient before making statements on the orientation efficiency. In case of underwater concrete slabs, Vos and Jager [Vos & Jager, 1993] distinguish two different methods of placing:

- The monolith method: a concrete mix, adjusted to the specific circumstances, is pumped and poured under water with the help of specially designed material.
- The injection method: a layer of coarse aggregates is applied on the bottom of the excavated building pit after which a mortar is injected through pipes.

In this case study, the monolith method was used to construct an underwater SFRC slab at the construction site of the Botlek railway tunnel near Rotterdam in the Netherlands. To receive the Tunnel Boring Machine (TBM) that was used to bore two separate tubes, a relatively deep construction pit had to be constructed. As a result of this large depth and the short construction time available a type of foundation was chosen that was expected to result in relatively large upward deflections. Preliminary design calculations based on properties of plain underwater concrete demonstrated that a conventional concrete mix did not answer the structural demands. Therefore, an experimental programme was carried out in which:

1. A SFRC mix was designed and tested to obtain a mix composition, answering demands concerning workability and strength; a good SFRC mix for underwater concrete needs to exhibit a certain mobility to have the capacity to flow in horizontal direction after pouring, since compaction under water is not possible.
2. The production process was tested in practice to gain insight into the practical behaviour of the mix. To test the mobility of the mixture in practice and gain experience with mixing and pumping of SFRC, the contractor placed the concrete in an excavated basin that was filled with water. The basin was 1 meter deep and had a ground surface of $3 \times 10 \text{ m}^2$. The concrete matrix was reinforced with 30 kg/m^3 of hooked-end steel wire fibres ($L_f/d_f = 60/0.75$). The SFRC mix was placed on one side of the basin (see Figure 6.12) and was slowly pumped from two different truck mixers resulting in two layers of concrete. The mean cube compressive strength of the concrete mix used in this test was 40 N/mm^2 .

After placing the underwater SFRC, cylindrical cores were drilled according to Figure 6.12 to check the concrete quality. The outer perimeter of the cylinders did not show any sign of the poured layers and only at the toe of the basin some silt formation was observed on the bottom side of the drilled core (see E2 in Figure 6.13). From the outer perimeter, however, it was impossible to conclude anything about the amount of fibres and whether or not the flow direction had influenced the average fibre orientation.

Therefore, the cylinders were crushed so that the weight of the fibre addition could be determined. Knowing the fibre volume and fibre type added, the number of fibres can be easily determined. According to the tests, mean fibre weight of 33.46 kg/m^3 was found with a standard deviation of 6.63 kg/m^3 .

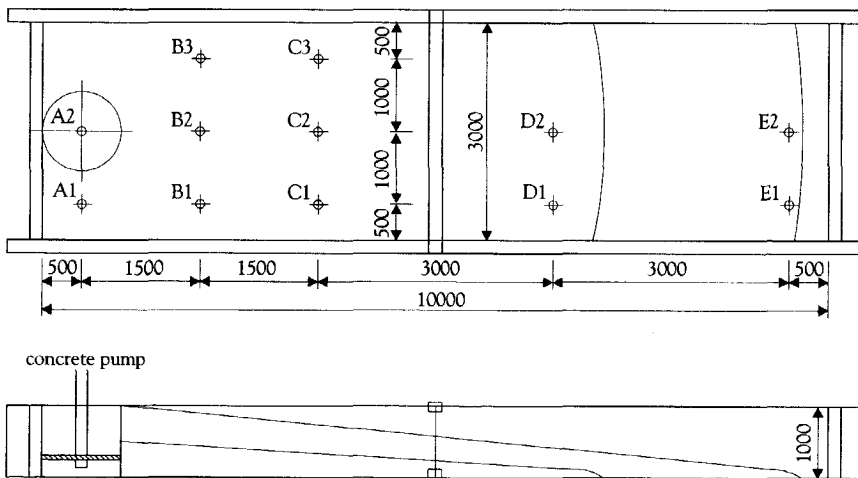


Figure 6.12 Testing basin (dimensions in mm) for placement of steel fibre reinforced underwater concrete slab (Source: Boortunnelcombinatie BTC)

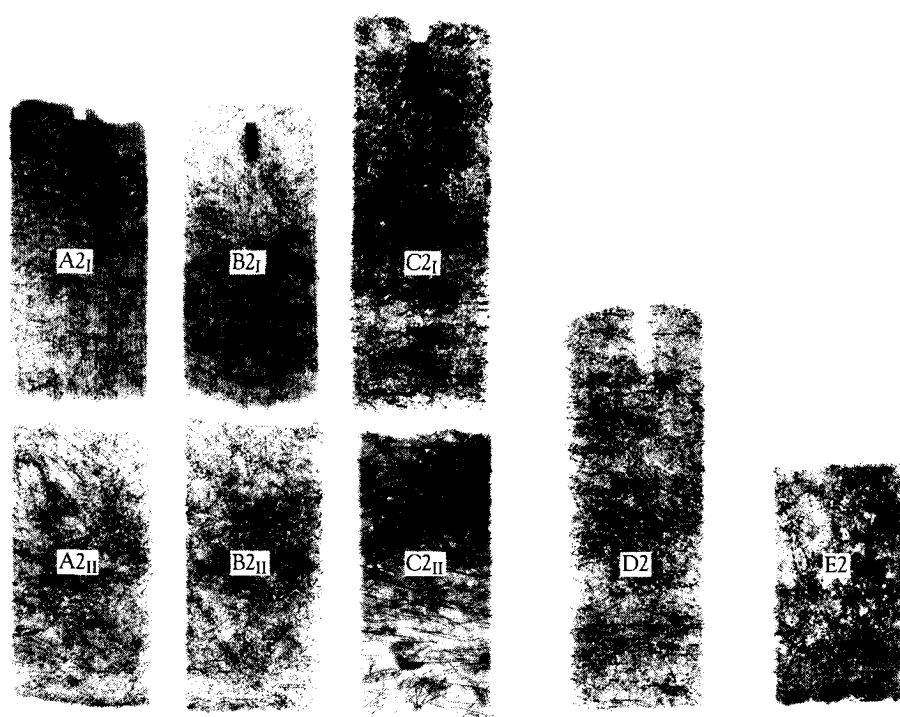


Figure 6.13 X-ray recordings of steel fibre orientation in cylinders cored from underwater concrete test slab

To check the fibre orientation, the contractor decided to use x-ray photography. Four millimetre thick slices were cut from the bored cylinders and photographs were taken before they were crushed to determine the fibre volume. Figure 6.13 shows the x-ray photographs of the slices cut from cylinders A2, B2, C2, D2 and E2 of which the positions are marked in Figure 6.12. For practical reasons, the first three cores were broken in two pieces.

Underneath the valve (A2) the fibres seem to have spatial-random orientation, but at larger distances (C2, D2) from the valve the fibres tend to prefer a planar-random orientation. It seems as if the fibres tend to orient in the flow direction and thus in plane with the slab. As a result, the effectiveness of the fibre reinforcement will be increased, since the flexural tensile stresses in reality are expected to occur in plane with the slab.

Comparing the design value of the orientation efficiency factor in underwater concrete slabs to the one found in 'standard' test specimens, it is obvious that the mean effectiveness in slabs is smaller than the one found in 'standard' beam specimens. In the design stage, this might lead to an overestimation of the bending capacity of steel fibre reinforced underwater concrete slabs. Figure 6.14 shows the result of multi-layer simulations of three point bending tests on 'standard-size' specimens in case of a unidirectional, a planar-random and a spatial-random fibre orientation. Obviously, the effect of a preferred fibre orientation on the bending capacity of the cross-section is quite small. However, the post-cracking behaviour is considerably affected. The latter is important in the analysis of statically indeterminate SFRC structures, since the ultimate load carrying capacity is strongly influenced by the structure's capacity of redistributing stresses after crack initiation.

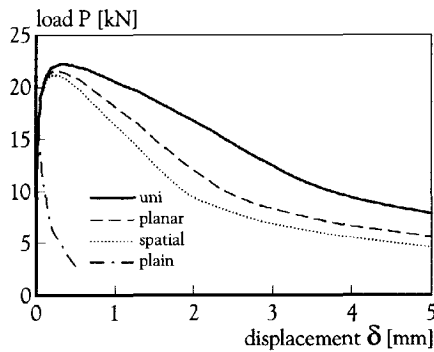


Figure 6.14 The effect of the orientation efficiency in beam specimens on the flexural behaviour of SFRC

It is difficult to conclude what is the actual effect of a possible overestimation of the post-cracking strength of the SFRC under consideration, because a steel fibre reinforced underwater concrete slab is a statically indeterminate structure. In such a structure a redistribution of stresses is expected to occur in the cross-section after the load at first crack is reached and the first plastic hinge is created. Subsequently, the external load can be increased, until the ultimate bending capacity of the cross-section is reached or another crack has occurred as a result of redistribution of stresses in the structure. In multiple statically indeterminate structures, such as SFRC slabs, the latter is quite likely to occur and will repeat itself until the last plastic hinge (or yield line) is created and the ultimate load is reached. Simulations on a structural level will most probably provide more insight, but the application of SFRC in underwater concrete slabs is expected to increase the ultimate load capacity. The latter might result in a reduction of the slab thickness or even in an increase in pile distance. However, the author doubts whether a reduction in slab thickness (of several centimetres) can be really managed at the building site.

Fibre orientation and orientation efficiency in prefabricated tunnel segments

Another example of a statically indeterminate structure is a tunnel structure, constructed with the help of a Tunnel Boring Machine (TBM). In the Netherlands this type of tunnelling is fairly new. Submerged tunnelling and cut-and-cover methods have been used in the past, mostly because of economic reasons. Nowadays, however, bored tunnelling is becoming more and more interesting in the densely populated urban areas. For that reason, the Dutch Government designated the 2nd Heineoord and the Botlek tunnel as pilot projects to gain knowledge and experience in tunnel boring techniques.

During construction of the 2nd Heineoord tunnel, the Civil Engineering Department of the Directorate-General of Public Works and Water Management wanted to investigate the applicability of SFRC in tunnel linings. After a literature survey [Kooiman, 1996] that indeed proved its applicability, the feasibility of applying several SFRC tunnel rings in the 2nd Heineoord Tunnel was investigated. Experimental research [Kooiman, 1997] was carried out at the Stevin Laboratory of the Delft University of Technology and the TNO Research Institute to support design calculations. The final design [Kooiman, 1997] showed that in this case 60 kg/m³ of high carbon steel fibres could replace the conventional reinforcement mesh. As a result, the Civil Engineering Department of the Directorate-General of Public Works and

Water Management ordered the joint venture of contractors that was involved in the complete research project, to produce 112 SFRC tunnel segments and 16 keystones for a pilot section of 25 meters.

The author recognised the following five stages in the production process of the segments:

1. Mixing
2. Casting and Compacting
3. Finishing
4. Demoulding
5. Storage

Only the first three stages are of any interest when considering the influence of the production process on the fibre distribution and orientation.

Mixing Stage

An important aspect of SFRC, especially with respect to the fibre orientation, is the workability of the mixture. In case of the prefabricated SFRC segments for the 2nd Heineoord Tunnel the mixture needed to be quite stiff because the moulds rotated in a production carousel. Table 6.2 shows the composition of the applied mixture. The glued steel fibres were added manually to the aggregates before mixing. In case of a large-scale application the steel fibres should be added automatically. After mixing the cement, a part of the water content and some additives the steel fibres were added together with the aggregates. Mixing time was prolonged from 3 minutes for the conventional mixture to 5½ minutes for the SFRC to ensure a homogeneous fibre distribution. The mixture was then transported to the casting location via a conveyor belt where it was poured into a small storage unit.

Table 6.2: SFRC mix composition used in prefabricated tunnel segments [Kooiman, 1998]

<i>Mix components</i>	<i>Quantity</i>
Portland cement CEM I 52.5	87.5 kg/m ³
Blast furnace cement CEM III/B 52.5	262.5 kg/m ³
Sand 0-4 mm	43 %
Gravel 4-16 mm	57 %
High strength hooked-end steel fibres ($L_f/d_f = 60/0.75$)	60 kg/m ³
Superplasticiser	1.4 % (relative to cement)
Water/cement ratio	0.42

Casting and compacting the segments

From the storage unit the SFRC mixture was supposed to drop on a short conveyor belt from which the mixture should be poured into the mould. Initially some problems arose underneath the storage unit where the stiff mixture choked up the opening between this unit and the conveyor belt. After adjusting the openings, the production process progressed without any more delays and the 118 segments were cast within two weeks.

Before the production process started, a casting test was carried out. It suggested a certain preference orientation to occur as a result of the pouring direction and shape of the mould. In the past, Casanova et al. [Casanova et al., 1995] already proved that there is no spatial-random orientation of steel fibres when applied in prefabricated tunnel segments. The latter was confirmed by the author [Kooiman, 1997], who performed tensile splitting tests on drilled core specimens, tested with the direction of the applied load according to Figure 6.15.

The test results showed that the quality of the composite material varied considerably over the segment's thickness. Obviously, the matrix is stronger at the mould side than at the casting surface. This can be explained by the fact that bleeding occurred during compaction. As a consequence, the water-binder ratio in the upper layers increased, causing a decrease in strength. In addition, the fact that the mould is filled in layers and that after each layer the vibration motors were activated for compaction might have intensified the degradation in strength. Since the first layer placed is compacted more often than the last, the matrix quality on the outer perimeter of the segment is lower than at the inner perimeter. Moreover, the steel fibres in prefabricated tunnel segments tend to segregate due to compaction by vibration, just like the fibres segregated after vibrating the test specimens in the laboratory.

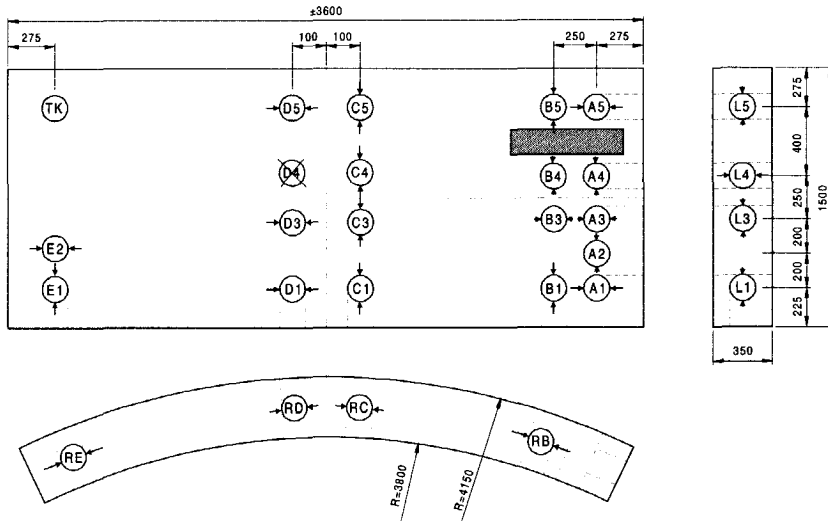


Figure 6.15 Layout of drilled core cylinders from prefabricated tunnel segment (dimensions in mm)

The effect of the casting and compaction process on the fibre orientation is visualised by Figure 6.16. It shows the effect of the geometrical boundaries on the short sides of the mould just after placing the first layer and the situation after compaction by vibration.

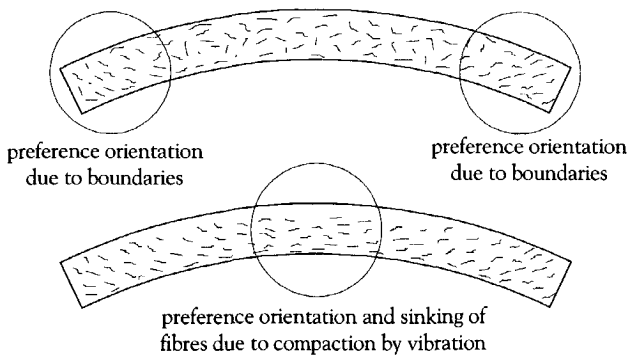


Figure 6.16 Effect of casting and compaction on the fibre orientation

Finishing the surface

Finishing the concrete surface proved to be more difficult for SFRC than for concrete mixtures without fibres. Because the fibres hooked behind the screed board the concrete surface of the segments was ripped open during levelling. Although scouring can produce a relatively smooth surface, several fibres can still penetrate the surface. However, most of the fibres in the boundary layer near the casting surface will be orientated parallel to the surface.

It is obvious that a homogeneous fibre distribution and orientation not occurred in the prefabricated SFRC segments for the 2nd Heinenoord Tunnel. This would not really matter in case the segments would have been subjected to only one single loading condition in one single direction. Unfortunately, this is not the case. Tunnel segments are subjected to various loads in different directions in multiple stages. For each loading condition, however, the fibre efficiency can be determined. This will be shown in Chapter 8.

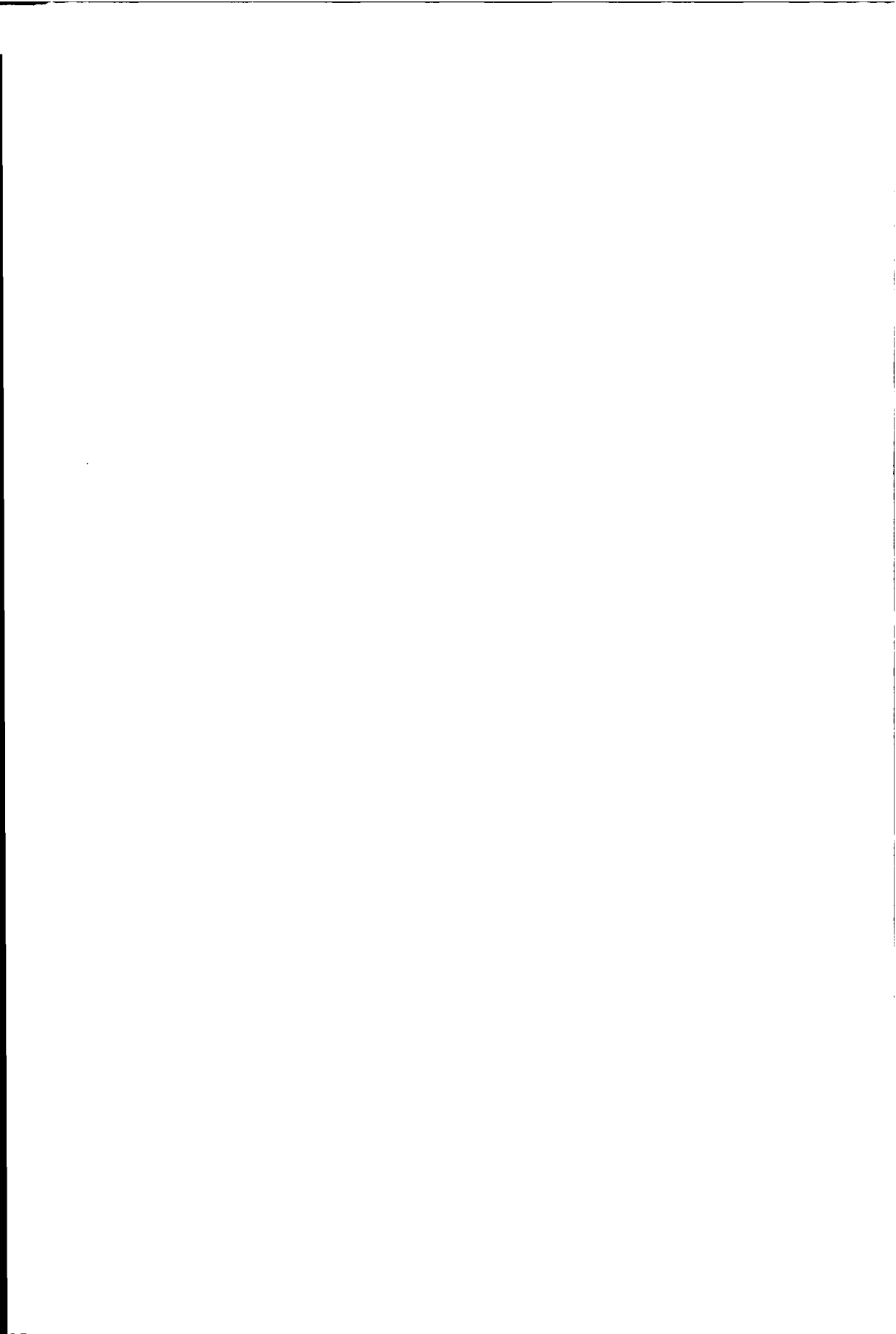
6.5 Concluding remarks

The orientation of steel fibres in concrete may be random after dispersion in the mixer, but this will not necessarily be the case after the material is placed into the mould or is discharged on site.

Based on both theoretical predictions and experimental findings, the overall orientation efficiency factor η_θ in horizontally cast test specimens, subjected to externally vibration and rotated 90 degrees before testing, depends on the beam depth to fibre length ratio h/L_f . For h/L_f over 7.5, η_θ approaches the planar-random value of $2/\pi$. For values smaller than 2.5, the fibre effectiveness approaches the uni-directional value ($\eta_\theta \approx 1$).

The fibre orientation in underwater SFRC is non-uniform. Depending on the flow distance the fibre orientation is in between a spatial-random and a planar random distribution. The average orientation efficiency factor is therefore somewhere in between $1/2$ and $2/\pi$. Although the effect of the fibre orientation efficiency on the ultimate bending capacity of a SFRC cross-section is relatively small, the post-cracking behaviour is strongly affected. This will most probably have an effect on the load-bearing capacity of the statically indeterminate structure, as the redistributing capacity of a cracked cross-section is considerably influenced by the fibre efficiency. In the design of SFRC slabs, it is therefore advised to assume a spatial random orientation of the steel fibres.

A much more complex situation was encountered after the production of prefabricated tunnel segments. The orientation was found to vary significantly over the segment. Due to this orientation but also as a result of the direction of the applied loads, the fibre efficiency in tunnel segments varies between 0 and 1.



Chapter 7

Reliability in design of SFRC structures

7.1 Introduction

All design guidelines on concrete structures contain a section on material properties of concrete, such as section 3 in the European prestandard Eurocode 2 [ENV 1992-1-1, 1991]. The design value of a material property is generally defined as the characteristic or representative value divided by the material safety factor for that particular material property.

According to Eurocode 1 [ENV 1992-1-1, 1994], the characteristic value corresponds to a fractile in the assumed statistical distribution of the particular material property, specified by relevant standards and tested under specified conditions. Usually, the characteristic value is determined by calculating the strength value corresponding to the lower 5% fractile in the distribution.

The material safety factor is assumed to take into account all differences between the strength of the structural material from test results and its strength in situ. The Dutch design regulations for concrete structures [NEN 6720, 1991] prescribe a material safety factor $\gamma_{cc} = 1.2$ for concrete in compression and $\gamma_{ct} = 1.4$ for concrete in tension, whereas Eurocode 2 defines one value for both properties ($\gamma_{cc} = \gamma_{ct} = 1.5$).

In this chapter the safety philosophy for application in structural design is explained in four steps. Firstly, it is explained how to determine characteristic values. The RILEM Technical Committee 162-TDF [RILEM TC 162-TDF, 2000] recommended a procedure to determine characteristic values for the post-cracking strength by means of statistical theories. Based on this procedure, the effect of the coefficient of variation on the characteristic value is determined.

Secondly, three common methods are described to enhance the reliability in structural design. One of these methods is a semi-probabilistic design approach to calculate partial safety factors. In this chapter, it is used to determine the effect of the coefficients of variation on the partial safety factors.

In the third step, the effect of scatter in the post-cracking behaviour on the design values is analysed. The influence of the coefficient of variation is determined by comparing load-displacement curves simulated with mean and design values of the input parameters of the bilinear post-cracking relation from Figure 5.24. In addition, the design curves of the different mixtures, tested in this research, are compared for a varying probability of failure.

Finally, some remarks are made on how to manage quality control in case of applying SFRC in practice.

7.2 Determination of characteristic values

7.2.1 Statistical parameters of physical variables

Before determining the characteristic values of the strength parameters in the bilinear post-cracking relation of Figure 5.24, it is advised to examine the uni-axial tensile strength $f_{ct,ax}$ and the equivalent post-cracking strength $f_{ct,eq,bil}$ as stochastic variables. Stochastic variables can be described by three statistical parameters: the probability density function (PDF), i.e. the distribution type of the stochastic variable, the mean value of the population and the corresponding standard deviation.

As the distribution of a stochastic variable determines the outcome of any statistical analysis, the choice of the type of distribution is of major importance. A probability density function of a stochastic variable can be easily derived by using frequency techniques on a large number of test data. However, the number of statistical data is often so small that the type of distribution needs to be estimated. In the scope of this dissertation, the number of statistical data is also very small, as each test series consisted of only six repetitions. Therefore, the exact distribution can not be determined.

Statistical distributions often have theoretical backgrounds. Hence, specific distribution types are applied to describe particular phenomena. For example, normal distributions are used to describe the sum of a large number of stochastic variables. On the other hand, lognormal distributions are used to describe the distribution of a phenomenon that arises as the result of a multiplicative mechanism acting on a number of factors. The latter type of distribution is often used to describe strength properties of plain concrete.

In case of a bilinear post-cracking behaviour of SFRC, as shown in Figure 5.24, the stochastic variables are the uni-axial tensile strength $f_{ct,ax}$ at $w=0$ and the equivalent post-cracking strength $f_{ct,eq,bil}$ at w_c . In reality, the characteristic crack width w_c and the critical crack width w_0 are also stochastic variables, as they depend on the orientation efficiency factor η_θ , which is influenced by the methods of placing and compaction and the vicinity of geometrical boundaries. However, as shown Chapter 6, it is possible to determine the effect of these influencing parameters on η_θ . It is therefore supposed that the average orientation efficiency factor is a deterministic parameter.

As in the case of strength values of plain concrete, the equivalent post-cracking strength $f_{ct,eq,bil}$ of SFRC is a variable that can be expressed as the product of a number of random variables. This was demonstrated by equations (5.1) to (5.3) in Chapter 5. It is supposed, therefore, that a lognormal distribution applies for the equivalent post-cracking strength $f_{ct,eq,bil}$ of SFRC. The general expression of a variable of resistance R is as follows:

$$R = Y_1 Y_2 \dots Y_n \quad (7.1)$$

Since Y_i is a random variable, the function $\ln Y_i$ is also a random variable. After taking the natural logarithms of both sides, the result is as follows:

$$\ln R = \ln Y_1 + \ln Y_2 + \dots + \ln Y_n \quad (7.2)$$

Calling upon the central limit theorem, one may predict that the sum of a number of lognormal variables will be approximately normally distributed [Benjamin & Cornell, 1970]. To estimate a confidence interval for the mean value of such a normal population, the t-test provides a powerful tool. It is valid for any sample size and is a good approximation, even though the actual population of R is non-normal [Crow et al., 1960]. It can be used to determine a confidence interval for the mean value of a population from a small sample, such as the test series in the scope of this research. According to the t-distribution, the $(1-\alpha)\cdot 100$ percent two-sided confidence interval of a sample statistic \bar{R} with sample size n , is:

$$\bar{R} - \frac{s_R}{\sqrt{n}} \cdot t_{\alpha/2, n-1} \leq m \leq \bar{R} + \frac{s_R}{\sqrt{n}} \cdot t_{\alpha/2, n-1} \quad (7.3)$$

with s_R as the standard deviation of random variable R :

$$s_R = \frac{\sqrt{\Sigma(R_i - \bar{R})^2}}{n-1} \quad (7.4)$$

and $t_{\alpha/2, n-1}$ according to statistical tables. For $\alpha = 20\%$, the confidence interval is illustrated in Figure 7.1.

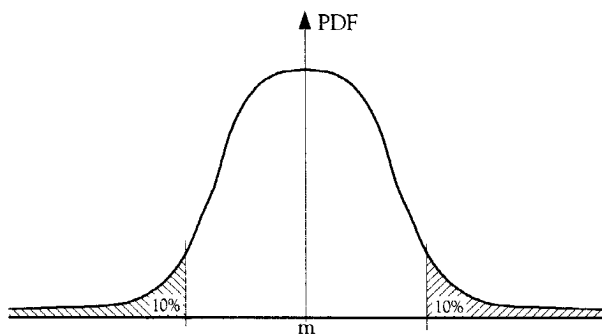


Figure 7.1 Two-sided confidence interval of a normally distributed sample statistic

7.2.2 Effect of the coefficient of variation on the characteristic strength values

As the previous section showed, the t-test can be used to determine a confidence interval for the mean value of a population from small samples. In the recommendations on test and design methods for SFRC of the RILEM Technical Committee 162-TDF [RILEM TC 162-TDF, 2000], this statistical method is also used to determine characteristic values for the post-cracking strengths. As it was already mentioned in section 4.2.3, the RILEM Committee recommends the following equation to calculate the characteristic value $f_{fctk,eq}$ of the equivalent post-cracking strength:

$$f_{fctk,eq} = f_{fctms,eq} - \frac{s_f \cdot t_{10, n-1}}{\sqrt{n}} - 1.645 \cdot s_f \cdot \left(1 + \frac{s_f \cdot t_{10, n-1}}{f_{fctms,eq} \cdot \sqrt{n}}\right) \quad (7.5)$$

In fact, the characteristic value is calculated as the lower value of the one-sided confidence interval of the 5%-fractile:

$$f_{fctk,eq} = f_{fctm,eq} - 1.645 \cdot s_f \tag{7.6}$$

However, in equation (7.6), the t-test is used to define the lower value of the 80% confidence interval as the mean equivalent tensile strength $f_{fctm,eq}$ of the population, calculated with the help of statistical parameters s_{fs} and $f_{fctms,eq}$ from the sample, consisting of n test results:

$$f_{fctm,eq} = f_{fctms,eq} - \frac{s_{fs} \cdot t_{10,n-1}}{\sqrt{n}} \tag{7.7}$$

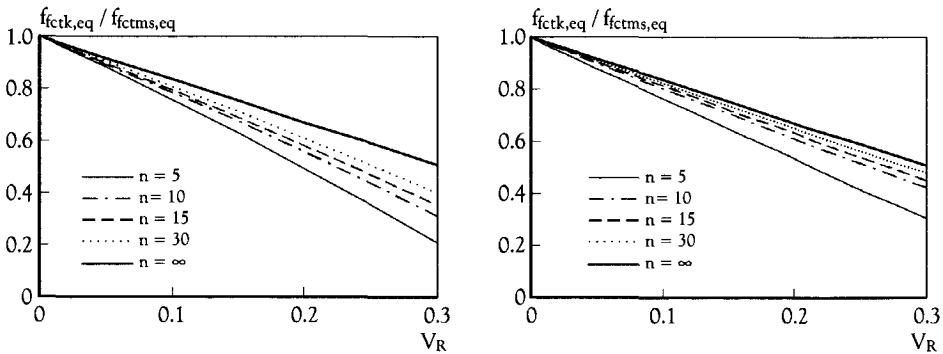
In the second term of equation (7.6), s_f is the standard deviation of the population. This standard deviation s_f is defined as the upper value of the 80% confidence interval:

$$s_f = s_{fs} \cdot \left(1 + \frac{s_{fs} \cdot t_{10,n-1}}{f_{fctms,eq} \cdot \sqrt{n}}\right) \tag{7.8}$$

To determine the effect of the coefficient of variation V_R on the characteristic value of the equivalent strength in the post-cracking behaviour, both arguments of equation (7.5) are divided by $f_{fctms,eq,bil}$.

$$\frac{f_{fctk,eq,bil}}{f_{fctms,eq,bil}} = 1 - \frac{V_R \cdot t_{10,n-1}}{\sqrt{n}} - 1.645 \cdot V_R \cdot \left(1 + \frac{V_R \cdot t_{10,n-1}}{\sqrt{n}}\right) \tag{7.9}$$

The above mentioned approach is quite conservative. Not only the lower value of the 80% confidence level is used for the mean value of the population, but it is also assumed that the standard deviation of the population s_f is higher than the standard deviation of the sample.



(a) $f_{fctk,eq}$ according to [RILEM TC 162-TDF, 2000]

(b) $f_{fctk,eq}$ according to Eurocode 1

Figure 7.2 Effect of the coefficient of variation V_R and the number of samples n on characteristic strength values

Based on equation (7.5), Figure 7.2a shows the effect of the coefficient of variation V_R on the characteristic value of the equivalent post-cracking strength $f_{ctk,eq}$. Obviously, this value decreases as the coefficient of variation increases. The sample size determines the slope of the decreasing lines.

Figure 7.2b shows the effect of the coefficient of variation V_R on the characteristic value of the equivalent post-cracking strength $f_{ctk,eq,bil}$ according to the following equation:

$$\frac{f_{ctk,eq,bil}}{f_{ctms,eq,bil}} = 1 - V_R \cdot t_{10,n-1} \cdot \sqrt{1 + \frac{1}{n}} \quad (7.10)$$

Instead of the frequency approach used in equation (7.5), the much simpler and less conservative Bayesian technique is applied in Equation (7.10). This approach is also described in Eurocode 1 for situations, in which V_R is not known, but must be estimated from the sample. This equation will be used hereafter for the determination of characteristic values.

7.3 Probabilistic design in general

7.3.1 Standard reliability methods

It is common practice to express structural reliability by the probability of failure. The probability of failure, however, depends on many factors related to the occurrence of particular limit states. With the help of limit states it is possible to define so-called performance functions. In the case of civil structures, the following performance function, or limit state function, is often applied:

$$Z = R - Q \quad (7.11)$$

In the performance function, the resistance R and load Q are stochastic variables. Hence, both R and Q are characterised by their distribution types, means and standard deviations. Figure 7.3 shows the example of the performance function Z for two normally distributed variables R and Q .

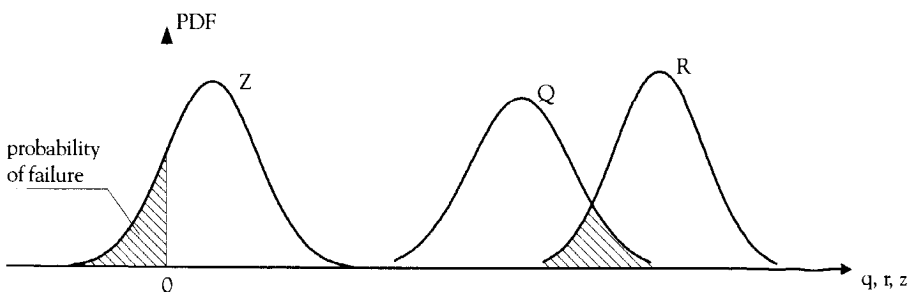


Figure 7.3 PDF's of load Q , resistance R and performance function Z

The reliability of a structure or structural element depends on the margin between resistance to failure and the load that causes failure. The methods used to calculate this margin can vary. According to CUR-report 190 [CUR-report 190, 1997], it is possible to distinguish three levels of calculation methods:

- Level III: The available calculation methods in level III, such as Monte Carlo sampling and Numerical Integration, are the most sophisticated methods to calculate the exact probability of failure. These methods take the exact probability density function (PDF) of all strength and load variables into account.
- Level II: Level II methods can also be used to determine the probability of failure, but do not take the exact PDF's into account. On this level, the PDF of each variable is estimated using an equivalent normal distribution function so that the probability of failure can be estimated in an analytical manner.
- Level I: A level I calculation is the design method according to regulations. In such a calculation it is only checked whether or not there is a margin between the representative values of the strength and loads. In practise this is often done by means of partial safety factors.

Level III reliability methods

Calculating the probability of failure according to a level III method leads to a fundamental solution. It is based on a mathematical expression of the probability of occurrence that says that failure occurs when:

$$Z = R - Q < 0 \tag{7.12}$$

When the joint probability density function $f_{R,Q}(r,q)$ of the resistance R (strength) and load Q is known, the probability of failure can be calculated as follows:

$$P_f = \iint_{Z < 0} f_{R,Q}(r,q) \cdot dr \cdot dq \tag{7.13}$$

Because $Z < 0$ when $R < Q$:

$$P_f = \int_{-\infty}^{\infty} \int_{-\infty}^Q f_{R,Q}(r,q) \cdot dr \cdot dq \tag{7.14}$$

If the resistance and load are stochastically independent, equation (7.14) becomes:

$$P_f = P(Z < 0) = \int_{-\infty}^{\infty} (1 - F_Q(r)) \cdot f_R(r) \cdot dr = 1 - \int_{-\infty}^{\infty} F_Q(r) \cdot f_R(r) \cdot dr \tag{7.15}$$

in which $F_Q(r)$ is the cumulative density function (CDF) of the load.

In case R and Q are stochastically independent and normally distributed variables, equation (7.15) can be solved analytically. For other types of distributions, the integration requires special numerical techniques. Numerical Integration and Monte Carlo Sampling techniques are well-known procedures to solve equation (7.15).

Level II reliability methods

In practice the probability of failure is often calculated indirectly, using Level II procedures. One of those procedures is a First Order Reliability Method (FORM), in which the performance function Z is linearised in the so-called design point. It means that the limit state function is assumed to be a normal distribution function, which forms a straight line on normal probability paper. A linear approximation in the design point will be accurate in cases of linear or relatively flat limit state functions. When the limit state function is not linear, there are other, more advanced techniques to perform reliability calculations. In case of a linearised limit state function, the mathematical expression is as follows:

$$Z = a_1X_1 + a_2X_2 + \dots + a_nX_n + b \quad (7.16)$$

The expected value μ_Z and standard deviation s_z of the limit state function can be determined with the help of the following equations:

$$\mu_Z = a_1\mu_{X_1} + a_2\mu_{X_2} + \dots + a_n\mu_{X_n} + b \quad (7.17a)$$

$$s_z = \sqrt{[\sum a_i a_j \text{cov}(X_i X_j)]} \quad (7.17b)$$

When the variables X_1, X_2, \dots, X_n are normally distributed, the performance function Z is also normally distributed. Then, the probability of failure P_f can be calculated with the help of the standard normal distribution:

$$P_f = P(Z < 0) = \Phi\left[\frac{(0 - \mu_Z)}{s_Z}\right] = \Phi\left[-\frac{\mu_Z}{s_Z}\right] = \Phi[-\beta] \quad (7.18)$$

The ratio of the expected value μ_Z and standard deviation s_z of the limit state function Z is also called the reliability index β . Therefore, the reliability index can also be expressed in terms of μ_R and μ_Q and the standard deviations s_R and s_Q :

$$\beta = \frac{\mu_R - \mu_Q}{\sqrt{s_R^2 + s_Q^2}} \quad (7.19)$$

Table 7.1 provides indications of how β varies with P_f and vice versa.

Table 7.1 Reliability index β corresponding to probability of failure P_f

P_f	β	P_f	β	P_f	β
10^{-1}	1.28	10^{-4}	3.71	10^{-7}	5.19
10^{-2}	2.33	10^{-5}	4.26	10^{-8}	5.62
10^{-3}	3.09	10^{-6}	4.75	10^{-9}	5.99

Hasofer and Lind [Hasofer & Lind, 1974] introduced the reduced variables Z_R and Z_Q to convert all random variables to their 'standard form':

$$Z_R = \frac{R - \mu_R}{s_R} \tag{7.20a}$$

$$Z_Q = \frac{Q - \mu_Q}{s_Q} \tag{7.20b}$$

Subsequently, they expressed the resistance R and load Q in terms of the reduced variables:

$$R = \mu_R + Z_R s_R \tag{7.21a}$$

$$Q = \mu_Q + Z_Q s_Q \tag{7.21b}$$

The limit state function then becomes:

$$g(Z_R, Z_Q) = (\mu_R - \mu_Q) + Z_R s_R - Z_Q s_Q \tag{7.22}$$

In the context of this level II procedure, the reliability index derived from equation (7.19) is nothing more than the mathematical expression of the shortest distance from the origin of reduced variables Z_R and Z_Q to the line $g(Z_R, Z_Q) = 0$, as illustrated in Figure 7.4.

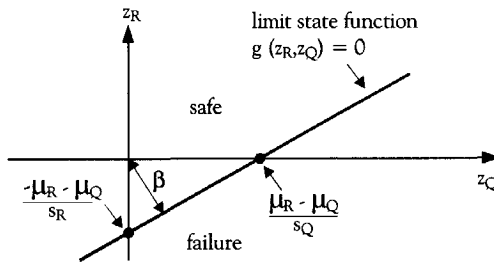


Figure 7.4 Reliability index defined as the shortest distance in the space of reduced variables

By definition, level II methods are performed on a component level or on single failure modes. Structural reliability analysis covers the complete failure domain. The difficulty is to identify the system of failure modes and to compute the system's reliability index. The probability of failure of the structural system can be evaluated, given the reliability of the separate failure modes. The structural system satisfies the safety demands, as long as:

$$P(Z < 0) \leq \Phi[-\beta] \tag{7.23}$$

According to ISO 2394 [7.9], the safety demands are satisfied when the design value of the load Q_d is smaller than the design value of the strength R_d . According to Eurocode 1 [7.2], both design values are chosen in such a way that they satisfy the following demands:

$$P(Q > Q_d) = \Phi(-\alpha_Q \beta) \quad (7.24a)$$

$$P(R < R_d) = \Phi(-\alpha_R \beta) \quad (7.24b)$$

For $\alpha_Q = s_Q/s_Z$ and $\alpha_R = s_R/s_Z$ and assuming a normal distribution function for stochastic variable Q , the design value of the load Q_d is determined:

$$Q_d = \mu_Q + \alpha_Q \beta s_Q = \mu_Q (1 + \alpha_Q \beta V_Q) \quad (7.25)$$

The design value of the resistance is determined assuming a lognormal distribution function:

$$R_d = \mu_R \exp(-\alpha_R \beta V_R) \quad (7.26)$$

For structural systems with one load and one resistance variable, Figure 7.5 shows all possible combinations of α_R and α_Q . The combinations are chosen in such a way that the failure surface is likely to be outside the boundary, defined by the reliability index β . The actual values of α_i depend on the structure under consideration. In any case $-1 < \alpha_i < 1$ and $\alpha_R^2 + \alpha_Q^2 \geq 1$.

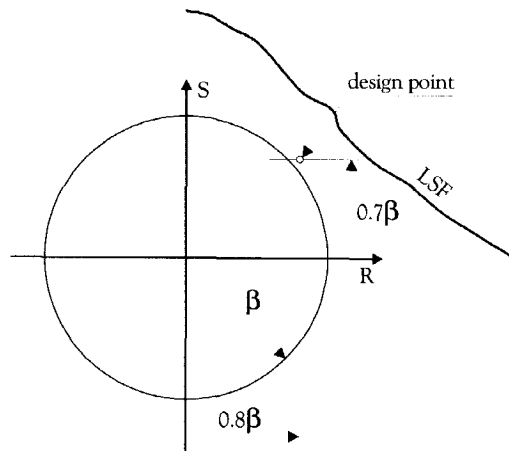


Figure 7.5 Reliability circle

Level I reliability methods

In this calculation method, design regulations are used to check whether or not a sufficient safety margin exists between the distributions of R and Q (see Figure 7.6). The safety margin can be determined in the following ways:

1. By calculating the ratio μ_R/μ_Q , i.e. the central safety coefficient γ_c , as a measure of safety.
2. By calculating the ratio R_k/Q_k , i.e. the overall safety coefficient γ_k .
3. By dividing the margin between R_k and Q_k in two partial safety factors γ_R and γ_Q ($\gamma_R \cdot \gamma_Q = \gamma_k$), which is common practice.

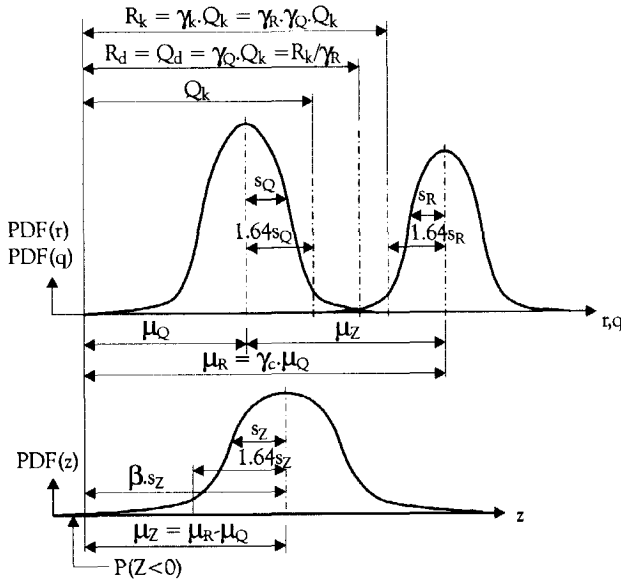


Figure 7.6 Illustration of normally distributed variables Q, R and Z and the (partial) safety factors γ_c , γ_k , γ_R and γ_Q

The central safety coefficient γ_c is a measure for the safety margin between the mean values of the load μ_Q and resistance μ_R . This central safety coefficient γ_c can be determined as follows:

$$\gamma_c = \frac{1 + \beta \sqrt{V_R^2 + V_Q^2} - \beta^2 V_R^2 V_Q^2}{1 - \beta^2 V_R^2} \quad (7.27)$$

Equation (7.27) shows that for the reliability index corresponding to limit state under consideration, the necessary margin between μ_Q and μ_R depends on the coefficients of variation V_R and V_S . Despite the fact that a safety margin can be determined with the help of equation (7.27), it is not common practice to perform level I calculations this way. In design codes, safety factors are applied after the characteristic values is determined, using 5% upper and lower limits of the one-sided confidence intervals for permanent loads and resistance respectively. Assuming normal distributions for load Q and resistance R, the overall safety factor γ_k can be derived from γ_c :

$$\gamma_k = \frac{1 - 1.645 \cdot V_R}{1 + 1.645 \cdot V_Q} \cdot \gamma_c \quad (7.28)$$

7.3.2 Effect of coefficient of variation and reliability index on partial factors

Equation (7.28) shows that the overall safety factor γ_k not only depends on the scatter in load, but also on the scatter in resistance. In reality, the same holds for the partial safety factors γ_R and γ_Q . For engineering purposes they are therefore expressed in a simplified way. In case of normal distributions for load and resistance, the expressions are as follows:

$$\gamma_R = \frac{1 - 1.645 \cdot V_R}{1 - \alpha_R \cdot \beta \cdot V_R} \quad (7.29)$$

$$\gamma_Q = \frac{1 + \alpha_Q \cdot \beta \cdot V_Q}{1 + 1.645 \cdot V_Q} \quad (7.30)$$

Obviously, the partial safety factors can be expressed in terms of the influence factor α . The chosen combination of α -values strongly influences the slopes of the safety factor functions. When increasing one α -value relative to the other, the uncertainty in the material or load can be more or less emphasised. In reality, these uncertainties are expressed by the coefficient of variation V_R and V_Q , but in the design codes one has tried to simplify this approach. In Eurocode 1 for example, $\alpha_R = 0.8$ and $\alpha_Q = 0.7$ have been used to define safety factors for the material and the load. The Dutch design regulations for concrete structures used $\alpha_R = \alpha_Q = 1/2\sqrt{2}$.

As it was mentioned earlier, the distribution type of the resistance R , i.e. the distribution of the strength values of (fibre reinforced) concrete, is assumed to be lognormal. Consequently, equation (7.29) changes into the following expression:

$$\gamma_R = \exp[(\alpha_R \cdot \beta - 1.645) \cdot V_R] \quad (7.31)$$

Equation (7.30) alters in case the applied load has a positive effect. In the scope of this research, the latter has not been studied.

Figure 7.7 shows the effect of the coefficient of variation in resistance V_R and in load V_Q on the partial safety factors γ_R and γ_Q , using equation (7.31) for γ_R and equation (7.30) for γ_Q . It shows that, theoretically, the material safety factor γ_R and the load factor γ_Q do not always increase when the coefficient of variation increases. The latter strongly depends on the reliability index that corresponds to the allowable probability of failure defined by the Limit State Function (LSF). The probability of failure is related to the reliability index, as Table 7.1 shows. Eurocode 1 demands a reliability index β of 1.5 and 3.8 for the Serviceability Limit State (SLS) and Ultimate Limit State (ULS) respectively. The Dutch design regulations for concrete structures use a reliability index β of 1.8 for the SLS and a reliability index of 3.6 for the ULS respectively.

The approach described above only applies to single load conditions. The situation changes considerably when the structural component is subjected to a combination of loads. Within the scope of this research, a combination of loads has not been taken into account.

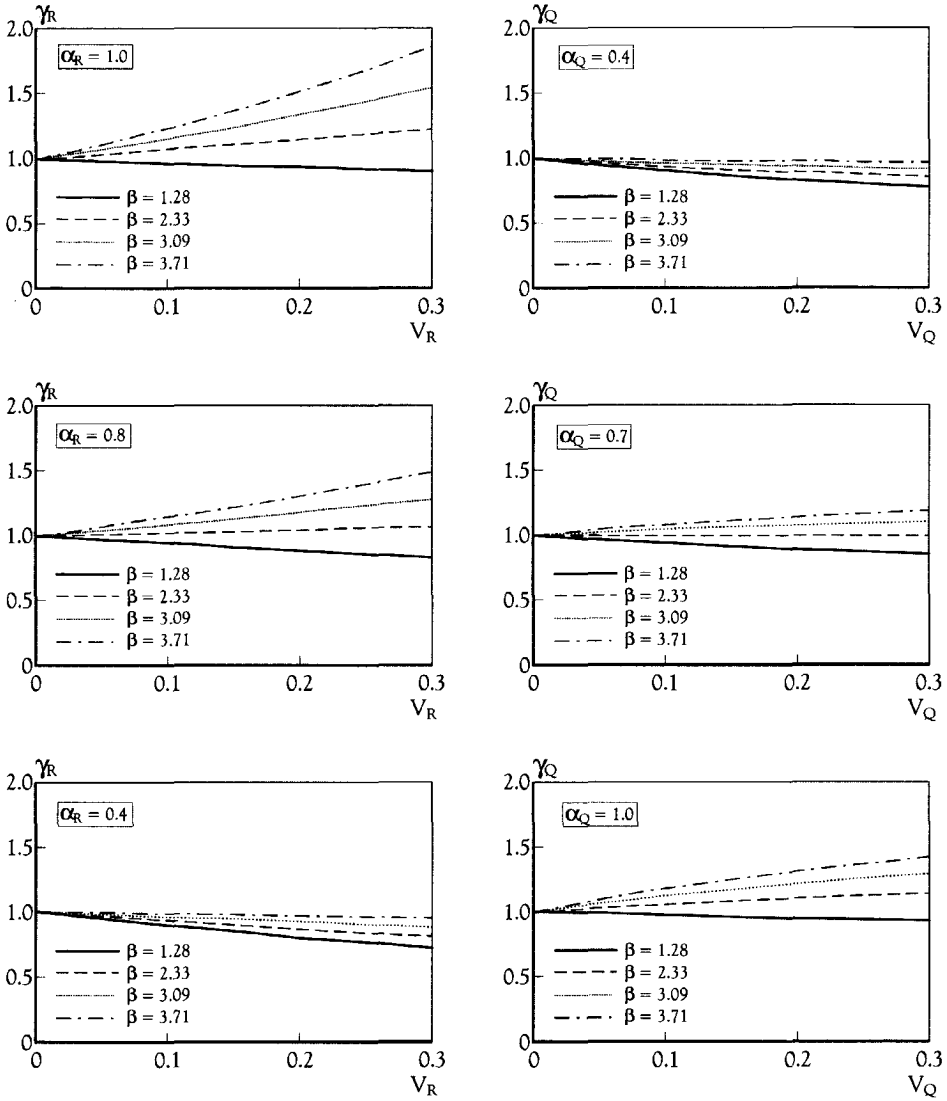


Figure 7.7 Effect of V_R , V_Q and β on the partial safety factors γ_R and γ_Q

7.3.3 Accuracy of the reliability method

According to Eurocode 1 [7.2], the partial safety factor should be calculated as follows, in case of a normally distributed stochastic variable:

$$\gamma_i = 1 + |\alpha_i| \cdot \beta \cdot V_i \tag{7.33}$$

and for a lognormal distribution as follows:

$$\gamma_i = 1 + \exp(-|\alpha_i| \cdot \beta \cdot V_i) \quad (7.34)$$

Eurocode 1 demands a reliability index β of 1.5 and 3.8 for the SLS and ULS respectively and uses values of 0.8 and 0.7 for α_R and α_Q respectively. The coefficient of variation in load V_Q depends on the load condition under consideration and V_R on the uncertainty in resistance. According to Nowak and Collins [7.10], there are three possible sources of uncertainty in resistance in the case of concrete structures: uncertainty in material properties (M), uncertainty in geometrical properties (S) and inadequacy of the material model (A). The coefficient of variation in resistance V_R is the result of the following equation:

$$V_R = \sqrt{(V_M)^2 + (V_S)^2 + (V_A)^2} \quad (7.35)$$

Although it is relatively easy to determine the scatter in material properties, the uncertainty in dimensions and the accuracy of the material model, the exactness of the reliability method itself is not that easy to determine. The exactness of the reliability method depends on the accuracy of the reliability index β , which is a function of the statistical parameters of the limit state function Z . As equation (7.19) shows, β can also be expressed in terms of the means and standard deviations of the probability density functions of resistance R and load Q . The accuracy of the reliability method is therefore determined by the accuracy of the estimated PDF's of R and Q .

In practice, and as will be shown for the case of shield tunnel linings in Chapter 8, the reliability index is often chosen according to predefined Limit States. The Serviceability and Ultimate Limit States are connected to different load conditions that correspond to particular β -values. By making a Level I check for all load conditions and various β -values, it is assumed that a sufficient accuracy is guaranteed.

Waarts [7.11] claims that only the Level III reliability methods result in exact solutions. In addition, he shows that Level II methods result in good approximations. But what about the semi-probabilistic approach suggested by Eurocode 1? In his dissertation, Waarts briefly deals with this question, but does not provide much more insight.

7.4 Bilinear design relationship for the post-cracking behaviour of SFRC

Determination of material safety factor for linear elastic behaviour of SFRC

Sections 7.2 and 7.3 showed how to calculate characteristic strength values and material safety factors. These sections also showed that the characteristic strength and the material safety factor very much depend on the coefficient of variation in resistance V_R . Equation (7.35) showed that the uncertainty in resistance not only depends on the scatter in material behaviour, expressed by the coefficient of variation in material properties (V_M), but also on uncertainty in geometrical properties (V_S) and the inadequacy of the method of analysis (V_A).

As the fibre reinforcement considered in the scope of this research only starts acting after cracking of the matrix, it is reasonable to assume that V_M in the linear elastic behaviour of SFRC is equal to the value of V_M for plain concrete, which is 0.15. Accounting for a 10% uncertainty in dimensions and an accuracy of 10% of the material model, the coefficient of variation in resistance V_R becomes:

$$V_R = \sqrt{(0.15)^2 + (0.10)^2 + (0.10)^2} = 0.21$$

Following Eurocode 1, the material safety factor for plain concrete γ_{ct} is calculated according to equation (7.34):

$$\gamma_{ct} = 1 + \exp(-0.8 \cdot 3.8 \cdot 0.21) = 1.5$$

When equation (7.31) instead of equation (7.34) is used, the material safety factor is lower:

$$\gamma_{fct,el} = \exp[(0.8 \cdot 3.8 - 1.645) \cdot 0.21] = 1.34$$

It is assumed that the material safety factor for the linear-elastic behaviour of SFRC is lower than in case of plain concrete and equals 1.34. The design value of the uni-axial tensile strength $f_{fctd,ax}$ for use in simulations of the flexural behaviour of cross-sections can be determined as follows:

$$f_{fctd,ax} = \frac{f_{fctk,ax}}{\gamma_{fct,el}} \tag{7.36}$$

The characteristic tensile strength $f_{fctk,ax}$ can be determined as follows:

$$f_{fctk,ax} = (1 - 1.645 \cdot V_R) \cdot f_{fctm,ax} \tag{7.37}$$

Initially, the mean uni-axial tensile strength $f_{fctm,ax}$ is determined from tensile splitting tests. As Chapter 5 showed, in the case of 60/0.75 fibres $f_{fctm,ax}$ is determined as follows:

$$f_{fctm,ax} = 0.8 \cdot f_{fctm,spl} \tag{7.38}$$

In the case of 30/0.75 fibres:

$$f_{fctm,ax} = 0.7 \cdot f_{fctm,spl} \tag{7.39}$$

Determination of design value of the equivalent post-cracking strength $f_{fctd,eq,bil}$ of SFRC

The design value of the equivalent post-cracking strength is determined as follows:

$$f_{fctd,eq,bil} = \frac{f_{fctk,eq,bil}}{\gamma_{fct,pl}} \tag{7.42}$$

The characteristic value of the equivalent post-cracking strength $f_{fctk,eq,bil}$ can be calculated with the help of equation (7.10) and depends on the coefficient of variation in resistance V_R and the mean value of the equivalent post-cracking strength $f_{fctm,eq,bil}$.

As equation (5.3) showed, the equivalent post-cracking strength can be expressed as the product of a large number of variables. It depends on the packing density, the water-binder ratio, the bond strength, the aspect ratio and the added fibre volume. It is therefore assumed that the distribution of this post-cracking strength is lognormal. The material safety factor for the post-cracking behaviour is calculated with the help of equation (7.31).

Experimental results presented in Chapter 3 showed that the maximum coefficient of variation $V_M = V_G$ is between 0.05 and 0.28. Chapter 5 and 6 showed that the inverse modelling procedure results in simulations that fit the mean test results quite well. Within the relevant displacement interval, the bilinear post-cracking relation used in the multi-layer procedure can easily result in a fit with an accuracy of 5%. The deviation in dimensions in practice is estimated to be 10%. Table 7.2 shows the effect of an increasing coefficient of variation V_R on the post-cracking material safety factor $\gamma_{\text{fct,pl}}$, based on equation (7.31). The influence factor α_R is again assumed to be equal to 0.8 and the reliability index β is 3.8.

Table 7.2 Post-cracking material safety factor $\gamma_{\text{fct,pl}}$ for SFRC

	$V_R = 0.05$	$V_R = 0.10$	$V_R = 0.15$	$V_R = 0.20$	$V_R = 0.25$	$V_R = 0.30$
$\gamma_{\text{fct,pl}}$	1.07	1.14	1.23	1.32	1.42	1.52

It is obvious that V_R strongly affects the design value. As Table 7.2 shows, the post-cracking material safety factor $\gamma_{\text{fct,pl}}$ increases from 1.07 to 1.52 when the coefficient of variation in resistance in the post-cracking behaviour increases from 0.05 to 0.30, assuming that $\alpha_R = 0.8$ and $\alpha_Q = 0.7$.

7.5 Material testing and quality control

Chapter 3 showed various ways to test the (post-cracking) material behaviour of SFRC. After the assessment of these test methods and considering several criteria, the three-point bending test seemed to be the most appropriate test method to determine the post-cracking behaviour of SFRC. In the assessment of these testing methods isotropy of the material was assumed. Chapters 3 and 6 showed, however, that the direction of casting, the way of compaction by vibration and the vicinity of geometrical boundaries can strongly affect the homogeneity of the composite. The production process influences in particular the fibre dispersion.

Obviously, the material will also show a certain degree of anisotropy in situ. However, the difference between the fibre orientation efficiency in test specimens and their efficiency in situ can deviate considerably, when the production method used in the lab does not correspond to the one used in practice. Although Chapter 6 showed that the effect of the average orientation efficiency factor on the ultimate load capacity P_u is quite small in three-point bending, the effect on the post-cracking behaviour is relatively large. The latter can considerably affect the ultimate load capacity of a statically indeterminate SFRC structure.

In the case of traditionally reinforced concrete structures, the concrete strength on site can be guaranteed by means of quality control. Quality control can be performed in many ways, but often only workability and compressive tests are carried out.

Due to the fact that the production process strongly influences the post-cracking behaviour of SFRC, it is necessary that the way of producing test specimens for quality control

corresponds to the production process used in practice. In addition, the test methods used in the laboratory and in quality control should be similar. In case of quality control, the test reports should therefore contain the following items:

- Scope of tests (type and dimensions of structural application, method of placing and compaction in situ, description of curing and conditioning in practice)
- Description of method of placing and compaction of test specimens
- Description of curing and conditioning prior to testing
- Dimensions of test specimens
- Schematic reproduction of test set-up
- Recordings of fibre dispersion by photographic registration of the fracture surface or x-rays
- Optional: count the number of fibres in the test specimen

After tests are carried out, the test data can be analysed as described in Chapter 3. In case of three-point bending tests, average load-displacement curves can be determined, after which the inverse modelling approach can be used to generate bilinear post-cracking relations. Whether or not the strength properties find approval after quality control testing depends on the method of evaluation and the permissible deviations.

In case there are doubts concerning the quality or durability of the SFRC structure or when the results of quality control tests do not satisfy the demands, the SFRC structure itself needs to be examined. One of the options is to use drilled core specimens, although this can only be done in slabs or prefabricated tunnel segments designed for testing.

If cored specimens are used, for example to perform uni-axial or tensile splitting tests, the coring procedure should also be described. The position of the cored specimens needs to be indicated and the direction of the applied load should be marked on the specimens.

7.6 Concluding remarks

In this chapter an effort was made to implement a safety philosophy into the modelling process of the post-cracking behaviour of SFRC. Since the reliability methods discussed in section 7.3 were not the main focus of this research, it was decided to base the determination of partial safety factors on the semi-probabilistic approach that is commonly used in practice. Safety factors used in structural calculations according to Eurocode 1, for instance, are all based on a similar safety approach.

The author is aware of the fact that some assumptions made in this chapter to determine the material safety factors provoke discussions. The assumed influence factor α_i , for instance, was not supported by objective arguments. However, the values of α_R and α_Q depend on the expected uncertainty in resistance and load. Since the expected uncertainty in load varies for every load condition, a solid assumption for α_R and α_Q is impossible to make without relating these values to the structural application.

Chapter 8

Design of SFRC tunnel segments

8.1 Introduction

In this chapter, design calculations are made for SFRC tunnel segments, making use of the design relation for the post-cracking behaviour of SFRC that was developed in the previous chapters. The case under consideration is the first shield tunnelling project in the Netherlands, also known as the 2nd Heinenoord tunnel. This 950 meter long, double tube tunnelling project was carefully selected by the Dutch Government as an experimental tunnel project to gain knowledge and enhance experience on large diameter shield tunnelling in soft soil and high groundwater levels.

Just after the construction of the first tube started in 1996, the author wrote a state-of-the-art report on the applicability of SFRC in shield tunnel linings [Kooiman, 1996]. It showed that some specific characteristics of SFRC make it a very promising material for application in prefabricated tunnel segments. After experimental research [Kooiman, 1997] in the Stevin Laboratory of the Delft University of Technology, design calculations [Kooiman, 1997] and final design reviews, the Civil Engineering Department of the Directorate-General of Public Works and Water Management decided to install several SFRC tunnel rings in the 2nd Heinenoord tunnel. In August of 1998, the joint venture of contractors that also participated in the feasibility study was ordered to prefabricate 112 SFRC tunnel segments and 16 keystones. After almost two years of research, 16 tunnel rings were installed in the second tube of the 2nd Heinenoord tunnel in June 1998 [Kooiman, 1999].

This chapter starts out with a short introduction on load conditions and limit states that occur in shield tunnel linings. After presenting case-specific data and demands on material properties, a SFRC mixture is proposed that satisfies the demands. Then, the design factors are determined for the different load conditions so that the design stresses can be checked. The latter was done with the help of the software application FRITS, developed by De Waal [De Waal, 1999], and is based on the original design of the 2nd Heinenoord tunnel.

8.2 Loads and limit states

8.2.1 Load conditions and structural design models

In case of a shield tunnel lining, the tunnel structure is subjected to various loads in different stages. In all kinds of combinations, the following load conditions need to be checked in the design stage of a tunnel lining:

- Dead weight of the structure
- Permanent loads (roads/railway)
- Soil pressure
- Grout pressure
- (Ground) water levels
- Installation loads
- Axial force from Tunnel Boring Machine (TBM)
- Temperature loads
- Traffic loads
- Extreme loads (fire, explosions, earthquakes)

Before the exact geometry of the segments and the necessary reinforcement can be determined, the cross-sectional forces and deformations have to be calculated. The cross-sectional forces are the result of the above mentioned load conditions and the dimensions of the tunnel lining, i.e. the internal diameter and the lining thickness (see section 8.3). To calculate the cross-sectional forces in the design stage, the tunnel lining is analysed in two separate directions. Firstly, the forces in the circular cross-section are determined. Secondly, after checking this 'ring' behaviour, the lining is checked in axial direction.

Analysis of the circular cross-section of a shield tunnel lining

Structural design models for analysing the circular cross-section of a shield tunnel lining are characterised by their approach. According to De Waal [De Waal, 1999], two different approaches can be distinguished.

The first approach is based on material strength theories, which depart from the assumption that solutions can be found by supposing equilibrium of internal and external forces. The models that have been developed over the years are often characterised by their soil schematisation, which is done by means of springs. Therefore, they are also known as bedded ring models. An overview of the available structural design models can be found in literature [Iftimie, 1994], but one of the best known was developed by Schulze and Duddeck [Schulze & Duddeck, 1964]. This type of model is preferred by structural engineers and was also used in the design of the 2nd Heinoord tunnel. It is schematised in Figure 8.1.

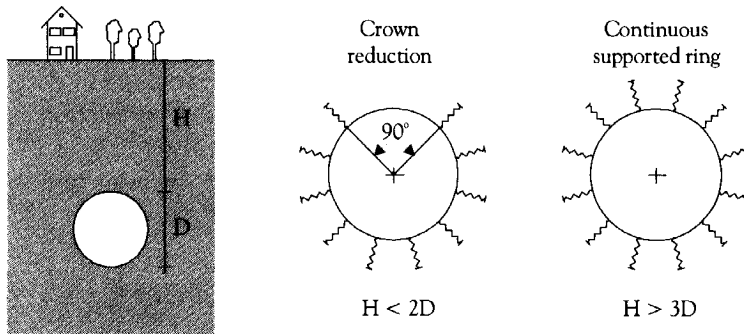


Figure 8.1 Example of a bedded ring model [Schulze & Duddeck, 1964]

In the second approach the soil-structure interaction is described by means of an elastic medium. The solution is based on the compatibility of stresses and deformations and is derived for a homogeneous, linear elastic medium. In these continuum models, the circular lining is initially assumed to deform as a result of the surrounding soil (and water) pressure, which is often simplified as a plane stress condition (see Figure 8.2).

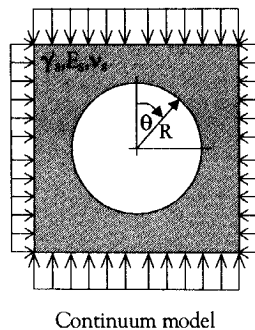


Figure 8.2 Example of a continuum model according to Erdmann [Erdmann, 1983]

With the help of the design equations resulting from bedded ring or continuum models, cross-sectional forces in the lining can be calculated. Important parameters in these equations are the depth of the soil cover on the tunnel lining, the radius of the circular cross-section, the bending stiffness of the tunnel ring and soil parameters such as the bedding stiffness, the Oedometer stiffness and the specific weight of the soil. Since an in-depth discussion on structural design models does not fit in the scope of this research, only the most important design parameters have been mentioned here. For complete design equations, appropriate literature should be checked.

In his comparison of structural design models, De Waal [De Waal, 1999] showed that the bending moment M and normal compressive force N can vary considerably in a single tunnel ring, depending on the position in the ring. In addition, De Waal also showed that the maximum bending moment and minimum normal compressive force are greatly influenced by the soil parameters.

Tunnel rings in a lining are connected to each other. Initially, this is done by means of bolts, which are removed after construction of a large number of rings. However, to provide stability of the lining after construction another type of connection is necessary in the serviceability stage. In the design of circular joints of segments, shear keys are often applied to provide this connection. Shear keys have also been applied in case of the segments for the 2nd Heinenoord tunnel (see Figure 8.3). The primary function of these shear key connections is to resist shear forces that occur as a result of the girder behaviour of the tunnel lining in axial direction.

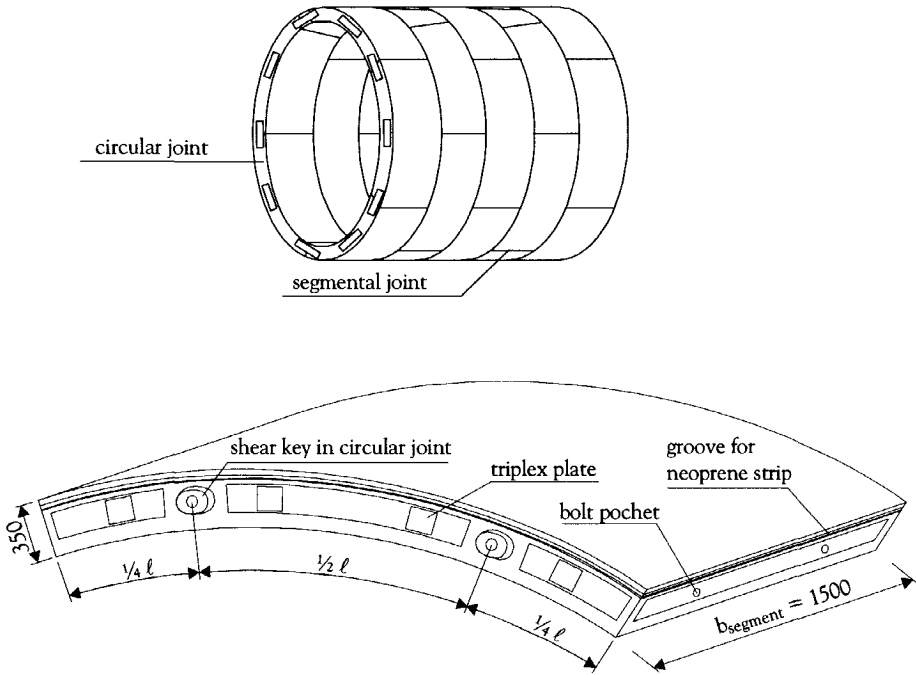


Figure 8.3 Shear keys as circular joint connection between tunnel rings

When tunnel segments are being installed in a ring, this particular ring is located within the shield machine and is therefore not directly subjected to soil, grout and ground water pressures. In contrast, the previously installed tunnel ring is partially located outside of the 'protective' environment of the shield machine. As a result of the acting soil, grout and ground water pressures, this tunnel ring deforms and tends to ovalise, as illustrated in Figure 8.4. In the mean time, the circular joint connections should provide stability of the tunnel lining and transfer a part of the load to the tunnel ring under construction. In the design stage, this phenomenon is often analysed by modelling a frame of two bedded rings that are connected by bars, as illustrated in Figure 8.5.

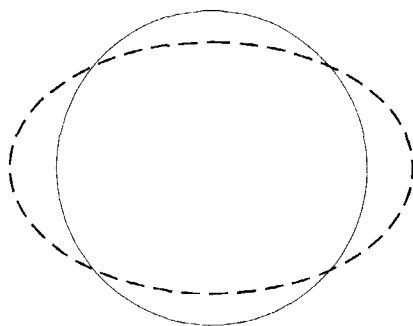


Figure 8.4 Elliptical deformation of tunnel ring

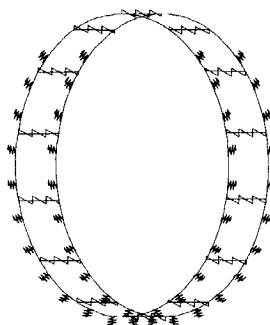


Figure 8.5 Frame model of two connected bedded rings

Analysis of the tunnel lining in axial direction

In contrast to structural design models for analysing the circular cross-section of a tunnel lining, the number of models that describe the behaviour in axial direction is rather small. Blom [Blom, 1995] developed the first model for what is called the 'girder behaviour' of a tunnel lining. Girder behaviour is often initiated by local changes in tunnel loading, such as a local change in bedding stiffness when the tunnel crosses an interface between two soil layers of different stiffness. Figure 8.6 shows a schematisation of this load condition. It shows that the tunnel lining is simply schematised as a spring bedded girder. As the bending and shearing stiffness of a segmental lining is smaller than in case of a monolithic lining, an equivalent bending stiffness EI_{eq} and an equivalent shearing stiffness GA_{eq} are used in the calculations to take the reduction in stiffness into account.

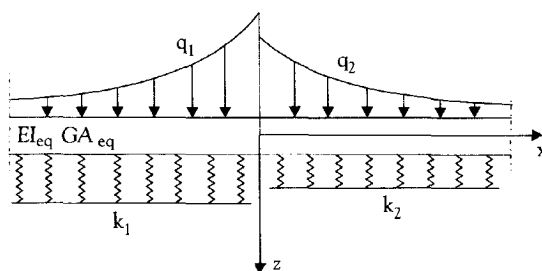


Figure 8.6 Schematisation of tunnel lining behaviour in axial direction [Blom, 1995]

By using schematisations like the one shown in Figure 8.6, bending moments and shear forces can be calculated as a result of girder behaviour. These cross-sectional forces can theoretically cause four deformation mechanisms. As a result of a bending moment, the tunnel might deform, as indicated in Figure 8.7a. Next to that, the shear force might cause a deformation, as illustrated in Figure 8.7b. As mentioned before, circular joint connections, e.g. shear keys, are often used to resist this kind of deformation.

Obviously, a combination of these cross-sectional forces will occur in practice. Therefore, the actual tunnel behaviour in axial direction will be a mix of the four extreme deformation mechanisms shown in Figure 8.7. In axial direction, however, a normal compressive force is present as a result of the thrust jacking force on the lining, which is introduced by the shield machine as it pushes itself forward during excavation. Measurements

in the 2nd Heinenoord tunnel confirmed that a considerable part of the axial force remains in the lining, but in time it will most probably reduce due to stress relaxation, temperature changes, etc.

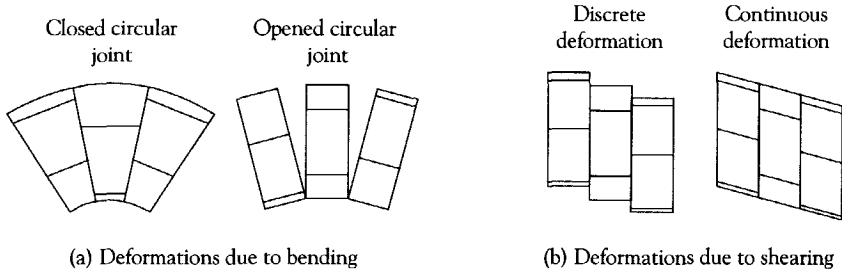


Figure 8.7 Deformation mechanisms due to girder action [Blom, 1995]

As already mentioned, the tunnel lining is subjected to thrust jacking forces in axial direction. This large compressive force is a critical load condition in the design of tunnel linings. During excavation, the shield machine pushes itself forward by means of hydraulic jacks. As a result, the tunnel segments are subjected to very high stress concentrations that can cause spalling of concrete and can initiate cracking due to splitting (see Figure 8.8).

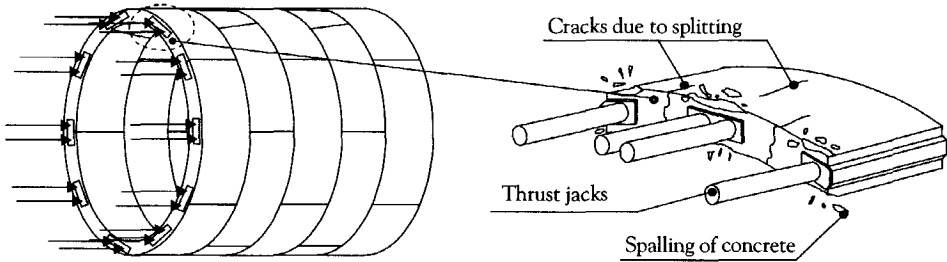


Figure 8.8 Damage due to thrust jacking of the shield machine [De Waal, 1999]

The actual stress concentrations due to thrust jacking obviously depend on the thrust jack capacity of the shield machine and the number of hydraulic jacks applied. The required thrust jack capacity of the shield machine is the result of the force that is needed to provide face stability at the excavation front and the friction along the shield of the machine. Therefore, the necessary thrust jack capacity is related to the tunnel diameter, the tunnel depth and soil parameters.

8.2.2 Limit states in the design of tunnel linings

For probabilistic design purposes, Vrouwenvelder [Vrouwenvelder, 1997] defined β -values for various Limit States. Table 8.1 shows ranges of β -values and their corresponding limit states.

Table 8.1 Categories of β -values corresponding to limit states in tunnel lining design [Vrouwenvelder, 1997]

β	Limit States
1-2	SLS repairable
2-3	SLS not repairable
2-3	ULS repairable
3-4	ULS local failure
4-5	ULS global failure

The question is, however, how these limit states can be translated to the case of a shield tunnel lining. In Table 8.2, an attempt is made to categorise the limit states. These limit states are linked to the relevant load conditions that were described in section 8.2.1.

Table 8.2 Limit states in tunnel lining design

SLS repairable	SLS not repairable	ULS repairable	ULS local failure	ULS global failure
Cracks and damage due to loads in the installation stage	Extreme deformations of tunnel lining	Damage at shear key connection in circular joint	Failure of a single tunnel ring	Structural failure of tunnel lining
Cracks in segments in serviceability stage	Extreme displacements at segmental joints	Structural failure of tunnel lining	Structural failure of tunnel lining	Structural failure of tunnel lining
Structural failure of tunnel lining	Structural failure of tunnel lining	Structural failure of tunnel lining	Structural failure of tunnel lining	Structural failure of tunnel lining

In the design example presented later in this chapter, the shaded load cases will not be examined, as for different reasons they are not of interest in this particular case study. The other load cases are far more interesting to examine, as they are applicable for the case under consideration and because they require an analysis of the structural behaviour of SFRC.

8.3 Design of SFRC tunnel segments for the 2nd Heinenoord tunnel

8.3.1 Introduction of the case

General data

The introduction of this chapter already mentioned that in the case of the 2nd Heinenoord tunnelling project two tubes have been constructed. Agricultural vehicles use one of the tubes, while the other is used by other slow traffic, such as pedestrians and cyclists. The tubes have an internal diameter of 7.60 meters and connect the banks of the river Oude Maas. At the deepest point the upper road surface in the tunnel is 26 meters below Amsterdam Ordnance Datum (AOD), while in the start/reception shaft this surface is 11.5 meters below AOD. The maximum gradient of the bored section is 1:30.

Boundary conditions and points of departure

As in every tunnelling project, an extensive soil survey was carried out in the 2nd Heinenoord tunnelling project. The soil consists of approximately 20% weak cohesive soil types and approximately 80% non-cohesive sand layers. An extensive soil survey showed that in the alignment of the tunnel the specific soil properties are somewhat irregular. In addition, the interface between the Holocene layer, with mainly clay and peat, and the Pleistocene layer, with mainly sand, was found at approximately 15 meters below Amsterdam Ordnance Datum. The highest water level in the river Oude Maas was 1 meter above AOD.

Assumptions in the lining design

In the design of the tunnel lining the following assumptions have been made:

- The tubes do not influence one another as they are more than $\frac{1}{2} \cdot D$ apart.
- Determination of girder behaviour is not necessary since no cohesive layers are present underneath the alignment of the tunnel lining. In the case that such layers would have been present, they could have caused an upward deformation in case of excavations at the ground surface level and a downward deformation in case of settlements as a result of additional loads at the surface level.
- Although 10 to 20 percent of the thrust jacking force is expected to remain in the lining, acting as a prestressing force in axial direction, the presence of this compressive force in axial direction is not taken into account.
- Stresses in the lining due to variable loads from traffic are negligible compared to the permanent soil and water pressure.
- Stresses in the lining due to temperature effects are neglected.

Structural demands

In Table 8.2, the critical load conditions in the construction and serviceability stage are categorised for several limit states. The structure has to be able to resist the forces that result from these load conditions. In addition to these structural demands, the structural material has to satisfy the following demands:

- Lining is constructed from prefabricated concrete segments
- Characteristic cube compressive strength of the concrete: 45 N/mm^2
- Make use of blast furnace cement for durability reasons
- Demoulding within 24 hours

The latter two demands, however, were in conflict. Because of the fact that the hydration process of blast furnace cement develops relatively slowly, a mix of blast furnace cement and a highly reactive Portland cement was allowed to be applied.

Geometry of the segment

In the design of tunnel linings, it is common practice to estimate the lining thickness h_{lining} as $1/10$ of the tunnel radius R . In reality the final lining thickness depends on many factors, such as the loads on the segments during installation (segment handling, thrust jacking), the necessity of a watertight rubber seal and, in case of conventional concrete, the required concrete cover. In case of the 2nd Heinenoord tunnel, the lining thickness was 350 mm.

The number of segments in a tunnel ring depends on the calculated ring connecting forces, cost considerations (the less the better), constructability (the smaller the segments, the better to handle), tolerances considering deviations in dimensions, etc. In this case, each

tunnel ring was constructed from 7 segments and a keystone. The geometry of a tunnel segment was already illustrated in Figure 8.3.

Tolerances considering deviations in dimensions of segments

The tolerances with respect to deviations in dimensions of tunnel segments are very limited. Maximum deviations in dimensions of 0.2 mm are demanded ($V_s < 0.1\%$). These kind of tolerances are not very realistic, as concrete expands and shrinks quite rapidly when subjected to temperature loads. A coefficient of variation V_s of 0.05 is much more realistic in this case, where the segments are prefabricated in controlled conditions.

The main reason for strict demands on tolerances is to guarantee a watertight tunnel lining, as the rubber strip around the perimeter of the segment has to seal the lining and avoid water and soft soil to flow in. In general, there are two other important reasons.

The load transfer in circumferential direction takes place between segments in a ring. In the segmental joints, two concrete planes have to transfer a compressive hoop force to one another. It is necessary that these two planes in the segmental joint fit very well. If not, peak stresses are inevitable, which might cause cracking or spalling.

The thrust jacks locally introduce very high forces on the tunnel lining. When the surface of the segments is not smooth and even, high peak stresses can occur in the circular joints, which might result in spalling and cracking of the concrete.

8.3.2 Material properties

Table 6.2 showed the mix composition that was used to prefabricate the SFRC tunnel segments for application in the 2nd Heineoord tunnel. After extensive testing in the scope of this research, however, it was found that mix 2 of Table 3.3 also satisfies the prefabrication demands. In this case study, it is checked whether or not mix 2, reinforced with 60 kg/m³ of hooked-end steel wire fibres with an aspect ratio L_f/d_f of 60/0.75 could also have been applied. Table 8.3 shows the mix composition of the material under consideration. Table 3.4 already showed the mean values of the cube compressive strength and the tensile splitting strength.

Table 8.3: SFRC mix composition for use in prefabricated tunnel segments

Mix components	Quantity
Portland cement CEM I 52.5	87.5 kg/m ³
Blast furnace cement CEM III/B 42.5	262.5 kg/m ³
Sand 0-4 mm	43 %
Gravel 4-16 mm	57 %
Normal strength hooked-end steel fibres ($L_f/d_f = 60/0.75$)	60 kg/m ³
Superplasticiser	1.4 % (relative to cement)
Water/cement ratio	0.42

Figure 8.9 shows the load-displacement diagrams of the mix composition shown in Table 8.3 after performing six standard three-point bending tests on 150 mm wide and 150 mm deep beams, with a notch depth of 25 mm and a span length of 500 mm. Furthermore, it shows the simulated curve of the mean test results after inverse analysis, as described in Chapter 5. Test results showed that the maximum coefficient of variation V_M in the post-cracking behaviour (up to a crack opening of 5 mm) was equal to 0.16 (see Figure 3.17).

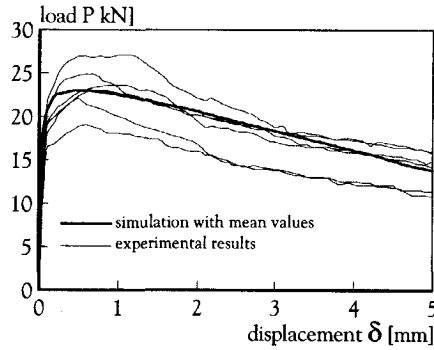


Figure 8.9 Load-displacement diagrams of mix composition under consideration

Figure 8.10 shows the mean uni-axial material relation that was used in these simulations. The inverse analysis showed that the obtained accuracy in the simulation was 5%.

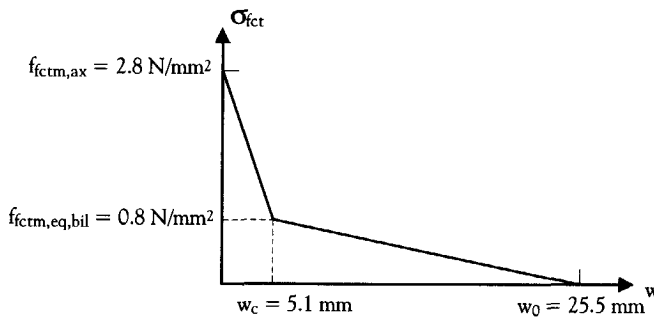


Figure 8.10 Mean bilinear post-cracking relation of mix composition under consideration

8.3.3 Partial safety factors for structural design

Equations (7.31) and (7.33) showed how to determine partial safety factors for design purposes. Obviously, the safety factors depend on the reliability index β , the coefficient of variation in resistance V_R , the coefficient of variation in load V_Q and the influence factors α_R and α_Q .

The reliability index β can be determined according to Table 8.1 and 8.2 and is clearly related to the Limit State and load condition under consideration. Furthermore, the coefficient of variation V_R can be easily determined. With $V_M = 0.16$, $V_S = 0.10$ and $V_A = 0.05$, V_R can be determined using equation (7.35), which results in a constant coefficient of variation of the post-cracking resistance of 0.20.

Vrouwenvelder [Vrouwenvelder, 1997] showed that the coefficient of variation in load sources V_Q varies considerably, depending on the type of load. According to Vrouwenvelder [Vrouwenvelder, 1997] the coefficient of variation is relatively small for permanent loads (0.05-0.10), while the scatter in soil characteristics and variable loads is relatively large. In this case study, variable loads are neglected and, as it was mentioned earlier, the soil parameters are not that uncertain due to an extensive soil survey. The coefficient of variation in soil

parameters is assumed to be equal to 0.20. With respect to the variation in thrust jacking force, it is assumed that the coefficient of variation in load is 0.15, as the exact data on thrust jacking capacities are lacking. Table 8.4 shows the coefficient of variation V_Q of the various types of loads examined in this case study. It is assumed that these load variables are normally distributed.

Table 8.4 Coefficient of variation V_Q for several load sources

V_Q	Load sources
0.05	Dead weight of the structure
0.10	Permanent loads (dead weight other than the structure itself)
0.15	Thrust jacking
0.20	Surrounding soil

With the help of the influence factors α_R and α_Q , the uncertainty in resistance or load can be emphasised. The coefficient of variation in resistance V_R of 0.20 and the coefficient of variation in load V_Q represent these uncertainties. As the coefficient of variation in load source V_Q varies and many of the examined load cases are combinations of several loading types, it is impossible to define a unique coefficient of variation for the load.

In the next section, the resistance of a SFRC tunnel segment to the earlier mentioned critical cross-sectional forces and the thrust jacking force will be checked. The critical cross-sectional forces, however, were determined after analysing 18 load cases, in which different combinations of load sources occurred. As it is beyond the scope of this research to analyse all load cases and to determine the correct partial safety factors for every load source, it is necessary to make some simplifying assumptions for the determination of the design values.

In this case, it is assumed that the critical cross-sectional forces are caused by only one fictitious load source. As it is reasonable to assume that the dead weight of the structure and the permanent load on the tunnel linings caused by soil and water pressures are more dominant than the variable temperature and traffic loads, it is supposed that the coefficient of variation of this fictitious load source V_Q is on average 0.15. After including 10% uncertainty in the structural design model, the coefficient of variation in load V_Q equals 0.18. As V_R equals 0.20, the uncertainty in resistance is a little bit higher than in load. Accordingly, the values for the influence factors α_R and α_Q were chosen equal to those applied in Eurocode 2 ($\alpha_R = 0.8$ and $\alpha_Q = 0.7$). In Serviceability Limit State calculations a reliability index β of 1.5 is applied, while $\beta = 3.8$ in the case of Ultimate Limit State calculations. Table 8.5 shows the partial safety factors that will be applied in the Limit State calculations of this design case. Equation (7.31) was used for the material safety factors and equation (7.33) for the load factor.

Table 8.5 Partial safety factors for Limit State calculations

Partial safety factor	Coefficient of variation V	SLS repairable ($\beta=1.5$)	SLS not repairable ($\beta=2.8$)	ULS repairable ($\beta=2.8$)	ULS local failure ($\beta=3.8$)
γ_D	0.18	1.19	1.35	1.35	1.48
γ_{fcc}	0.20	1.00	1.13	1.13	1.34
$\gamma_{fct,el}$	0.20	1.00	1.13	1.13	1.34
$\gamma_{fct,ol}$	0.20	1.00	1.13	1.13	1.34

8.3.4 Maximum cross-sectional forces and working load of thrust jacks

In the original design, the critical cross-sectional and external forces have been determined according to DIN 1045 [DIN 1045-1, 1999], i.e. the German design guideline for concrete structures. This means that in the analysis of load conditions load safety factors have not been applied. The DIN 1045 does not apply partial safety factors in design, but prescribes an overall safety coefficient of 1.75 for ductile failure mechanisms and 2.1 for brittle failure.

Making use of the bedded ring model of Schulze and Duddeck [Schulze & Duddeck, 1964], 18 different load cases were analysed in the original design process of the 2nd Heinenoord tunnel. In addition to the dead weight of the structure, the surrounding soil and ground water, the tunnel lining is subjected to various loads along its axis. In the design calculations of the tunnel segments in the next section, it will be checked whether or not these cross-sectional forces can be resisted. The segments will be checked on flexural stresses due to the critical combination of bending moment and normal force in a ring, tensile splitting and compressive stresses near joints and shearing stresses at the shear key connections.

To check the flexural stresses in the tunnel lining, the critical combination of bending moment M and normal compressive force N has to be determined. In practice, this is defined as the highest ratio of M/N . According to the original 2nd Heinenoord tunnel lining design, a bending moment M of 95.1 kNm and an accompanying normal compressive force N of 899 kN result in the highest ratio of M/N in the critical cross-section.

Next to the critical combination of M and N , the 18 loading conditions have also been analysed to determine the maximum occurring hoop force in the lining, again by using the bedded ring model of Schulze and Duddeck [8.7]. It is necessary to know the maximum hoop force N_{\max} , as the resistance to high tensile splitting and compressive stresses near the segmental joints needs to be checked (see section 8.4.3). According to the 2nd Heinenoord tunnel lining design, the design hoop force is a normal compressive force of 2483 kN.

Another important cross-sectional force that needs to be checked is the maximum ring connecting force. As a result of the frame model of two connected bedded rings that was shown in Figure 8.5, it was calculated that each segment is subjected to a shear force of 161 kN. This shear force is supposed to be transferred from one ring to the other by the shear keys in the circular joints. As a result, each shear key connection should resist 80.5 kN.

Next to the internal, cross-sectional forces that result from (restrained) deformations in the tunnel lining, one other type of load needs to be considered in design. This type of load is an externally applied force on the tunnel segment, which results from the thrust jacking process. In the case of the 2nd Heinenoord tunnel, the shield tunnel machine pushes itself forward with the help of 28 hydraulic thrust jacks, working in couples (see Figure 8.8). A steel plate of 900x200 mm² couples two hydraulic thrust jacks and is in direct contact with the concrete surface of the tunnel segment during the excavation process. The ultimate thrust jacking capacity of the shield machine was 56 MN, resulting in a maximum thrust jacking force of 4000 kN per couple. The working load is estimated at 2500 kN per couple.

8.3.5 Design calculations of SFRC tunnel segments

Design values of material strength properties

In the design calculations presented this section, the resistance to several internal forces and external loads will be checked for the hardened material of which the mix composition was shown in Table 8.3. Obviously, the design values of the strength parameters must be determined first.

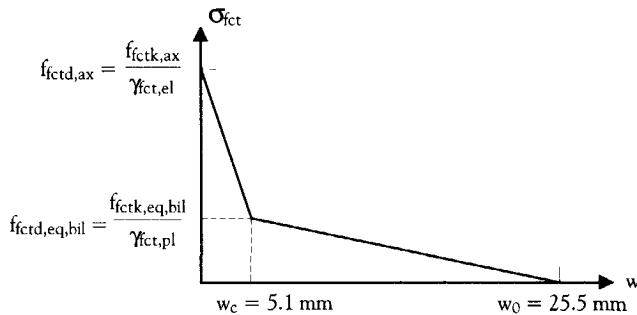


Figure 8.11 Bilinear design relation for the post-cracking behaviour of the SFRC under consideration

Figure 8.11 shows the design post-cracking relation of the SFRC under consideration. The material design values $f_{fctd,ax}$ and $f_{fctd,eq,bil}$ can be determined by using equations (7.36) to (7.42), the mean strength values shown in Figure 8.10 and the material safety factors presented in Table 8.5. To check the maximum flexural stress, the material design values $f_{fctd,ax}$ and $f_{fctd,eq,bil}$ were determined (see the first column of Table 8.6). Since the mean values of the bilinear post-cracking material relation of Figure 8.10 are based on 'standard' three-point bending tests, the fibre orientation efficiency factor used in this relation differs from the actual orientation efficiency in tunnel segments. However, as Figure 6.14 already showed, the effect of the orientation efficiency on the ultimate load capacity of a cross-section subjected to bending is very small. As long as the following design calculations are based on cross-sectional analyses, it is not important which fibre orientation efficiency factor is used in the determination of w_0 .

Table 8.6 Values for SFRC in flexural tension

	SFRC in flexural tension
$f_{fctm,ax}$	2.80 N/mm ²
$f_{fctk,ax}$	1.88 N/mm ²
$\gamma_{fct,el}$	1.34
$f_{fctd,ax}$	1.40 N/mm ²
$f_{fctm,eq,bil}$	0.80 N/mm ²
$f_{fctk,eq,bil}$	0.45 N/mm ²
$\gamma_{fct,pl}$	1.34
$f_{fctd,eq,bil}$	0.34 N/mm ²
w_c	5.1 mm
w_0	25.5 mm

Maximum flexural stress due to the critical combination of bending moment and normal force

The previous section showed that the critical cross-section needs to be checked on the presence of a bending moment of 95 kNm and an accompanying normal compressive force of 899 kN. The critical situation in this load case is local failure in Ultimate Limit State. Multiplied with the load factor $\gamma_Q = 1.48$ given in Table 8.5, the design values become 141 kNm and 1331 kN for the bending moment and normal compressive force respectively.

To check critical combinations of bending moments and normal forces, the software program FRITS (Fibre Reinforcement In Tunnel Segments) was used [De Waal, 1999]. Based on the same multi-layer procedure as described in section 5.2, FRITS calculates the M-N failure envelope, using the bilinear post-cracking relation of the SFRC under consideration (Table 8.6) and the dimensions of the cross-section ($1500 \times 350 \text{ mm}^2$) as input parameters.

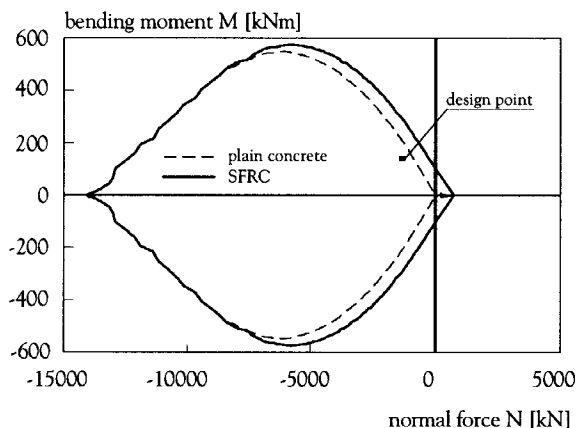


Figure 8.12 M-N failure envelope for the SFRC under consideration

Figure 8.12 shows that the design point is located within the envelope. It also shows that in this case a plain concrete lining can also resist the critical combination of M and N in Ultimate Limit State. As the tensile strength of the plain concrete matrix is not reached, the Serviceability Limit State is also covered

Compressive and tensile splitting stresses near segmental joints in case of a maximum hoop force

In the case of elliptical deformation of a tunnel ring, the joints between segments rotate. As a result, the contact surface between segments decreases and the hoop force is eccentrically introduced. In the original 2nd Heinenoord tunnel design, it was assumed that in case of elliptical deformation only half of the contact surface in the segmental joint should be able to transfer hoop stresses (see Figure 8.13). It is the author's opinion that this kind of extreme deformation is quite unlikely to occur. Furthermore, in the hypothetical case that it does occur, the serviceability of the tunnel is no longer guaranteed. Due to the geometry of the segmental joint, the lining is no longer watertight (see Figure 8.3). However, just like in the original 2nd Heinenoord tunnel design, the load case that results from this extreme deformation is checked in the Serviceability Limit State.

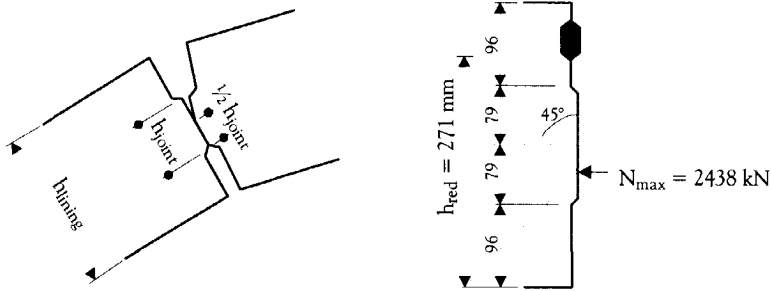


Figure 8.13 Reduction of contact surface as a result of segmental joint rotation

Obviously, the compressive and tensile splitting stresses are increased, as a result of a decrease in contact surface. The resistance to these stresses needs to be checked using the maximum hoop force $N_{max} = 2483 \text{ kN}$. The maximum compressive stress in the Serviceability Limit State (not repairable) is calculated as follows:

$$\sigma_{cm,max} = \frac{\gamma_Q \cdot N_{max}}{0.5 \cdot h_{joint} \cdot b_{segment}} = \frac{1.35 \cdot 2483 \cdot 10^3}{79 \cdot 1500} = 28.3 \text{ N/mm}^2$$

According to the Dutch design guidelines for concrete structures [NEN 6720, 1991], the allowable compressive stress in case of concentrated loads can be calculated as follows:

$$\sigma_{fccd} = \frac{0.72 \cdot f_{cck}}{\gamma_{fcc}} \cdot \sqrt{\frac{h_{red}}{0.5 \cdot h_{joint}}} = \frac{0.72 \cdot 45}{1.13} \cdot \sqrt{\frac{271}{79}} = 53.1 \text{ N/mm}^2 > 28.3 \text{ N/mm}^2$$

The maximum compressive strength in the segmental joint can be easily resisted. However, the occurring tensile splitting stress may exceed the SFRC splitting strength. To determine the maximum occurring splitting stress, the theory of Iyengar and Prahakara [Iyengar & Prahakara, 1969] was used. Figure 8.14 shows the relation between the occurring tensile splitting stresses in a plain concrete prism and the acting compressive stresses as a function of the loading geometry.

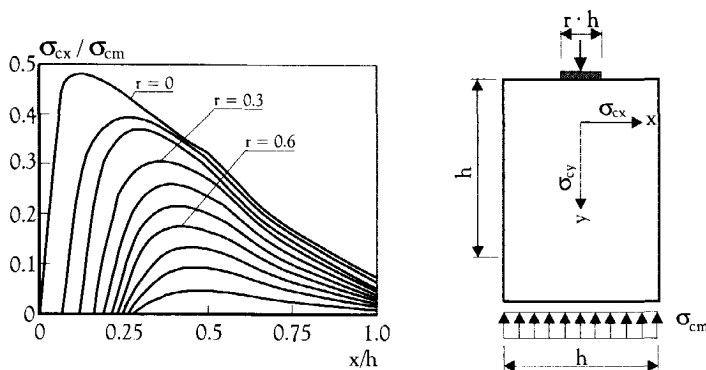


Figure 8.14 Tensile splitting stresses in a plain concrete prism [Iyengar & Prahakara, 1969]

If h_{red} in Figure 8.13 is equal to h in Figure 8.14, then $r = 79/271 = 0.29$. Figure 8.14 shows that in that case $\sigma_{cx,max}/\sigma_{cm,max} \approx 0.32$. With:

$$\sigma_{cm,max} = \frac{\gamma_Q \cdot N_{max}}{h_{red} \cdot b_{segment}} = \frac{1.35 \cdot 2483 \cdot 10^3}{271 \cdot 1500} = 8.21 \text{ N/mm}^2$$

The maximum tensile splitting stress $\sigma_{cx,max}$ is as follows:

$$\sigma_{cx,max} = 0.32 \cdot \sigma_{cm,max} = 2.64 \text{ N/mm}^2$$

According to the RILEM Technical Committee 162-TDF [RILEM TC 162-TDF], the uni-axial tensile strength of SFRC is equal to that of plain concrete and can be determined as a function of the cylindrical compressive strength:

$$f_{fctd,ax} = \frac{f_{fctk,ax}}{\gamma_{fct}} = \frac{0.7 \cdot f_{fctm,ax}}{\gamma_{fct}} = \frac{0.7 \cdot 0.3 \cdot (f_{fck})^{2/3}}{1.13} = 1.99 \text{ N/mm}^2$$

However, the tensile splitting strength of SFRC is higher than the uni-axial strength value. In case of plain concrete, Eurocode 2 prescribes the following relation between the uni-axial tensile strength and the tensile splitting strength:

$$f_{ctd,spl} = \frac{f_{ctd,ax}}{0.9} = 2.21 \text{ N/mm}^2$$

In Chapter 5, however, it was already mentioned that due to the addition of steel fibres the tensile splitting strength is increased relative to the splitting strength of the plain matrix. Körmeling [Körmeling, 1986] showed that the margin between the splitting strength and the uni-axial strength of the composite is increased:

$$f_{fctd,spl} = \frac{f_{fctd,ax}}{0.8} = 2.49 \text{ N/mm}^2$$

Obviously, the maximum occurring tensile splitting stress exceeds the tensile splitting strength of SFRC. However, the tensile splitting strength in radial direction is much higher at the segmental joint than at other locations of the segment, as was found after splitting several drilled cores from a SFRC segment [Kooiman, 1998]. As a matter of fact, the cores taken near the segmental joint showed an average strength increase of 34% relative to the stress at crack initiation $f_{fctd,ax}$. This increase was attributed to the favourable fibre orientation near the segmental joints. However, the exact effect of the fibre orientation on the tensile splitting strength of SFRC is unclear. Further investigation on this matter is definitely necessary.

Compressive and tensile splitting stresses in circular joints due to thrust jacking forces

As mentioned before, the thrust jacks introduce large concentrated forces on the tunnel lining during the excavation process. This process lasts about 30 minutes, which means that the thrust jacking load is a short-term load. In the case of the 2nd Heinenoord tunnel, the tunnel segments are loaded, as illustrated in Figure 8.8.

The resistance to the compressive stress needs to be checked at the circular joint and at the location where the thrust jacking plate makes contact with the tunnel segment, using the working load of the thrust jacking force F_{work} , which is equal to 2500 kN. The maximum compressive stress behind the thrust jack plates in Serviceability Limit State (repairable) is calculated as follows:

$$\sigma_{\text{fcc}} = \frac{\gamma_Q \cdot F_{\text{work}}}{h_{\text{plate}} \cdot \ell_{\text{plate}}} = \frac{1.19 \cdot 2500 \cdot 10^3}{200 \cdot 900} = 16.5 \text{ N/mm}^2$$

According to the Dutch design guidelines for concrete structures, the allowable compressive stress in case of a short-term concentrated load can be calculated as follows:

$$\sigma_{\text{fccd}} = \frac{0.85 \cdot f_{\text{ceck}}}{\gamma_{\text{fcc}}} \cdot \sqrt{\frac{h_{\text{lining}}}{h_{\text{plate}}}} = \frac{0.85 \cdot 45}{1.00} \cdot \sqrt{\frac{350}{200}} = 50.6 \text{ N/mm}^2 > 16.7 \text{ N/mm}^2$$

The maximum compressive strength in the circular joint can be easily resisted. However, the thrust jacking loads also cause direct and indirect tensile splitting stresses in the segments. In radial direction, the direct splitting stress can be determined with the help of Figure 8.14. If h_{lining} is equal to 350 and h_{plate} equal to 200, then $r = 200/350 = 0.57$. Figure 8.14 shows that in that case $\sigma_{\text{cx,max}}/\sigma_{\text{cm,max}} \approx 0.19$. With:

$$\sigma_{\text{cm,max}} = \frac{\gamma_Q \cdot F_{\text{work}}}{h_{\text{lining}} \cdot \ell_{\text{plate}}} = \frac{1.2 \cdot 2500 \cdot 10^3}{350 \cdot 900} = 9.5 \text{ N/mm}^2$$

The maximum occurring tensile splitting stress $\sigma_{\text{cx,max}}$ is as follows:

$$\sigma_{\text{cx,max}} = 0.19 \cdot \sigma_{\text{cm,max}} = 1.81 \text{ N/mm}^2$$

The tests on SFRC cylinders, drilled from a tunnel segment of the 2nd Heinenoord tunnel, showed that the tensile splitting strength in the radial direction is not increased by the addition of fibres at the circular joints as the fibres tend to orient in line with the crack. Consequently, the splitting stress caused by the working load needs to be checked using the splitting strength of the matrix and not the splitting strength of the composite. According to Eurocode 2, it follows that:

$$f_{\text{ctd,spl}} = \frac{f_{\text{ctd,ax}}}{0.9} = 2.5 \text{ N/mm}^2$$

with:

$$f_{ctd,ax} = \frac{f_{ctk,ax}}{\gamma_{ct}} = \frac{0.7 \cdot 0.3 \cdot (35)^{2/3}}{1.00} = 2.25 \text{ N/mm}^2$$

However, this is the long-term tensile strength. According to the Dutch design guidelines on concrete structures, the long-term tensile strength is a function of the characteristic cube compressive strength and can be determined as follows:

$$f_{ctd,ax} = \frac{f_{ctk,ax}}{\gamma_{ct}} = \frac{0.7 \cdot (1.05 + 0.05 \cdot f_{ck})}{\gamma_{ct}} = \frac{0.7 \cdot (1.05 + 0.05 \cdot 45)}{1.00} = 2.31 \text{ N/mm}^2$$

De Waal [8.5] proposed to use the short-term strength to check the stresses introduced by the thrust jacks:

$$f_{ctd,ax} = \frac{f_{ctk,ax}}{\gamma_{ct}} = \frac{0.95 \cdot (1.05 + 0.05 \cdot f_{ck})}{\gamma_{ct}} = 3.14 \text{ N/mm}^2 > 1.81 \text{ N/mm}^2$$

Obviously, the direct tensile splitting stress in radial direction does not exceed the short-term tensile splitting strength of the matrix and thus the SFRC will not crack in the circular cross-section.

As Figure 8.15 points out, the indirect tensile splitting stresses in tangential direction can be visualised with the help of the software programme FRITS. The white peaks in Figure 8.16 show that the (linear elastic) tensile stresses in tangential direction exceed the short-term tensile strength of the matrix. The maximum indirect tensile stress is 6.97 N/mm^2 so cracks can be expected in between the thrust jacking plates. The latter was also observed in practice [Kooiman, 1999]. However, the maximum crack width will be small, as the tensile strength is only locally exceeded. Furthermore, when the tunnel ring under consideration is pushed off the shield machine after the next ring is installed, the hoop force in the lining will close the cracks that occurred during the excavation process.

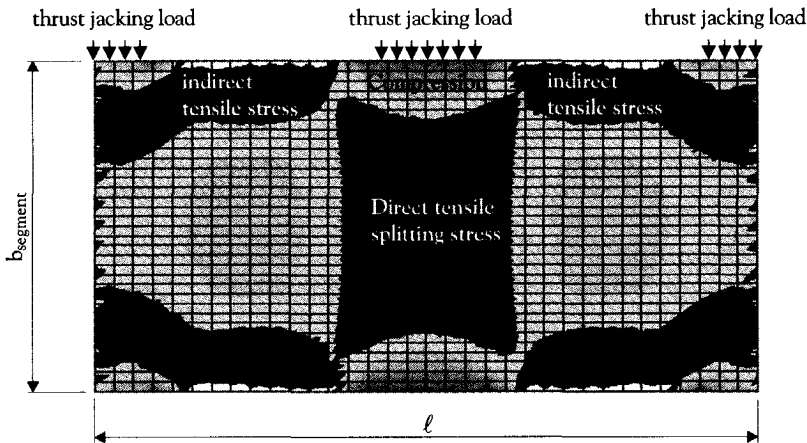


Figure 8.15 Stresses in tangential direction in segments of the 2nd Heinenoord tunnel

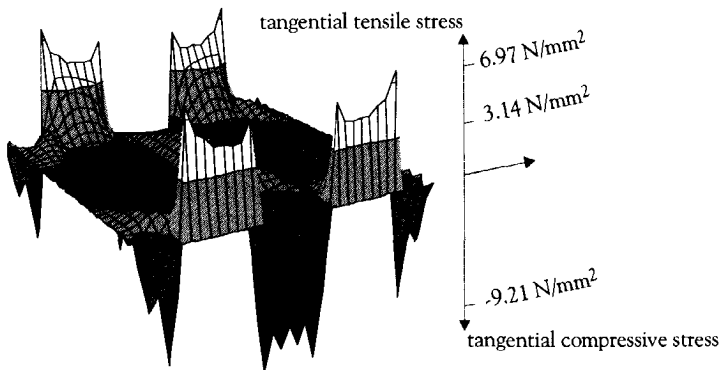


Figure 8.16 Tangential tensile stresses in tunnel segments of the 2nd Heinenoord tunnel

Shear key capacity and tensile stresses due to the maximum ring connecting forces

According to the original design calculations of the 2nd Heinenoord tunnel, the design value of the ring connecting force is 161 kN per segment. The capacity of the shear key connection had been checked in the original design, although they were initially not designed for any structural purposes. The design calculations showed that cracks were likely to occur in case of the design load, but the reinforcement was expected to prevent any major damage. In practice, however, damage was observed near the shear keys.

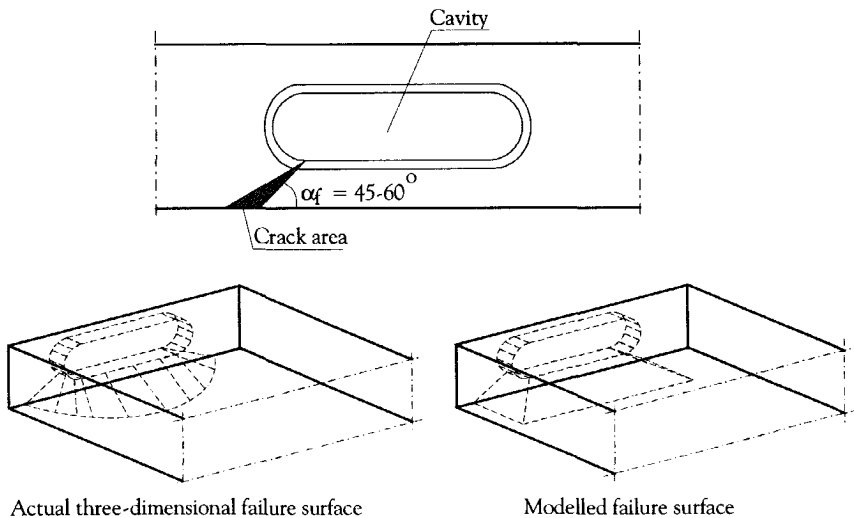


Figure 8.17 Shear key connection and failure mechanisms [De Waal, 1998]

To predict the shear key capacity, it is important to understand its failure mechanism. Figure 8.17 shows the failure mechanisms according to De Waal [De Waal, 1998]. This first failure mechanism has been observed in tests as well as in practice, while the second has been used for modelling purposes. Figure 8.18 shows how this second mechanism was modelled by Willemsen [Willemsen, 1998].

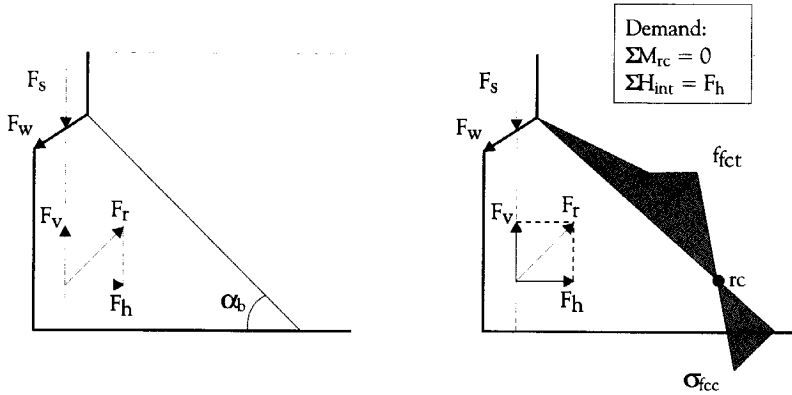


Figure 8.18 Modelling the failure mechanism at the shear key connection [Willemen, 1998]

The first model applies for the linear elastic case, while the other includes the bilinear softening behaviour of SFRC. With the help of FRITS, De Waal [De Waal, 1999] showed that the maximum resistance of a SFRC shear key connection is reached after crack initiation. Although the capacity of a SFRC shear key connection is higher than in case of plain concrete, the shear key connection, as it was originally designed for the 2nd Heinenoord tunnel, fails in the Ultimate Limit State. Tests on the traditionally reinforced and SFRC shear key connection showed, however, that the capacity of the SFRC connection was 25% higher than the originally designed shear key connection. De Waal [De Waal, 1999] demonstrated how to strengthen the shear key connection.

8.4 Concluding remarks

The tunnel lining case studied in this chapter clearly showed that the flexural behaviour of SFRC was not at all a dominant factor in the calculations. The resistance to concentrated loads was a much more dominant parameter and deserves more attention in the future. The case showed that it might be interesting to investigate in what way and to what extent fibre reinforcement influences the tensile splitting strength. Influencing parameters of the post-cracking behaviour, such as the matrix quality, the fibre characteristics and the fibre orientation will again be of great importance in this respect.

In other types of structural applications, the flexural behaviour of the material will be of much more importance than in case of a tunnel lining. The question, however, is not longer how to model the post-cracking behaviour of the material but in what way can the favourable post-cracking behaviour be taken into account in structural calculations? What is the redistributing capacity of the SFRC structure? To what extent is the external load increased before the statically indeterminate structure fails? What is the structural safety in reality?

Chapter 9

Conclusions and future perspectives

9.1 Conclusions

This thesis provides a procedure to develop a reliable, bilinear stress-crack width relation to describe the post-cracking behaviour of SFRC. With the help of inverse analysis, the material model can be used to fit mean results from three-point bending tests on medium strength SFRC with sufficient accuracy (<5%), taking several material parameters into account. Furthermore, this thesis provides relations to determine design values in the material model, based on common reliability methods. Taking scatter in load and resistance into account, material safety factors were determined for the post-cracking behaviour of SFRC. The resulting design model can be easily used to perform structural design calculations, although these calculations are limited to cross-sectional analyses.

Literature on the pullout behaviour of individually embedded steel fibres clearly showed that the matrix quality, the fibre characteristics and the fibre orientation are important influence parameters of the post-cracking behaviour of SFRC.

The matrix quality is an important factor as it influences the interfacial bond between the steel fibre and the matrix. As the matrix quality increases, the bond strength increases and the maximum pullout load increases. However, when the matrix quality exceeds a certain strength value the fibre might break, depending on the fibre characteristics.

Steel fibres are characterised by their aspect ratio, tensile strength and shape. Each fibre characteristic is important in the resistance to pullout. Therefore, every fibre type is characterised by its own pullout behaviour.

Pulling an inclined fibre from a cementitious matrix showed that the fibre orientation strongly influences the pullout behaviour. In the case that the fibre pullout direction is in line with the fibre orientation, the maximum pullout load is higher than when the fibre orientation is inclined towards the pullout direction.

It is obvious that the parameters that influence the pullout behaviour of individual steel fibres also affect the post-cracking behaviour of SFRC. Tests carried out in the scope of this research showed that in addition to these parameters the applied fibre volume and the fibre distribution also influence the post-cracking behaviour of SFRC.

Three-point bending tests were carried out to investigate the scatter in the post-cracking behaviour of SFRC. The test results show a wide range of scatter, as the coefficient of

variation V_M varied between 0.05 and 0.30, depending on the specimen size and the same parameters that affect the mean post-cracking behaviour.

After increasing the matrix quality, the coefficient of variation increased. Most probably, the matrix quality was increased to such a level that the mean pullout load per fibre approached the maximum pullout load of the fibre type in that specific matrix. Depending on the coincidental fibre distribution in the cross-section, the fibres in the mostly stressed cross-section immediately start to slip after crack initiation. In the case that there are few fibres located near the mostly stressed zone, the fibres immediately slip and the load-displacement diagram drops after crack initiation. On the other hand, when many fibres are located in the most stressed zone, the load might still increase after crack initiation.

Obviously, the number of fibres in the cross-section also influences the mean pullout load per fibre at crack opening. By decreasing the fibre volume, it was confirmed that the scatter increases. This is again attributed to the theory that at low fibre volumes, the mean pullout load per fibre at the moment of crack initiation increases to a level that corresponds to or even exceeds the maximum pullout load.

Just as the number of fibres in the cross-section is an important influencing parameter, the fibre distribution is also important. The actual fibre distribution depends on the mixing process and the method of compaction. The observed fibre distribution in the cross-section of test specimens showed that compaction by external vibration causes segregation of fibres and a planar fibre orientation perpendicular to the direction of vibration.

Although material size effects in the post-cracking behaviour of SFRC were not observed, some size-related effects were found that seem to be of significance when modelling the post-cracking behaviour of SFRC. The size of the cross-section, for instance, strongly affects the scatter in the post-cracking behaviour. It was observed that the scatter decreased considerably when the size of the loaded cross-section was increased.

The influence of scatter, expressed by the coefficient of variation V_M , on the design value of the equivalent post-cracking strength is considerable. Depending on the sample size (number of tests), the design value of the equivalent post-cracking strength decreases considerably. In this case, the test series consisted of 6 test samples. As a consequence, design values decrease to a value of only 30% of the mean value for a coefficient of variation $V_M = 0.30$.

It is not clear whether the observed scatter in test results applies for practical applications. Although the scatter seemed to decrease for increasing beam sizes, the scatter in practice also depends on the effectiveness of the fibre reinforcement. This depends on the fibre orientation as well as the orthogonal direction(s) of the occurring tensile stress(es).

In the tested beam specimens, the fibres tend to prefer a planar orientation as a result of the method of compaction. This was in line with the occurring tensile stresses. In practice, however, this is not necessarily the case.

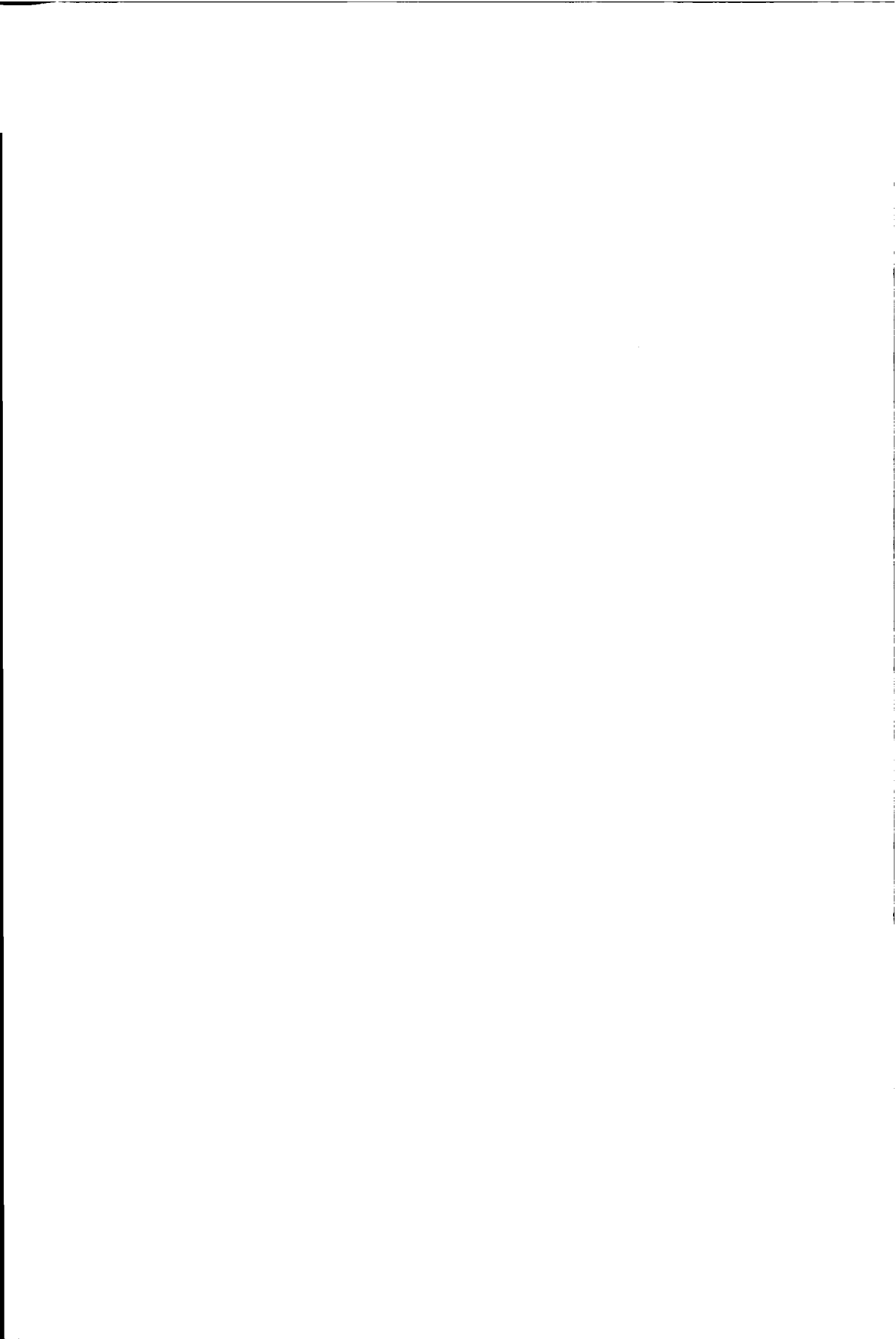
In case of SFRC tunnel segments, the fibre orientation is also tending to a planar orientation. In the centre of the circular joint, however, tensile stresses can occur perpendicular to the planar orientation as a result of the thrust jacking load. Therefore, the fibre reinforcement is not effective at that location and the capacity of the cross-section is equal to the plain matrix. In the segmental joints, however, the fibres are much more effective. The tunnel lining case that was studied in this thesis clearly showed that the flexural behaviour of SFRC was not at all a dominant factor in the calculations. The resistance to concentrated loads was much more dominant.

9.2 Future perspectives

The case study showed that it might be interesting to investigate in what way and to what extent fibre reinforcement influences the tensile splitting strength. Influencing parameters of the post-cracking behaviour, such as the matrix quality, the fibre characteristics and the fibre orientation will again be of great importance in this respect. The test method used, however, will also be an important influencing parameter.

In other types of structural applications, the flexural behaviour of the material will be of much more importance than in case of a tunnel lining. The application of SFRC in slabs or underwater concrete, for example, can only be stimulated when it can be proven that the fibre reinforcement contributes to the resistance of the structure to the applied loads. The question, therefore, is no longer how to model the post-cracking behaviour of the material but in what way can the favourable post-cracking behaviour be taken into account in structural calculations? Important in that respect is that the redistributing capacity of the SFRC structure can be demonstrated by determining to what extent the external load can be increased before statically indeterminate structures fail.

Structural calculations using Finite Element Methods may be useful in providing insight into the real contribution of fibre reinforcement to the structural load-bearing capacity. In that respect, the smeared crack approach seems attractive to use. The only problem is that the stress-crack width relation needs to be transformed to a stress-strain relation using the average crack spacing. This is however hard to determine and does not only depend on the material properties. Whether or not multiple cracking occurs also depends on the structural system, the load configuration and the geometry of the structure. Therefore, the discrete crack approach seems more appropriate to use. By carrying out structural analyses with a varying number of discrete cracks on different locations, the insight into the structural behaviour of SFRC can be enhanced.



Bibliography

- ACI Committee 544, *Design considerations for Steel Fibre Reinforced Concrete*, ACI Structural Journal, Vol. 85 (6), 1988, pp. 563-580.
- ACI committee 544, *Guide for specifying, proportioning, mixing, placing & finishing SFRC*, ACI Materials Journal, Jan-Feb 1993, pp. 94-101.
- Alwan, J.M., Naaman, A.E. & P. Guerrero, *Effect of mechanical damping on the pullout response of hooked steel fibres embedded in cementitious matrices*, Concrete Science & Engineering, Vol. 1, March 1999, pp. 15-25.
- Balagaruh, P.N. & S.P. Shah, *Fiber Reinforced Cement Composites*, McGrah Hill Publishers, 1992.
- Bartos, P.J.M. & C.W. Hoy, *Interaction of particles in Fibre Reinforced Concrete*, Proceedings of the International RILEM Conference 'Production Methods & Workability of Concrete', Paisley, Scotland, June 3-5, 1996, pp. 451-459.
- Bartos, P.J.M. & M. Duris, *Inclined tensile strength of steel fibres in a cement-based composite*, Composites, Vol. 25 (10), 1994, pp. 945-952.
- Bartos, P.J.M., *Fresh Concrete, Properties and Tests*, Developments in Civil Engineering part 38, Elsevier, Paisley, Scotland, 1992, p. 292.
- Bazant, Z.P. & B.H. Oh, *Crack band theory or fracture of concrete*, Materials and Structures, Vol. 16, 1983, pp. 155-177.
- Bazant, Z.P., *Size effect in blunt fracture: concrete, rock, metal*, ASCE Journal of Engineering Mechanics 110, 1984, pp. 518-535.
- Benjamin, J.R. and C.A. Cornell, *Probability, Statistics and Decision for Civil Engineers*, McGraw-Hill Book Company, 1970, pp. 249-285.
- Blom, C., *Girder action of a shield driven tunnel lining*, Masters thesis, Delft University of Technology (in Dutch), 1995.
- Campione, G. & S. Mindess, *Fibres as shear reinforcement for high strength reinforced concrete beams containing stirrups*, Proceedings of the IIIrd International RILEM Workshop 'High Performance Fibre Reinforced Cementitious Composites' (HPRCC 3), Mainz, 1999, pp. 519-530.
- Carpinteri, A. & B. Chaia, *Multifractal nature of concrete fracture surfaces and size effects on nominal fracture energy*, Materials and Structures, Vol.28, 1995, pp. 435-443.
- Casanova P., Rossi, P., Renwez, S. & A. Belloc, *Fabrication de Voussoirs en Béton de Fibres – Etude du Matériau*, Bulletin Liaison 196 du Laboratoire des Ponts et Chaussées, pp. 97-99, mars-avril 1995.

- Chanvillard, G. & O. Roque, *Behaviour of a fibre reinforced concrete cracked section under sustained load*, Proceedings of the IIIrd International RILEM Workshop 'High Performance Fibre Reinforced Cementitious Composites' (HPRCC 3), Mainz, 1999, pp. 239-250.
- Crow, E.L., Davis, F.A. & M.W. Maxfield, *Statistics Manual*, U.S. Naval Ordnance Test Station, Dover Publications Inc., New York, 1960, pp. 44-48.
- CUR-report 190: *Kansen in de Civiele Techniek - Deel 1 Probabilistisch ontwerpen in theorie*, CUR/Ministerie van Verkeer en Waterstaat, 1997, p. 240.
- DBV-Merkblatt, *Bemessungsgrundlagen für Stahlfaserbeton im Tunnelbau*, Design guidelines for the application of SFRC in tunnels (in German), Wiesbaden, September 1992, p. 19.
- De Larrard, F., *Concrete mixture proportioning, a scientific approach*, Modern Concrete Technology part 9, E&FN Spon, London & New York, 1999, p. 421.
- De Waal, R.G.A., *Steel Fibre Reinforced Tunnel Segments for the application in shield driven tunnel linings*, PhD-thesis, Department of Concrete Structures, Faculty of Civil Engineering, Delft University of Technology, Netherlands, 1999, p. 202.
- DIN 1045-1, *Tragwerke aus Beton, Stahlbeton und Spannbeton – Teil 1: Bemessung und Konstruktion*, Betonkalender 1999, Ernst & Sohn, Berlin.
- Edgington, J. & D.J. Hannant, *Steel fibre reinforced concrete, The effect on fibre orientation of compaction by vibration*, Materials and Structures, Vol. 5 (25), 1972, pp. 41-44.
- Edgington, J., Hannant, D.J. & R.I.T. Williams, *Steel fibre reinforced concrete*, Building Research Establishment, Department of the Environment, Current Paper 69/74, 1974.
- ENV 1992-1-1, *Eurocode 1: Basis of design and actions on structures – Part 1: Basis of design*, CEN, 1994.
- ENV 1992-1-1, *Eurocode 2: Design of Concrete Structures – Part 1: General rules and rules for buildings*, CEN, 1991.
- Erdmann, J., *Comparison of plain and the development of multi-dimensional tunnel design methods*, PhD-thesis, TU Braunschweig, 1983 (in German).
- Falkner, H. & V. Henke, *Steel Fibre Reinforced Concrete for underwater concrete slabs*, Proceedings of the International RILEM Conference 'Production Methods & Workability of Concrete', Paisley, Scotland, June 3-5, 1996, pp. 79-92.
- Glavind, M., *Evaluation of the compressive behaviour of Fibre Reinforced High Strength Concrete*, PhD-dissertation, Department of Structural Engineering, Technical University of Denmark, 1992, pp. 90-91.
- Guinea, G.V., Planas, J. & M. Elices, *Measurement of the fracture energy using three point bend tests: Part 1 - Influence of experimental procedures*, Materials & Structures, Vol. 25 (148), 1992, p. 212-218.
- Hasofer, A.M. & N. Lind, *An Exact and Invariant First-Order Reliability Format*, Journal of Engineering Mechanics Vol. 100, 1974, pp. 111-121.
- Hillerborg, A. & J. Rots, *Crack concepts and numerical modelling*, in 'Fracture Mechanics of Structures, from theory to applications', Edited by L. Elfgren, Chapman and Hall, London, 1989, pp. 128-146.
- Hillerborg, A., Modéer, M. & P.E. Petersson, *Analysis of crack formation & crack growth in concrete by means of fracture mechanics and finite elements*, Cement & Conc. Res., 6, 1976, pp. 773-782.
- Hordijk, D., *Local approach to fatigue of concrete*, PhD-thesis, Department of Concrete Structures, Faculty of Civil Engineering, Delft University of Technology, the Netherlands, 1991, pp. 131-134.

- Hoy, C.W. & P.J.M. Bartos, *Interaction and packing of fibres: effect on mixing proces*, Proceedings of the IIIrd International RILEM Workshop 'High Performance Fibre Reinforced Cementitious Composites' (HPFRCC 3), Mainz, 1999, pp. 181-193.
- Hoy, C.W., *Mixing and mix proportioning of fibre reinforced concrete*, PhD-thesis, Department of Civil, Structural and Environmental Engineering, University of Paisley, Scotland, 1998, p. 284.
- Iftimie, T., *Prefabricated lining, conceptional and comparative studies for optimal solution*, Proceedings of the international congress on tunnelling and ground conditions, Cairo, Egypt, Balkema, 1994, pp. 339-346.
- Imam, M.A., *Shear-moment interaction of steel fibre high strength concrete*, PhD-thesis, Catholic University of Leuven, Belgium, 1995, p. 199.
- ISO 2394, *General principles on reliability for structures*, International Organization for Standardization, 1996.
- Iyengar, S.R. & M.K. Prahakara, *A three dimensional elasticity solution for rectangular prisms under end loads*, Journal for Mathematics & Mechanics no. 6, 1969, pp. 321-332.
- Johnston, C.D. & R.W. Zemp, *Flexural fatigue behaviour of SFRC, influence of fibre content, fibre type and aspect ratio*, ACI Materials Journal, July-August 1995, pp. 374-383.
- Johnston, C.D., *Proportioning, mixing & placement of fibre reinforced cements and concrete's*, Proceedings of the International RILEM Conference 'Production Methods & Workability of Concrete', Paisley, Scotland, June 3-5, 1996, pp. 155-179.
- Kameswara Rao, C.V.S., *Effectiveness of random fibres in composites*, Cem. Conc. Res., 9, 1979, pp. 685-693.
- Kaushik, S.K. & V. Menon, *Behaviour of fibrous composites under impact and blast loads*, Fibre Reinforced Cements & Concretes 'Recent developments', Elsevier Applied Science, London & New York, 1989, pp. 240-250.
- Keer, J.G., *Fibre Reinforced concretes*, Concrete Technology and Design, Vol. 2, New Reinforced Concretes, 1984, pp. 52-102.
- König, G. & L. Kützing, *Modelling the increase of ductility of HPC under compressive forces, a fracture mechanical approach*, Proceedings of the IIIrd International RILEM Workshop 'High Performance Fibre Reinforced Cementitious Composites' (HPFRCC 3), Mainz, 1999, pp. 251-260.
- Konter, E., *A stress-strain model for steel fibre reinforced concrete*, Master's thesis, Delft University of Technology, 1999, p. 142.
- Kooiman, A.G., *Schaaleffecten in het nascheurgedrag van staalvezelbeton*, Laboratory report on size-effects in the post-cracking behaviour of SFRC (in Dutch), Stevinreport no. 25.5-98-9, Delft University of Technology, Netherlands, 1998, p. 27.
- Kooiman, A.G., *Staalvezelbeton in de linings van boortunnels, een state-of-the-art*, Literature survey (in Dutch), Stevinreport no. 25.5-96-10, Delft University of Technology, Netherlands, December 1996, p. 45.
- Kooiman, A.G., *Staalvezelbeton in de Tweede Heinenoord Tunnel, het definitieve ontwerp*, Design calculations (in Dutch), Stevinreport no. 25.5.97-3, Delft University of Technology, Netherlands, 1997, p. 25.
- Kooiman, A.G., *Staalvezelbeton in de Tweede Heinenoord Tunnel, het laboratoriumonderzoek*, Laboratory experiments (in Dutch), Stevinreport no. 25.5.97-7, Delft University of Technology, Netherlands, 1997, p. 32.

- Kooiman, A.G., *Staalvezelbeton in de Tweede Heinoord Tunnel, voorkeursorientatie vezels ten gevolge van productieproces*, Evaluation of the production process of SFRC tunnel segments (in Dutch), Stevinreport no. 25.5-98-3, Delft University of Technology, Netherlands, 1998, p. 21.
- Kooiman, A.G., Van der Veen, C. & M.H. Djourai, *Steel Fibre Reinforced Concrete segments suitable for application in the second Heinoord tunnel*, Proceedings of the XIIIth FIP Conference 'Challenges for concrete in the next Millenium', 23-29 May 1998, Amsterdam, Netherlands, pp. 719-722.
- Kooiman, A.G., Van der Veen, C. & M.H. Djourai, *Steel Fibre Reinforced Concrete segments in the Second Heinoord Tunnel*, Proceedings of the fib Symposium 1999 'The bridge between people', Prague, Czech Republic, 12-15 October 1999, pp. 685-690.
- Körmeling, H.A., *Strain rate and temperature behaviour of steel fibre concrete in tension*, PhD-thesis, Department of Concrete Structures, Faculty of Civil Engineering, Delft University of Technology, the Netherlands, 1986, pp. 4.13-4.14.
- Kosa, K. & A.E. Naaman, *Corrosion of steel fibre reinforced concrete*, ACI Materials Journal, Jan-Feb, 1990, pp. 27-37.
- Li, V.C. & H.C. Wu, *Conditions for pseudo strain hardening in fibre reinforced brittle matrix composites*, J. Applied Mechanics Review Vol. 45, no. 8, 1992, pp. 390-398.
- Li, V.C., Stang, H. & H. Krenchel, *Micro mechanics of crack bridging in fibre reinforced concrete*, Materials and Structures, Vol. 26, 1993, pp. 486-494.
- Lilliu, G. & J.G.M. van Mier, *Analysis of crack growth in the Brazilian test*, in Construction Materials – Theory and application, IBIDEM-Verlag, Stuttgart, Nov 1999, pp. 123-137.
- Love, A.E.H., *A treatise on the mathematical theory of elasticity*, Dover Publications, New York, 1944, pp. 131-132.
- Maidl, B.R., *Steel Fibre Reinforced Concrete*, Ernst & Sohn, 1995, Berlin, p. 292
- Mangat, P.S. & K. Gurusamy, *Permissible crack widths in steel fibre reinforced marine structures*, Materials & Structures, Vol. 20, 1987, pp. 339-347.
- Mangat, P.S. & R.N. Swamy, *Compactability of SFRC*, Concrete, vol. 8, May 1974, pp. 34-35.
- Markeset, G., *Failure of concrete under compressive strain gradients*, PhD-thesis, Norwegian Institute of Technology, Trondheim, Norway, December 1993, p. 168.
- Naaman, A.E. & S.P. Shah, *Pullout mechanism in steel fibre reinforced concrete*, ASCE Journal Struct. Div., Vol. 102, 1976, pp. 1537-1548.
- Naaman, A.E., *Fibres with hardening bond*, Proceedings of the IIIrd International RILEM Workshop 'High Performance Fibre Reinforced Cementitious Composites' (HPRCC 3), Mainz, 1999, pp. 471-486.
- Narayanan, R. & F.Y.S. Darwish, *Use of steel fibres as shear reinforcement*, ACI Journal, May-June 1987, pp. 216-227.
- Nemegeer, D., *Self levelling Fibre Reinforced Concrete*, Contribution to the Dutch Engineers Symposium at 'de Reehorst', Ede, Netherlands, June 1999.
- NEN 6720, *Technische grondslagen voor bouwconstructies TGB 1990 - Voorschriften beton: Constructieve eisen en rekenmethoden (VBC)*, NNI/CUR, 1991, p. 239.
- Neville, A.M., *Properties of Concrete*, Pitman International, London, 1978, pp. 480-483.
- Nowak, A.S. & K.R. Collins, *Reliability of Structures*, McGraw-Hill Book Company, 2000, pp. 181-208.

- Ong, K.C.G. & P. Paramisivam, *Cracking of steel fibre reinforced mortar due to restrained shrinkage*, Fibre Reinforced Cements & Concretes 'Recent developments', Elsevier Applied Science, London & New York, 1989, pp. 179-187.
- Pederson, C, *New production processes, Materials and Calculation Techniques for Fibre Reinforced Pipes*, PhD-thesis, Department of Structural Engineering and Materials, Technical University of Denmark, 1996.
- RILEM TC 162-TDF Draft Recommendation, *Test and design methods for SFRC, bending test*, Materials and Structures Vol. 33, Jan-Feb 2000, pp. 3-5.
- RILEM TC 162-TDF Draft Recommendation, *Test and design methods for SFRC, σ - ϵ design method*, Materials and Structures, Vol. 33, 2000, pp. 75-81.
- RILEM TC-89 FMT Draft Recommendation, *Determination of the fracture parameters of plain concrete using three-point bend tests*, Materials & Structures, Vol. 23, 1990, pp. 457-460.
- Roelfstra, P.E. & F.H. Wittmann, *Numerical method to link strain softening with failure of concrete*, In 'Fracture Toughness and Fracture Energy', Edited by F.H. Witmann, Elsevier, London, 1986.
- Romualdi, J.P. & J.A. Mandel, *Tensile strength of concrete affected by uniformly distributed and closely paced short lengths of wire reinforcement*, ACI Journal, Vol. 61 (6), June 1964, pp. 27-37.
- Schnütgen, *Structural applications of steel fibre reinforced concrete*, to be published in the proceedings of the RILEM workshop 'Structural applications of SFRC', in Milan, Italy, April 2000.
- Schönlín, K., *Ermittlung der Orientierung, Menge und Verteilung der Fasern in faserbewehrten Beton*, Beton und Stahlbetonbau 83, Heft 6, 1988, pp. 168-171.
- Schulze, H. & H. Duddeck, *Stresses in shield driven tunnel linings*, Beton- & Stahlbetonbau, 8, 1964, pp. 169-175.
- Shah, S.P., Peled, A., Aldea, C.M. & Y. Akkaya, *Scope of high performance fibre reinforced cementitious composites*, Proceedings of the IIIrd International RILEM Workshop 'High Performance Fibre Reinforced Cementitious Composites' (HPFRCC 3), Mainz, 1999, pp. 113-130.
- Soroushian, P. & C-D Lee, *Constitutive modelling of steel fibre reinforced concrete under direct tension and compression*, In 'Fibre Reinforced Cements and Concretes, Recent Developments', Elsevier Applied Science, London & New York, 1989, pp. 363-375.
- Soroushian, P. & C-D Lee, *Distribution and Orientation of fibres in SFRC*, ACI Materials Journal, Sept-Oct 1990, pp. 433-439.
- Souwerbren, C., *Betontechnologie*, Concrete technology (in Dutch), Cement en Betonreeks, Betonprisma, Den Bosch, Netherlands, 1995, p. 338.
- Stang, H. & T. Aarre, *Evaluation of crack width in FRC with conventional reinforcement*, Cement & Concrete Comp. 14, 1992, pp. 143-154.
- Stang, H., Li, V.C. & H. Krenchel, *Design and structural applications of stress crack width relations in fibre reinforced concrete*, Materials & Structures, Vol. 28, 1995, pp. 210-219.
- Stang, H., Li, Z. & S.P. Shah, *Pullout problem: stress versus fracture mechanical approach*, Journal of Eng. Mech., Vol. 116, October 1990, pp. 2136-2150.
- Stroband, J., *Standardisation of test methods for Steel Fibre Reinforced Concrete*, Laboratory report (in Dutch) no. 25.5.98-14, Delft University of Technology, Netherlands, 1998, p. 41.

- Stroeven, P. & S.P. Shah, *Use of radiography-image analysis for steel fibre reinforced concrete*, Testing and Test Methods of Fibre Reinforced Composites, Proceedings of the RILEM Symposium 1978, The Construction Press Ltd.
- Stroeven, P., *Morphometry of fibre reinforced cementitious materials*, Materials and Structures, Vol. 11 (61), 1978, pp. 31-37.
- Stroeven, P., *Steel fibre reinforcement at boundaries in concrete elements*, Proceedings of the IIIrd International RILEM Workshop 'High Performance Fibre Reinforced Cementitious Composites' (HPFRCC 3), Mainz, 1999, pp. 251-260.
- Sun, W., Pan, G., Yan, H., Qi, C. & H. Chen, *Study on the anti-exploding characteristics of fibre reinforced cement based composites*, Proceedings of the IIIrd International RILEM Workshop 'High Performance Fibre Reinforced Cementitious Composites' (HPFRCC 3), Mainz, 1999, pp. 565-574.
- Taerwe, L. & A. van Gijsel, *Influence of toughness effect of steel fibres on the design stress strain curve for high strength fibre reinforced concrete*, Contribution to Proceedings of the IInd International RILEM Workshop 'High Performance Fibre Reinforced Cementitious Composites' (HPFRCC 2), Ann Arbor (MI), USA, 1995, pp. 220.
- Taerwe, L., De Schuter, G., Van Gijsel, A., Vyncke, J., & S. Schaerlaekens, *Quantification of variations in the steel fibre content of fresh and hardened concrete*, Proceedings of the IIIrd International RILEM Workshop 'High Performance Fibre Reinforced Cementitious Composites' (HPFRCC 3), Mainz, 1999, pp. 213-222.
- Theodorakopoulos, D.D. & R.N. Swamy, *Steel fibres to resist punching shear, an engineering model to enhance durable service life*, Proceedings of the IIIrd International RILEM Workshop 'High Performance Fibre Reinforced Cementitious Composites' (HPFRCC 3), Mainz, 1999, pp. 575-582.
- Tschegg, E.K. & H.N. Linsbauer, *Testing procedure for determination of fracture mechanics parameters*, Patentschrift no. A-233/86, Österreichisches Patentamt, 1986.
- Van Gijsel, A., *A pullout model for hooked end steel fibres*, Proceedings of the IIIrd International RILEM Workshop 'High Performance Fibre Reinforced Cementitious Composites' (HPFRCC 3), Mainz, 1999, pp. 351-360.
- Van Gijsel, A., *Studie van het uitrekgedrag van staalvezels ingebed in een cementgebonden matrix met toepassing op staalvezelbeton onderworpen aan buiging*, Study of the pullout behaviour of steel fibres embedded in cementitious matrices for application in SFRC subjected to bending moments (in Dutch), PhD-thesis, Department of Buildings and Structures, Faculty of Applied Sciences, University of Gent, Belgium, 2000.
- Van Mier, J.G.M., *Fracture processes of concrete*, CRC Press, Boca Raton, Florida, 1997, pp. 241-242.
- Van Vliet, M.R.A., *Size effect in tensile fracture of concrete and rock*, PhD-thesis, Department of Concrete Structures, Faculty of Civil Engineering, Delft University of Technology, Netherlands, December 2000, p. 202.
- Vos, Ch. & H. Jager, *Construction technology of concrete structures*, Lecture notes on special subjects, Delft University of Technology, Sept. 1993, p. 240.
- Vrouwenvelder, A., *Design methods and models for shield driven tunnel linings – Reliability aspects*, Report of the L550 group for the committee L500 of the Dutch Centre for Underground Construction (in Dutch), 1997.
- Waal, R.G.A de, *Experiments on SFRC shear key connections*, Laboratory report (in Dutch) no. 25.5-98-1, Delft University of Technology, Netherlands, 1998.

- Waarts, P.H., *Structural Reliability using Finite Element Methods – An appraisal of Directional Adaptive Response Surface Sampling*, PhD-thesis, Delft University of Technology, Netherlands, June 2000, pp. 7-38.
- Wang, Y., Li, V.C. & S. Backer, *Modelling of fibre pullout from a cement matrix*, Intern. Journal of Cem. Comp. L. Conc. 10 (3), 1988, pp. 143-149.
- Weiler, B., Grosse, C. & H.W. Reinhardt, *Debonding behaviour of steel fibres with hooked ends*, Proceedings of the IIIrd International RILEM Workshop 'High Performance Fibre Reinforced Cementitious Composites' (HPRFCC 3), Mainz, 1999, pp. 423-436.
- Willemen, F.J., *Modelling of structural circular joint connections*, Masters thesis, Delft University of Technology (in Dutch), 1998.
- Wittmann, F.H., Rokugo, K., Brühwiler, E., Mihashi, H. & Simonin, P., *Fracture energy and strain softening of concrete as determined by means of compact tension specimens*, Materials and Structures, Vol. 20, 1988, pp. 21-32.
- Wolinski, Hordijk, Reinhardt & Cornelissen, *Influence of aggregate size on fracture mechanics parameters of concrete*, International Journal of Cementitious Composites & Lightweight Concrete, 9, 1987, pp. 95-103.



Appendix A

Scenarios for Multiple Criteria Analysis of test methods

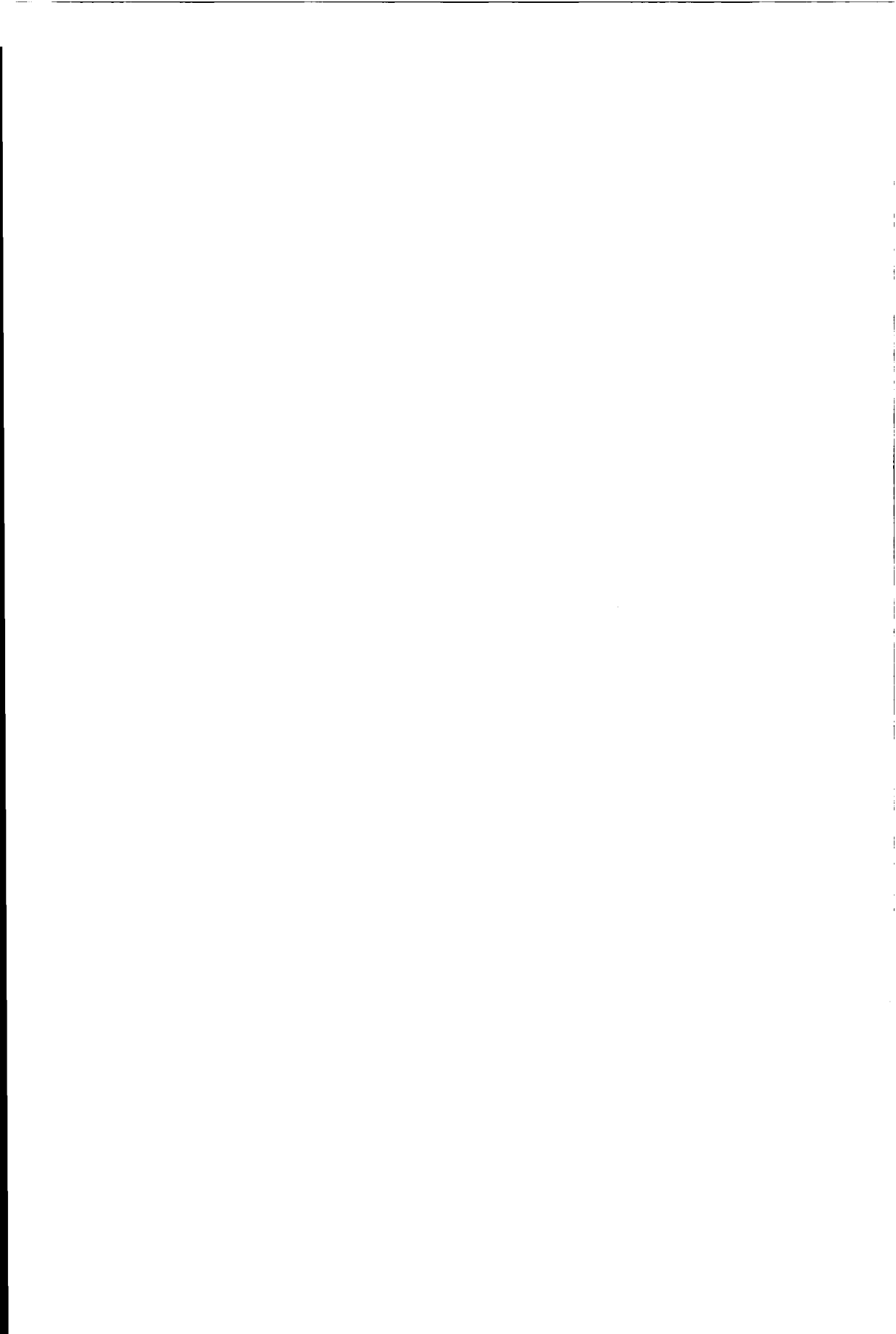
Scenario A: Different weight scale

Criteria	weight factor	Four-point bending test ¹		Three-point bending test		Brazilian splitting test		Wedge splitting test		Uni-axial tensile test	
		score	Π	score	Π	score	Π	score	Π	score	Π
Complexity of test set-up	1	3	3	3	3	5	5	4	4	1	1
Complexity of preparation	2	4	8	3	6	5	10	3	6	1	2
Complexity of execution	3	3	9	3	9	3	9	3	9	1	3
Reproducibility of the tests	5	3	15	3	15	3	15	3	15	3	15
Costs per experiment	1	3	3	2	2	5	5	4	4	1	1
Acceptance of test method	3	2	6	5	15	3	9	3	9	3	9
Processing complexity	2	2	4	3	6	4	8	3	6	5	10
Reliability of test results	5	3	15	3	15	1	5	3	15	3	15
Total score Σ			63		71		66		68		56

Scenario B: Neglecting acceptance criterion

Criteria	weight factor	Four-point bending test ¹		Three-point bending test		Brazilian splitting test		Wedge splitting test		Uni-axial tensile test	
		score	Π	score	Π	score	Π	score	Π	score	Π
Complexity of test set-up	1	3	3	3	3	5	5	4	4	1	1
Complexity of preparation	2	4	8	3	6	5	10	3	6	1	2
Complexity of execution	3	3	9	3	9	3	9	3	9	1	3
Reproducibility of the tests	5	3	15	3	15	3	15	3	15	3	15
Costs per experiment	1	3	3	2	2	5	5	4	4	1	1
Processing complexity	2	2	4	3	6	4	8	3	6	5	10
Reliability of test results	5	3	15	3	15	1	5	3	15	3	15
Total score Σ			57		56		57		59		47

¹ without notch



Appendix B

Compensation of specimen's weight in determination of G_{fc}

To enable a comparison of results from three-point bending tests on beam specimens with different dimensions the toughness value D_{fc} was divided by the beam's cross-section above the notch. For that same reason, the effect of the beam's dead load P_d had to be taken into account.

In the determination of the total toughness D_{fc} , the effect of the specimen's weight is accounted for by the additional toughness ΔD_{fc} , illustrated by the shaded area under the P- δ curve in Figure B.1. In this case, the tests were stopped at a deformation δ_s . To account for the weight-effect in the comparison of $G_{fc,2.0}$ -values in Chapter 3, only the contribution $\Delta D_{fc}(2.0)$ up to the deformation at test stop $\delta = 2.0$ mm is taken into account. For practical reasons, the triangle $OO'O''$ is not account for. Its contribution to $\Delta D_{fc}(2.0)$, however, is negligible.

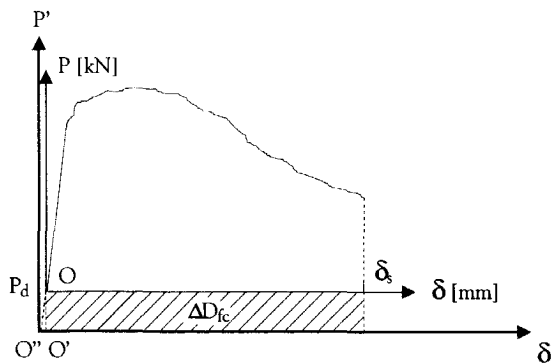
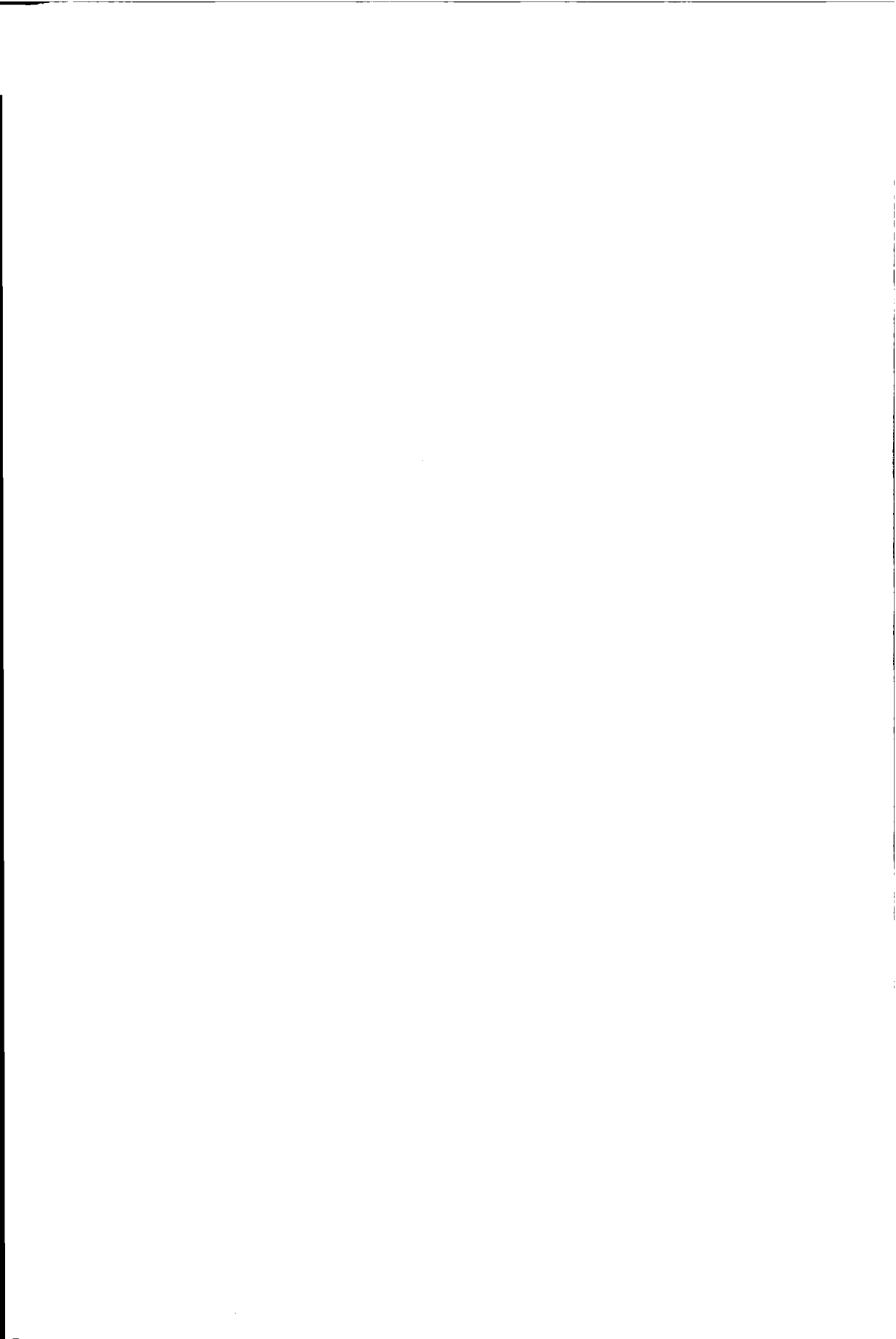


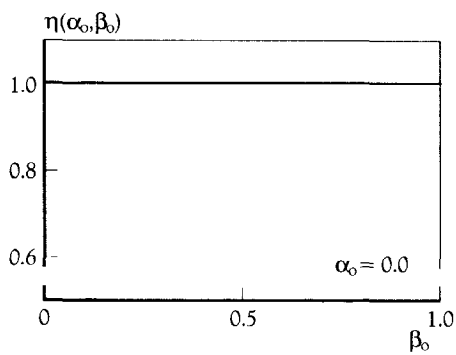
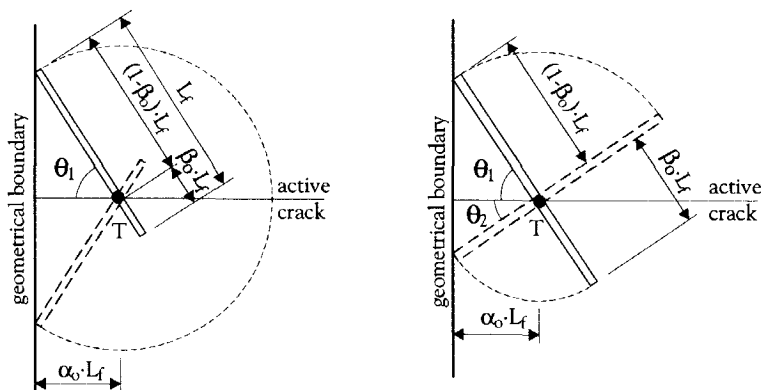
Figure B.1 Contribution to the total toughness of the specimen's weight

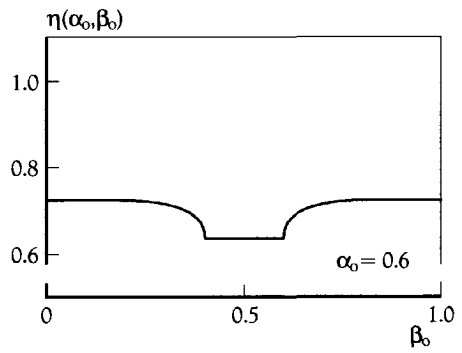
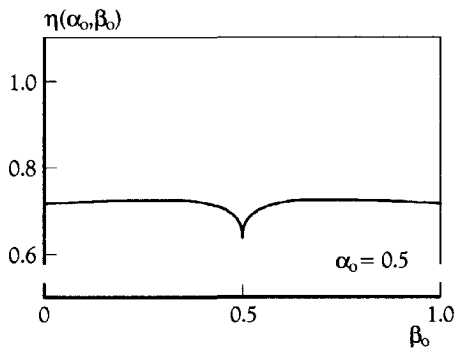
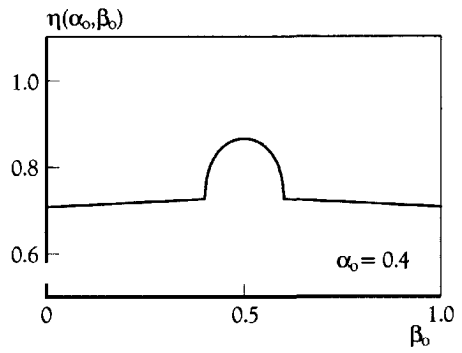
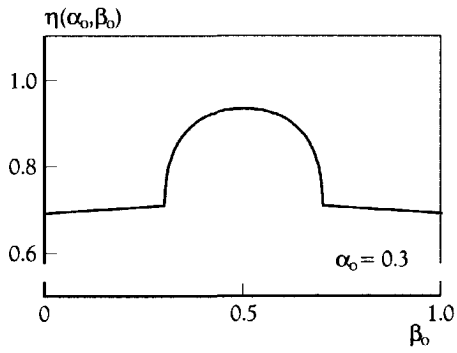
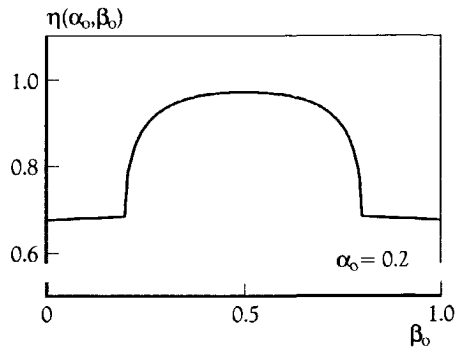
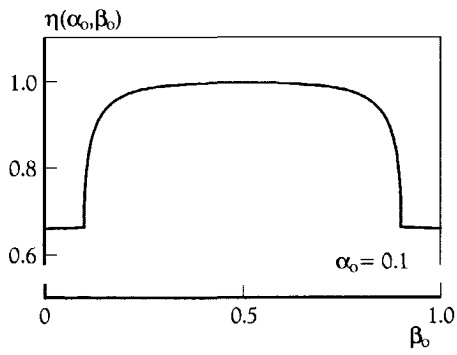
The contribution of the dead load as demonstrated in Figure B.1 is considerably exaggerated. Calculations showed that in case of the SFRC mixtures under consideration, the contribution to the energy absorption capacity G_{fc} up to $\delta = 2.0$ mm was less than 1%. In addition, the dead load that was accounted for in these calculations was less than 1% of the maximum load.

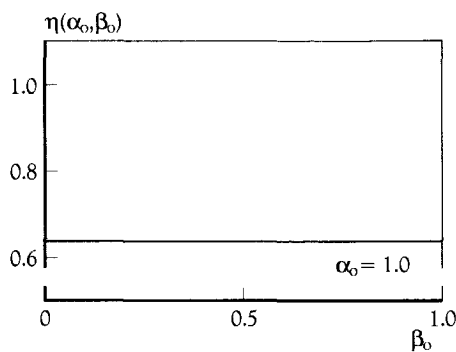
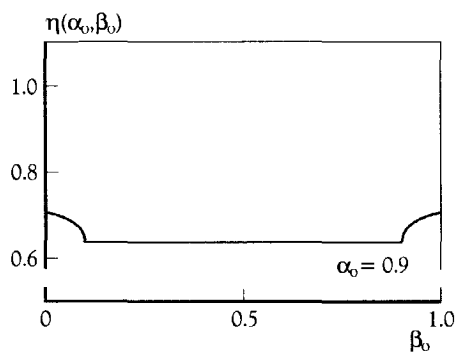
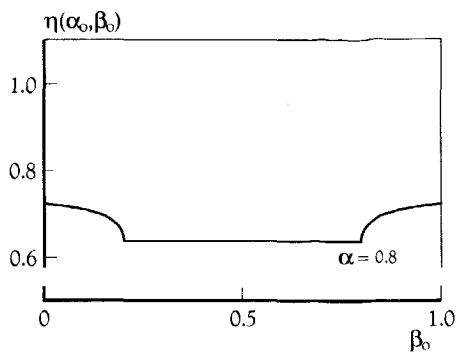
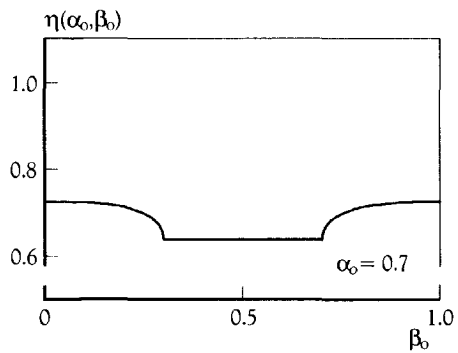


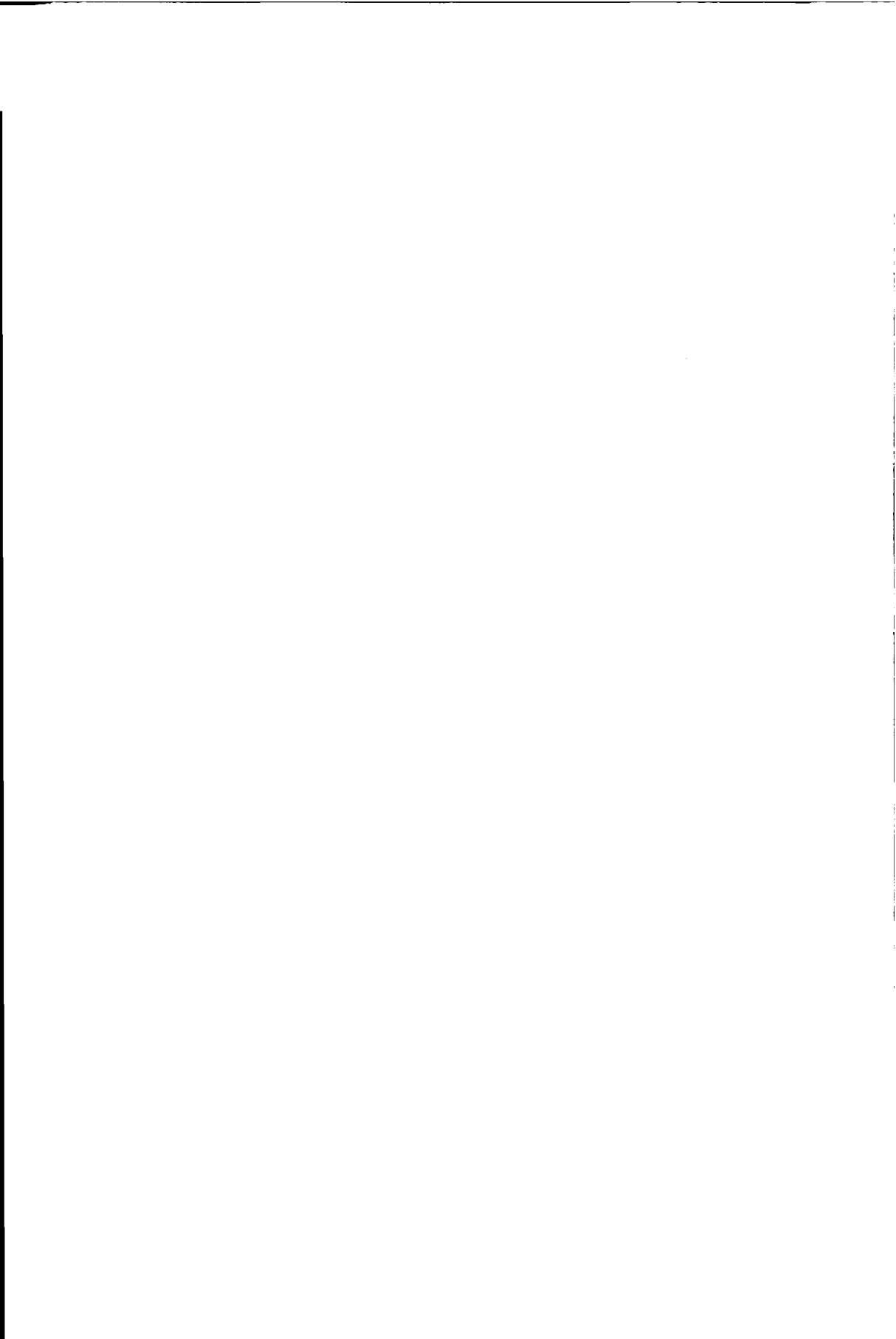
Appendix C

Orientation efficiency close to a boundary









Notations and Symbols

Properties of plain concrete

f_{cc}	= compressive strength of plain concrete matrix	[N/mm ²]
f_{ccd}	= design compressive strength of plain concrete matrix	[N/mm ²]
f_{cek}	= characteristic compressive strength of plain concrete matrix	[N/mm ²]
$f_{ct,ax}$	= tensile strength of plain concrete matrix	[N/mm ²]
ℓ_{cb}	= crack band width	[mm]
p	= empirical shape factor for softening behaviour of plain concrete	[-]
w	= crack width	[mm]
w_c	= characteristic crack width	[mm]
$w_{c,50}$	= characteristic crack width at 50% of the peak stress	[mm]
w_0	= critical crack width	[mm]
D_c	= toughness of plain concrete	[kNmm]
E_c	= Young's modulus of plain concrete matrix	[N/mm ²]
G_f	= fracture energy of plain concrete	[N/mm ²]
δ	= crack opening displacement	[mm]
ϵ_c	= strain in plain concrete	[%o]
ϵ_0	= ultimate strain in plain concrete	[%o]
ϵ_{cc}	= compressive strain in plain concrete	[%o]
ϵ_{ccu}	= compressive strain in plain concrete at compressive strength	[%o]
ϵ_{ct}	= linear elastic strain limit of plain concrete in tension	[%o]
σ_c	= stress in plain concrete	[N/mm ²]
σ_{cc}	= compressive stress in plain concrete	[N/mm ²]
σ_{ct}	= tensile stress in plain concrete	[N/mm ²]

Components in SFRC Mix

c	= cement weight	[kg]
$d_{g,max}$	= maximum grain size	[mm]
g	= aggregate content	[kg]
F	= fibre content	[kg]
V_c	= volume fraction of plain concrete matrix	[%]
V_f	= volume fraction of fibres	[%]
$V_{f,max}$	= maximum volume fraction of fibres	[%]
V_p	= volume fraction of pores	[%]
V_w	= volume fraction of water	[%]
ρ_c	= specific gravity of cement	[kg/m ³]
ρ_g	= specific gravity of aggregates	[kg/m ³]

Fibre characteristics and features of fibre pullout test

d_f	= fibre diameter	[mm]
f_{fu}	= yield stress of steel fibre	[N/mm ²]
n_f	= number of fibres in cross section	[-]
n_{fm}	= mean number of fibres in cross section	[-]
E_f	= Young's modulus of fibre	[N/mm ²]
L_f	= fibre length	[mm]
L_{fd}	= debonded fibre length	[mm]
L_{fe}	= embedded fibre length	[mm]
P^i	= pullout load	[N]
δ_f^i	= fibre-end displacement in pullout test	[mm]
η_θ	= efficiency factor depending on fibre orientation	[-]
η_l	= efficiency factor depending on fibre length	[-]
ρ_f	= specific gravity of fibre material	[kg/m ³]
σ_f^i	= fibre bridging stress for a single fibre system	[N/mm ²]
τ_0	= adhesive bond between fibre and matrix at $w = 0$	[N/mm ²]
$\tau(\delta_f)$	= bond stress between fibre and matrix	[N/mm ²]

Properties of SFRC

f_{fc}	= stress in fibre reinforced cementitious composite	[N/mm ²]
f_{fcc}	= compressive strength of SFRC	[N/mm ²]
f_{fccd}	= design compressive strength of SFRC	[N/mm ²]
f_{fcck}	= characteristic compressive strength of SFRC	[N/mm ²]
f_{fccm}	= mean compressive strength of SFRC	[N/mm ²]
$f_{fct,ax}$	= axial tensile strength of SFRC	[N/mm ²]
$f_{fct,eq,bil}$	= equivalent post-cracking strength of SFRC in bilinear softening relationship	[N/mm ²]
$f_{fctd,eq}$	= design value of equivalent post-cracking strength of SFRC	[N/mm ²]
$f_{fctd,fl}$	= design value of flexural strength of SFRC	[N/mm ²]
$f_{fctk,ax}$	= characteristic axial tensile strength of SFRC	[N/mm ²]
$f_{fctk,eq}$	= characteristic value of equivalent post-cracking strength of SFRC	[N/mm ²]
$f_{fctk,fl}$	= characteristic flexural strength of SFRC	[N/mm ²]
$f_{fctm,ax}$	= mean axial tensile strength of SFRC	[N/mm ²]
$f_{fctm,eq}$	= mean value of equivalent post-cracking strength of SFRC	[N/mm ²]
$f_{fctm,fl}$	= mean flexural strength of SFRC	[N/mm ²]
$f_{fctm,spl}$	= mean tensile splitting strength of SFRC	[N/mm ²]
$f_{fctms,eq}$	= mean equivalent post-cracking strength of SFRC determined from test sample	[N/mm ²]
$f_{fctms,eq,bil}$	= mean equivalent post-cracking strength of SFRC in bilinear relationship determined from test sample	[N/mm ²]
$f_{fctms,fl}$	= mean flexural strength of SFRC determined from test sample	[N/mm ²]
f_{ps}	= pre-stress in steel fibre	[N/mm ²]
$f_{fct,fl}^1$	= measured flexural strength of SFRC	[N/mm ²]
$f_{fct,eq}^1$	= equivalent post-cracking strength of SFRC in individual test sample	[N/mm ²]
f_{ps}^0	= initial pre-stress in steel fibre before cracking of matrix	[N/mm ²]
w_c	= characteristic crack width	[mm]
w_0	= critical crack width	[mm]
w^*	= crack width corresponding to full debonding	[mm]
E_{fc}	= Young's modulus of fibre reinforced cementitious composite	[N/mm ²]
G_{fc}	= energy absorption capacity of SFRC	[kN/mm]
G_{fcm}	= mean energy absorption capacity of SFRC	[kN/mm]
D_f	= contribution to toughness of SFRC by fibres	[kNmm]
D_{fc}	= toughness of SFRC	[kNmm]

D_{fcm}	= mean toughness of SFRC	[kNmm]
PD_f	= packing density of the dry material in SFRC	[-]
RI	= reinforcement index	[-]
α_f	= bond factor	[N/mm ²]
β_f	= fibre factor (incorporates difference in shear stress between different types of fibres)	[N/mm ²]
δ_{max}	= crack opening displacement at maximum bending load	[mm]
δ^*	= crack opening displacement corresponding to full debonding	[mm]
δ_{cg}	= additional crack opening displacement resulting from the Cook-Gordon effect	[mm]
ϵ_{fc}	= strain in fibre reinforced cementitious composite	[%o]
ϵ_{fcc}	= compressive strain in fibre reinforced cementitious composite	[%o]
ϵ_{fct}	= tensile strain in fibre reinforced cementitious composite	[%o]
λ_f	= fibre reinforcement factor	[N/mm ²]
σ_{fc}	= stress in fibre reinforced cementitious composite	[N/mm ²]
σ_{fcc}	= compressive stress in fibre reinforced cementitious composite	[N/mm ²]
σ_{fct}	= tensile stress in fibre reinforced cementitious composite	[N/mm ²]
ξ	= post-cracking factor for long-term loading and size-effects	[-]

Probabilistic parameters

n	= number tests	[-]
s_f	= standard deviation of population of f_{fc}	[N/mm ²]
s_{fs}	= standard deviation of f_{fc} in test sample	[N/mm ²]
s_G	= standard deviation of population of G_{fct}	[kN/mm]
s_Q	= standard deviation in load	[N/mm ²]
s_R	= standard deviation in resistance	[N/mm ²]
s_Z	= standard deviation in reliability function	[N/mm ²]
$t_{\alpha/2, n-1}$	= value for a t-test with $(1-\alpha)$ -100% confidence level	[-]
P_f	= probability of failure	[-]
Q	= stochastic load variable	[-]
R	= stochastic resistance variable	[-]
Z	= reliability function	[-]
V_A	= coefficient of variation in uncertainty in material or structural	[-]
V_G	= coefficient of variation in energy absorption capacity	[-]
V_M	= coefficient of variation in material properties	[-]
V_Q	= coefficient of variation in load	[-]
V_R	= coefficient of variation in resistance	[-]
V_S	= coefficient of variation in geometrical properties	[-]
α_Q	= influence factor to emphasise scatter in load	[-]
α_R	= influence factor to emphasise scatter in resistance	[-]
β	= reliability index	[-]
γ_c	= central safety coefficient	[-]
γ_{cc}	= material safety factor for plain concrete in compression	[-]
γ_{ct}	= material safety factor for plain concrete in tension	[-]
γ_{fcc}	= material safety factor for SFRC in compression	[-]
γ_{fct}	= material safety factor for SFRC in tension	[-]
$\gamma_{fct,el}$	= material safety factor for the linear-elastic behaviour of SFRC	[-]
$\gamma_{fct,pl}$	= material safety factor for the post-cracking behaviour of SFRC	[-]
γ_k	= overall safety coefficient	[-]
γ_Q	= load safety factor	[-]
γ_R	= material safety factor	[-]
μ_R	= expected value of resistance variable	[-]
μ_Q	= expected value of resistance variable	[-]
μ_Z	= expected value of resistance variable	[-]

Features of three point bending test

a	= notch depth of specimen	[mm]
b	= width of specimen	[mm]
h	= depth of specimen	[mm]
h_{lig}	= effective beam depth = $h-a$	[mm]
l	= span length of specimen	[mm]
n	= number of tests in test series	[-]
A	= surface of the cross section	[mm ²]
P	= applied load on specimen	[kN]
P_{max}	= maximum bending load	[kN]
P_{crack}	= bending load at first crack	[kN]
δ	= crack opening displacement at notch tip	[mm]

Features of multi-layer simulations

h_i	= layer depth	[mm]
ℓ_i	= influence length	[mm]
P_c	= computed load on specimen	[kN]
P_m	= measured load on specimen	[kN]
$P_{c,crack}$	= computed load on specimen at first crack	[kN]
$P_{c,max}$	= maximum computed load on specimen	[kN]

Parameters in the case study

k_i	= bedding stiffness of soil layer	[kN/m]
q_i	= effective load on tunnel lining in axial direction	[N/mm ²]
EI_{eq}	= equivalent bending stiffness	[N/mm ²]
GA_{eq}	= equivalent shearing stiffness	[N/mm ²]
E_s	= stiffness of soil layer	[m]
D	= diameter of tunnel lining	[m]
F_{work}	= working load of the shield machine per couple of thrust jacking	[kN]
H	= total depth of soil layers above tunnel lining	[m]
N	= normal force in the circular cross section	[kN]
M	= bending moment in the circular cross section	[kNm]
R	= radius of tunnel lining	[m]
γ'_s	= effective weight soil	
ν_s	= Poisson ratio of soil	

Samenvatting

Nu het aantal praktische toepassingen van staalvezelbeton toeneemt, ontstaat de behoefte aan gestandaardiseerde beproevingsmethoden en ontwerprichtlijnen. Om deze behoefte te bevredigen, moeten bestaande testmethoden worden geëvalueerd, zodat een keuze gemaakt kan worden voor een geschikte beproevingsmethode. De meetresultaten uit deze beproevingsmethode dienen vervolgens te worden omgezet naar een betrouwbaar materiaalmodel dat kan worden gebruikt in het ontwerp van constructieve toepassingen.

Een betrouwbaar materiaalmodel leidt echter niet automatisch tot betrouwbare, met staalvezels gewapende, betonnen constructies. In werkelijkheid zal inzicht in het constructieve gedrag van staalvezelbeton verworven dienen te worden om daadwerkelijk tot betrouwbare constructieve toepassingen te leiden. Kennis en inzicht in het nascheurgedrag van staalvezelbeton zijn echter van essentieel belang om het constructieve gedrag überhaupt te kunnen onderzoeken.

Om inzicht te krijgen in het nascheurgedrag van staalvezelbeton, gaat deel I van dit proefschrift in op de eigenschappen van het materiaal. Aan de hand van het uittrekgedrag van individuele vezels wordt uitgelegd dat de matrixkwaliteit, de vezeleigenschappen en de vezeloriëntatie van invloed zijn op het nascheurgedrag van staalvezelbeton (Hoofdstuk 2).

Na een evaluatie van verschillende bestaande beproevingsmethoden is een beargumenteerde keuze gemaakt voor een testmethode die is gebruikt tijdens het experimentele onderzoek (Hoofdstuk 3). Proeven op voor de praktijk interessante, standaard proefstukken vertonen een spreiding in breukenergie, uitgedrukt in de variatiecoëfficiënt V_G . Deze variatiecoëfficiënt is afhankelijk van de matrixkwaliteit, de toegevoegde vezelhoeveelheid en de vezelverdeling. De vezelverdeling blijkt grotendeels afhankelijk te zijn van de wijze waarop de mal is gevuld en de manier waarop verdichting heeft plaatsgevonden. In proefstukken waarbij de balkhoogte en breedte 7,5 maal groter zijn dan de vezellengte, is de waargenomen variatiecoëfficiënt aanzienlijk kleiner dan in de standaardproefstukken waarbij de vergrotingsfactor gelijk is aan 2.5.

In deel II van dit proefschrift gaat het om het modelleren van het nascheurgedrag van staalvezelbeton. De bestaande methoden zijn beschreven en geëvalueerd, waarna een beargumenteerde keuze is gemaakt voor het modelleren van het nascheurgedrag door inverse analyse van staalvezelbetonnen doorsneden in buiging (Hoofdstuk 4).

Er zijn verschillende invoerparameters die bij het invers modelleren een rol kunnen spelen. Met behulp van een eenvoudige procedure is de invloed van deze invoerparameters op de gesimuleerde buigproefresultaten systematisch onderzocht. Op basis van deze

parameterstudie en een vergelijking van gesimuleerde resultaten met meetresultaten, blijkt dat een bi-lineaire spanning-scheurwijdte relatie tot een nauwkeurige beschrijving leidt van het nascheurgedrag van staalvezelbeton (Hoofdstuk 5).

In deel III wordt een vertaling gemaakt van het nascheurgedrag van staalvezelbeton dat is waargenomen in experimenten, naar het gedrag in praktische toepassingen. Dit is mogelijk gemaakt door de oriëntatie en effectiviteit van de vezelwapening te bepalen aan de hand van proefresultaten en dat te relateren aan de wijze van productie van deze proefstukken. Na de theoretisch bepaalde vezeffectiviteit te hebben gekoppeld aan de bi-lineaire relatie voor het nascheurgedrag, en verschillende resultaten van driepuntsbuigproeven te hebben gesimuleerd, lijkt er een duidelijk verband te bestaan tussen de kritische scheurwijdte in het spanning-scheurwijdte diagram en het gemiddelde van de geprojecteerde lengte van de ingebedde vezels. Als gevolg van het feit dat aan de hand van de stort- en verdichtingswijze een voorspelling mogelijk is van de voorkeursoriëntatie, kan het buiggedrag van een constructieve doorsnede worden voorspeld (Hoofdstuk 6).

Er zijn echter altijd bepaalde onzekerheden waar rekening mee moet worden gehouden bij het ontwerpen van een constructie. Deze onzekerheden worden in de praktijk vaak verwerkt tot veiligheidsfactoren, die op basis van standaard betrouwbaarheidsmethoden tot stand komen. Op basis van de gevonden spreiding in het materiaal, de nauwkeurigheid van de spanning-scheurwijdte relatie en de spreidingen in de optredende belastingen, zijn veiligheidsfactoren bepaald die kunnen worden toegepast op het gemodelleerde nascheurgedrag van staalvezelbeton (Hoofdstuk 7).

Deel IV toont op welke wijze het materiaalmodel kan worden gehanteerd in ontwerpberoeeningen. Uit de gekozen casus, het berekenen van de bezwijkcapaciteit van staalvezelbetonnen tunnelsegmenten voor de 2^e Heinenoordtunnel, blijkt dat de maatgevende combinatie van buigend moment en normaaldrukkracht totaal niet kritisch is. De optredende slijtspanningen vormen echter wel een kritisch belastinggeval.

Dit proefschrift laat een procedure zien waarmee een betrouwbaar bi-lineaire spanning-scheurwijdte relatie ontwikkeld kan worden, ter beschrijving van het nascheurgedrag van staalvezelbeton. Het blijft echter de vraag op welke manier het gunstige nascheurgedrag kan worden benut in ontwerpberoeeningen van meervoudig statisch onbepaalde constructies. Aanbevolen wordt dan ook onderzoek te doen naar scheurvorming in (meervoudig) statisch onbepaalde systemen van staalvezelbeton. Daarnaast is ook nader onderzoek gewenst ten aanzien van de weerstand tegen slijtbelastingen.

Alain Kooiman

Stellingen

De stortrichting, de afstand waarover het natte mengsel kan uitvloeien en de eventueel gebruikte methode van verdichten is bepalend voor de werkelijke herverdelingscapaciteit van met staalvezels gewapend betonnen constructies.

The direction of pouring, the distance of flowing and, if applicable, the method of compaction determine the actual redistributing capacity of steel fibre reinforced concrete structures.

De variatie in het nascheurgedrag van staalvezelbeton is relatief groot. De variatie in deze variatie is echter groter.

The variation in the post-cracking behaviour of SFRC is relatively large. However, the variation in this variation is larger.

Het op een accurate wijze modelleren van het materiaalgedrag van staalvezelbeton zal het aantal praktische toepassingen niet vergroten.

Accurate modelling of the material behaviour of steel fibre reinforced concrete will not increase the number of applications in practice.

Zachte persoonskenmerken zijn essentiële eigenschappen om de materiaaleigenschappen van verhard staalvezelbeton experimenteel te kunnen onderzoeken.

Soft personality characteristics are of paramount importance to investigate the properties of steel fibre reinforced concrete by experiments.

Door promovendi te trainen in sociale en communicatieve vaardigheden zal de inhoudelijke kwaliteit van hun proefschriften verbeteren.

By training PhD students in their social and communicative skills the quality of content of their dissertations will be improved.

Een planning dient niet om het werk af te ronden binnen de werktijd die er voor gepland is.

A work schedule does not serve to finish the work within the amount of working time that has been planned for it.

De enige echte deadline is een horizontale lijn.
The only real deadline is a flat-line.

De voetbalsport herbergt een belangrijke levensles: als het positiespel goed gespeeld wordt, houd je controle over de wedstrijd.
Football can teach us an important lesson for life: when the positional game is played well, one is able to control the match.

Tijdens EURO 2000 hebben de voetbalmiljonairs van het Nederlands Elftal wederom bewezen dat superieure technische vaardigheden niet voldoende zijn om de top te bereiken.
During EURO 2000 the millionaires of the Dutch National Football Team once again showed that superior technical skills are not sufficient to reach the top.

De Nieuwe Economie is een term die alleen verzonnen kan zijn door zij die geen tekort hebben aan schaarse (primaire) goederen.
The New Economy is term that can only have been invented by those having no shortage of scarce (primary) goods.

Curriculum vitae

- 13 oktober 1973 Geboren te Capelle aan den IJssel als Alain Geoffré KOOIMAN.
- Sept. 1985 - juni 1991 VWO, Emmauscollege, Rotterdam.
- Sept. 1991 - juni 1996 Civiele Techniek, Technische Universiteit Delft, Nederland.
Scriptie over drijvende betonnen ondersteuningsconstructies van gasplatforms ter ontwikkeling van marginale velden op het Nederlands Continentaal Plat.
- Juni 1992 - mei 1995 Semi-professioneel voetballer, Feyenoord Rotterdam, Nederland.
- Juni 1996 - aug. 2000 Promovendus, Sectie betonconstructies, Faculteit Civiele Techniek en Geowetenschappen, Technische Universiteit Delft, Nederland.
- Sept. 1997 - juni 1999 Post-academische vorming Bedrijfskunde,
Limburg Universitair Centrum, Hasselt, Belgium.
- Jan. 1998 - jan. 2000 Voorzitter Promovendi Overleg Delft (PROMOOD),
Technische Universiteit Delft, Nederland.
- Sept. 2000 - okt. 2000 Adviseur van de Sectie Betonconstructies ter ontwikkeling van beleid op het gebied van Opleiding en Begeleiding van promovendi,
Faculteit Civiele Techniek en Geowetenschappen,
Technische Universiteit Delft, Nederland.

